



Virginia Commonwealth University
VCU Scholars Compass

Theses and Dissertations


Graduate School

2015

Gas-Phase Reactions and Mechanistic Details of Gold, Silver, and Iridium Complexes

Christopher Swift
Virginia Commonwealth University

Follow this and additional works at: <https://scholarscompass.vcu.edu/etd>

 Part of the [Organic Chemistry Commons](#), [Other Chemistry Commons](#), and the [Physical Chemistry Commons](#)

© The Author

Downloaded from

<https://scholarscompass.vcu.edu/etd/3731>

This Dissertation is brought to you for free and open access by the Graduate School at VCU Scholars Compass. It has been accepted for inclusion in Theses and Dissertations by an authorized administrator of VCU Scholars Compass. For more information, please contact libcompass@vcu.edu.

© Christopher Allen Swift 2015

All Rights Reserved

**Gas-Phase Reactions and Mechanistic Details of Gold, Silver, and Iridium
Complexes**

A dissertation submitted in partial fulfillment of the requirements for the degree of Doctor
of Philosophy at Virginia Commonwealth University

By

Christopher Allen Swift
B.S., Milligan College, 2011

Director: Scott Gronert
Professor Department of Chemistry

Virginia Commonwealth University
Richmond VA,
April 2015

Acknowledgements

I thank my family, especially my wife Kayla, for supporting me and providing encouragement along this journey. I especially thank Dr. Scott Gronert for all of the helpful advice and guidance that he provided me along the way. I also would like to acknowledge my fellow group members, Dr. Mark Davis, Keyanna Conner, Dr. Dave Simpson, Chelsea Coffey, Dr. Suresh Narayanasamy, Dr. Jamal Aldajaei, Dr. Zafer Uger, Dr. Qingyuan Liu and Malissa Grose for their helpful and lively discussions.

Table of Contents

Acknowledgements	ii
Table of Contents	iii
List of Figures.....	vii
List of Tables.....	xxi
List of Schemes.....	xxii
List of Abbreviations	xxv
Abstract.....	iii
Chapter 1 – Mass Spectrometry.....	1
1.1 – Mass Spectrometers	1
1.2 – Electrospray Ionization (ESI).....	1
1.2.1– Droplet Formation	2
1.2.2– Charged Residue Model.....	5
1.2.3– Ion Desorption Model	7
1.3 – Mass Analyzers.....	9
1.3.1– Ion Traps	10
1.4– Ion-Trap Theory	12
1.4.1– Motion of Ions.....	13
1.4.2– Ion Ejection	17
1.4.2.1– Mass Selective Instability.....	17

1.4.2.2– Resonance Excitation	20
1.4.3– Collision Induced Dissociation.....	22
1.5– Conclusions	23
Chapter 2 – Ion-Molecule (IM) Reactions and Organometallic Chemistry in Mass Spectrometry	25
2.1– Reactions in the Gas Phase in Mass Spectrometry	25
2.2– Organometallic Chemistry in Mass Spectrometry	26
2.3– History of Ion-Molecule Reactions in the Gas Phase.....	28
2.4– Instruments for Gas-Phase Reactions	28
2.5– Ion Trap as a Reaction Vessel.....	33
2.6– Neutral Reagent Introduction	34
2.6.1– Gas-Phase Introduction.....	34
2.6.1.1– Pulsed-Valve Introduction.....	35
2.6.1.2– Leaked-Valve Introduction	37
2.6.1.3– Syringe-Pump Introduction	38
2.7– Kinetic Measurements in the Gas-Phase.....	40
2.8– Conclusions	44
Chapter 3 – Formation and Reactivity of Gold (I) Carbenes in the Gas Phase	46
3.1– Introduction.....	46
3.2– Carbenes	46

3.3– Gold-Carbene Complexes	49
3.4– Experimental Procedures	50
3.5– Synthetic Procedures.....	51
3.6- Results and Discussion	57
3.7- Conclusions.....	79
Chapter 4 – Formation and Reactivity of Silver (I) Carbenes in the Gas Phase.....	81
4.1– Introduction.....	81
4.2– Experimental Procedures	81
4.3– Synthetic Procedures.....	83
4.4– Results and Discussion	84
4.5– Conclusion.....	93
Chapter 5 – Mechanistic Details of Gold-Catalyzed Alkyne Rearrangements in the Gas Phase.....	95
5.1– Introduction.....	95
5.2– Experimental Procedures	101
5.3– Synthetic Procedures.....	102
5.4– Results and Discussion	104
5.4.1– Propargyl Acetates.....	104
5.4.2– Propargyl Ethers	119
5.4.3– Propargyl Acetals.....	121

5.4.4– Propargyl Carbonates	123
5.4.5– Related Propargyl Compounds	125
5.5– Conclusions	127
Chapter 6 – C-H bond Activation by Cationic Iridium (III) Complexes in the Gas Phase	128
6.1– Introduction	128
6.2– Experimental Procedures	129
6.3– Synthetic Procedures.....	129
6.4– Results and Discussion	130
6.4.1– Cyclohexane	130
6.4.2– Toluene Series	135
6.4.3– Alcohol Series	148
6.4.4– Amine Series.....	159
6.4.5– Ether Series	164
6.4.6– Other Compounds.....	170
6.5– Conclusions	176
List of References	178
Appendix	187

List of Figures

- Figure 1.** Diagram of ESI source. Reprinted from Gaskell, S. J. *J. Mass Spectrom.* 1997, 32, 677–688. Copyright 1997, with permission from John Wiley and Sons.⁸ 3
- Figure 2.** Diagram of charged droplet formation. Reprinted from Gaskell, S. J. *J. Mass Spectrom.* 1997, 32, 677–688. Copyright 1997, with permission from John Wiley and Sons.⁸ 4
- Figure 3.** Three stages of evaporation of a droplet containing five molecules. Reprinted from Fenn, J. B. *J. Am. Soc. Mass Spectrom.* 1993, 4, 524–535. Copyright 1993, with permission from Springer.¹¹ 5
- Figure 4.** Diagram of Charged Residue Model. Reprinted with permission from Hogan, C. J.; Carroll, J. A.; Rohrs, H. W.; Biswas, P.; Gross, M. L. *Anal. Chem.* 2009, 81, 369–377. Copyright 2009 American Chemical Society.¹⁵ 7
- Figure 5.** Diagram of Iribarne and Thompson’s ion desorption model. Reprinted with permission from Kebarle, P.; Tang, L. *Anal. Chem.* 1993, 65, 972–986. Copyright 1993 American Chemical Society.¹⁰ 8
- Figure 6.** Diagram of a quadrupole mass analyzer.¹⁸ 10
- Figure 7.** Picture of the endcaps and ring electrode of an ion trap. Reprinted from March, R. E. *J. Mass Spec.* 1997, 32, 351–369. Copyright 1997, with permission from John Wiley and Sons.²⁴ 11
- Figure 8.** Diagram of an ion trap that has been cut in half. Reprinted from March, R. E. *J. Mass Spec.* 1997, 32, 351–369. Copyright 1997, with permission from John Wiley and Sons.²⁴ 12

- Figure 9.** Mathieu stability diagram. Reprinted from March, R. E. *J. Mass Spec.* 1997, 32, 351–369. Copyright 1997, with permission from John Wiley and Sons.²⁴ 14
- Figure 10.** Simultaneous stability in the Mathieu stability diagram. Reprinted with permission from Todd, J. F. J.; Penman, a. D.; Smith, R. D. *Int. J. Mass Spectrom. Ion Process.* 1991, 106, 117–135. Copyright 1991 American Chemical Society.²⁶ 15
- Figure 11.** Potential surface of a quadrupole field (left). Trajectory of an ion in a quadrupole ion trap (right). Reprinted from March, R. E. *J. Mass Spec.* 1997, 32, 351–369. Copyright 1997, with permission from John Wiley and Sons.²⁴ 16
- Figure 12.** First example of mass selective ejection (left). Diagram illustrating the pushing nature of mass selective ejection (right). Reprinted from Stafford, G. *Am. Soc. Mass Spectrom.* 2002, 13, 589–596. Copyright 2002, with permission from Springer.²⁸ 18
- Figure 13.** Ejecting ions via mass-selective instability mode. Reprinted with permission from Jonscher, K. R.; Yates, J. R. *Anal. Biochem.* 1997, 244, 1–15. Copyright 1997 American Chemical Society.²⁹ 19
- Figure 14.** Timing of mass-selective instability mode. Reprinted from Stafford, G.; Kelley, P.; Syka, J. E. P.; Reynolds, W. E.; Todd, J. F. J. *Int. J. Mass Spectrom. Ion Process.* 1984, 60, 85–98. Copyright 1984, with permission from Elsevier B.V..³⁰ 20
- Figure 15.** Ejecting ions via resonant excitation. Reprinted with permission from Jonscher, K. R.; Yates, J. R. *Anal. Biochem.* 1997, 244, 1–15. Copyright 1997 American Chemical Society.²⁹ 21

- Figure 16.** Mass spectra of Ru(phen)₃²⁺ on the left and Ru(bpy)₃²⁺ on the right. Reprinted with permission from Katta, V.; Chowdhury, S.; Chait, B. T. *J. Am. Chem. Soc.* 1990, 5348–5349. Copyright 1990 American Chemical Society. ⁴²..... 27
- Figure 17.** Diagram of a TQMS. Reprinted with permission from Yost, R. A.; Enke, C. G. *Anal. Chem.* 1979, 51, 1251–1262. Copyright 1979 American Chemical Society. ⁴⁶ 30
- Figure 18.** Diagram of an ion beam MS used for IM reactions. Reprinted from Muntean, F.; Armentrout, P. B. *J. Chem. Phys.* **2001**, 115, 1213–1228. Copyright 2001, with permission from AIP Publishing LLC. ⁵⁸ 31
- Figure 19.** Flowing afterglow-selected ion drift tube-TQ MS. Reprinted from Bierbaum, V. M. *Int. J. Mass Spectrom.* 2014, In Press. Copyright 2014, with permission from Elsevier B.V. ⁵⁹ 32
- Figure 20.** The sequence for pulsing neutrals into a QIT. Reprinted from Emary, W. B.; Kaiser, R. E.; Kenttiimaa, H. I.; Cooks, R. G. *J. Am. Soc. Mass Spectrom.* 1990, 1, 3–6. Copyright 1990, with permission from Springer. ⁷² 36
- Figure 21.** QIT instrument that has been modified to allow leaking of neutrals into the bath gas manifold. Reprinted from Liere, P.; March, R. E.; Blasco, T.; Tabet, J.-C. *Int. J. Mass Spectrom. Ion Process.* 1996, 153, 101–117. Copyright 1996, with permission from Elsevier B.V. ⁷³ 38
- Figure 22.** Diagram of a Gronert modified QITMS. 39
- Figure 23.** The reaction of thiophenolate with 2,2,2-trifluoroethanol which describes the temperature inside an ion trap. Reprinted from Gronert, S. *Mass Spectrom. Rev.* 2005, 24, 100–120. Copyright 2005, with permission from John Wiley and Sons. ⁶⁵ 44
- Figure 24.** Ground states of carbenes. 47

Figure 25. Frontier orbitals of carbenes. Reprinted with permission from Bourissou, D.; Guerret, O.; Gabbai, F. P.; Bertrand, G. Chem. Rev. 2000, 100, 39–91. Copyright 2000 American Chemical Society. ⁸⁹	48
Figure 26. Gold (I) ylides used to form carbenes in the gas phase.	58
Figure 27. Isolating gold benzylidene fragment of ylide.....	59
Figure 28. Cyclopropanation of gold benzylidene with 4-vinylanisole. Selection of m/z 549 followed by a reaction with 4-vinylanisole with a reaction time of 1300 ms.	60
Figure 29. Substitution of cyclopropane product with 4-vinylanisole. Gold benzylidene at m/z 549 was selected and allowed to react with 4-vinylanisole for 2000 ms. The adduct at m/z 683 m/z was then selected and allowed to react for 10000 ms.	62
Figure 30. Hammett plot of the reactions of <i>para</i> -substituted styrenes with the Ph ₃ PAu ⁺ benzylidene complex (addition process) and its adducts (substitution process).	65
Figure 31. Metathesis reaction of gold benzylidene with 4-vinylanisole. The carbene is selected at 549 m/z and is allowed to react with 4-vinylanisole for 2000 ms. The adduct is selected m/z 683 and subjected to CID at 22%.	67
Figure 32. Degradation of ester ylide. The ester ylide was isolated at m/z 793 and subjected to CID at 32%.	69
Figure 33. Gold (I) ions that were used for the degradation of diazo compounds.	70
Figure 34. Reaction of AuPPh ₃ with ethyl diazoacetate. The precursor ion (AuPPh ₃) was isolated at m/z 459 and allowed to react with ethyl diazoacetate.....	70
Figure 35. Reaction of AuPPh ₃ with tert-butyl diazoacetate. The precursor ion (AuPPh ₃) was isolated at m/z 459 and allowed to react with tert-butyl diazoacetate.	71

- Figure 36.** Degradation of ether ylide. The ether ylide was isolated at m/z 765 and subjected to CID at 35%..... 75
- Figure 37.** Reaction of AuPPh_3 with 2-methoxyethyl 2-diazoacetate. AuPPh_3 was selected at m/z 459 and allowed to react with 2-methoxyethyl 2-diazoacetate. 76
- Figure 38.** Reaction of AuPPh_3 with (diazomethyl)trimethylsilane. AuPPh_3 was selected at m/z 459 and allowed to react with (diazomethyl)trimethylsilane. 77
- Figure 39.** Isolation of triphenylphosphine silver (I) ion with a 30 ms reaction time. 85
- Figure 40.** Reaction of triphenylphosphine silver (I) ion with ethyl diazoacetate..... 86
- Figure 41.** Reaction of triphenylphosphine silver (I) ion with a 1:1 mix of ethyl diazoacetate and ethyl vinyl ether. Initially, AgPPh_3 is isolated at m/z 369 and is allowed to react with a 1:1 mix of ethyl diazoacetate and ethyl vinyl ether. Then the alkoxy carbene is isolated at m/z 427..... 87
- Figure 42.** Isolation of 1,10 phenanthroline silver (I) ion with a 30 ms reaction time. ... 88
- Figure 43.** Reaction of 1,10 phenanthroline silver (I) ion with a 1:1 mix of tert-butyl diazoacetate and ethyl vinyl ether. 89
- Figure 44.** Reaction of 1,10 phenanthroline silver (I) ion with a 1:1 mix of tert-butyl diazoacetate and ethyl vinyl ether. Initially, $\text{Ag}(\text{phen})$ is isolated at m/z 287 and is allowed to react with a 1:1 mix of tert-butyl diazoacetate and ethyl vinyl ether. Then the alkoxy carbene is isolated at m/z 373 and allowed to react for 1000 ms..... 90
- Figure 45.** Formation of 1,10 phenanthroline silver (I) betaine complex. The 1,10 phenanthroline silver (I) betaine complex is selected at m/z 406. Some degradation of the complex is observed at m/z 362..... 92

Figure 46. Degradation of 1,10 phenanthroline silver (I) betaine complex. The 1,10 phenanthroline silver (I) betaine complex was isolated at 404 and subjected to CID.... 92

Figure 47. Degradation of 1,10 phenanthroline silver (I) betaine complex. The 1,10 phenanthroline silver (I) betaine complex was isolated at 404 and subjected to CID. Then m/z 362 was isolated and subjected to CID. 93

Figure 48. Reaction of AuPPh₃ with 1-phenylprop-2-yn-1-yl acetate. The adduct of AuPPh₃ with 1-phenylprop-2-yn-1-yl acetate was selected at m/z 633 and subjected to CID at 25%..... 105

Figure 49. Reaction of AuPPh₃ with a 5:2 mixture of 1-phenylprop-2-yn-1-yl acetate and 4-vinylanisole. The adduct of AuPPh₃ with 1-phenylprop-2-yn-1-yl acetate was selected at m/z 633 and subjected to CID at 25%. Then, the carbene was selected at m/z 573 and allowed to react for 500 ms. 108

Figure 50. Reaction of AuPPh₃ with a 5:2 mixture of 1-phenylprop-2-yn-1-yl acetate and 4-vinylanisole. The adduct of AuPPh₃ with 1-phenylprop-2-yn-1-yl acetate was selected at m/z 633 and subjected to CID at 25%. Then, the carbene was selected at m/z 573 and allowed to react for 500 ms. The reaction product at m/z 707 was then selected and allowed to react for 10000 ms. 109

Figure 51. Reaction of AuPPh₃ with a 5:2 mixture of 1-phenylprop-2-yn-1-yl acetate and 4-vinylanisole. The adduct of AuPPh₃ with 1-phenylprop-2-yn-1-yl acetate was selected at m/z 633 and subjected to CID at 25%. Then, the carbene was selected at m/z 573 and allowed to react for 500 ms. The reaction product at m/z 707 was then selected and allowed to react for 10000 ms and subjected to CID at 27%..... 110

Figure 52. Reaction of AuPPh₃ with 1,1-dimethyl-2-propynyl acetate. 112

- Figure 53.** Reaction of AuPPh₃ with a 1:2 mixture of 2-methylbut-3-yn-2-yl acetate and styrene. The adduct of AuPPh₃ with 1,1-dimethyl-2-propynyl acetate was selected at m/z 585 and subjected to CID at 10%. Then the reaction product was selected at m/z 629 and subjected to CID at 30%..... 113
- Figure 54.** Reaction of AuPPh₃ with a 1:2 mixture of 1,1-dimethyl-2-propynyl acetate and styrene. The adduct of AuPPh₃ with 1,1-dimethyl-2-propynyl acetate was selected at m/z 585 and allowed to react for 5000 ms and subjected to CID at 10%. 114
- Figure 55.** Reaction of AuPPh₃ and 1,1-dimethyl-2-propynyl acetate. The adduct of AuPPh₃ with 1,1-dimethyl-2-propynyl acetate was selected and subjected to CID. 114
- Figure 56.** Reaction of AuPPh₃ with ethyl 2-acetoxybut-3-ynoate. The adduct of AuPPh₃ with ethyl 2-acetoxybut-3-ynoate was selected at m/z 629 m/z and subjected to CID at 25%..... 116
- Figure 57.** Reaction of AuPPh₃ with ethyl 2-acetoxybut-3-ynoate. The adduct of AuPPh₃ with ethyl 2-acetoxybut-3-ynoate was selected at m/z 629 m/z and subjected to CID at 25%. Then, the degradation product at 587 was selected at m/z 587 and subjected to CID at 25%..... 117
- Figure 58.** Reaction of AuPPh₃ with a 5:2 mixture of ethyl 2-acetoxybut-3-ynoate and 4-vinylanisole. The adduct of AuPPh₃ with ethyl 2-acetoxybut-3-ynoate was selected at m/z 629 m/z and subjected to CID at 17% and allowed to react for 5000 ms. 118
- Figure 59.** Reaction of AuPPh₃ with benzyl propargyl ether. 120
- Figure 60.** Reaction of AuPPh₃ with benzyl propargyl ether. The adduct of AuPPh₃ with benzyl propargyl ether was selected at m/z 605 m/z and subjected to CID at 20%. ... 121

- Figure 61.** Reaction of AuPPh₃ with 3-(1-ethoxyethoxy)prop-1-yne. The adduct of AuPPh₃ with 3-(1-ethoxyethoxy)prop-1-yne was selected at *m/z* 587 and subjected to CID..... 122
- Figure 62.** Reaction of AuPPh₃ with ethyl prop-2-yn-1-yl carbonate. The adduct of AuPPh₃ with ethyl prop-2-yn-1-yl carbonate was selected at *m/z* 587 and subjected to CID..... 124
- Figure 63.** Reaction of AuPPh₃ with N,N-dimethylprop-2-yn-1-amine. The adduct of AuPPh₃ with N,N-dimethylprop-2-yn-1-amine was selected at *m/z* 542 and subjected to CID..... 125
- Figure 64.** Cationic iridium(III) dichloride phenanthroline complex I 128
- Figure 65.** Mass spectrum of complex I reacting with cyclohexane. The reactant ion at *m/z* 441 is mainly the, ¹⁹¹Ir¹²C₁₂¹⁴N₂¹H₈³⁵Cl₂ isotopomer. C-H activation corresponds to the peak at *m/z* 489, while the peaks at *m/z* 459 and 477 are single and double adducts of I with adventitious water in the ion trap. 132
- Figure 66.** Mass spectrum of complex I reacting with cyclohexane with application of CID to the C-H activation product. C-H activation corresponds to the peak at *m/z* 489 which was isolated and then subjected to CID. The peak at *m/z* 451 corresponds to a loss of HCl..... 134
- Figure 67.** Mass spectrum of complex I reacting with cyclohexane with application of CID to 451 *m/z*. A mass loss of 2HCl corresponds to the peak at *m/z* 451, which was isolated and subjected to CID. The peak at *m/z* 449 corresponds to a loss of H₂. 134
- Figure 68.** Compounds in this series that were allowed to react with complex I..... 135

Figure 69. Mass spectrum of complex **I** reacting with cyclohexene. The adduct of complex **I** with cyclohexene was selected at allowed to react. An adduct of cyclohexadiene with complex **I** corresponds to the peak at m/z 451 and the peak at m/z 523 corresponds to an addition of cyclohexene to complex **I**. 136

Figure 70. Mass spectrum of complex **I** reacting with cyclohexene. The adduct of complex **I** with cyclohexene was selected at allowed to react. Then, the adduct of cyclohexadiene with complex **I** was selected and subjected to CID. An adduct of cyclohexadiene with complex **I** corresponds to the peak at 451 m/z , which was isolated and subjected to CID. The peak at 449 m/z corresponds to a loss of H_2 137

Figure 71. Mass spectrum of complex **I** reacting with toluene. The addition of toluene to complex **I** corresponds to m/z 535. While, the m/z at 553 is an addition of toluene and H_2O to complex **I**. The addition of toluene and loss of HCl can be seen at m/z 499. .. 138

Figure 72. Mass spectrum of complex **I** reacting with toluene- d_3 . The addition of toluene- d_3 to complex **I** corresponds to m/z 536 while, m/z 554 is an additional addition of H_2O . The addition of toluene- d_3 and loss of DCl can be seen at m/z 499. 138

Figure 73. Mass spectra of complex **I** reacting with a 1:1 ratio of toluene:toluene- d_8 . The ion at m/z 499 corresponds to **II**. The ion at m/z 506 corresponds **II**- d_7 . The ions at m/z 531 and 538 are adducts of **II** and **II**- d_7 with adventitious $MeOH$, respectively. In (a), m/z 499 is isolated and allowed to react with the gas mixture. In (b), m/z 506 is isolated and allowed to react with the gas mixture. 141

Figure 74. Mass spectrum of complex **I** reacting with ethylbenzene. 143

Figure 75. Mass spectrum of complex **I** reacting with cumene. An addition of H_2O and two H_2O to complex **I**, corresponds to m/z 461 and m/z 479 respectively. An addition of

cumene to complex **I** with a loss of HCl corresponds to m/z 527 and m/z 545 corresponds to an addition of H_2O . While, m/z 525 is a loss of H_2 from this complex. The adduct of cumene to complex **I** can be seen at m/z 563 and m/z 581 is an addition of H_2O to this complex..... 143

Figure 76. Mass spectrum of complex **I** reacting with ethylbenzene- d_2 . An addition of H_2O and two H_2O to complex **I**, corresponds to m/z 461 and m/z 479 respectively. An addition of ethylbenzene- d_2 to complex **I** with a loss of HCl is seen at m/z 514, with m/z 532 being an addition of H_2O to this complex. While, m/z 551 corresponds to an addition of ethylbenzene- d_2 to complex **I** and m/z 569 an addition of H_2O to this complex..... 144

Figure 77. Mass spectrum of complex **I** reacting with t-butylbenzene. An addition of H_2O and two H_2O to complex **I**, corresponds to m/z 461 and m/z 479 respectively. An addition of t-butylbenzene to complex **I** with a loss of HCl corresponds to m/z 541, with m/z 559 being an addition of H_2O to this complex. An addition of t-butylbenzene to complex **I** is seen at m/z 577 and m/z 595 is an addition of H_2O to this complex..... 145

Figure 78. Geometries of key species in reaction of **I** with 2° hydrogen of propane. (a) **I**; (b) addition complex; (c) transition state; (d) product. Computations were completed with M06 functional and a mixed lanl2dz/6-311+G** basis set. 147

Figure 79. Alcohols that were allowed to react with complex **I**. 149

Figure 80. Mass spectrum of complex **I** reacting with methanol. An addition of methanol to complex **I** is seen at m/z 475, with m/z 493 being an addition of H_2O to this complex. An addition of two methanol compounds to complex **I** can be seen at m/z 507. 150

Figure 81. Mass spectrum of complex **I** reacting with ethanol. An addition of ethanol to complex **I** m/z 489, with m/z 507 being an addition of H_2O to this complex and m/z 535 corresponding to an addition of two ethanol molecules to complex **I**. Dehydrogenation products can be seen at m/z 487 and m/z 533..... 151

Figure 82. Mass spectrum of complex **I** reacting with ethanol-d. An addition of ethanol-d to complex **I** is seen at m/z 490, with m/z 508 being an addition of H_2O to this complex. While, m/z 537 corresponds to an addition of two ethanol-d molecules to complex **I**. A dehydrogenation product can be seen at m/z 487. 152

Figure 83. Mass spectrum of complex **I** reacting with ethanol- d_3 . An addition of ethanol- d_3 to complex **I** is seen at m/z 492, with m/z 510 being an addition of H_2O to this complex. An addition of two ethanol- d_3 molecules to complex **I** can be seen at m/z 541. Dehydrogenation product can be seen at m/z 490 and m/z 539. 153

Figure 84. Mass spectrum of complex **I** reacting with isopropanol. An addition of isopropanol to complex **I** is seen at m/z 503. While, an addition of two isopropanol compounds to complex **I** can be seen at m/z 563. Dehydrogenation products can be seen at m/z 501 and m/z 561. 154

Figure 85. Mass spectrum of complex **I** reacting with 1-phenylethanol. An addition of 1-phenylethanol to complex **I** with a loss of HCl can be seen at m/z 529. While, m/z 651 is an addition of two 1-phenylethanol compounds to complex **I**. 155

Figure 86. Mass spectrum of complex **I** reacting with 1-propanol. An addition of 1-propanol to complex **I** with a loss of HCl can be seen at m/z 467. While adduct formations with complex **I** and 1-propanol are seen at m/z 503 and m/z 563. Shown with modification at the γ carbon, but could also be at the β carbon..... 156

- Figure 87.** Mass spectrum of complex **I** reacting with 1-butanol. The addition of 1-butanol with a loss of HCl is observed at m/z 481. While, an adduct of complex **I** with 1-butanol is seen at m/z 517. Shown with modification at the γ carbon, but could also be at the β carbon. 157
- Figure 88.** Mass spectrum of complex **I** reacting with 1-octanol. An addition of 1-octanol to complex **I** with a loss of HCl can be observed at m/z 537. While, adduct formations of complex **I** with 1-octanol can be seen at m/z 573 and m/z 703. Shown with modification at the γ carbon, but could also be at the β carbon..... 158
- Figure 89.** Mass spectrum of complex **I** reacting with 2-octanol. An addition of 2-octanol to complex **I** with a loss of HCl can be observed at m/z 537. While, adduct formations of complex **I** with 2-octanol can be seen at m/z 573 and m/z 703. Shown with modification at the γ carbon, but could also be at the β carbon..... 159
- Figure 90.** Amines that were allowed to react with complex **I**..... 160
- Figure 91.** Mass spectrum of complex **I** reacting with 1-butylamine. An addition of 1-butylamine to complex **I** with a loss of HCl is observed at m/z 480. While, an adduct of complex **I** with 1-butylamine is seen at m/z 516 and an addition of a second 1-butylamine with a loss of HCl at m/z 553. Shown with modification at the γ carbon, but could also be at the β carbon. 161
- Figure 92.** Mass spectrum of complex **I** reacting with isopropylamine. An addition of isopropylamine to complex **I** is seen at m/z 502. While, m/z 561 is an addition of two isopropylamine compounds to complex **I**, with m/z 525 corresponding to a loss of HCl. 162

- Figure 93.** Mass spectrum of complex **I** reacting with triethylamine. An addition of triethylamine to complex **I** can be observed at m/z 544, with loss of HCl seen at m/z 508. 163
- Figure 94.** Ethers that were allowed to react with complex **I**. 164
- Figure 95.** Mass spectrum of complex **I** reacting with diethyl ether. An addition of diethyl ether to complex **I** can be observed at m/z 517, with a loss of HCl present at m/z 481. While an addition of two diethyl ethers to complex **I** can be seen at m/z 591. 165
- Figure 96.** Mass spectrum of complex **I** reacting with diethyl ether. The adduct of complex **I** with diethyl ether and a loss of HCl is selected at m/z 481 and subjected to CID at 22%. 166
- Figure 97.** Mass spectrum of complex **I** reacting with ethoxybenzene-d5 (deuterated on the ethoxy). 168
- Figure 98.** Mass spectrum of complex **I** reacting with ethoxybenzene-d5 (deuterated on the ethoxy). The adduct of complex **I** with ethoxybenzene-d5 (deuterated on the ethoxy) and a loss of HCl is selected at m/z 534 and subjected to CID at 15%. 169
- Figure 99.** Mass spectrum of complex **I** reacting with ethoxybenzene-d5 with the phenol ring deuterated. 169
- Figure 100.** Mass spectrum of complex **I** reacting with ethoxybenzene-d5, with the phenol ring deuterated. The adduct of complex **I** with ethoxybenzene-d5 (deuterated on the phenol ring) and a loss of DCl is selected at m/z 533 and subjected to CID at 15%. 170
- Figure 101.** Compounds in this series that were allowed to react with complex **I**. 170

- Figure 102.** Mass spectrum of complex **I** reacting with acetone. An addition of acetone to complex **I** can be seen at m/z 501, with a loss of HCl at m/z 465. An adduct of two acetones with complex **I** is seen at m/z 559 and loss of HCl from this complex at m/z 523. 171
- Figure 104.** Mass spectrum of complex **I** reacting with tert-butyl bromide. 174
- Figure 105.** Mass spectrum of complex **I** reacting with 1-bromopropane. An addition of 1-bromopropane to complex **I** can be seen at m/z 565 and 567, with a loss of HCl at m/z 529 and 531. While, m/z 688 is an addition of two 1-bromopropane compounds to complex **I**. Shown with modification at the γ carbon, but could also be at the β carbon. 175
- Figure 106.** Mass spectrum of complex **I** reacting with diethyl disulfide. An addition of diethyl disulfide to complex **I** can be seen at m/z 565, with a loss of HCl seen at m/z 529. While, m/z 651 is addition of two diethyl disulfide compounds to complex **I** and 625 m/z is a loss of HCl. 176

List of Tables

Table 1. Common mass analyzers in use. ¹⁸	9
Table 2. Methods for dissociation of ions in the gas phase. ³²	22
Table 3. Rate constants for the reaction of the Ph_3PAu^+ benzylidene complex with olefins ^a	60
Table 4. Rate constants for the reaction of the addition complexes with olefins (Scheme 3). ^a	63
Table 5. Rate constants for Ph_3PAu^+ benzylidene complex with substituted styrenes ^a . 64	
Table 6. Rate constants for complex I ^a	133

List of Schemes

Scheme 1. Chen's method of gold(I) carbene formation from ylide fragmentation.	50
Scheme 2. Synthesis of 1,3-diisopropylimidazolium hydrogen carbonate.	52
Scheme 3. Synthesis of 1,3-diisopropylimidazolium gold (I) chloride.	52
Scheme 4. Synthesis of compound 2.	53
Scheme 5. Synthesis of compound 3.	54
Scheme 6. Synthesis of compound 4.	54
Scheme 7. Synthesis of compound 5.	55
Scheme 8. Synthesis of compound 7.	56
Scheme 9. Synthesis of 2-methoxyethyl diazoacetate.....	57
Scheme 10. Gold(I) benzylidene precursor.	61
Scheme 11. Reactions of gold(I) benzylidene with olefins.....	63
Scheme 12. Fragmentation of the ylide precursor of an ester-substituted carbene.....	69
Scheme 13. Wolff rearrangement and CO loss from ester-substituted carbene.....	71
Scheme 14. Alkoxy carbene rearrangement to form aldehyde.	72
Scheme 15: Resonance forms for gold-carbene complex.	73
Scheme 16. Isodesmic reaction for evaluating carbene stability.	74
Scheme 17. Alkoxy carbene generation by ylide degradation.	76
Scheme 18. Reactivity of 2-methoxyethyl 2-diazoacetate with gold (I) ions.	78
Scheme 19. Fragmentation pathways of gold(I) methylene precursor.....	78
Scheme 20: CH ₂ carbene precursor using 1,3-diisopropylimidazolium as the ligand on gold.	79
Scheme 21. Synthesis of triphenylphosphine silver (I) chloride.....	83

Scheme 22. Synthesis of 1,10 phenanthroline silver (I) nitrate.....	84
Scheme 23. Synthesis of 1,10 phenanthroline silver (I) betaine.....	84
Scheme 24. Reaction of silver (I) salts with diazoacetates.....	86
Scheme 25. Stabilization of silver alkoxy carbenes through resonance.....	88
Scheme 26. Degradation of silver betaine complex.....	91
Scheme 27. Activation of alkynes by gold.....	97
Scheme 28. Gold-catalyzed addition of methanol to acetylene.....	98
Scheme 29. Rearrangement of propargyl acetates in the condensed phase.....	100
Scheme 30. Gold-catalyzed rearrangement and degradation of propargyl ethers in the condensed phase.....	101
Scheme 31. Synthesis of propargyl acetates. ¹⁴⁷	102
Scheme 32. Synthesis of propargyl ethers. ¹⁴⁸	103
Scheme 33. Synthesis of ethyl prop-2-yn-1-yl carbonate. ¹⁴⁹	103
Scheme 35. Cyclopropanation and metathesis processes of carbene I with olefins...	110
Scheme 36. Triphenylphosphine gold (I) reacting with 1,1-dimethyl-2-propynyl acetate.	115
Scheme 37. Triphenylphosphine gold (I) reactivity with ethyl 2-acetoxybut-3-ynoate.	118
Scheme 38. Triphenylphosphine gold (I) reactivity with propargyl ethers.....	121
Scheme 39. Triphenylphosphine gold (I) reacting with acetaldehyde ethyl propargyl acetal.....	123
Scheme 40. Triphenylphosphine gold (I) reacting with ethyl prop-2-yn-1-yl carbonate.	124
Scheme 41. Triphenylphosphine gold (I) reacting with 1-dimethylaminoprop-2-yne...	126

Scheme 42. Triphenylphosphine gold (I) reacting with 3-methylaminoprop-1-yne.	126
Scheme 43. Synthesis iridium (III) trichloride phenanthroline complex (I).	129
Scheme 44. Synthesis of ethoxybenzene compounds.	130
Scheme 45. Reaction of compound I with cyclohexane.....	131
Scheme 46. H/D exchange process.	142
Scheme 47. Proposed dehydrogenation mechanism for complex I reacting with alcohols.....	151
Scheme 48. Dehydrogenation of isopropanol.....	154
Scheme 49. Proposed reaction mechanism of amines with complex I.	161
Scheme 50. Proposed mechanism for complex I reacting with ethers.....	166
Scheme 51. C-H activation of ethoxybenzene-d ₅ by complex I.	168
Scheme 52. Proposed reaction mechanism of complex I reacting with tert-butyl bromide.	174

List of Abbreviations

ADO	Average Dipole Orientation
AMU	Atomic Mass Unit
CAD	Collision Activated Dissociation
CI	Chemical Ionization
CID	Collision Induced Dissociation
DFT	Density Functional Theory
ECP	Effective Core Potential
EI	Electron Ionization
ESI	Electrospray Ionization
FAB	Fast Atom Bombardment
FD	Field Desorption
ICR	Ion Cyclotron Resonance
IM	Ion-Molecule
MALDI	Matrix Assisted Laser Desorption Ionization
MS	Mass Spectrometer
m/z	Mass-to-Charge Ratio
NHC	N-heterocyclic carbene
Phen	Phenanthroline
QIT	Quadrupole Ion Trap
r^2	Correlation Coefficient
SIFT	Selected Ion Flow Tube
TS	Transition State
TQ	Triple Quadrupole

Abstract

Gas-Phase Reactions and Mechanistic Details of Gold, Silver, and Iridium Complexes

By: Christopher Allen Swift

A dissertation submitted in partial fulfillment of the requirements for the degree of Doctor of Philosophy at Virginia Commonwealth University

Virginia Commonwealth University

Director: Scott Gronert, Professor, Department of Chemistry

The ever increasing demand for more efficient and environmentally benign routes for synthesizing target compounds, has led to the use of organometallic catalysts. This demand has created the need to understand the mechanistic details that are at work in these organometallic catalytic cycles. Along with this, there is a demand for new organometallic catalysts that are tailored for specific transformations. This presents a myriad of challenges for organometallic chemists. Unfortunately, it is often difficult to gain an understanding of the reaction mechanisms at work when the intermediates are too short lived to be observed in the condensed phase. It is also very time consuming to synthesize, purify, and characterize organometallic catalysts following standard condensed phase methods. Therefore, it would be beneficial to probe organometallic reactions in a way that the inherent reactivity of the organometallic complex can be uncovered and where purity is not a prerequisite.

Using an ion-trap mass spectrometer that has been modified to allow introduction of neutral reagents to the buffer gas, organometallic ion-molecule reactions can be probed in an environment free from solvation effects. This enables the study of the inherent reactivity of the complexes and also provides insight into reaction mechanisms by allowing reactive intermediates to be probed. In addition, organometallic complexes probed in this manner do not need to be pure due to ability of the ion trap to function as a mass filter. This results in a quick and efficient method. This dissertation presents results found during the investigation of the reactions and mechanistic details of gold, silver, and iridium complexes using a modified ion-trap mass spectrometer.

Chapter 1 – Mass Spectrometry

1.1 – Mass Spectrometers

Mass spectrometry (MS) is an analytical technique that measures the mass to charge (m/z) ratio of ions in the gas phase. It has become one of the most useful analytical techniques since its discovery in the early 20th century.¹ In 1913 J.J. Thompson, whom is credited as the founder of mass spectrometry, discovered that he was able to separate ²⁰Ne from its heavier isotope ²²Ne by applying electric and magnetic fields to cathode rays containing Ne.² Since around the 1940's, when instruments started becoming commercially available, mass spectrometry has steadily increased in popularity and usefulness with both research and industrial chemists.¹ Mass spectrometry is a technique that is continually utilized and improved upon to meet the needs of today's chemists.

1.2 – Electrospray Ionization (ESI)

Since mass spectrometers measure m/z of ions, ion production is a necessary first step. Electrospray ionization is a technique that transfers charged molecules and compounds in the gas phase from the solution phase. It was developed in the early 1980's by John B. Fenn through a project that focused on developing an ionization source for mass spectrometry that could produce low molecular weight ions from polar

organic molecules. This research subsequently earned him the Nobel Prize in Chemistry in 2002.³⁻⁶ Electrospray ionization is a unique ionization technique in that it has the ability to produce highly-charged molecules, enabling the study of high-molecular-weight compounds such as proteins and large synthetic polymers at modest m/z values.^{7,8} It is also unique in its ability to produce these ions in a “soft” manner so as not to break non-covalent interactions. These two unique features of ESI have been the driving factors for the steady increase in usage. Due to its ability to produce ions from very dilute solutions it is easily adaptable to common separation techniques making it a versatile tool.

1.2.1– Droplet Formation

Operating at atmospheric pressure, electrospray ionization is a method that does not necessarily ionize compounds but rather creates an environment where a separation of charge can occur and small droplets of ions can subsequently be formed. This charged droplet formation occurs by flowing a polar solution containing the analyte through a capillary where a potential is applied (Figure 1). This potential difference, typically from 2-6 kV, causes the ions to be drawn down-field to the surface of the liquid causing a cone to be formed (known as a Taylor Cone).³ The potential is able to operate in a negative or positive ion mode, allowing for the formation of positive or negative ionic droplets. Once the Taylor cone is formed the tip of the cone is drawn into a filament where the electrostatic repulsions begin to exceed the surface tension of the solution causing charged droplets to break off of the filament and traverse down field through the

bath gas. This process is often aided by a nebulization gas, typically nitrogen or argon, that is flowed past the Taylor Cone.

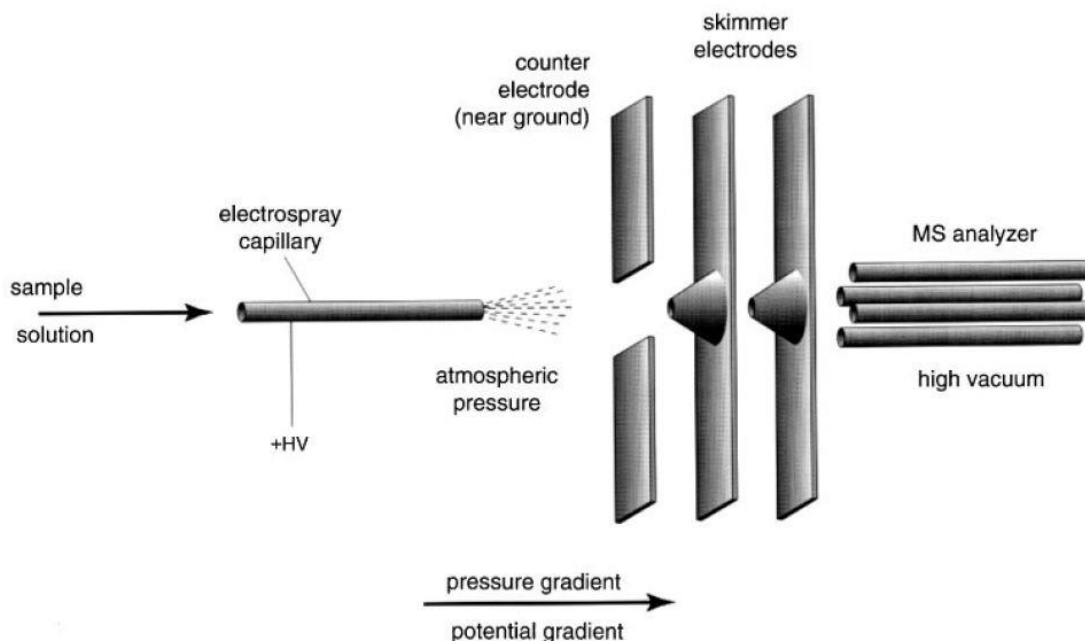


Figure 1. Diagram of ESI source. Reprinted from Gaskell, S. J. J. Mass Spectrom. 1997, 32, 677–688. Copyright 1997, with permission from John Wiley and Sons. ⁸

From the point at which the droplets are formed from the Taylor Cone, the solvent in the droplet begins to evaporate. The bath gas provides the enthalpy necessary for the droplets to evaporate while also helping to control the internal and translational energies.⁹ This solvent will continue to evaporate until it reaches the critical point at which the Coulombic repulsion exceeds the surface tension of the solvent. At this point, Coulombic fissions occur breaking the droplets into smaller droplets which then repeat the process of evaporating and fracturing, producing the precursors of the

gas phase ions (Figure 2,3). From these small droplets ions are then formed through a mechanism that is still debated.¹⁰

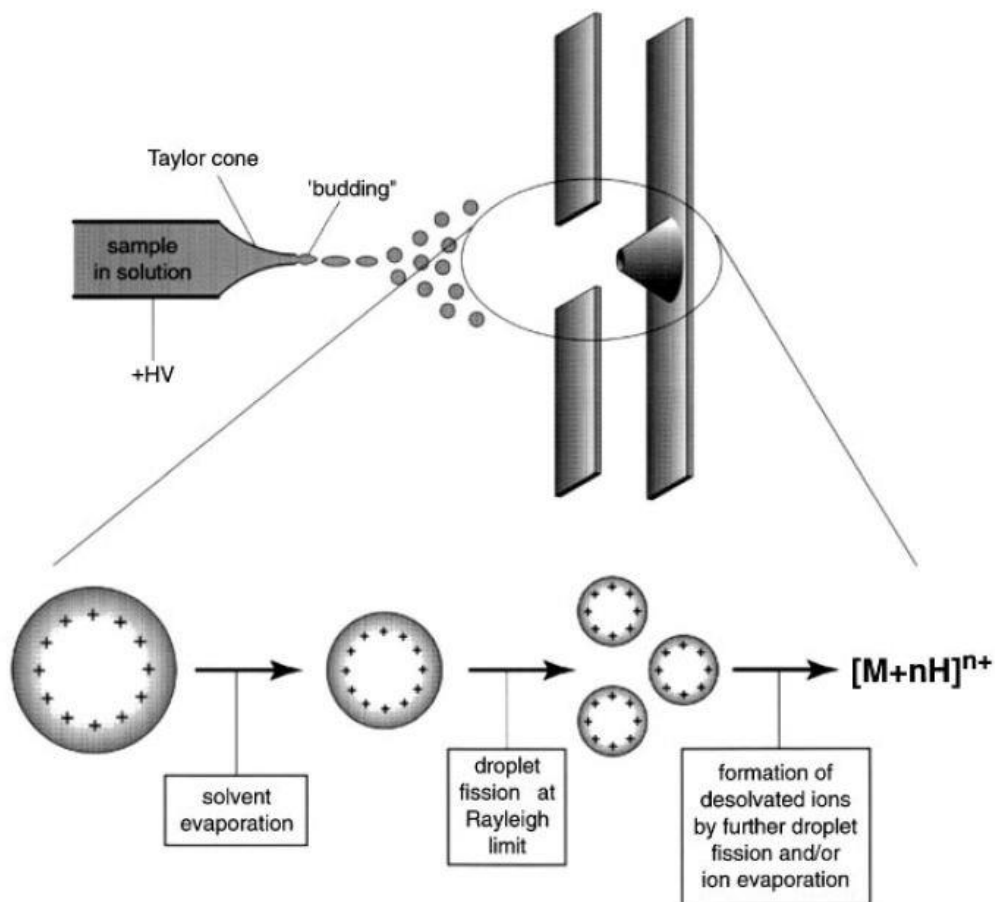


Figure 2. Diagram of charged droplet formation. Reprinted from Gaskell, S. J. J. Mass Spectrom. 1997, 32, 677–688. Copyright 1997, with permission from John Wiley and Sons.⁸

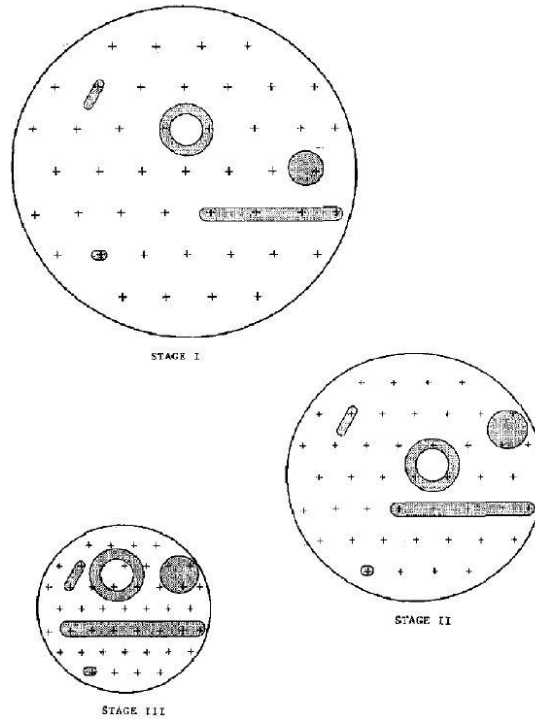


Figure 3. Three stages of evaporation of a droplet containing five molecules. Reprinted from Fenn, J. B. *J. Am. Soc. Mass Spectrom.* 1993, 4, 524–535. Copyright 1993, with permission from Springer.¹¹

1.2.2– Charged Residue Model

The Charged Residue Model (CRM) is one of the two theories of how ions are actually transferred to the gas phase from the small charged droplets that are formed from the Taylor Cone. This model that was developed by Dole, suggests that the droplets then continue to evaporate and undergo multiple stages of Coulombic fissions, caused by the Coulombic repulsion becoming greater than the surface tension (Figure 4).¹² This is known as the Rayleigh limit and can be calculated by equation (1).¹³

$$q = 8\pi(\varepsilon_0\gamma R^3)^{1/2} \quad (1)$$

Where ε_0 is the permittivity of a vacuum, γ is the surface tension of the liquid, and R the radius of the droplet. The droplets continually undergo this process until only one residual solute is left in the charged sphere. From that point, the charges are then transferred to the solute and the remaining solvent evaporated. This is one plausible mechanism for the production of ions in the gas phase via ESI and it is believed to be the operating mechanism for large compounds where multiply charged species are observed.¹⁴

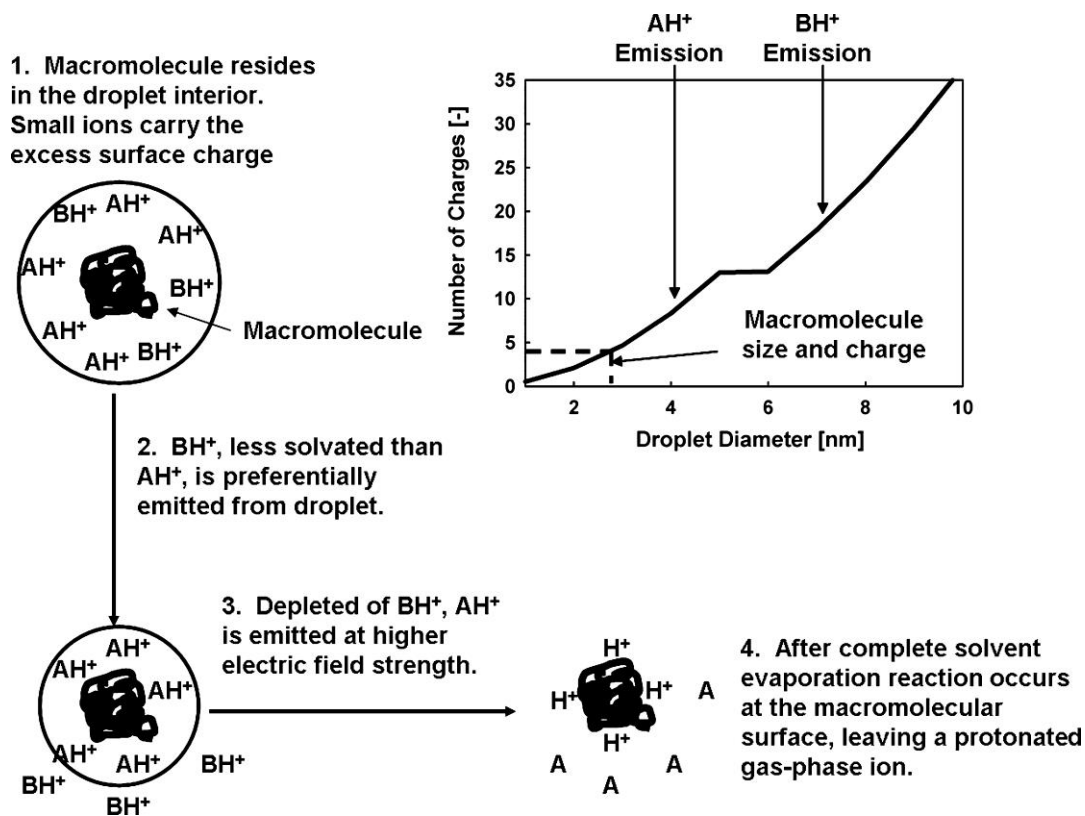


Figure 4. Diagram of Charged Residue Model. Reprinted with permission from Hogan, C. J.; Carroll, J. A.; Rohrs, H. W.; Biswas, P.; Gross, M. L. *Anal. Chem.* 2009, 81, 369–377. Copyright 2009 American Chemical Society.¹⁵

1.2.3– Ion Desorption Model

The ion desorption model is an alternative method for producing ions in the gas phase from the charged droplets that are formed from the Taylor Cone. This model was proposed by Iribarne and Thompson in 1976 while investigating whether ions that were produced by vaporization still retained solvent with the solute.^{16,17} The conclusion they came upon was, that there was enough energy to desorb ions from charged droplet

below the Rayleigh limit (Figure 5). They then proposed a rate constant for the emission of these ions from the charged droplets. This rate can be calculated from equation (2).

$$k_1 = \frac{kT}{h} \exp(-\Delta G^\ddagger/RT) \quad (2)$$

Where k is the Boltzmann constant, T is the temperature of the droplet, h is Planck's constant, and ΔG^\ddagger is the free energy of activation. This model, that is in opposition to the CRM model has been credited by Fenn as the most probable method for ion formation by ESI.⁹

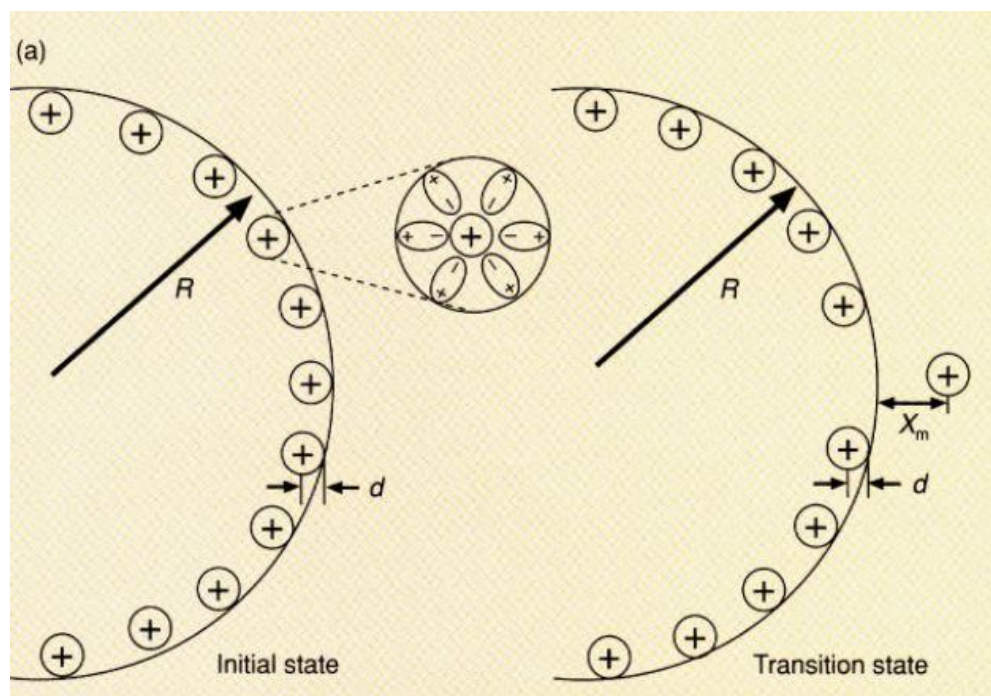


Figure 5. Diagram of Iribarne and Thompson's ion desorption model. Reprinted with permission from Kebarle, P.; Tang, L. *Anal. Chem.* 1993, 65, 972–986. Copyright 1993 American Chemical Society.¹⁰

1.3– Mass Analyzers

Mass analyzers are the heart of the mass spectrometer. They are what measure and separate compounds based on their m/z ratio. Mass analyzers effectively separate these charged compounds by the application of electric fields and in some instances magnetic fields.¹⁸ Table 1 provides a general overview of the more common mass analyzers in use. The table highlights the differences of the different types of mass analyzers, with each having its advantages. The quadrupole mass analyzer has become the most common of these to be used, however that is mostly due to its cost and general ease of maintenance (Figure 6).¹⁹ However, the ion trap with its ability to confine ions in an effective electric-field test tube has led to its popularity in the field of ion-molecule reactions.²⁰

Table 1. Common mass analyzers in use.¹⁸

Method	Quantity Measured	Mass/charge (m/z) range	Resolution at $m/z = 1,000$	Dynamic Range
Sector Magnet	momentum/charge	10^4	10^5	10^7
Time of Flight	flight time	10^6	$10^3 - 10^4$	10^4
Ion Cyclotron Resonance	cyclotron frequency	10^5	10^6	10^4
Ion Trap	frequency	10^4	10^4	10^4
Quadrupole mass filter	filters for m/z	$10^3 - 10^4$	$10^3 - 10^4$	10^5

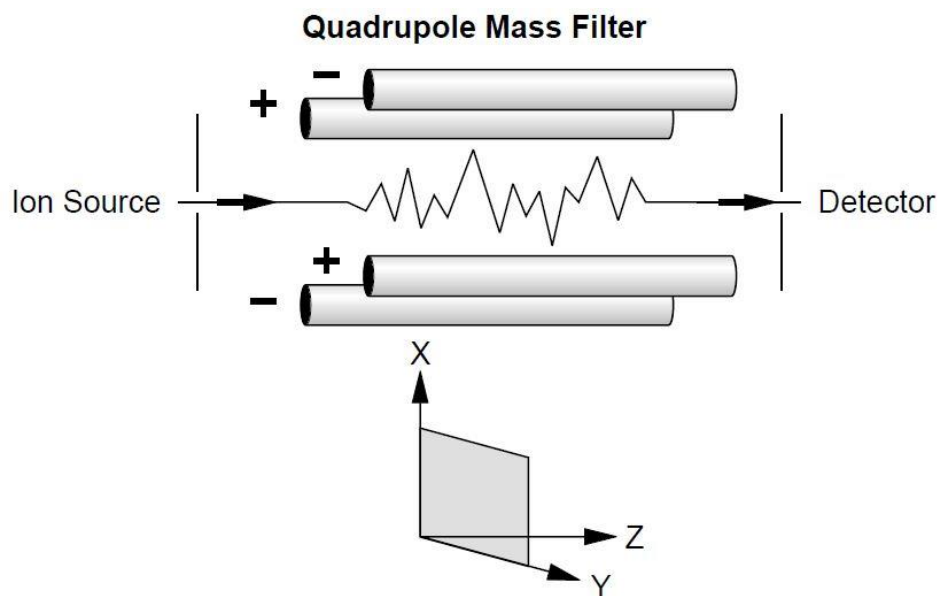


Figure 6. Diagram of a quadrupole mass analyzer.¹⁸

1.3.1– Ion Traps

The quadrupole ion trap (QIT) was developed by Paul and Steinwedel in the 1950s and they were awarded a German patent for their trap in 1956.²¹ Years later, in 1989, Paul was recognized for this achievement and was awarded the Nobel Prize for Physics.²² The quadrupole ion trap is a device that permits the confinement of ions, positively or negatively charged, in the gas phase. It is a small device that operates under rf potentials to achieve this trapping (Figure 7). Along with confining ions, the ion trap is also able to radially eject ions, by the ramping of the rf potential, based on their m/z ratios to an external detector, producing mass spectra. The structure of the ion trap contains three components, two endcaps and one ring electrode. These three components are of hyperboloidal geometry with the endcaps having a resemblance of

bowls (Figure 7). Each endcap contains a small hole in the center which used to gate the ions into and out of the trap. The hyperboloidal shape of the ion trap is critical for the effective trapping of ions in the trap being responsible for creating the parabolic wells in which the ions are trapped. A depiction of an ion trap cut in half revealing the hyperbolic geometry is given in Figure 8.²³

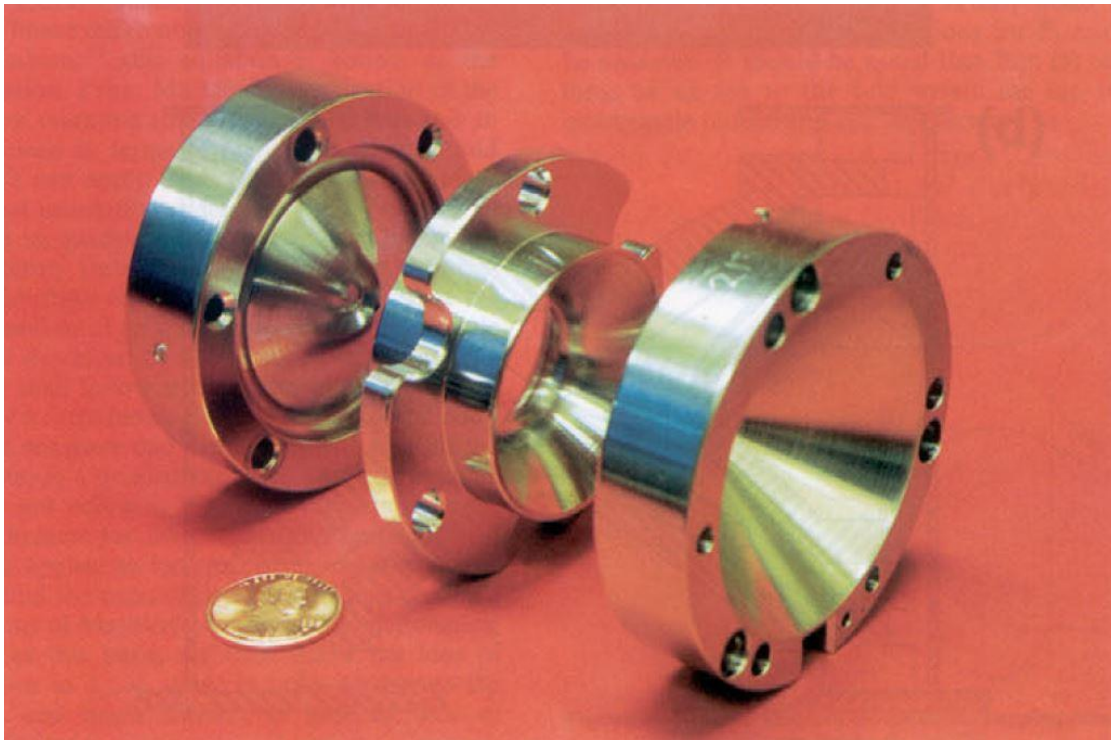


Figure 7. Picture of the endcaps and ring electrode of an ion trap. Reprinted from March, R. E. *J. Mass Spec.* 1997, 32, 351–369. Copyright 1997, with permission from John Wiley and Sons.²⁴



Figure 8. Diagram of an ion trap that has been cut in half. Reprinted from March, R. E. J. Mass Spec. 1997, 32, 351–369. Copyright 1997, with permission from John Wiley and Sons.²⁴

1.4– Ion-Trap Theory

The theory, that supports how quadrupole ion traps function, addresses the movement of ions as well as their excitation and ejection. In order to grasp an understanding of this theory one must be conscious of the fact that QITs operate by

sampling many small packets of ions that are gated into and out of the trap over and over again. This process is typically repeated many times in the process of producing a mass spectrum.¹⁸

1.4.1– Motion of Ions

The movements of ions in a quadrupole ion trap are complex. They do not move in straight lines or circles. This complexity is due to the dynamic focusing nature of the QIT that causes an increase in exertion of force on the ions as they move away from the center of the trap. This focusing is aided by a background pressure of helium (~1 mTorr) which helps “cool” the ions by removing some of their kinetic energy, focusing the ions toward the center of the ion trap. The theory that explains the motion of ions inside of the QIT is based on Mathieu’s studies on the vibrations of stretched skins in the late 19th century in which he was able to mathematically define the stretching in terms of stability and instability.²⁵ From Mathieu’s equation we are able to derive the regions of stability and instability of ions inside of a QIT. Equation (3) is the commonly accepted form of the Mathieu equation.

$$\frac{d^2u}{d\xi^2} + (a_u - 2q_u \cos 2\xi)u = 0 \quad (3)$$

Where u is representative of the coordinate axis $x, y,$ and z, ξ represents a parameter equal to $\Omega t/2$ where t represents time and Ω is a frequency, while a_u and q_u represent

dimensionless trapping parameters. This equation provides us with the necessary components to create a Mathieu stability diagram, shown in Figure 9, which highlights the areas of radial and axial stability.²⁴

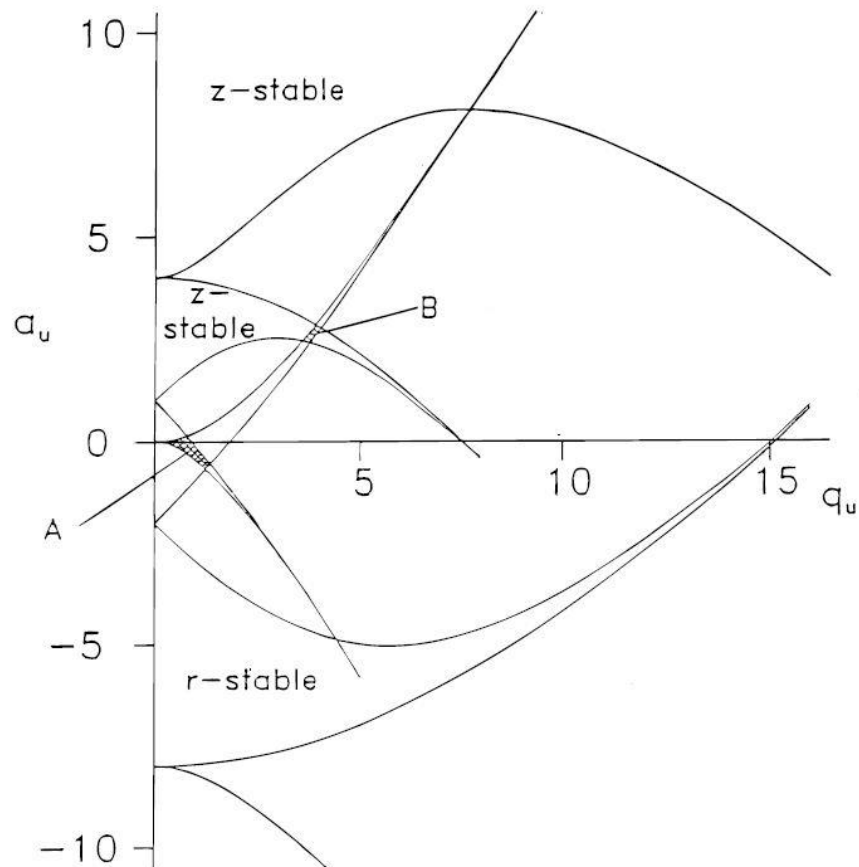


Figure 9. Mathieu stability diagram. Reprinted from March, R. E. J. Mass Spec. 1997, 32, 351–369. Copyright 1997, with permission from John Wiley and Sons.²⁴

The areas where radial and axial stability overlap, are the regions where ions are able to be trapped inside the QIT. There are two of these regions, however only one of

which is currently utilized by commercial instruments.^{18,24} This utilized region of stability is highlighted in Figure 10.²⁶

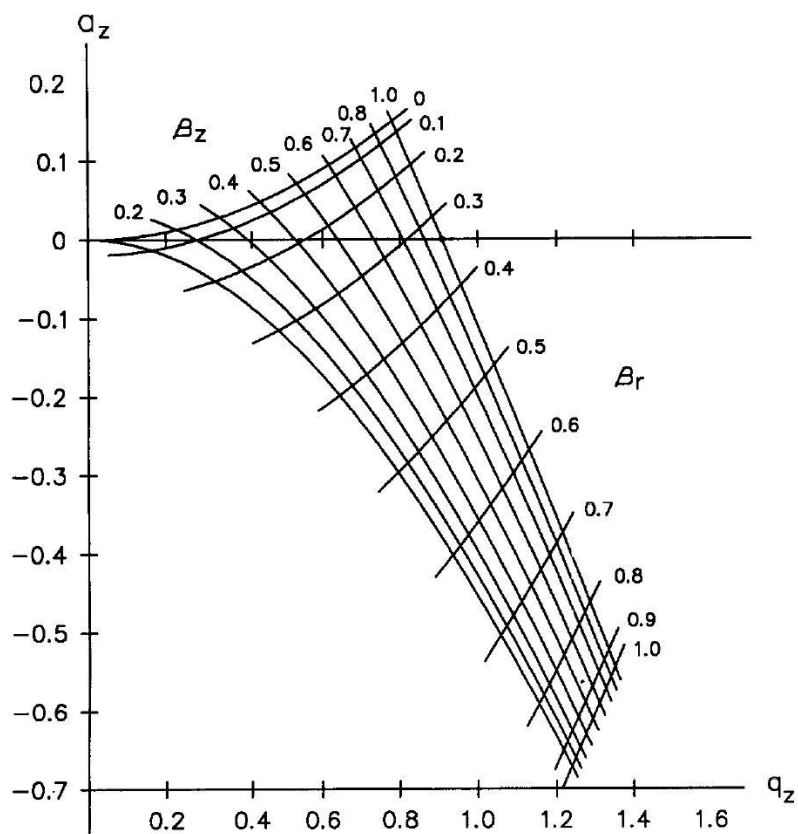


Figure 10. Simultaneous stability in the Mathieu stability diagram. Reprinted with permission from Todd, J. F. J.; Penman, a. D.; Smith, R. D. *Int. J. Mass Spectrom. Ion Process.* 1991, 106, 117–135. Copyright 1991 American Chemical Society.²⁶

The motion of the ions inside this stable region is prescribed by the potential surface, an oscillating quadrupole field, that exists inside the ion trap. The trajectory of the ions therefore mimics this surface and oscillates in a Lissajous curve (Figure 11).

This motion is given by secular frequencies that are directly related to the m/z of the

trapped ions. Therefore the lower m/z compounds will be closer to the center and compounds with higher m/z ratios will be further from the center. Equations (4) and (5) describe these secular frequencies.²⁰

$$\omega_{u,n} = (n + \frac{1}{2} \beta_u)\Omega \quad \text{and} \quad \omega_{u,n} = -(n + \frac{1}{2} \beta_u)\Omega \quad (4)$$

$$\beta_u \approx \sqrt{\left(a_u + \frac{q_u^2}{2}\right)} \quad (5)$$

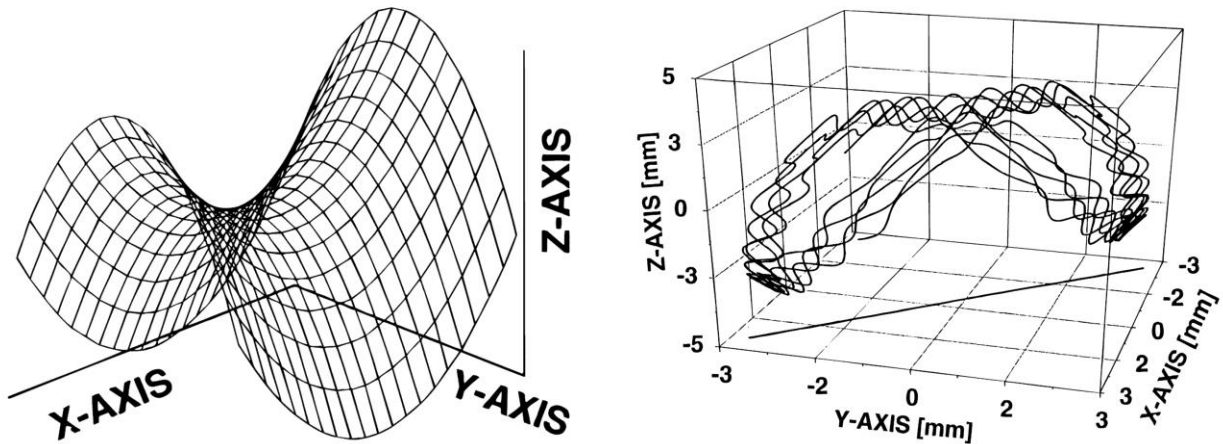


Figure 11. Potential surface of a quadrupole field (left). Trajectory of an ion in a quadrupole ion trap (right). Reprinted from March, R. E. J. Mass Spec. 1997, 32, 351–369. Copyright 1997, with permission from John Wiley and Sons.²⁴

1.4.2– Ion Ejection

In order for the quadrupole ion trap to operate as a mass spectrometer it must eject the ions that it traps to an external detector. The ejection of ions from the QIT is useful for not only producing a mass spectrum of the sampled ions but it is also useful for ejecting unwanted ions and selectively isolate wanted ions in the trap. This ability highlights an extremely useful feature of a QIT in that it allows multiple stage mass spectrometry experiments to be performed, otherwise known as MS^n .¹⁸ Two different methods can be used for this ejection from the ion trap, mass selective instability and resonance excitation.

1.4.2.1– Mass Selective Instability

For ion ejection QITs typically utilize a mass selective instability scan mode.²⁷ This method of ion ejection and subsequent detection was a revolution for ITMS when it first was developed in 1980. It significantly limits the current of ions that are sent to the detector and therefore produces excellent signal to noise ratios. The first example of this can be seen in Figure 12 along with the pulsing nature of this method of ejection.²⁸

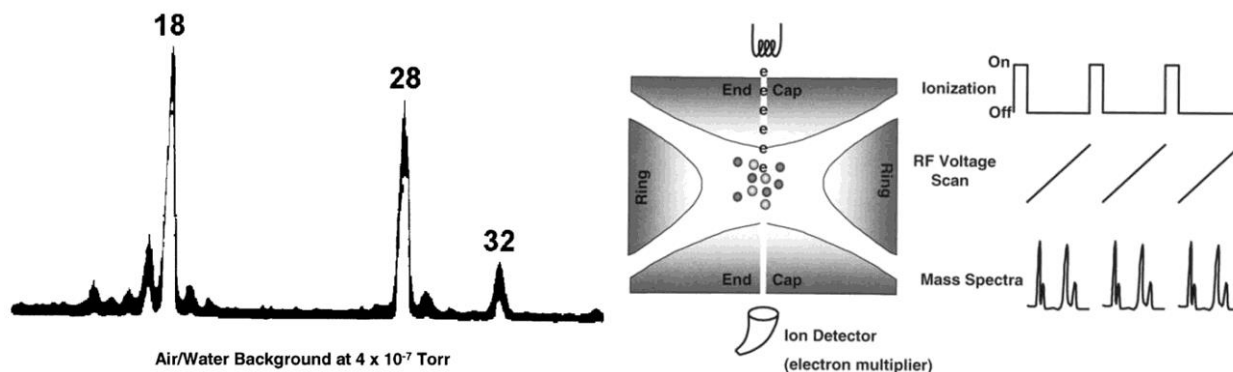


Figure 12. First example of mass selective ejection (left). Diagram illustrating the pushing nature of mass selective ejection (right). Reprinted from Stafford, G. Am. Soc. Mass Spectrom. 2002, 13, 589–596. Copyright 2002, with permission from Springer.²⁸

The mass selective instability mode operates by ramping the amplitude of the rf potential which increases the q_z value until the ions become unstable and are axially ejected through the hole in the endcap. The point at which these ions are unstable in the axial direction is known as q_{eject} which is where $q_z = 0.908$. This point can be seen in the Mathieu stability diagram Figure 10.²⁶ This is also demonstrated by the diagram given in Figure 13 which highlights the positions of ions with different m/z ratios along the mass-selective instability line.²⁹ From the position of the ions it is apparent that the mass-selective instability mode ejects the compounds of the lowest m/z first followed by the higher m/z ratio compounds. The m/z of the compounds ejected is given by

$$m/z = \frac{8V}{q_z(r_0^2 + 2z_0^2) \omega^2} \quad (6)$$

where V amplitude of the rf potential applied to the ring electrode with ω being its angular frequency, r_0 is the internal radius of the ring electrode, and z_0 the closest distance from the center of the trap to the end-cap.¹⁸ The drawback of this method being that the q_z value is fixed, therefore limiting the resolution of ions with a high m/z ratio (for LCQ this is about 2000 m/z).¹⁸ The timing of the sequences in this mode is given in Figure 14.³⁰

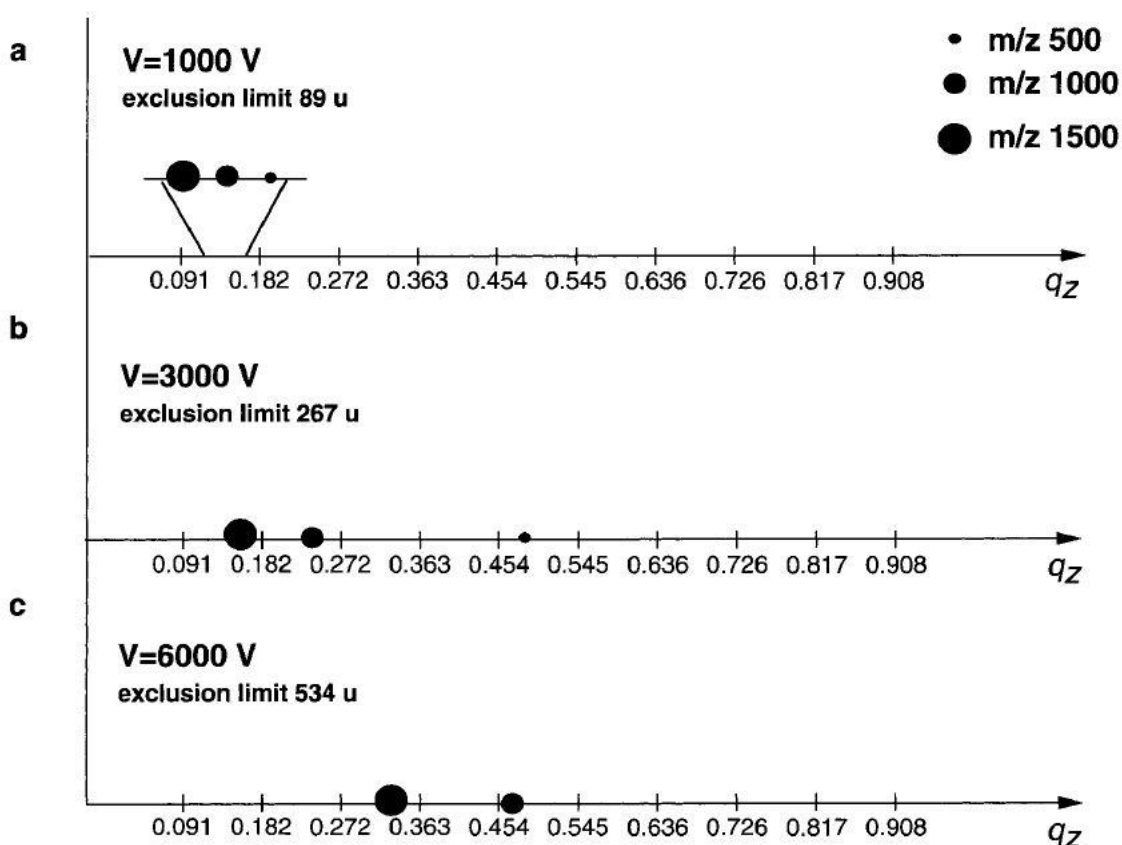


Figure 13. Ejecting ions via mass-selective instability mode. Reprinted with permission from Jonscher, K. R.; Yates, J. R. *Anal. Biochem.* 1997, 244, 1–15. Copyright 1997 American Chemical Society.²⁹

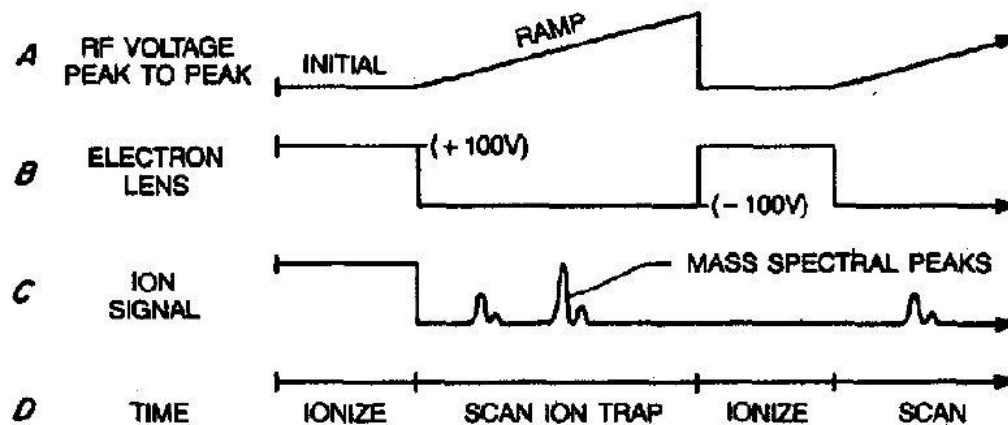


Figure 14. Timing of mass-selective instability mode. Reprinted from Stafford, G.; Kelley, P.; Syka, J. E. P.; Reynolds, W. E.; Todd, J. F. J. *Int. J. Mass Spectrom. Ion Process.* 1984, 60, 85–98. Copyright 1984, with permission from Elsevier B.V..³⁰

1.4.2.2– Resonance Excitation

Resonant excitation is another method of ion ejection that addresses the principle drawback of mass selective instability allowing for higher m/z ratios to be ejected. For this method the secular frequencies of the ions (described in equation 4) are matched with the frequency of an applied oscillating signal.³¹ This is an axial modulation where an a.c. voltage is applied to the end-cap electrodes and results in the increase in translational energy of the ions in which the frequency matches.²⁹ Thus, allowing for the ejection of ions at an effective lower q_z and increasing the m/z limit that can be ejected.²⁹ This can be viewed as a “hole” in the Mathieu stability diagram as depicted in Figure 15.^{29,31} For the ejection of the ions in this mode, the resonance excitation is an addition to the mass-selective instability mode.

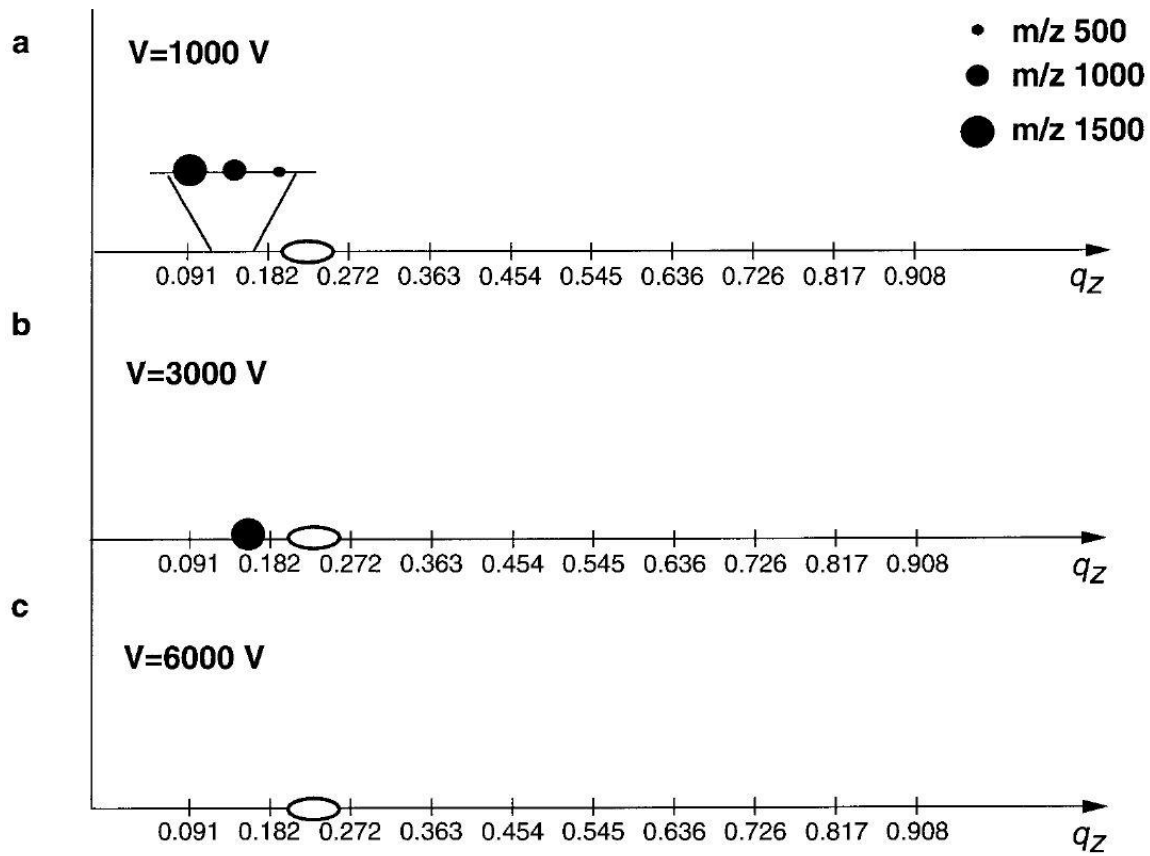


Figure 15. Ejecting ions via resonant excitation. Reprinted with permission from Jonscher, K. R.; Yates, J. R. *Anal. Biochem.* 1997, 244, 1–15. Copyright 1997 American Chemical Society.²⁹

This resonance excitation is also useful as a means of adding energy to ions without ejection. This instability of the ions produced by the resonant excitation leads to an increase in ion-molecule interactions inside the trap which can lead to dissociations occurring. This highlights a popular use for resonance excitation, collision induced dissociation (CID).

1.4.3– Collision Induced Dissociation

Collision induced dissociation (CID) is the dissociation of ions in the gas phase through collisions with neutral molecules or “targets”.³² This is not the only method of dissociating ions in the gas phase, however it is the most popular.^{32–35} A brief description of other methods of dissociation is given in Table 2, here we will only discuss CID as it is relevant to our work.

Table 2. Methods for dissociation of ions in the gas phase.³²

Method	Energy Range	Instruments	Description
PSD	Low	RETOF	Metastable or collision-induced dissociations in flight tube of reflectron time-of-flight instrument
CID	Low	QqQ, IT, QqTOF, QqLIT, FTICR	Collision-induced dissociation by collision of precursor ions with inert target gas molecules in collision cell. Energy range 1–100 eV
SID	High	Tandem TOF, sectors	Same as above with keV energies
	Low	Hybrid (BqQ), QqQ, IT, FTICR	Collisions between precursor ions and solid target surface with or without self-assembled monolayer causing fragmentations as well as other side reactions
	High	Tandem TOF, RETOF	Same as above with precursors of higher translational energies (instrument dependent)
ECD	Low	FTICR	Low-energy beam of electrons resulting in electron capture at protonation (or cationic) site with subsequent fragmentation following radical ion chemistry
IRMPD	Low	IT, FTICR	Continuous-wave low-energy infrared laser activates precursor ions by multiphoton absorption with consequent fragmentation
BIRD	Low	IT, FTICR	Low-energy thermal activation method ideal for calculations of energy thresholds and thermodynamic properties

Collision induced dissociation is accomplished by increasing the internal energy of ions until decomposition occurs. This is accomplished by inelastic collisions of an ion with sufficient translational energy with a neutral species.^{32,36} The extent of this dissociation is dependent on the internal energy that these collisions produce in the ion.

This process was originally developed for use in tandem-in-space mass spectrometers, but it has been adapted for use in tandem-in-time mass spectrometers, such as a quadrupole ion trap.³⁴ For tandem-in-space instruments ions are directed through a region of high pressure of argon or helium where there is a higher probability of the ions interacting with the gas. Whereas in a tandem-in-time mass spectrometer, such as an ion trap, a background pressure of helium is held constant at around 1 mTorr and the ions are excited through resonance excitation to induce an increase in collision energies with the gas.^{20,34}

1.5– Conclusions

In conclusion, mass spectrometry has revolutionized the field of chemistry, providing us with the ability to accurately measure the mass to charge ratio of ions of all types. The analytical technique that J. J. Thompson founded in 1913 still lives on today with ever-increasing utility and ease of use. This functionality has been aided by Fenn's discovery of electrospray that has enabled us to make molecular elephants fly and also by Paul's development of the quadrupole ion trap allowing tandem-in-time mass spectrometry.

The gas-phase environment of the quadrupole ion trap provides us with a reaction vessel in which ions can be isolated and undergo ion-molecule interactions. This environment is unique due to the lack of solvation effects on the ions and neutral molecules, making the QIT an excellent place to study the inherent reactivity in ion-

molecule reactions. In the next chapter we will explore ion-molecule reactions in the gas phase.

Chapter 2 – Ion-Molecule (IM) Reactions and Organometallic Chemistry in Mass Spectrometry

2.1– Reactions in the Gas Phase in Mass Spectrometry

The gas phase is a unique environment for the study of IM reactions. It provides many benefits for the study of these IM reactions. Firstly, it provides the ability to study the inherent reactivity of compounds without interference from solvation effects. This is helpful with attempting to rationalize what happens in the condensed phase relative to the inherent reactivity of compounds. Another substantial benefit of studying reactions in the gas phase is that reactive intermediates, which form in the condensed phase but are readily reacted away, are able to be probed. This is allowed by the ability to study reactions in a wall-less vessel where only desired reagents are allowed to interact. This provides experimental data that more closely resembles theoretical calculations. For example in a QITMS with trapping parameter, q_z , set at 0.25 the average velocity of the ions is 7m/ms. This corresponds to a mean free path of 7m, when at a vacuum pressure of 7×10^{-6} Torr, which is orders of magnitude greater than what is observed in the condensed phase.³⁷

In addition to the ability to be able to study inherent reactivities and access reactive intermediates, collision induced dissociation is available to probe the structures of the ions formed. Another benefit of gas-phase IM reactions is the limited quantities of compounds needed, often times orders of magnitude less than what is needed to

characterize a reaction in the condensed phase. Gas-phase reactions are also relatively quick to complete, with reactions occurring on the millisecond time frame. These all lead to the gas-phase reactions being cheaper to complete than comparative condensed-phase experiments. Gas-phase IM reactions provide invaluable experimental information that is difficult or impossible to attain from other methods.

2.2– Organometallic Chemistry in Mass Spectrometry

Studying organometallics in the gas phase provides invaluable information on the inherent reactivity of organometallic complexes. The gas phase provides an environment to study organometallics free from solvation effects. Early attempts to study organometallics in the gas phase were limited due to the harsh ionization techniques that were used and the need for the complexes to be volatile. The development of “soft” ionization methods for MS that allowed non-volatile compounds to be transferred to the gas phase as an ion, prefaced and allowed for organometallics to be studied in the gas-phase environment of a MS. The development of ESI by Fenn in the 1980’s stemmed studies of organometallics in MS, a field that is ever-growing to this day.^{38–40} Other soft ionization techniques have been utilized for the formation of organometallic complexes in the gas phase, such as fast atom bombardment (FAB), field desorption (FD) and matrix-assisted laser desorption (MALDI). However as Sheil et al. noted, ESI is the most convenient and informative ionization method for organometallics.⁴¹

ESI provides the ability to study ionic organometallic complexes in their intact form, allowing the analysis of complexes and intermediates that are active in the condensed phase. The realization of the potential of ESI to be useful for the study of organometallics was recognized early in its development.³⁸ The first example of this was given by Chait et al. in 1990 when they described the formation of ruthenium bipyridine and ruthenium phenanthroline complexes using a quadrupole mass analyzer equipped with ESI (Figure 16).⁴² In this study they also described the effect the capillary voltage has on the production of clusters of solvated complexes, similar to what Fenn proposed for organic compounds earlier in 1984 when he described the formation of clusters generated by ESI.^{38,42} Throughout the years organometallic studies in the gas phase have increased in popularity due to the ever-increasing use of catalysts in reaction schemes.³⁹

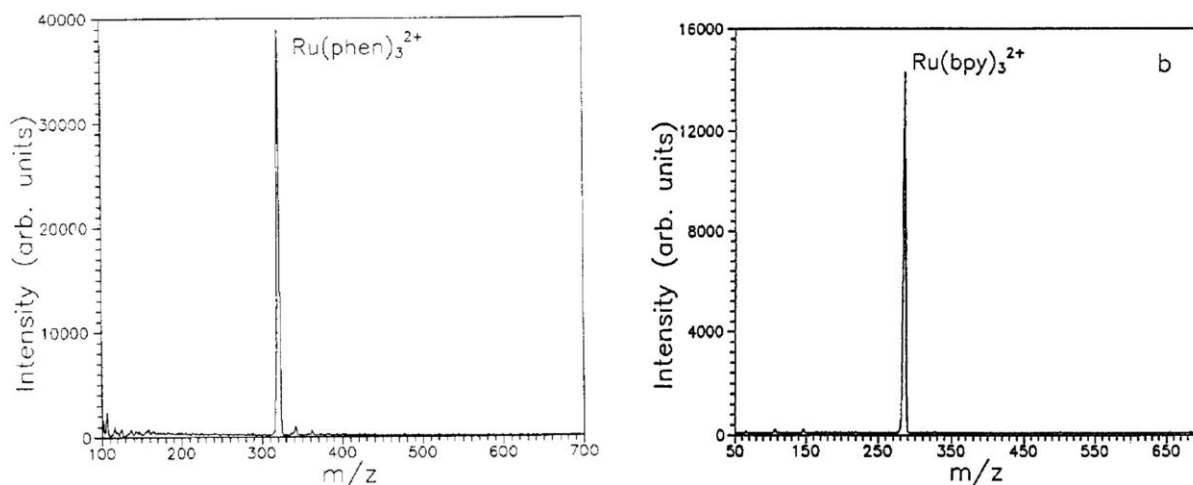


Figure 16. Mass spectra of Ru(phen)₃²⁺ on the left and Ru(bpy)₃²⁺ on the right.

Reprinted with permission from Katta, V.; Chowdhury, S.; Chait, B. T. J. Am. Chem. Soc. 1990, 5348–5349. Copyright 1990 American Chemical Society.⁴²

2.3– History of Ion-Molecule Reactions in the Gas Phase

The history of IM reactions in the gas phase is long starting with J. J. Thompson, the founder of mass spectrometry in 1913, when he suggested that gas-phase reactions could be possible in his new device.² Only a few years later Dempster observed the first ion-molecule reaction when he observed a m/z ratio of three, which he attributed to a reaction between H_2^+ and H_2 .⁴³ However, many years passed before IM reactions were revisited. They were overlooked due to the harsh nature of the ionization sources that were in use; namely electron ionization (EI) that produced complicated dissociation spectra that were of little use for IM reactions.⁴⁴ It wasn't until 1966 that Munson revisited IM reactions.⁴⁵ This was driven by the development of a softer ionization method, chemical ionization (CI), which permitted the ionization of mostly intact volatile compounds rather than dissociated molecules like in EI. To this day CI remains a popular ionization method.⁴⁴ Since, the initial interest in IM reactions many types of MS instruments have been utilized as a gas-phase reaction vessel.

2.4– Instruments for Gas-Phase Reactions

Instrumentation for gas-phase ion molecule reactions has progressed much since the discharge tube MS of Thompson. Initially, tandem-in-space instruments such as the quadrupole MS were employed for these IM studies.⁴⁵ For these instruments, IM molecule reactions are able to occur in the high pressure region of the ionization chamber. The negative aspect of this method is that the reactant ions are not able to be

selected. Further development of instrumentation led to multiple quadrupole instruments that were even more useful for the study of IM reactions. Notably the development of the triple quadrupole (TQ) MS, by Yost in 1979, led to IM reactions where the reactant ion could be characterized before being allowed to react with a neutral reagent.⁴⁶ Foreshadowed by the development of the double sector quadrupole by Beynon in 1973, the TQMS offers more utility for IM reactions than any other preceding instrument.⁴⁷

In a TQMS IM reactions are allowed to take place in the second quadrupole of this instrument, allowing for the characterization and selection of the reactant ion (Figure 17).⁴⁶ The introduction of the neutral reagent is typically accomplished by the injection of a neutral to the collision cell of the TQMS.⁴⁸ The TQMS also allows for the product ions to be characterized in the third sector of the instrument. This ability is useful in providing structural characterization and product distribution data for the studied reactions. Since the development of the TQMS many IM reactions have been studied, and it continues to be utilized in the study of IM reactions to this day.⁴⁸⁻⁵¹

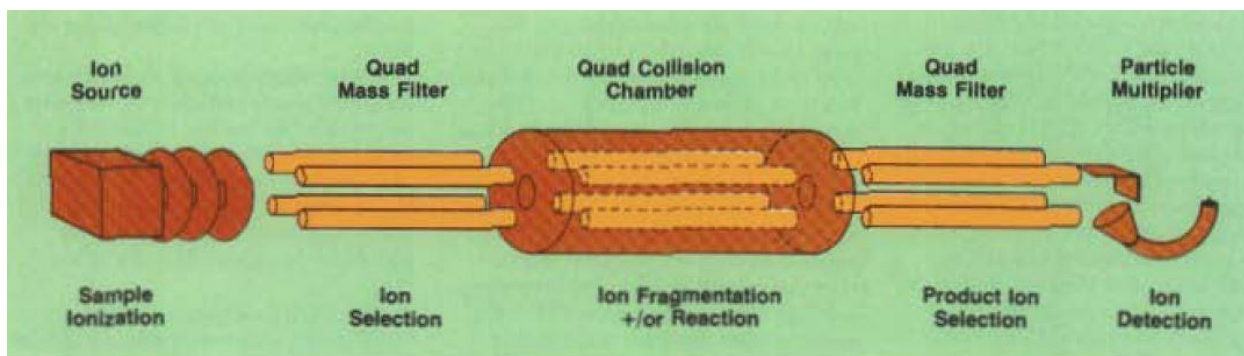


Figure 17. Diagram of a TQMS. Reprinted with permission from Yost, R. A.; Enke, C. G. *Anal. Chem.* 1979, 51, 1251–1262. Copyright 1979 American Chemical Society.⁴⁶

Other instruments have been used for IM reactions as well as the TQMS with much success. The ion beam MS has been used for IM reactions to determine reaction dynamics and cross-sectional energy dependencies, providing information on chemical binding energies.⁵² A diagram of an ion beam MS used for IM reactions can be seen in Figure 18. In these instruments ions are excited, mass selected and then decelerated before being guided by an octopole and allowed to react with neutral reagents in a high pressure region.⁵³ Upon the ions being allowed to react with the neutral reagent the ions are passed through a quadrupole where they are mass analyzed.⁵³ The pulsed electron beam MS has also been used for IM reactions, providing information on gas-phase proton transfer equilibria, clustering equilibria, as well as kinetic data on temperature dependent IM reactions.^{54–57}

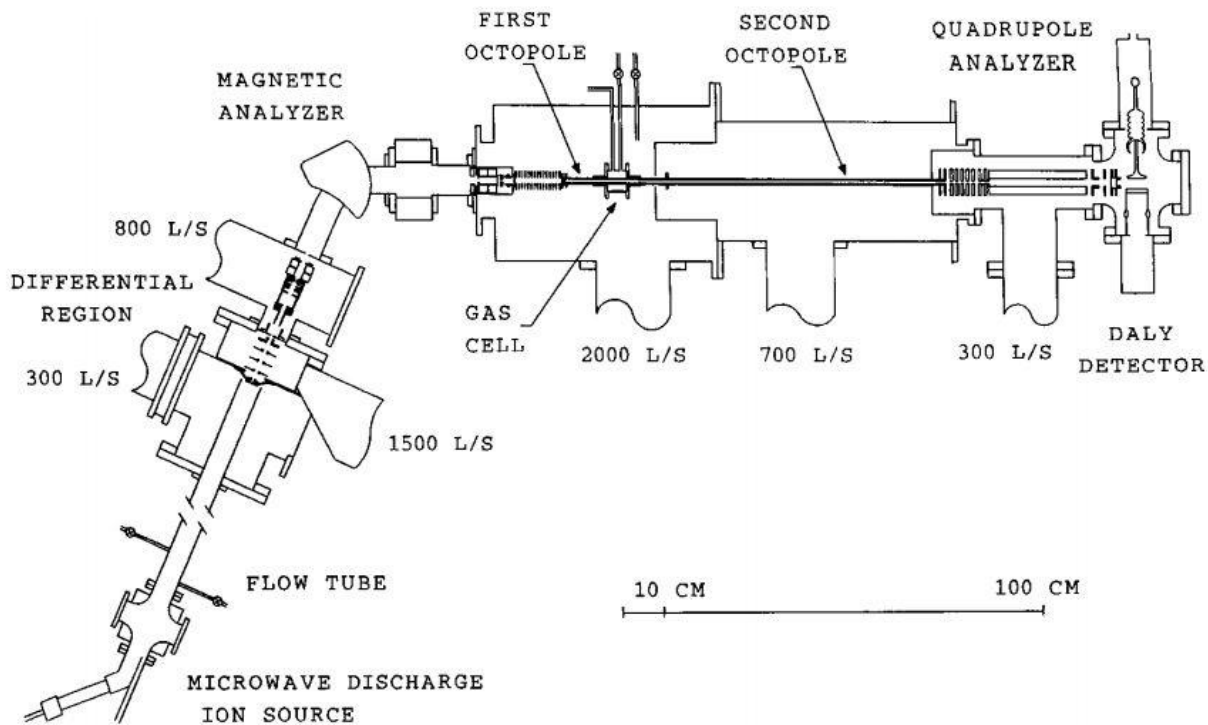


Figure 18. Diagram of an ion beam MS used for IM reactions. Reprinted from Muntean, F.; Armentrout, P. B. *J. Chem. Phys.* **2001**, *115*, 1213–1228. Copyright 2001, with permission from AIP Publishing LLC.⁵⁸

The flowing afterglow MS has been used extensively for IM reactions in the gas-phase.⁵⁹ The primary use of this instrument has been to obtain kinetic rates for IM reactions. These instruments operate by exiting helium ions and allowing them to interact with reactant gasses to form reactant ions, this process is known as electron impact (EI). Once formed, the reactant ions flow down the flow tube where they are thermalized and then allowed to react with neutral reagents for a set distance. Upon reaching the end of the tube, most of the gasses are evacuated by a Roots blower with the ions sampled through a skimmer and mass analyzed. These instruments can be

used in tandem to create a selected ion flow tube (SIFT) which allows mass selection of the reactant ion. A diagram of this instrument is given in Figure 19.⁵⁹

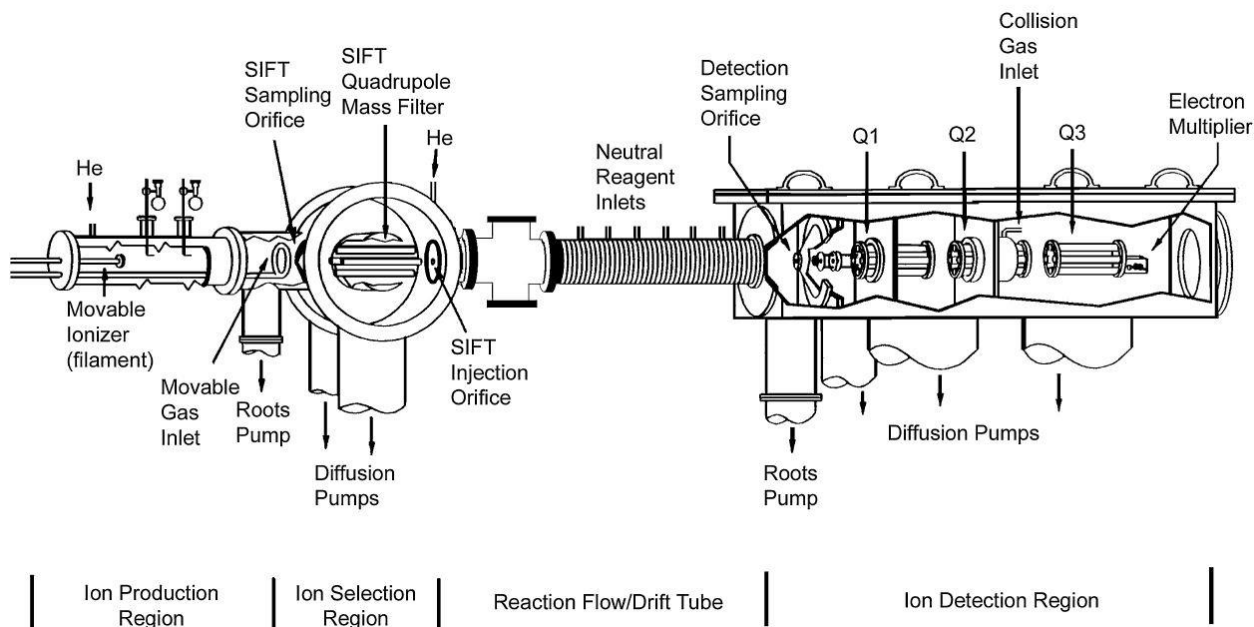


Figure 19. Flowing afterglow-selected ion drift tube-TQ MS. Reprinted from Bierbaum, V. M. *Int. J. Mass Spectrom.* 2014, In Press. Copyright 2014, with permission from Elsevier B.V.⁵⁹

While tandem-in-space instruments have been the most prominent instruments used for IM reactions in the gas phase, trapping mass spectrometers have increasingly played a role in this field. The benefits of using a trapping instrument over a tandem-in-space instrument include being able to repetitively select product ions and probe their structure using CID. Another benefit of using trapping instruments for IM reactions is the ability to easily define the time the neutral reagent is allowed to react with the ionic reactant. Ion cyclotron resonance (ICR) MS was the first trapping instrument that was

utilized for gas-phase IM reactions.⁶⁰⁻⁶² The method in which these work is that the ions produced from the ion source are pulsed into the ICR cell where a background pressure of the neutral reagent can be pulsed in by a solenoid valve and reactions are allowed to occur.⁶⁰ Once ions and the neutral reagents are allowed to react for a defined time, their secular frequencies are measured and a spectrum is produced and the ions can be pulsed out of the cell. Along with ICR instruments, ion traps have become prominent in the field of IM reactions. Ion traps have the ability to do IM reactions and MS^n in a smaller footprint and lower cost relative to ICR instruments making them a practical choice for the study of reaction kinetics.

2.5- Ion Trap as a Reaction Vessel

The ion trap, with its ability to contain ions in an electronic vessel, provides a unique environment for the study of IM reactions. Unlike other trapping instruments the ion trap is able to contain ions in a constant background pressure of gas. This is in sharp contrast to an ICR, which can only function under extremely high vacuum conditions.⁶³ The ion trap, while not initially designed for IM reactions, has been utilized for IM reactions since Retinhaus observed the first IM reaction in an ion trap in 1967.⁶⁴ While studying hydrocarbons he observed the reaction of CO^+ with a neutral hydrogen atom from the background gas forming COH^+ .⁶⁴ This study was completed closely after the Munson and Field observed the first gas-phase IM reaction in 1966, thereby demonstrating the intertwinement of the ion trap and IM reactions.⁴⁵ Since these initial studies, the ion trap has been utilized for a wide variety of IM reactions from the

fundamental studies of organic reactions, to organometallics, and even proteomics.^{65–68}

When attempting to perform IM reactions in an ion trap one must first address the issue of how to get the neutral reagent into the gas phase for these reactions to occur. Since ion traps were not designed for this purpose they typically require modifications to allow the neutral reagents in the trap, which we will discuss in more detail in the next section.

2.6– Neutral Reagent Introduction

Neutral reagent introduction into the gas phase of an ITMS is generally regarded as one of the larger challenges when attempting to have IM reactions inside of an ion trap.⁶⁵ A limiting factor for IM reactions in the gas phase that must be taken into consideration is that the neutral reagents must be volatile so that they can be transferred to the gas phase. Multiple methods have been proposed to transfer these neutral compounds to the gas phase of the ion trap. These methods range from simple methods to modifications of the bath gas delivery manifold. This section will discuss the benefits and drawbacks of each of these methods.

2.6.1– Gas-Phase Introduction

Introducing neutral reagents in the gas-phase of an MS is a challenging endeavor due to the high vacuum conditions that exist in the mass analyzer. However, gas-phase introduction is the only feasible and controllable manner in which a neutral reagent can be transferred into the mass analyzer. An alternative is solution-phase

introduction where a neutral is mixed with the ionic precursor and then transferred to the gas phase through the ionization source. The benefit of this is that no modification to the instrument needs to be made. However, this method only allows for a small amount of intact neutral to be transferred to the gas phase due to dissociation and ionization that occurs in the ionization source, depending upon ionization source.⁶⁹ Therefore, gas-phase introduction is with its ability to provide more control of the neutral is the preferred method.

2.6.1.1– Pulsed-Valve Introduction

Pulsed-valve introduction was the first method developed for introducing neutral reagents into the gas phase of a trapping instrument.⁷⁰ This was initially developed for ICR instruments as a means to have IM reactions in the trap yet also allow for the collection of high resolution spectra.⁷¹ Since ICR instruments function under high-vacuum conditions to obtain high resolution data, a constant background pressure of a neutral is not feasible. Therefore to subvert this, neutral reagents are pulsed in via a solenoid valve at a specific time and duration that is controlled by the MS software, allowing neutral to react with the ions in a period of relatively high pressure before the neutrals are eventually evacuated by the vacuum pumps and spectra collected.⁷⁰ This method is still the standard method for neutral injection in an ICR.

This pulsed-valve injection method has also been used on other instruments that do not demand such rigorous vacuum regimens as ICRs, specifically QIT instruments.

To accomplish this in a QIT a small hole must be drilled into the trap to allow the neutral reagents to be pulsed in via a solenoid valve. For this method in a QIT ions are gated into the trap, an ion is isolated and neutrals are allowed to react with the ions for a selected reaction time before the rf voltage is ramped and the ions in the trap ejected.⁷² This method can be seen in Figure 20.⁷² While useful for the study of IM reaction products and their structures it is not effective for the study of kinetics due to uncertainty in the pressure of the neutral in the trap.

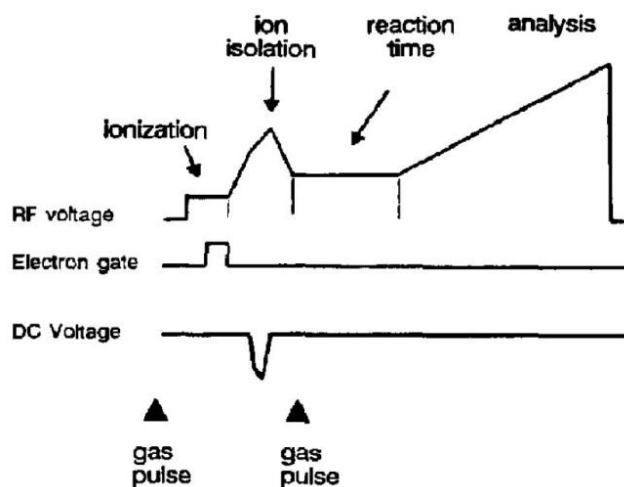


Figure 20. The sequence for pulsing neutrals into a QIT. Reprinted from Emary, W. B.; Kaiser, R. E.; Kenttiimaa, H. I.; Cooks, R. G. J. Am. Soc. Mass Spectrom. 1990, 1, 3–6. Copyright 1990, with permission from Springer.⁷²

2.6.1.2– Leaked-Valve Introduction

Another method that has been utilized for introduction of neutral into the gas phase of trapping instruments is the leak-valve introduction method. This is accomplished by modifying the helium manifold to allow neutrals to be leaked into the manifold and a small percentage of them to be carried to the trap.^{73,74} A diagram of this method is given in Figure 21.⁷³ This is only applicable to trapping instruments that operate with a background pressure of bath gas, such as QITs. This method eliminates the need for drilling an additional hole into the ion trap, and therefore makes it a more achievable modification. Neutrals are continuously flowed into the trap at a constant rate making this method inherently more useful for the study of kinetics. However, uncertainties in the partial pressures of the neutrals limit the usefulness of this method. This concept of modifying the bath gas manifold rather than the trap formed the basis for this method.

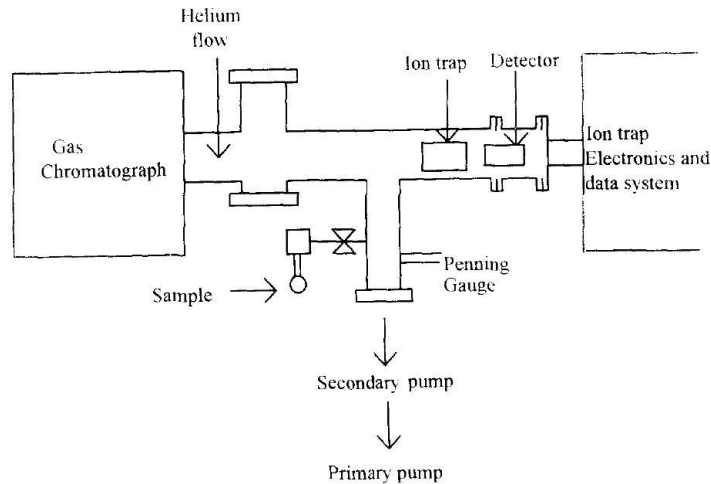


Figure 21. QIT instrument that has been modified to allow leaking of neutrals into the bath gas manifold. Reprinted from Liere, P.; March, R. E.; Blasco, T.; Tabet, J.-C. *Int. J. Mass Spectrom. Ion Process.* 1996, 153, 101–117. Copyright 1996, with permission from Elsevier B.V.⁷³

2.6.1.3– Syringe-Pump Introduction

Syringe-pump introduction was a method that was developed to address the issues with the leaked-valve introduction method, specifically control and understanding of the partial pressures of neutral in the trap. Developed by Gronert, this method allows introduction of the neutral reagent into a modified bath gas manifold. Neutrals are injected via a syringe pump, operating at 30-300 $\mu\text{L/hr}$, through a septum on the manifold. Once injected the neutrals are carried by the helium to trap through a restriction capillary and T connection allowing the majority of the helium and neutrals be sent to waste. The pressure of the helium in the manifold is kept at 3 psi by a regulator on the helium source, while the flow of the helium is regulated by a flow meter that is

downstream of the T connection at the trap and is set to 1.250 L/min. This allows mixing ratios of $10^{-3} - 10^{-5}$ He/neutral. The largest limitation of this system is that neutral molecules must be volatile so that they can be transferred to the gas phase in the 3 psi environment of the helium manifold. A diagram of this system can be seen in Figure 22.

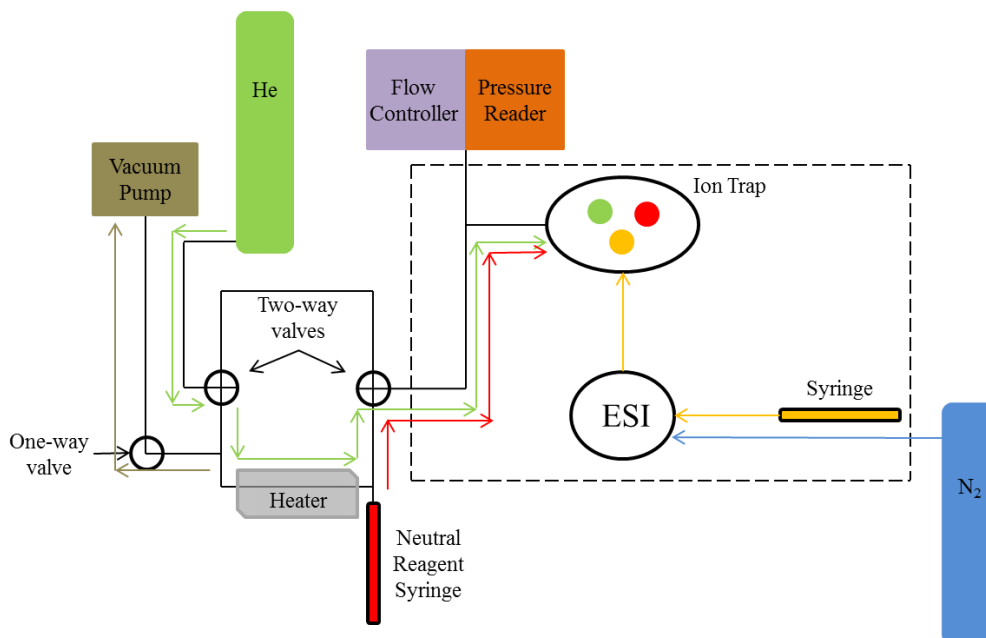


Figure 22. Diagram of a Gronert modified QITMS.

For this modification, the gasses are able to freely effuse into the trap necessitating for differential effusion to be taken into account.⁶⁵ Due to the gasses having different molecular weights, they have different velocities and therefore different effusion rates, meaning that the larger molecules will effuse slower and effectively build up in the trap. Therefore, to determine the reagent pressure a correction must be made and it is described by

$$P_{\text{RX}} = 1.75 \times 10^{-3} \times \frac{F_{\text{RX}}}{F_{\text{He}}} \times \frac{d_{\text{RX}}}{\text{MW}_{\text{RX}}} \times \left(\frac{\text{MW}_{\text{RX}}}{\text{MW}_{\text{He}}} \right)^{1/2} \quad (7)$$

where F_{RX} is the neutral flow rate, F_{He} is the helium flow rate, d_{RX} is the neutral density, MW_{RX} is the molecular weight of the neutral, and MW_{He} is the atomic weight of helium. With an understanding of reagent pressures in the trap, kinetics are feasible to study in a QITMS. This method provides excellent precision, $\pm 5\text{-}10\%$, and uncertainties in accord with other gas-phase introduction methods, $\pm 20\text{-}30\%$.⁶⁵

2.7– Kinetic Measurements in the Gas-Phase

Kinetic measurements are a common focus for studies in the gas phase. These measurements have most commonly been focused in flowing afterglow instruments due to their efficient thermalization of the reactant ions.^{75,76} However, due to their low cost and general robustness the ITMS has become useful for measuring rates for reactions in the gas phase.^{65,76} Being a tandem-in-time instrument capable of MS^n the ITMS is perfectly suited for the study of reaction kinetics as well as providing mechanistic information. Recording kinetic rates in an ITMS has become possible as a result of the development by Gronert, in which he described a method to modify the bath gas delivery manifold allowing a neutral reagent to be injected into the ion trap at a controlled and variable rate.⁷⁷

Many factors must be considered for the recoding of rate constants in a ITMS. The first issue that must be taken into consideration is the kinetic window of the instrument, that is the range of kinetic rates that can be analyzed. When determining the kinetic window for an instrument there are three things to consider.⁶⁵ The first is the maximum time an ion is able to be held in a stable trajectory inside the instrument. For an ITMS it has been demonstrated that ions are very stable in their trajectory and are able to be contained in the trap for minutes to days in extreme examples.²⁸ Therefore, in the case of the ITMS the residence time of the ion is rarely a limiting factor.

A second limitation that must be considered is the amount of neutral reagent gas that can be tolerated in the trap.⁷⁸ Ion traps have the unique ability to have an increase in resolution with the addition of a bath gas. This ability along with the extremely stable trajectory of the ions makes the ion trap an abundantly robust instrument for the addition of a neutral reagent. Gronert has reported that a neutral reagent in the ion trap is able to be tolerated up to 1% of the helium bath gas.⁶⁵ Considering that ion traps function best when held at around 1 mTorr of helium, we can conclude that partial pressures of a neutral reagent in the trap can be as much as 1×10^{-5} Torr. Kinetic rates as slow as $1 \times 10^{-13} \text{ cm}^3 \text{ molecule}^{-1} \text{ sec}^{-1}$ are able to be recorded in an ion trap.⁶⁵ This is limited by the purity of the neutral reagents and the cleanliness of the ion trap. A factor that must be taken into consideration for recording rates in an ITMS, is the purity of the neutral reagent. Upon reaching the lower limit of the reactions that can be recorded, any impurity in the neutral may begin to react with the ion at a faster rate than the analyte neutral. Impurities are also inherently present in the ion trap itself and can cause similar

issues. This issue can subsequently shrink the kinetic window depending on the composition of the neutral.

The partial pressure of the neutral reagent while being the determining factor for the lower limit of rates that can be recorded, the upper limit of rates that can be recorded in the trap is instead controlled by the collision rate. This is the rate of the reaction when a reaction occurs at every collision of a neutral molecule and an ion. It is generally around $2 \times 10^{-9} \text{ cm}^3 \text{ molecule}^{-1} \text{ sec}^{-1}$ for a polar neutral molecule reacting with an ion, while a non-polar molecule reacting with an ion will be slower due to the decreased attraction. There are two methods for calculating the collision-controlled of these IM reactions. The first method is the Langevin method which is useful for calculating collision-controlled rates of IM reactions where the molecule is not polar. This method can be described by the equation

$$k_L = 2\pi e \left(\frac{\alpha_n}{\mu} \right)^{1/2} \quad (8)$$

where e is the elementary charge, α_n is the polarizability of the neutral, and μ the reduced mass of the IM pair.^{79,80} This method while sufficient for non-polar neutrals does not take into consideration dipole interactions of a neutral with an ion and gives collision-controlled rates that are too slow for polar IM reactions. Therefore to address

the polar neutrals, the averaged-dipole-orientation (ADO) theory was described by Su and Bowers.^{81,82} This method can be described by the equation

$$k_{\text{ADO}} = (2\pi e/\mu^{1/2})[\alpha_n^{1/2} + c\mu_D(2/\pi kT)^{1/2}] \quad (9)$$

where e is the elementary charge, α_n is the polarizability of the neutral, μ the reduced mass of the IM pair, μ_D the permanent dipole of the molecule, k the Boltzmann constant, and c the locking constant. The locking constant is a term that compensates for the charge “locking in” the dipole and is given by the equation

$$\mu_D/\alpha_n^{1/2} \quad (10)$$

where α_n is the polarizability of the neutral, and μ_D the permanent dipole of the molecule. This method accurately describes and can therefore predict the collision-controlled rate of IM reactions where the neutral is polar.

Useful kinetic data from a MS is only achieved when the temperature is known. Without an understanding of the internal energy distribution of the ions, quantitation cannot be accomplished. For instruments such as an ITMS many experiments have been conducted and concluded that the ions in the ion trap are essentially the same temperature as the bath gas, which is around 300 K.^{65,83} This can be seen in Figure 23, which is a graphical representation of a study concerning the temperature of the ions in

an IT. This has led to research in the area of heated traps for the study of kinetics at varying temperatures.⁸⁴ Mass spectrometers are useful tools for measuring gas-phase kinetics that are unrivaled by other instrumentation.

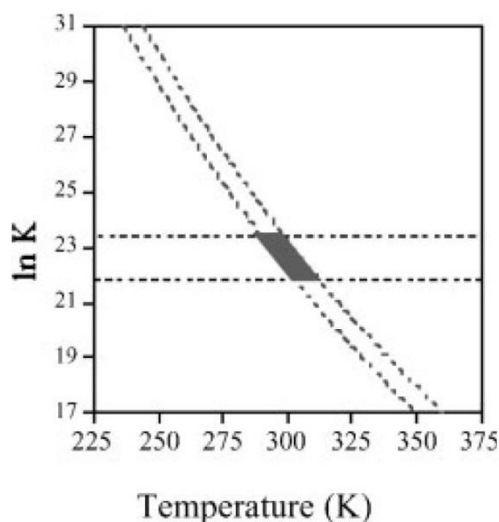


Figure 23. The reaction of thiophenolate with 2,2,2-trifluoroethanol which describes the temperature inside an ion trap. Reprinted from Gronert, S. *Mass Spectrom. Rev.* 2005, 24, 100–120. Copyright 2005, with permission from John Wiley and Sons.⁶⁵

2.8– Conclusions

In conclusion, mass spectrometers provide a platform for the study of IM reactions in the unique environment of the gas phase. These gas-phase studies enable us to probe the inherent reactivity of complexes providing experimental data that more closely corresponds with theoretical calculations, while also allowing reactive intermediates to be probed and their structures determined through dissociation. The

wide variety of reactions that are able to be studied and the speed in which this can be accomplished by this method leaves little doubt that analyzing reactions in the gas phase of a MS will continue to become increasingly relevant.

Chapter 3 – Formation and Reactivity of Gold (I) Carbenes in the Gas Phase

3.1– Introduction

Gas phase studies have become a useful tool in examining intermediates in condensed-phase reactions catalyzed by organometallic species.^{85–88} The key advantage of the gas phase is that short-lived intermediates can be isolated in the inert environment of a mass spectrometer and probed in the absence of side reactions with solvent and other components in reaction mixtures.^{65,78} Transition metal-stabilized carbenes have been incorporated in many important catalytic cycles, including cyclopropanation and metathesis processes.^{89–92} Gronert et al. have reported the gas-phase synthesis of iron and cobalt carbene complexes by the reaction of a ligated metal with diazoacetate esters.^{93,94} In those cases, the metal carbenes were prone to rearrangement processes, particularly metal-ligand insertions that converted the carbene to an ylide. As an alternative we have applied a variety of approaches to prepare and explore the reactivity of gold(I) carbene complexes in the gas-phase. We are inspired to do so because gold catalysis has become very popular due to the unique reactivity that gold exhibits.⁹⁵

3.2– Carbenes

Carbenes are neutral molecules that have a divalent carbon atom with only six valence electrons. These are reactive species that have the general formula R-C:-R.

Carbenes were first discovered in 1855 by Geuther and Hermann when they proposed a dichlorocarbene as an intermediate in a reaction.⁹⁶ Little attention was given to them until after the general acceptance of free radicals as intermediates in the 1930s.^{97,98} There was a lack of interest in carbenes until 1953, when Doering reported the synthesis of cyclopropanes by the addition of dichlorocarbene to olefins.⁹⁹ This began immense research on carbene species that is still ongoing to this day.^{89,100}

Carbenes exist in two different electronic states, singlet and triplet (Figure 24). Substituents attached to the carbene carbon play a major role in determining which ground state the carbene will have, with triplet carbenes acting as radicals and singlets stabilized by π -electron donating groups.^{89,100} The structure of the carbene, linear or bent, also plays a role in the spin state of the carbenes by causing a change in the nature of the frontier orbitals (Figure 25).⁸⁹

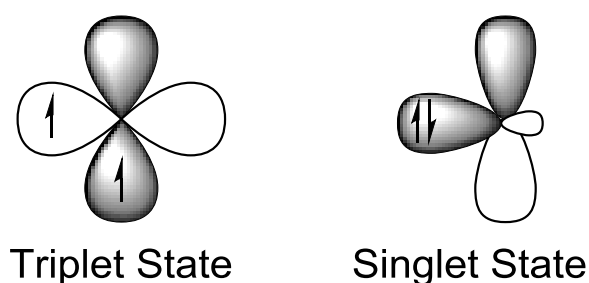


Figure 24. Ground states of carbenes.

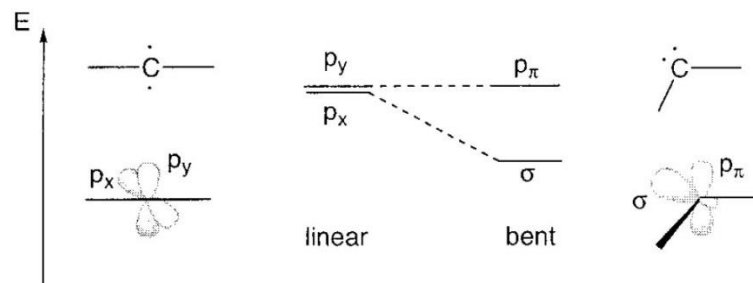


Figure 25. Frontier orbitals of carbenes. Reprinted with permission from Bourissou, D.; Guerret, O.; Gabbai, F. P.; Bertrand, G. *Chem. Rev.* 2000, 100, 39–91. Copyright 2000 American Chemical Society.⁸⁹

In 1964, Fischer described the first metal-carbene complex, a tungsten-benzylidene complex.¹⁰¹ He examined metal-carbene complexes with low-oxidation state metals having singlet ground states, with a significant gap in the singlet and triplet states.¹⁰⁰ These carbenes are now regarded as Fischer carbenes and possess an electrophilic character.¹⁰⁰ They have characteristics similar to both carbanions and carbocations in that these carbenes have both a lone pair of electrons and an empty orbital on the carbon atom. Because the lone pair is coordinated to the metal, the carbocationic characteristic is the more dominant in controlling the nature of these singlet carbenes. Later in 1974, Schrock described the formation of a metal-carbene complex with a high oxidation state metal.¹⁰² These carbenes, now regarded as Schrock carbenes, are in the triplet spin state and are nucleophilic in nature, exhibiting radical-like behavior.^{89,100}

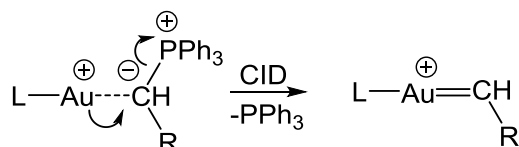
Carbenes exhibit a high degree of reactivity due to their desire to fulfill the octet rule and have been shown to undergo C-H activation, cyclopropanation, and metathesis reactions.^{89,100} This high reactivity potential along with evidence of carbenes as intermediates in reactions has led to an increasing demand to understand and attempt to tame these species. The most prevalent method of modulating the reactivity of carbenes is to stabilize them with transition metals.^{89,100} When bonded to a metal, the carbene can be stabilized by back donation from the metal d-orbitals forming species known as carbenoids. However, the extent of this stabilization and the formation of these carbenoids have been brought into question in recent studies.¹⁰³

3.3– Gold-Carbene Complexes

In the recent years, Chen and co-workers have presented several papers focused on the gas-phase formation and reactions of gold(I) benzyldiene complexes of the general form LAuCHPh^+ , where L is an N-heterocyclic carbene (NHC).^{104–107} The carbenes were not generated directly by electrospray ionization, but were formed by the collision-induced dissociation of an ylide precursor (Scheme 1). In their studies, they have shown that the gold(I) benzyldiene reacts with alkenes to give addition products, and that under collision-induced dissociation conditions (CID), the addition product decomposes either by loss of a cyclopropanation product (combined elements of the benzyldiene and alkene) or by metathesis to produce a new gold(I) carbene complex. In the current study, we have tested the generality of this approach for forming gold(I) carbenes and explored the kinetics of the bimolecular reactions of the gold(I)

benzylidenes. The results are supported by density functional theory (DFT) calculations that highlight the important intermediates on the reaction surface.

Scheme 1. Chen's method of gold(I) carbene formation from ylide fragmentation.



3.4– Experimental Procedures

All experiments were conducted in a modified ThermoFinnigan LCQ Deca XP Plus quadrupole ion trap mass spectrometer equipped with ESI. Gold(I) salts and carbene precursors were dissolved in methanol at 10^{-4} - 10^{-5} M. Typical ESI conditions involved flow rates of 3-5 μ L/min with needle potentials between 3.5 and 6 kV and heated capillary temperatures from 125 to 200 °C. A notched waveform is used for isolating the cationic gold (I) species. Upon obtaining a stable signal, neutral reagents can be spiked into the helium stream via a custom gas-handling system which has been described above.

Kinetic measurements were completed by establishing an appropriate flow rate for the neutral reagent and varying the time between the isolation of the ion and the expulsion of all the ions to obtain a mass spectrum. Ten different time delays were used in each reaction. Neutral reagent flows and time delays were varied to obtain plots that

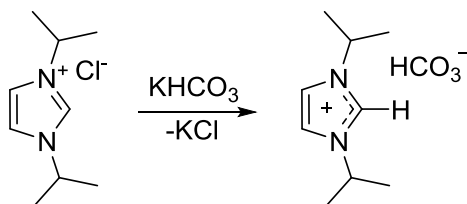
cover two to three half-lives of the ionic reagent. This allows for a sampling of the majority of the ions that are in the trap. Data were obtained over at least two days with multiple neutral and ionic solution preparations to ensure reproducibility. Kinetic plots showed sufficient linearity with correlation coefficients (r^2) of 0.98 or greater.

Most neutral reagents were obtained from commercial sources in the highest purity available and used without further purification. The neutral reagent 2-methoxyethyl 2-diazoacetate was synthesized by adapting a procedure reported by Doyle.¹⁰⁸⁻¹¹⁰ As needed, neutral reagents were diluted in cyclohexane. Gold salts, triphenylphosphine gold (I) chloride and dimethylsulfide gold (I) chloride, were obtained from commercial sources and used without further purification. 1,3-diisopropylimidazolium gold (I) chloride was synthesized following a previously reported synthesis by Taton et al.¹¹¹ Gold ylides of the form $\text{PPh}_3\text{RCHAu}^+\text{L}$ (where R = H, Ph, OMe, COOMe and L = PPh_3 , 1,3-diisopropylimidazolium) were synthesized by a ligand exchange procedure that has been reported by Chen et al.¹⁰⁴

3.5– Synthetic Procedures

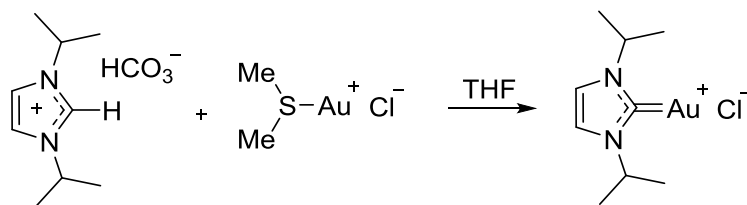
Compounds that were transferred to the gas phase via ESI were not purified. Rather, these compounds were electrosprayed and isolated in the ion trap.

Scheme 2. Synthesis of 1,3-diisopropylimidazolium hydrogen carbonate.



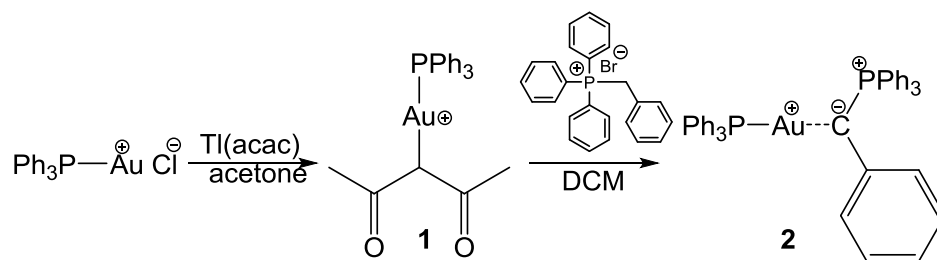
Using an established method¹¹¹, a mixture of 1,3-diisopropylimidazolium chloride (253.91 mg, 1.35 mmol) and KHCO_3 (140.60 mg, 1.41 mmol) was dried under a vacuum. Dry methanol (1.25 mL) was then added and mixture stirred for two days at rt. The suspension was then filtered over Celite. The methanol was evaporated under a vacuum to reveal 267.1 mg of a sticky solid (yield varying up to 92%). The sticky solid was triturated with acetone and filtered. The acetone was evaporated under a vacuum leaving a white powder.

Scheme 3. Synthesis of 1,3-diisopropylimidazolium gold (I) chloride.



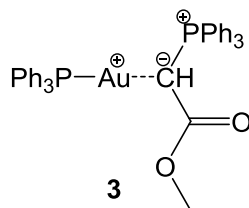
Using an established method¹¹¹, a mixture of chloro(dimethylsulfide)gold(I) (11.4 mg, 39.0 μmol) and 1,3-diisopropylimidazolium hydrogen carbonate (9.8 mg, 47.0 μmol) was stirred in THF (0.7 mL) for 1 h at 50 °C. The THF was removed under vacuum.

Scheme 4. Synthesis of compound **2**.



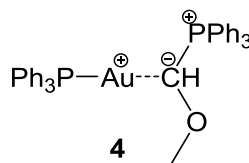
Using an established method ¹⁰⁷, a mixture of chloro(triphenylphosphine)gold (I) (187.1 mg, 0.4 mmol) and thallium(I) acetylacetonate (128.0 mg, 0.4 mmol) was stirred in 5 mL of acetone under N_2 for 5 h. The suspension was dried under a vacuum and extracted 4 times (8 mL) with an acetone and diethyl ether mixture (1:15). The extracts were combined, filtered through Celite and dried under a vacuum revealing a white solid **1**. A mixture of compound **1** (6.0 mg, 10.75 μmol) and benzyltriphenylphosphonium bromide (4.4 mg, 10.15 μmol) was stirred in DCM (0.5 mL) at rt for 6 h.

Scheme 5. Synthesis of compound **3**.



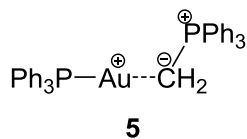
Following the same method used for compound **2**, a mixture of compound **1** (6.68 mg, 11.97 μmol) and (methoxycarbonylmethyl)triphenylphosphonium bromide (5.25 mg, 12.64 μmol) was stirred in DCM (0.5 mL) at rt for 6 h. For mass spectrometric analysis this solution was diluted to 10^{-5} mol/L.

Scheme 6. Synthesis of compound **4**.



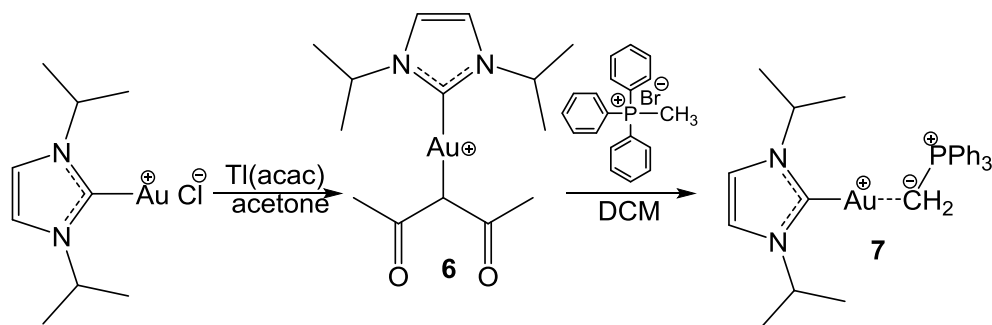
Following the same method used for compound **2**, a mixture of compound **1** (8.25 mg, 14.78 μmol) and (methoxymethyl)triphenylphosphonium bromide (8.05 mg, 20.79 μmol) was stirred in DCM (0.5 mL) at rt for 6 h. For mass spectrometric analysis this solution was diluted to 10^{-5} mol/L.

Scheme 7. Synthesis of compound **5**.



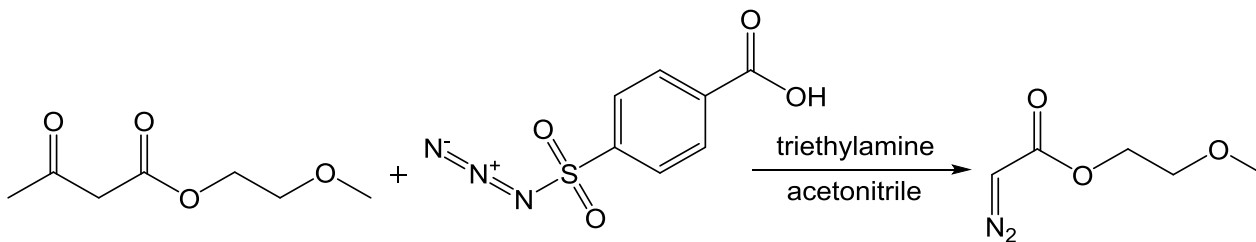
Following the same method used for compound **2**, a mixture of compound **1** (5.66 mg, 10.14 μmol) and methyltriphenylphosphonium bromide (4.35 mg, 12.18 μmol) was stirred in DCM (0.5 mL) at rt for 6 h. For mass spectrometric analysis this solution was diluted to 10^{-5} mol/L.

Scheme 8. Synthesis of compound **7**.



Following the same method used for compound **2**, a mixture of 1,3-diisopropylimidazolium gold (I) chloride (163.8 mg, 0.4 mmol) and thallium(I) acetylacetonate (126.5 mg, 0.4 mmol) was stirred in 5 mL of acetone under N₂ for 5 h. The suspension was dried under a vacuum and extracted 4 times (8 mL) with an acetone and diethyl ether mixture (1:15). The extracts were combined, filtered through Celite and dried under a vacuum revealing a white solid **1**. A mixture of compound **6** (8.17 mg, 18.22 μmol) and methyltriphenylphosphonium bromide (6.49 mg, 18.17 μmol) was stirred in DCM (0.5 mL) at rt for 6 h. For mass spectrometric analysis this solution was diluted to 10⁻⁵ mol/L.

Scheme 9. Synthesis of 2-methoxyethyl diazoacetate.



Adapting a previously reported synthesis from Doyle et al.^{108,110}, p-carboxybenzenesulfonyl azide (1 g, 4.4 mmol) was added to a solution of trimethylamine (613 μ L) and anhydrous acetonitrile (1.33 mL). This solution was then added dropwise to a solution containing 2-methoxyethyl acetoacetate (587.8 μ L, 4 mmol) and anhydrous acetonitrile (2.67 mL). This mixture was stirred for 19 h at RT, after which LiOH (395 mg in 3 mL of H₂O) was added and mixed. After mixing for 90 min H₂O (6.7 mL) was added to the mixture. This solution was then extracted with diethyl ether (4 mL) three times. The combined ether solutions were then washed over a brine solution and dried over MgSO₄. The resulting solution was forced to pass through a neutral alumina column and dried under reduced pressure.

3.6- Results and Discussion

Chen and co-workers have focused considerable attention on gold(I) benzylidenes that bear an NHC on the gold as the second ligand.^{104–107} As noted above, they can be

formed by the fragmentation of a phosphorous ylide (Scheme 1). They have shown that these gold carbenes react with alkenes to give addition products, which under CID yield cyclopropanes as well as metathesis products.¹⁰⁵ Given the nature of their apparatus, it was not possible to examine the kinetics of the addition or the subsequent bimolecular reactions of the addition products. In our quadrupole ion trap, we can complete MSⁿ (tandem mass spectrometry) experiments and therefore can probe each step in the complex reaction process. In the current study, we have adopted Chen's methodology with triphenylphosphine as the second ligand on gold, along with a variety of other ligands that can be seen below in Figure 26.

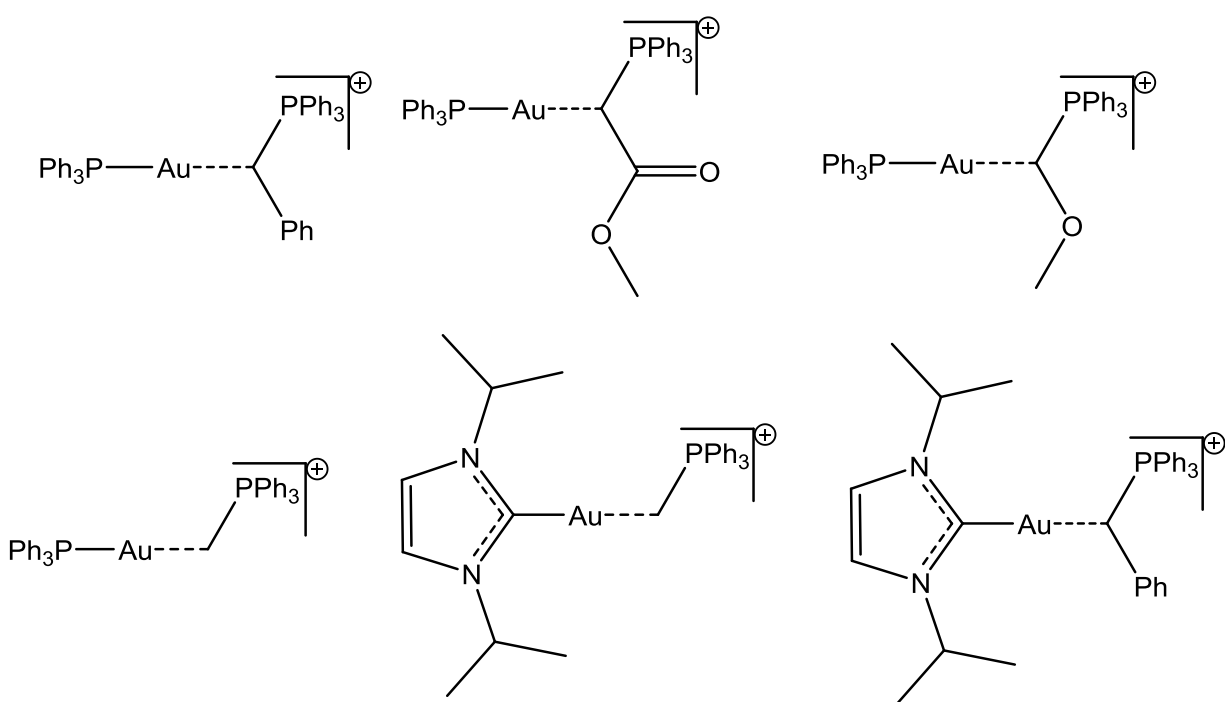


Figure 26. Gold (I) ylides used to form carbenes in the gas phase.

When subjected to CID, the ylide precursor (Scheme 10) readily loses triphenylphosphine and produces a species with characteristic carbene reactivity. A mass spectrum for the carbene is shown in Figure 27, where the precursor ylide was isolated, CID applied, and the carbene isolated.

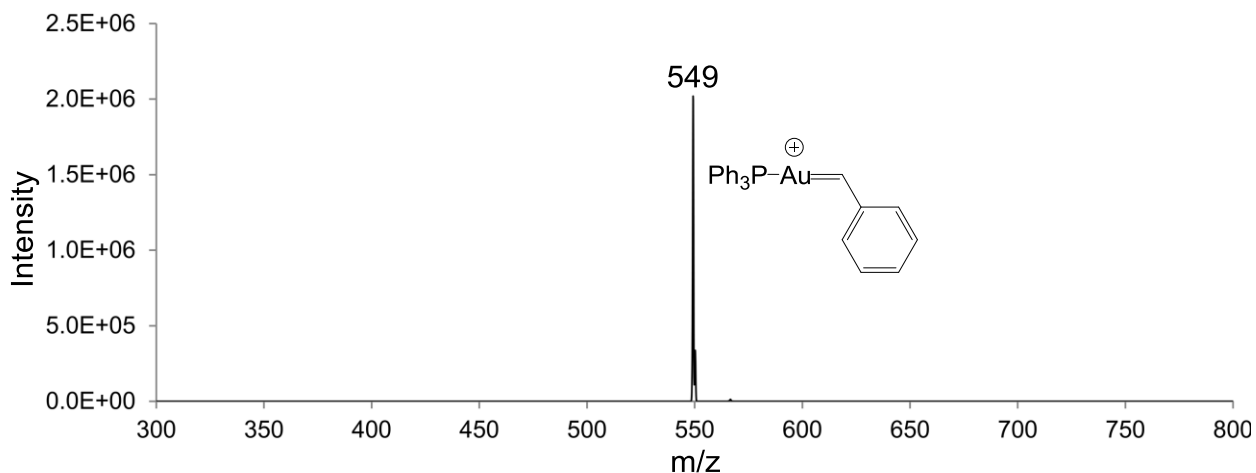


Figure 27. Isolating gold benzylidene fragment of ylide.

The gold(I) benzylidene was isolated in the ion trap and allowed to react with four olefins: cyclohexene, ethyl vinyl ether, 2,3-dihydrofuran, and 1,1-dichloroethylene. An example of this reactivity can be seen in Figure 28 where the carbene species was allowed to react with an olefin, forming an addition product which we interpret as cyclopropanation. It gave addition complexes with each of the olefins, except the most electron-deficient one, 1,1-dichloroethene. The bimolecular rate constants for the olefin reactions are presented in Table 3.

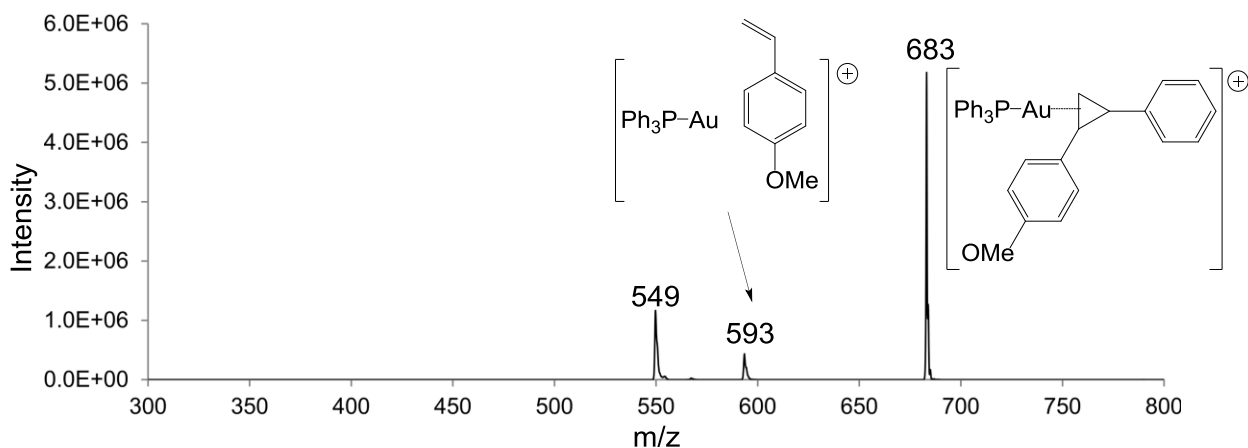


Figure 28. Cyclopropanation of gold benzylidene with 4-vinylanisole. Selection of m/z 549 followed by a reaction with 4-vinylanisole with a reaction time of 1300 ms.

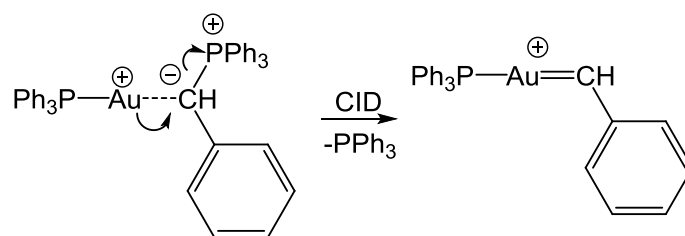
Table 3. Rate constants for the reaction of the Ph_3PAu^+ benzylidene complex with olefins^a.

Olefin	k	Efficiency ^c
1,1 dichloroethylene	NR ^b	NR ^b
Cyclohexene	3.34	39 %
2,3 dihydrofuran	7.75	62 %
ethyl vinyl ether	10.10	76 %

^aRate constants in units of $10^{-10} \text{ cm}^3 \text{ molecule}^{-1} \text{ sec}^{-1}$. ^bReaction too slow to characterize, $<10^{-12} \text{ cm}^3 \text{ molecule}^{-1} \text{ sec}^{-1}$. ^c k/k_{coll} where the collision rate is calculated by the method of Su and Bowers.⁸²

With the electron-rich olefins, ethyl vinyl ether and 2,3-dihydrofuran, the rate constants approach the estimated collision-controlled limit, indicating a relatively facile process.⁸² With dichloroethylene, the rate is too slow to characterize accurately in our system. The correlation between olefin nucleophilicity and reactivity is consistent with a Fisher carbene electronic structure.

Scheme 10. Gold(I) benzylidene precursor.



When held in the ion trap for an extended time period, the adduct from this reaction undergoes a second reaction with the olefin, leading to displacement of the benzylidene/olefin components of the adduct and formation of a new Ph_3PAu^+ /olefin complex. We assume that this reaction is the completion of a cyclopropanation process (Scheme 11). An example of this can be seen in Figure 29 where the cyclopropane adduct was held in the ion trap for an extended period with a constant background pressure of the olefin.

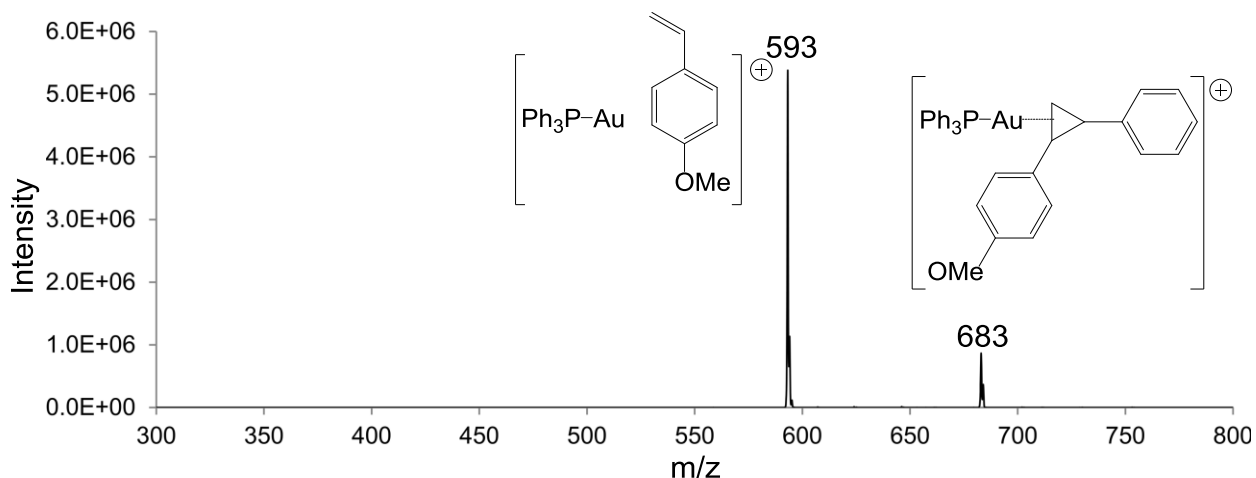


Figure 29. Substitution of cyclopropane product with 4-vinylanisole. Gold benzylidene at m/z 549 was selected and allowed to react with 4-vinylanisole for 2000 ms. The adduct at m/z 683 m/z was then selected and allowed to react for 10000 ms.

As a part of this study, DFT calculations were conducted in our lab.¹⁰³ DFT calculations with the M06 functional suggest that the gold coordinates with the cyclopropane rather than forming a metallocyclobutane. Chen and co-workers came to the same conclusion with calculations at the B3LYP level and identified a strong interaction between the gold and the benzene ring of the former benzylidene unit.¹⁰⁵ The reaction exhibits strict second-order kinetics and is best interpreted as a substitution reaction with the olefin replacing the cyclopropane in the addition complex.¹¹² The rate constants for this substitution process are well below those for the addition of the olefin to the gold(I) benzylidene, so the addition product can be observed and isolated as an intermediate in the ion trap, and there is sufficient kinetic separation to obtain rate constants for each reaction. This outcome is consistent with previous DFT calculations in related systems that show that the rate limiting step the

cyclopropanation reactions of gold(I) benzylidenes is the dissociation of the cyclopropane from the metal.¹¹³

Scheme 11. Reactions of gold(I) benzylidene with olefins.

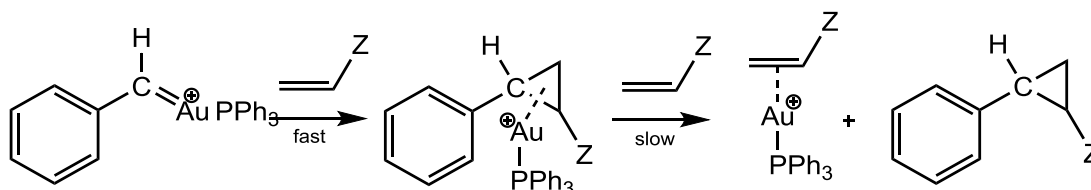


Table 4. Rate constants for the reaction of the addition complexes with olefins (Scheme 3).^a

Olefin	<i>k</i>	Efficiency ^b
Cyclohexene	1.40	1.66 %
2,3 dihydrofuran	0.70	0.56 %
ethyl vinyl ether	1.50	1.14 %

^aRate constants in units of $10^{-11} \text{ cm}^3 \text{ molecule}^{-1} \text{ sec}^{-1}$. ^b k/k_{coll} where the collision rate is calculated by the method of Su and Bowers.⁸²

Kinetic data for the substitution reactions are presented in Table 4. The rate constants for the reactions of the adducts with the olefins are 30- to 100-fold lower than those that were observed in the reactions of the gold(I) benzylidene. Analyzing the rate data is more complicated in the substitution reactions because features that make the

olefin more nucleophilic will also enhance the binding of the cyclopropane to the gold and attenuate the impact of the substituent. In order to achieve a greater understanding of the electronic effects, we used para-substituted styrenes to establish linear free energy relationships with the kinetics of the olefin reactions. Styrene, 4-fluorostyrene, 4-chlorostyrene, 4-methylstyrene, and 4-methoxystyrene were used in the study. The kinetics are presented in Figure 30 and Table 5.

Table 5. Rate constants for Ph_3PAu^+ benzylidene complex with substituted styrenes^a.

Neutral Reagent	σ_p	k (addition)	k (substitution)
4-Chlorostyrene	0.23	7.82	0.194
4-Fluorostyrene	0.06	8.94	0.250
Styrene	0	15.4	0.822
4-Methylstyrene	-0.17	17.2	1.56
4-Vinylanisole	-0.27	21.6	5.63

^aRate constants in units of $10^{-10} \text{ cm}^3 \text{ molecule}^{-1} \text{ sec}^{-1}$.

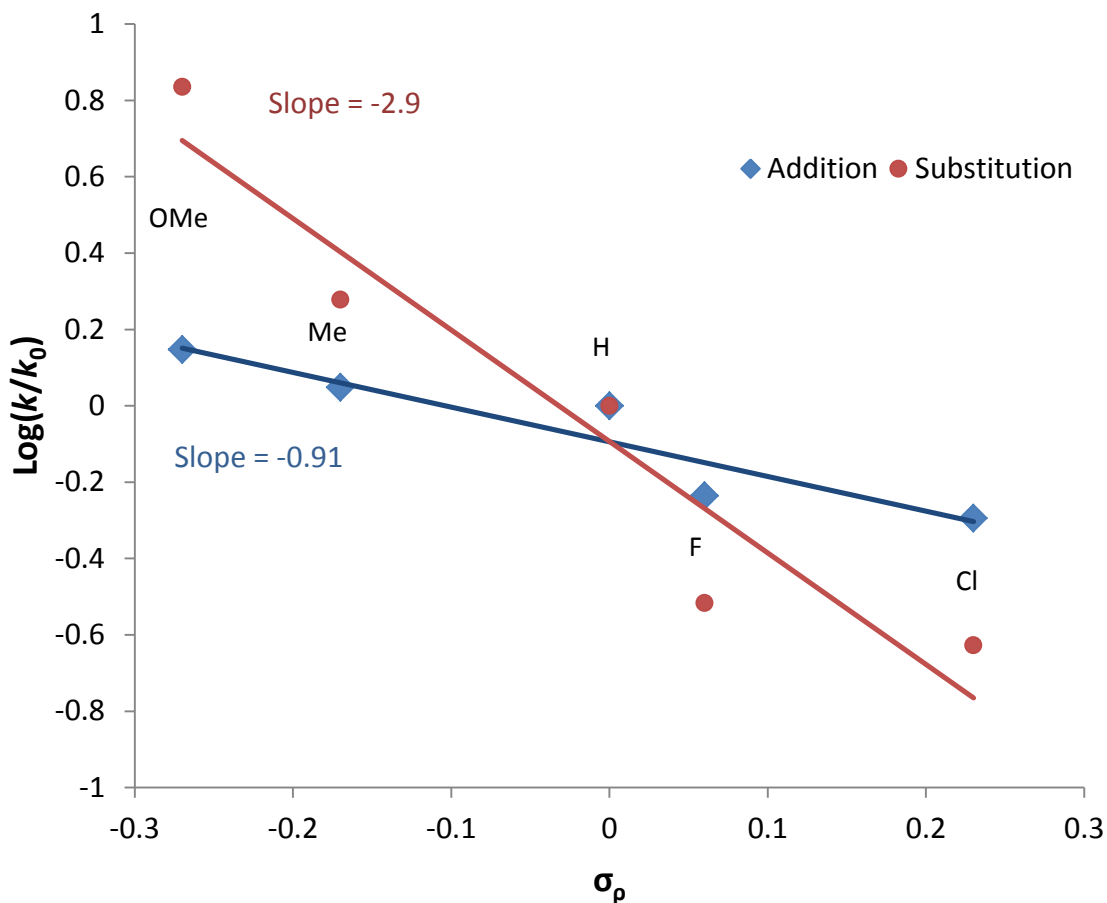


Figure 30. Hammett plot of the reactions of *para*-substituted styrenes with the Ph_3PAu^+ benzylidene complex (addition process) and its adducts (substitution process).

As with the other olefins, the styrenes give addition rates that are generally fast and approach the collision-controlled limit. The Hammett plot (Figure 30) illustrates the correlation between the electron-donating capability of the substituent (nucleophilicity of the olefin) and the rate constant of the reaction. In the reaction of the gold(I) benzylidene with the styrenes, the slope gives $\rho = -0.9$, which is a modest value for a gas-phase process. Systems such as substituted benzoic acids give rho values greater

than 10 in the gas phase.¹¹⁴ The value suggests that relatively little positive charge is developing on the olefin and points to an early transition state. To probe this system in the absence of substituents, we allowed the benzyldiene to react with a mixture of styrene and d₈-styrene. As expected for a fast reaction, the secondary kinetic isotope effect is small ($k_H/k_D = 1.13$). In the subsequent substitution reactions of the adducts, the ρ value triples in magnitude to -2.9, indicating that the process is much more sensitive to the electron density of the olefin's π -system. These reactions are slower and should have later transition states than the addition reactions – it is likely that there is more charge on the olefin in the transition state. Using a trimethylphosphine complex as a model, the substitution reaction with styrene is computed to be exothermic by about 10 kcal/mol.^{115,116} The large ρ value is also consistent with a metal/cyclopropane structure because if the addition product were a metallocycle, the electron-donating substituents on the metallocycle should be strongly stabilizing and attenuate the impact of electron-donating substituents on the incoming olefin.

It was also possible to probe the CID behavior of the addition products. Under CID, two pathways are apparent. One involves the loss of the cyclopropane followed by the addition of an olefin. The olefin used to prepare the addition complex is still in the ion trap during the CID experiment in our system and can react very readily with the ligated gold(I) cation that is formed after cyclopropane loss. This represents an activated, 2-step version of the substitution process described above. The other pathway is a metathesis and leads to a new carbene. An example of this can be seen in

Figure 31 where the cyclopropanation adduct is isolated at m/z 683 and CID is applied, revealing a metathesis product.

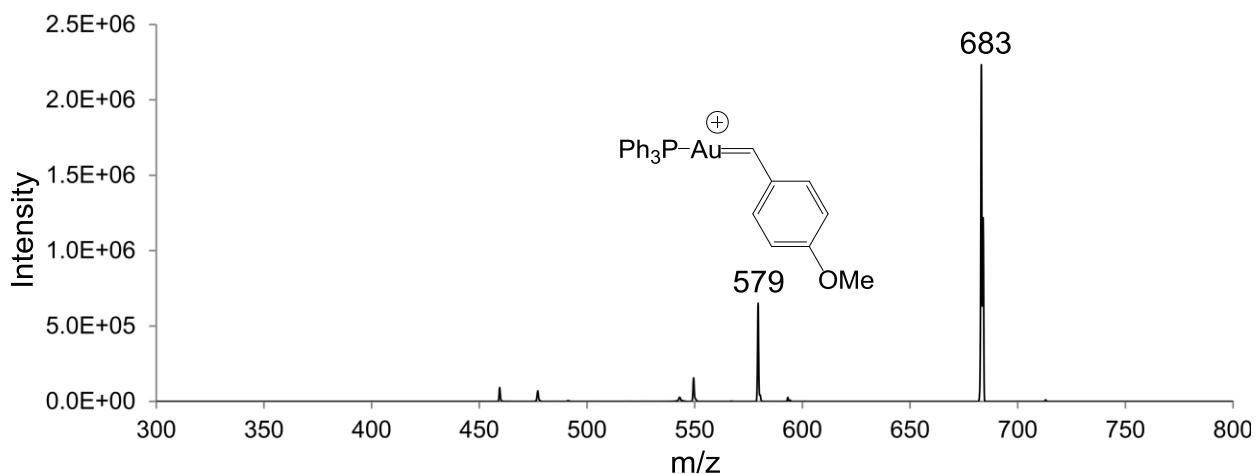


Figure 31. Metathesis reaction of gold benzylidene with 4-vinylanisole. The carbene is selected at 549 m/z and is allowed to react with 4-vinylanisole for 2000 ms. The adduct is selected m/z 683 and subjected to CID at 22%.

CID mainly produces a 4-methoxybenzylidene complex ($m/z = 579$), which results from the loss of styrene in the fragmentation process. This outcome indicates that under activated conditions, the addition product can access a metallocycle, or related ring-opened intermediate, which is consistent with Chen's observations in the reactions of substituted cyclopropanes with gold(I) complexes.¹⁰⁵ As expected, the reaction shows a strong preference for forming the more stable, methoxy-substituted carbene, as opposed to the original benzylidene ($m/z = 549$). A similar metathesis process also occurs in the CID of the addition product of ethyl vinyl ether with the gold(I) benzylidene.

Using the same ylide decomposition strategy, we attempted to synthesize other gold(I) carbene complexes. Metal-stabilized, ester-substituted carbenes are widely used in synthesis, in part because they can be generated by the decomposition of relatively stable diazoacetate (or other ester) precursors.^{113,117-121} To probe these species, a phosphorous ylide complex was synthesized that could produce an ester-substituted gold(I) carbene by the loss of triphenylphosphine (Scheme 12). However during CID, methanol was lost rather than triphenylphosphine. Similar structures have been observed in the condensed phase.¹²² Subsequent CID of the product led to the free triphenylphosphine-ligated gold cation. This is demonstrated in Figure 32, where CID is applied to the ester ylide. Ester-substituted carbenes are destabilized relative to simple carbenes, and apparently, this factor is sufficient to inhibit triphenylphosphine loss and allow the alcohol dissociation channel to dominate. In this case, ylide dissociation is not a viable approach to forming the carbene.

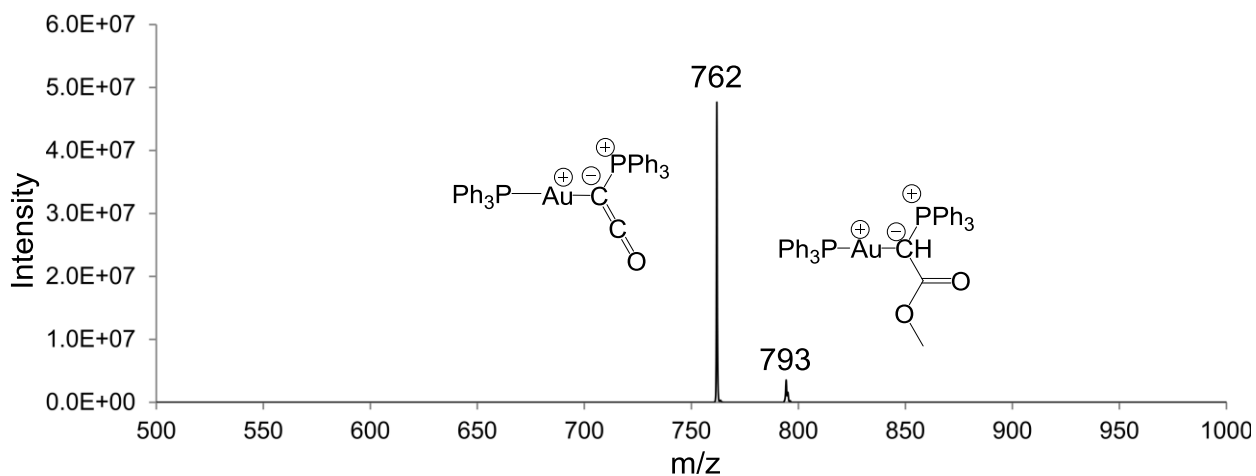
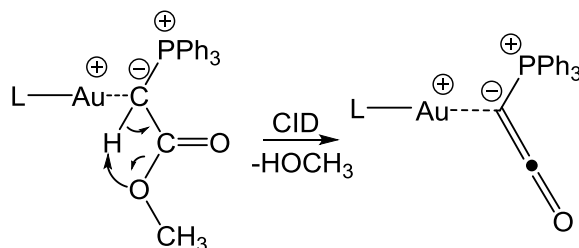


Figure 32. Degradation of ester ylide. The ester ylide was isolated at m/z 793 and subjected to CID at 32%.

Scheme 12. Fragmentation of the ylide precursor of an ester-substituted carbene.



As an alternative route to an ester-substituted gold carbene, we also investigated the reaction of a ligated gold(I) cation with ethyl and *t*-butyl diazoacetate in the gas phase. As noted earlier, this is a common route to metal carbenes in the condensed phase. We employed triphenylphosphine gold(I), dimethylsulfide gold(I), and 1,3-diisopropylimidazolium gold(I) in order to explore the impacts of these three

general classes of ligands shown in Figure 33. In these gas-phase reactions of diazoacetates with ligated gold cations, the products indicate the combined loss of N_2 and CO. Examples of this can be seen in Figures 34 and 35, where ethyl and tert-butyl diazoacetate were allowed to react with triphenylphosphine gold(I). The likely explanation is that the initial carbene intermediate formed by the loss of N_2 spontaneously undergoes a Wolff rearrangement followed by CO loss to give an alkoxy carbene (Scheme 13).

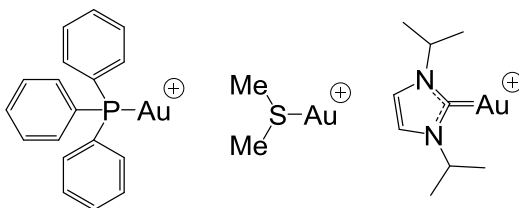


Figure 33. Gold (I) ions that were used for the degradation of diazo compounds.

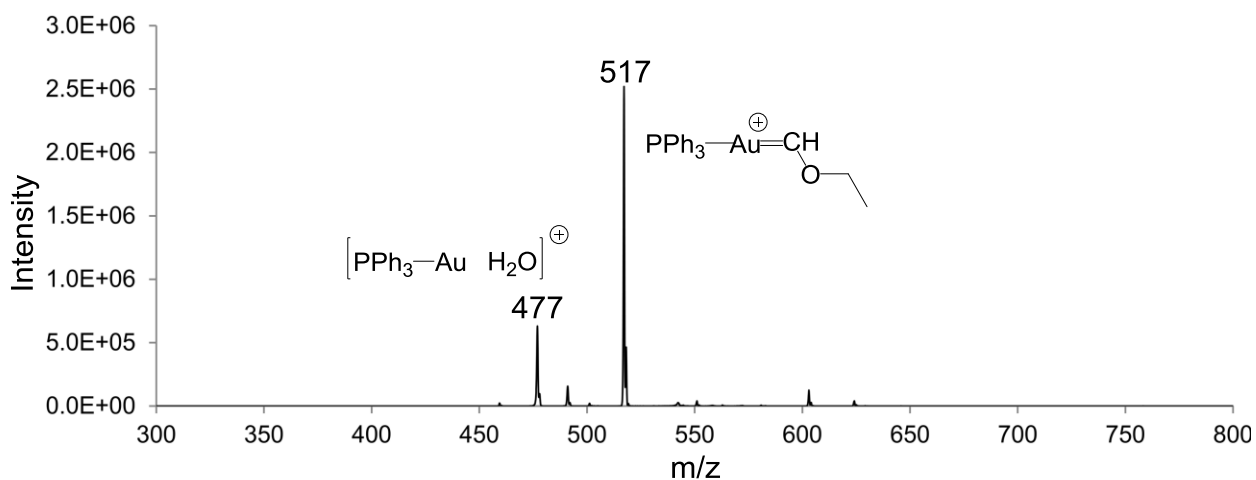


Figure 34. Reaction of $AuPPh_3$ with ethyl diazoacetate. The precursor ion ($AuPPh_3$) was isolated at m/z 459 and allowed to react with ethyl diazoacetate.

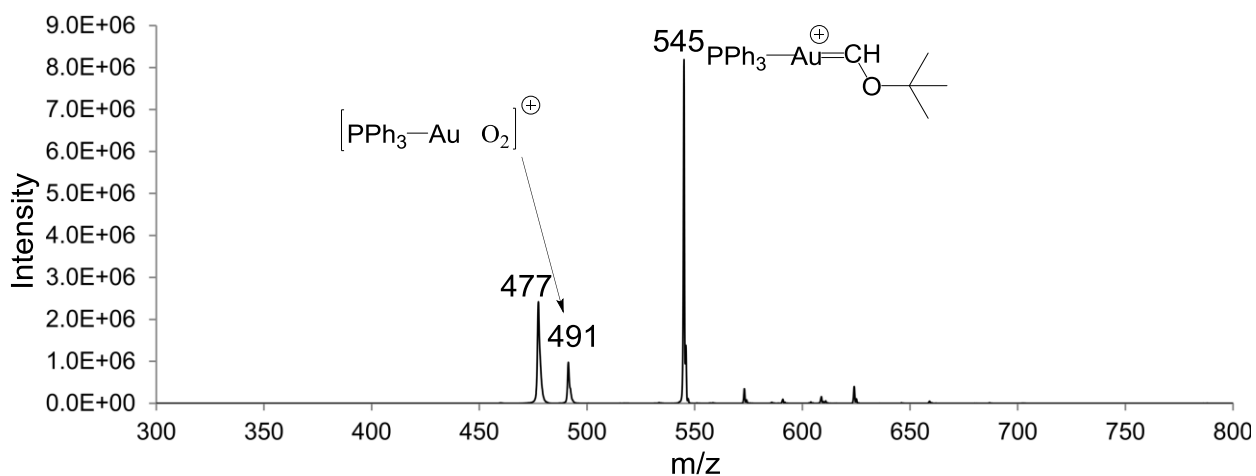
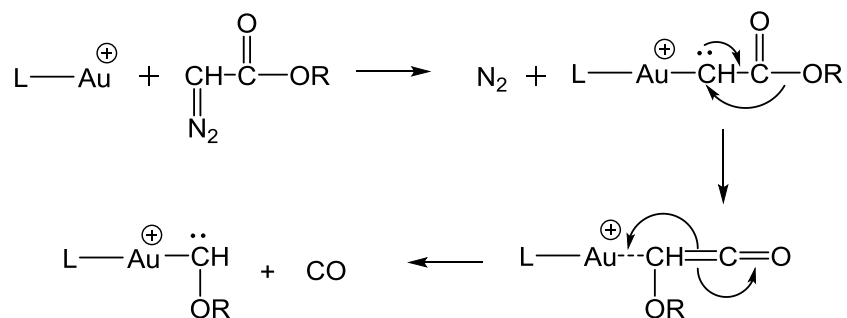


Figure 35. Reaction of AuPPh₃ with tert-butyl diazoacetate. The precursor ion (AuPPh₃) was isolated at m/z 459 and allowed to react with tert-butyl diazoacetate.

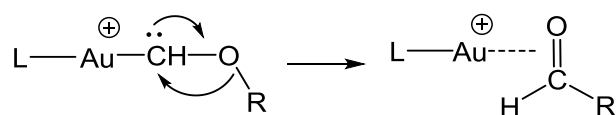
Scheme 13. Wolff rearrangement and CO loss from ester-substituted carbene.



It should be noted that Beauchamp and co-workers saw similar rearrangements in the gas-phase reactions of diazomalonates with silver and copper cations.¹²³ More recently, Roithova and co-workers presented an elegant gas-phase study aimed at closely related gold carbenes.¹²⁴ They observed and carefully characterized this pathway. In our experiments, there is no evidence of adducts with the diazoacetates or

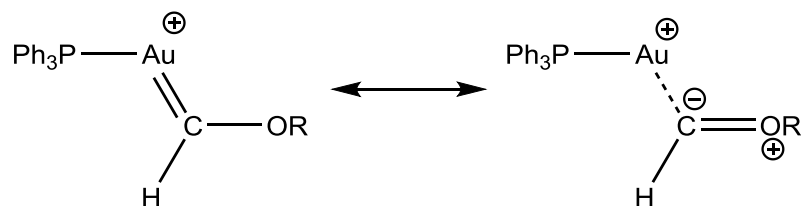
the desired carbene product, so it appears that the rate-limiting step is the initial addition of the diazo compound to the metal. All three ligand systems afforded the same reactivity with the diazoacetates, indicating that the electronic characteristics of the ligand do not control the reactivity in these reactions. Application of CID to the products of the Wolff rearrangement/CO loss leads back to the initial ligated gold cation. This could be the result of a direct cleavage of the gold-carbene bond or a rearrangement of the alkoxy carbene to an aldehyde followed by dissociation (Scheme 14).

Scheme 14. Alkoxy carbene rearrangement to form aldehyde.



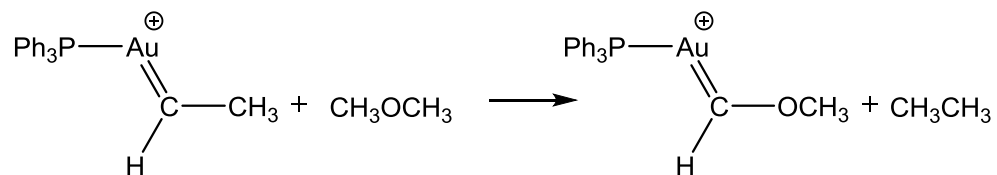
DFT computations on a model system ($\text{Me}_3\text{P-Au-CH-OMe}$) using the M06 functional (see experimental section for details) indicate that the gold-carbene bond is relatively weak (~ 66 kcal/mol) and not much greater than the computed barrier to the rearrangement in Scheme 6 (~ 57 kcal/mol), so it is possible that an alkoxy carbene is directly lost during CID rather than rearranging to the acetaldehyde complex before dissociation. The weak gold-carbene bond suggests that this species is best described as a gold-ylide complex with limited back-bonding from the metal (Scheme 15).

Scheme 15: Resonance forms for gold-carbene complex.



To explore their reactivity, the putative alkoxy carbenes from the decomposition of the diazoacetate esters (Scheme 13) were allowed to react with four olefins having varying structural and electronic properties: cyclohexene, ethyl vinyl ether, 2,3-dihydrofuran, and 1,1-dichloroethylene. No reactions were observed with any of the olefins. We had anticipated typical carbene reactivity such as cyclopropanation or metathesis, but apparently the alkoxy-substituted gold(I) carbene is sufficiently stabilized to inhibit any reactivity, even adduct formation. Of course, there is ample evidence that alkoxy groups greatly stabilize free carbenes.¹²⁵ To examine this effect in the gold carbenes, we have used the isodesmic reaction in Scheme 16 as a model. Employing DFT calculations with the M06 functional, the methoxy group stabilizes the gold-carbene by about 28 kcal/mol relative to an alkyl carbene. This is a large energetic effect and is the likely reason why these complexes are unreactive in the gas phase with olefins. The stabilization of the gold carbene is similar to what is seen in free carbenes (32 kcal/mol at the same level of theory), which indicates that the gold has a limited impact on the electronic structure of the carbene. Again, these results suggest that the alkoxy carbene behaves more like an ylide in this system.

Scheme 16. Isodesmic reaction for evaluating carbene stability.



To further probe the alkoxy carbenes, we utilized a phosphorous ylide that when dissociated, would form a methoxy-substituted gold(I) carbene. This is an alternative route to these gold carbenes and allows us to confirm the reactivity patterns seen in the decomposition products of diazoacetates. Upon electrospray ionization and isolation of this ylide, the triphenylphosphine group was disassociated by CID providing a product with a mass to charge ratio (m/z) that corresponds to the methoxy-substituted gold carbene (Scheme 17). An example of this can be seen in Figure 36, where CID is applied to the ether ylide.

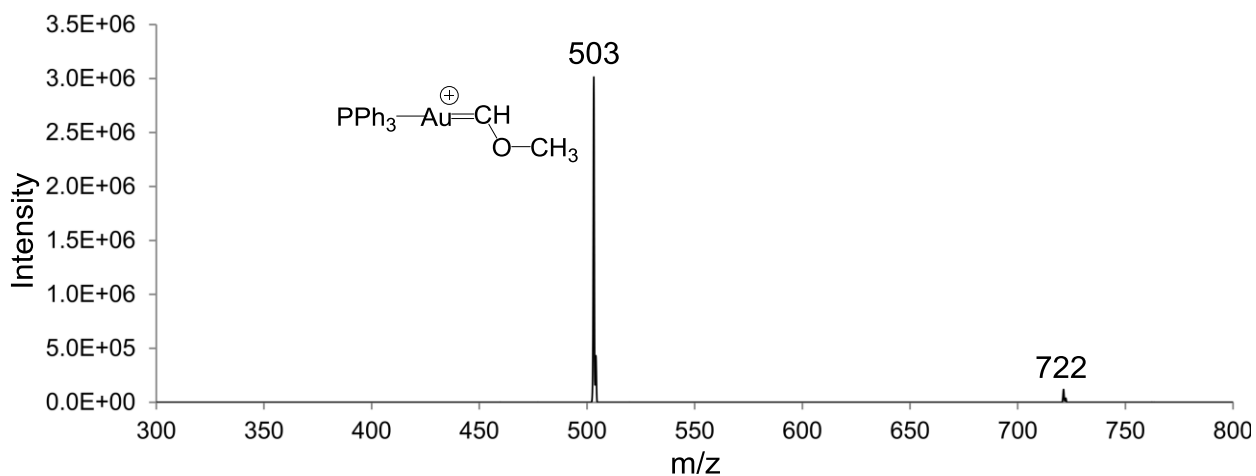
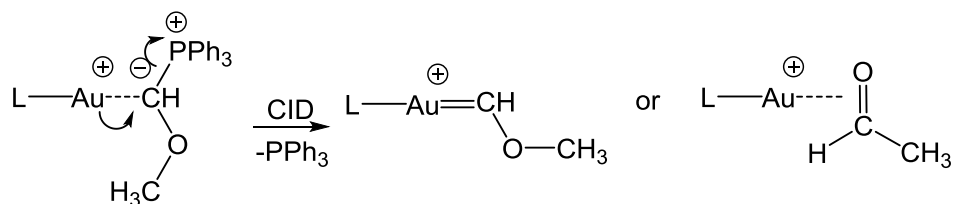


Figure 36. Degradation of ether ylide. The ether ylide was isolated at m/z 765 and subjected to CID at 35%.

Further CID of this complex led to the ligated gold complex, as was seen with the products from the diazoacetate decompositions. When allowed to react with the same set of olefins, no reactions occurred. This behavior suggests that identical species were formed in both proposed pathways to alkoxy-substituted carbenes. The lack of reactivity in the alkoxy carbenes is consistent with computations presented by Chen.¹⁰⁵ They showed that in related systems, intermediates in the reaction of an alkoxy carbene with an olefin are bound by less than 20 kcal/mol, which is the working threshold for observing them in our ion trap system.

Scheme 17. Alkoxy carbene generation by ylide degradation.



In order to circumvent this rearrangement that occurs upon the degradation of the diazoacetates we synthesized 2-methoxyethyl 2-diazoacetate with the idea that the methoxy group would be able to stabilize the non-Wolff rearranged carbene as is shown in Scheme 18 following the red arrow. Upon allowing 2-methoxyethyl 2-diazoacetate to react with a ligated gold (I) ion we observed an initial adduct formation with a loss of N₂ and CO. This result can be seen in Figure 37, where 2-methoxyethyl 2-diazoacetate was allowed to react with triphenylphosphine gold(I).

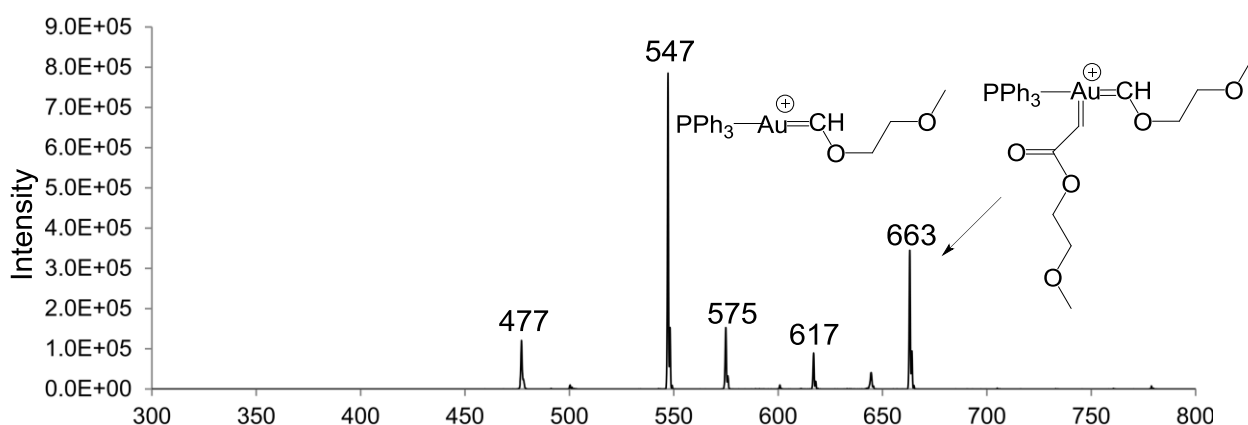


Figure 37. Reaction of AuPPh₃ with 2-methoxyethyl 2-diazoacetate. AuPPh₃ was selected at m/z 459 and allowed to react with 2-methoxyethyl 2-diazoacetate.

This indicated that the intramolecular stabilization was sufficient enough to prevent the Wolff rearrangement and subsequent CO loss. We also attempted to form a carbene by using (trimethylsilane)diazomethane to avoid these rearrangements and CO losses. This led to compounds that were again unreactive with olefins, indicating that the methyl group on the trimethylsilane group had most likely migrated to the carbene. These results can be seen in Figure 38, where (trimethylsilane)diazomethane was allowed to react with triphenylphosphine gold(I). These results give more validity to the theory that these carbenes are not stabilized much by the metal complex and that they undergo rapid rearrangements whenever possible.

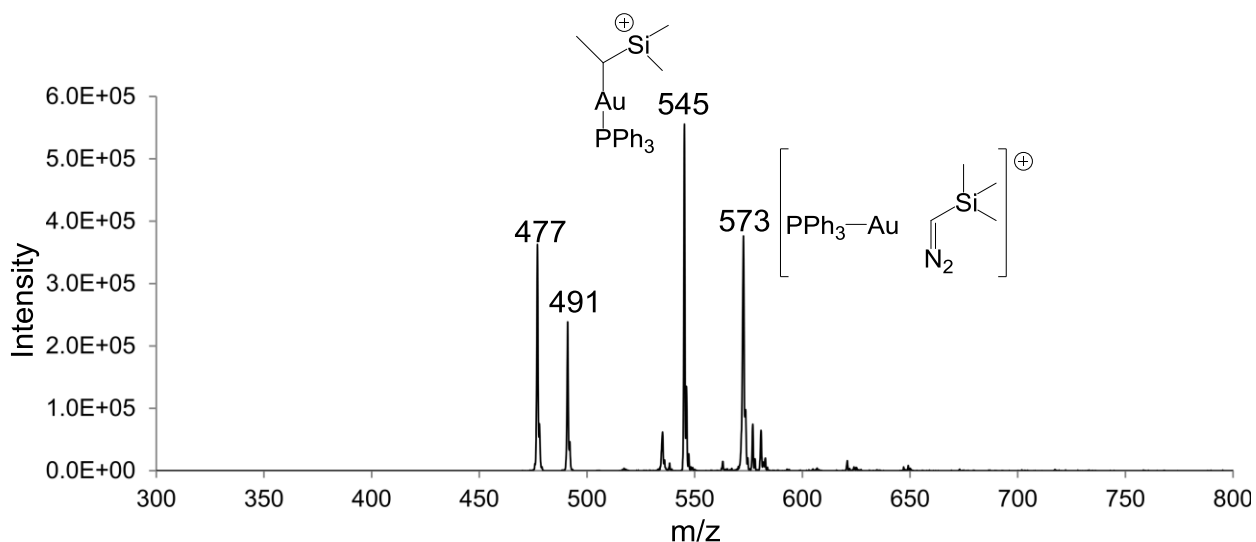
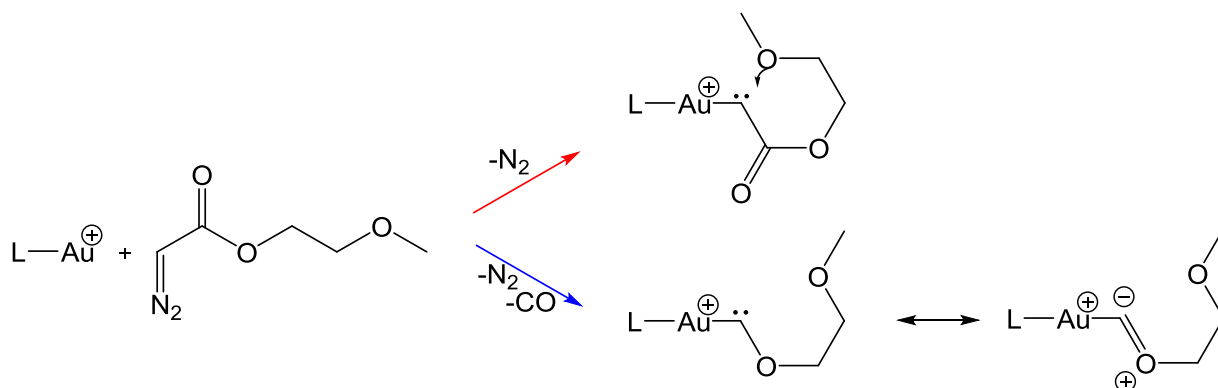


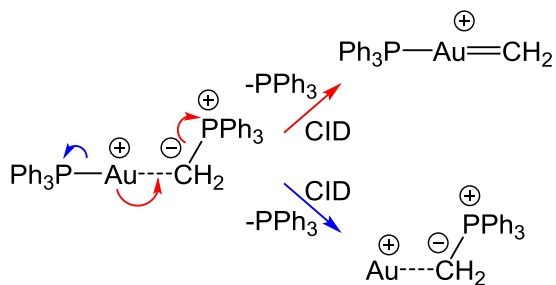
Figure 38. Reaction of AuPPh₃ with (diazomethyl)trimethylsilane. AuPPh₃ was selected at m/z 459 and allowed to react with (diazomethyl)trimethylsilane.

Scheme 18. Reactivity of 2-methoxyethyl 2-diazoacetate with gold (I) ions.



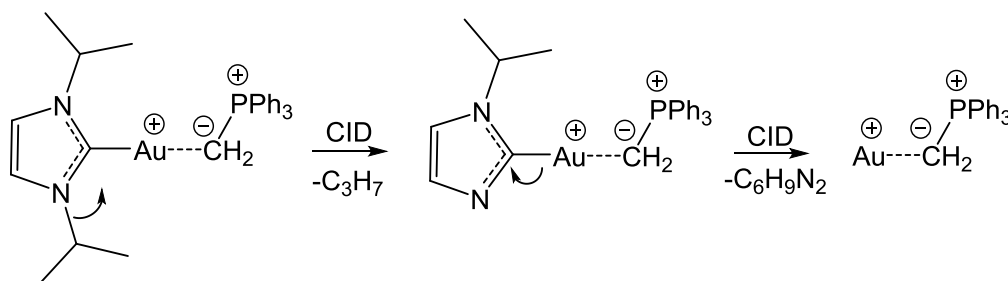
To complete our investigation of the generality of Chen's ylide dissociation synthesis of gold(I) carbenes, we prepared a phosphorous ylide precursor that would yield a gold(I) methylene complex (Scheme 19). The obvious advantage of this system is that the carbene is not capable of internal rearrangements. The ylide loses triphenylphosphine during CID, but the product did not have reactivity with olefins. This suggested that the triphenylphosphine loss might be from the gold center rather than from the ylide.

Scheme 19. Fragmentation pathways of gold(I) methylene precursor.



To avoid this complication, an ylide with a 1,3-diisopropylimidazolium ligand was synthesized (Scheme 20). Under CID, this complex undergoes fragmentations related to the 1,3-diisopropylimidazolium ligand. Specifically, propyl loss as well as ligand loss is observed. This behavior was not seen in the CID reactions of the precursors to the NHC gold (I) benzylidenes. These results again suggest that the ylide dissociation pathway is best suited for the formation of stabilized carbenes. In the absence of stabilization, other pathways dominate and useful yields of carbenes are not possible. This is consistent with the conclusions from Roithova's recent study.¹²⁴

Scheme 20: CH₂ carbene precursor using 1,3-diisopropylimidazolium as the ligand on gold.



3.7- Conclusions

Ligated gold(I) carbene complexes can be formed in the gas-phase by several pathways including reactions with diazo species and dissociations of phosphorous ylide precursors. Gold(I) benzylidenes react with olefins to give addition products, with rates that are sensitive to the electron density of the olefin's π-system and that increase to

near the collision-controlled limit for olefins with electron-donating groups (e.g., ethyl vinyl ether). Chen has previously shown that the addition products of the gold(I) benzylidenes complete what appear to be cyclopropanation and metathesis reactions during CID.¹⁰⁵ Here, we show that they have bimolecular reactivity with olefins and secondary substitution reactions occur (olefin displacing cyclopropane). These substitution reactions are slower than the addition reactions of the gold(I) benzylidenes. A Hammett plot analysis shows that the ligand swapping process is more sensitive to the electron density of the olefin's π -system and is consistent with a later transition state and greater positive charge on the olefin unit.

The gas phase syntheses of gold(I) carbenes tend to have limited scopes. When the carbene is not stabilized, the ylide dissociation pathway produces other decomposition products. This limitation can be overcome by employing diazo precursors in bimolecular reactions, but in the case of ester-substituted carbenes, the desired carbene undergoes a spontaneous Wolff rearrangement followed by CO loss. The product is a gold(I) complex of an alkoxy carbene, which is highly stabilized and does not give reactivity with olefins. Future work should focus on alternative, more general avenues to gold(I) carbene formation.

Chapter 4 – Formation and Reactivity of Silver (I) Carbenes in the Gas Phase

4.1– Introduction

Carbenes and their transient nature lend themselves to gas-phase studies where reactive intermediates are able to be probed more easily than in the condensed phase. Throughout the years, much attention has been given to coinage metals and their ability to form Fischer type carbene complexes.¹²⁶ They have been shown to induce C-H activation, metathesis, as well as cyclopropanation.^{127–133} However, as much of this effort has focused on copper, and then later gold, with relatively little attention given to silver. Much of the studies on silver-carbene complexes focus on silver's ability to form facile bonds with N-heterocyclic (NHC) carbenes.^{132,134} In these studies, the facile nature of the silver-NHC bond is exploited to transfer NHCs to other metals. Only a few studies have attempted to explore the reactivity of silver-carbene complexes.¹³⁵ Here we explore silver's ability to form silver-carbene complexes and probe their reactivity with olefins in the gas phase.

4.2– Experimental Procedures

All experiments were conducted in a modified ThermoFinnigan LCQ Deca XP Plus quadrupole ion trap mass spectrometer equipped with ESI. Silver(I) salts and carbene precursors were dissolved in methanol at 10^{-4} - 10^{-5} M. Typical ESI conditions involved flow rates of 3-5 μ L/min with needle potentials between 3.5 and 6 kV and

heated capillary temperatures from 125 to 200 °C. A notched waveform is used for isolating the cationic silver (I) species. Upon obtaining a stable signal, neutral reagents can be spiked into the helium stream via a custom gas-handling system which has been described above.

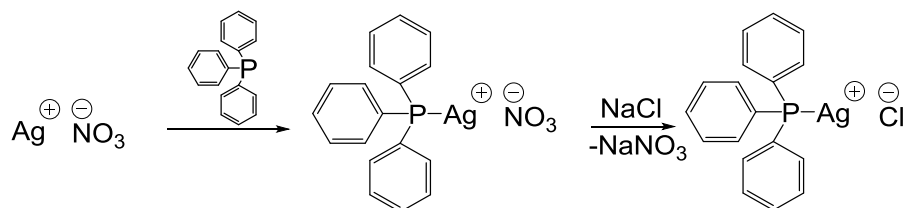
Kinetic measurements were completed by establishing an appropriate flow rate for the neutral reagent and varying the time between the isolation of the ion and the expulsion of all the ions to obtain a mass spectrum. Ten different time delays were used in each reaction. Neutral reagent flows and time delays were varied to obtain plots that cover two to three half-lives of the ionic reagent. Data were obtained over at least two days with multiple neutral and ionic solution preparations to ensure reproducibility. Kinetic plots showed sufficient linearity with correlation coefficients (r^2) of 0.98 or greater.

Most neutral reagents were obtained from commercial sources in the highest purity available and used without further purification. The neutral reagent 2-methoxyethyl 2-diazoacetate was synthesized as described above, by adapting a procedure reported by Doyle.^{108–110} As needed, neutral reagents were diluted in cyclohexane. Silver salts, triphenylphosphine silver (I) chloride and 1,10-phenanthroline silver (I) chloride, were synthesized by mixing silver chloride with one equivalent with the desired ligand and were used without further purification.

4.3– Synthetic Procedures

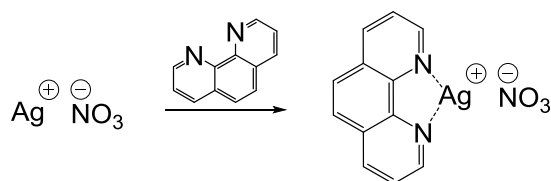
The complexes that were synthesized were diluted to $10^{-5} - 10^{-4}$ M in methanol and used without purification. Upon electrospray of the complexes the desired complex is isolated and the isotope ratio analyzed for characterization.

Scheme 21. Synthesis of triphenylphosphine silver (I) chloride.



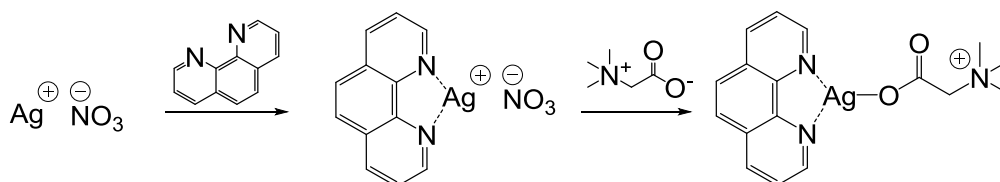
Silver nitrate and triphenylphosphine was mixed in a 5:2 solution of methanol and acetonitrile under N_2 at -30°C for 24 hours. The resulting solution is mixed with 1.5 equivalent of sodium chloride for 1 hour at room temperature.

Scheme 22. Synthesis of 1,10 phenanthroline silver (I) nitrate.



Silver nitrate and 1,10 phenanthroline were mixed in a 5:2 mixture solution of methanol and acetonitrile for 30 min at room temperature. The resulting solution was diluted methanol and used without further purification.

Scheme 23. Synthesis of 1,10 phenanthroline silver (I) betaine.



A solution of 1,10 phenanthroline silver (I) nitrate was mixed with approximately one equivalent of betaine monohydrate in a 5:2 mixture of methanol and acetonitrile. This solution was then diluted in methanol and used without further purification.

4.4– Results and Discussion

In this study we were able to synthesize and successfully form three silver (I) ions in the gas phase, triphenylphosphine silver (I), 1,10 phenanthroline silver (I), and

1,10 phenanthroline silver(I) betaine. For the triphenylphosphine silver (I) ion, an adduct with water was observed. This is consistent with previous studies with gold (I), which also formed adduct with adventitious water in the ion trap. An example of this can be seen in Figure 39, where triphenylphosphine silver (I) is isolated in the ion trap. Having been able to form these complexes in the gas phase, we then probed their ability to form silver-carbene complexes. For the formation of silver-carbene complexes we utilized two methods, a diazo degradation method and a betaine degradation method.

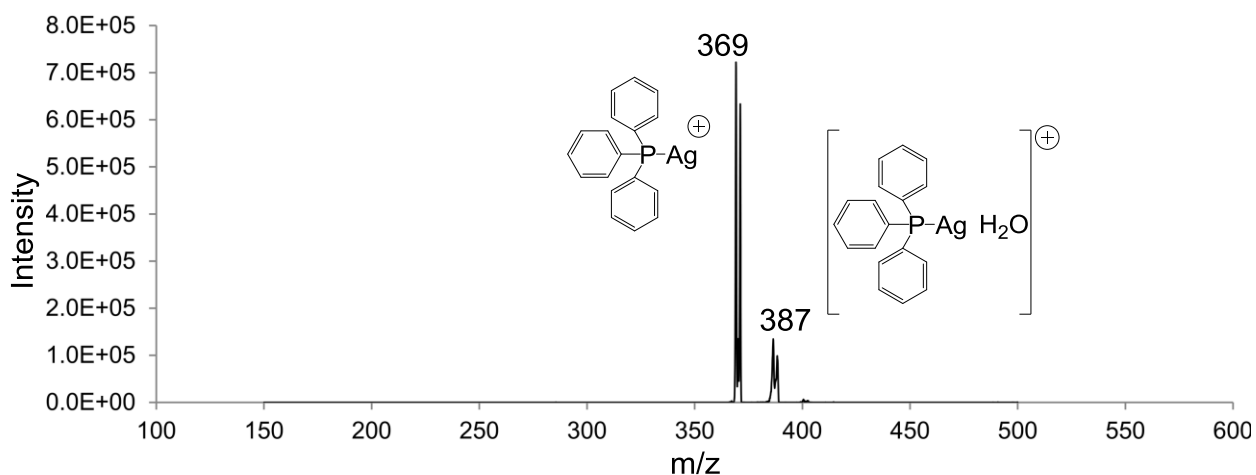


Figure 39. Isolation of triphenylphosphine silver (I) ion with a 30 ms reaction time.

Starting with the triphenylphosphine silver (I) complex, we surveyed its ability to degrade diazo acetates in the gas phase. To do so, we isolated the silver complex and allowed it to react with ethyl diazoacetate and tert-butyl diazoacetate. Upon allowing the silver complex to react with ethyl diazoacetate, we observed the rapid formation of an adduct which corresponded to an addition of ethyl diazoacetate with a loss of N₂ and CO (Figure 40). These results can be seen in Figure 40, where triphenylphosphine

silver (I) is isolated and allowed to react with ethyl diazoacetate. This is indicative of a Wolff rearrangement and CO loss occurring, which is similar to what has been observed in related gold systems (Scheme 24).¹⁰³

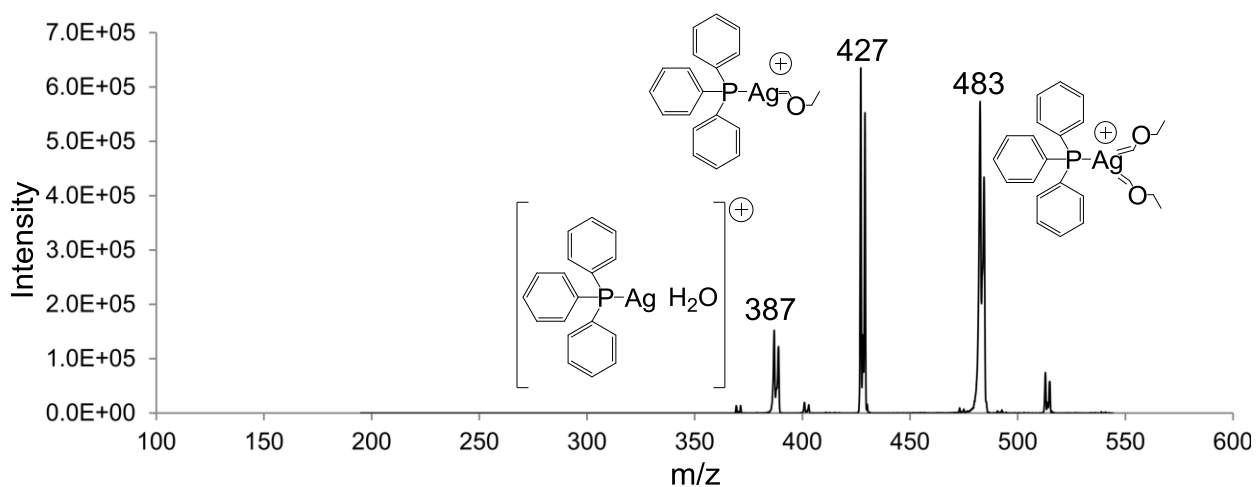
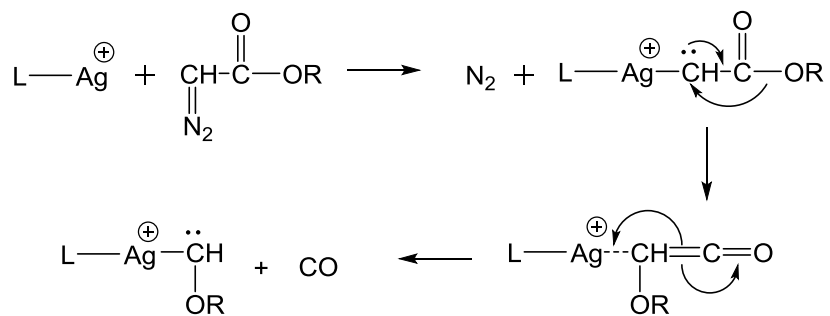


Figure 40. Reaction of triphenylphosphine silver (I) ion with ethyl diazoacetate.

Scheme 24. Reaction of silver (I) salts with diazoacetates.



A double addition ethyl diazoacetate was also observed, having lost N₂ and CO as well (Figure 41). These data are shown in Figure 41. This is most likely due to

silver's desire to have a larger coordination sphere. Upon isolation of these alkoxy carbenes and allowing them to react with olefins, we observed no adduct formation and no indication of carbene chemistry. These data can be seen in Figure 42, where triphenylphosphine silver (I) was allowed to react with a mixture of ethyl diazoacetate and ethyl vinyl ether. In Figure 42 the reaction product of triphenylphosphine silver (I) with ethyl diazoacetate is was selected. This lack of carbene chemistry indicates that these complexes are ylides rather than carbenes and are effectively stabilized (Scheme 25). Tert-butyl diazoacetate yielded similar results.

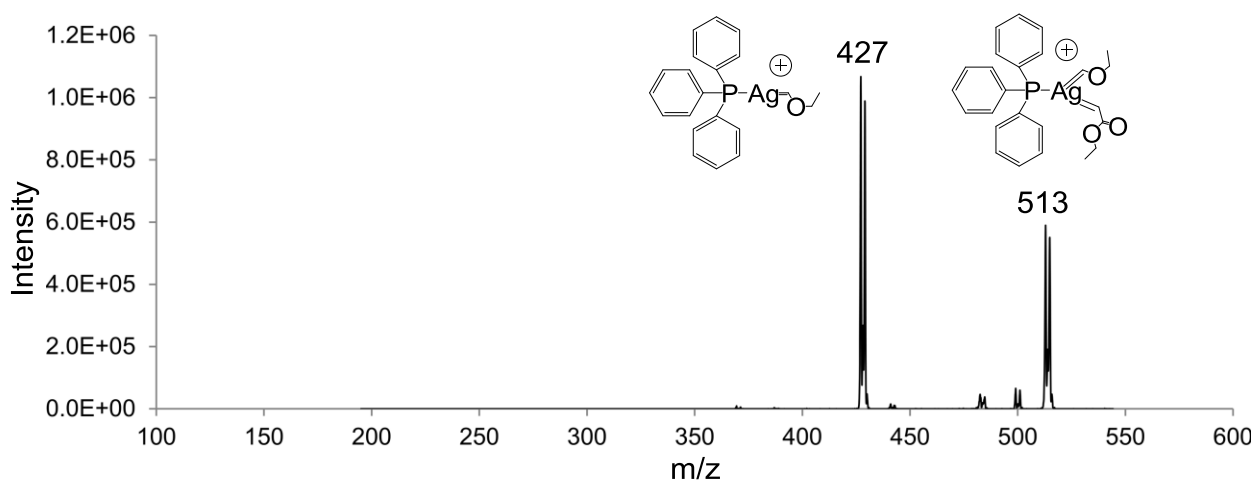


Figure 41. Reaction of triphenylphosphine silver (I) ion with a 1:1 mix of ethyl diazoacetate and ethyl vinyl ether. Initially, AgPPh_3 is isolated at m/z 369 and is allowed to react with a 1:1 mix of ethyl diazoacetate and ethyl vinyl ether. Then the alkoxy carbene is isolated at m/z 427. The 109 isotope of silver can be observed as a mass shift of 2.

Scheme 25. Stabilization of silver alkoxy carbenes through resonance.

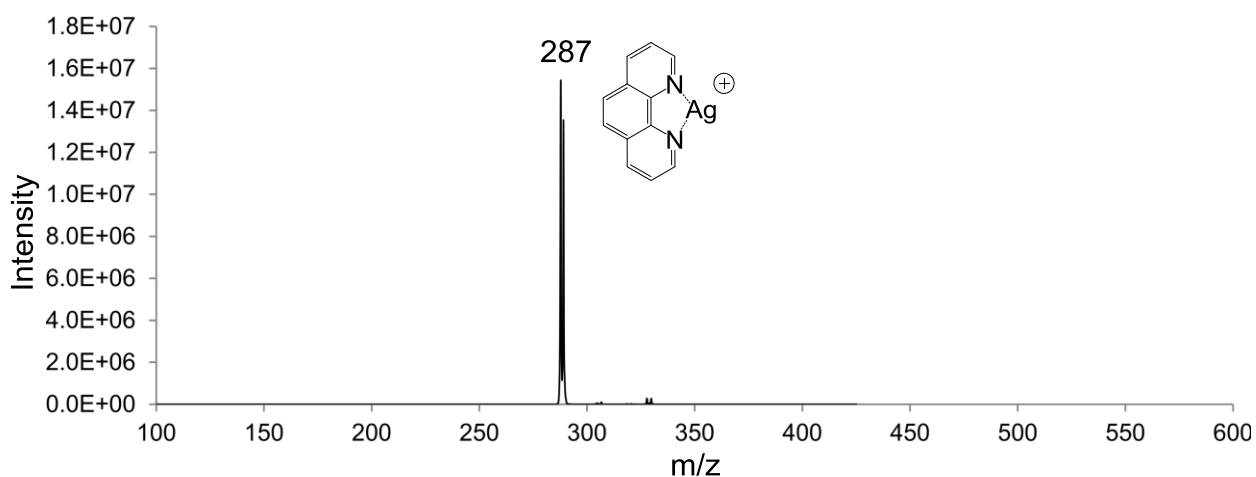
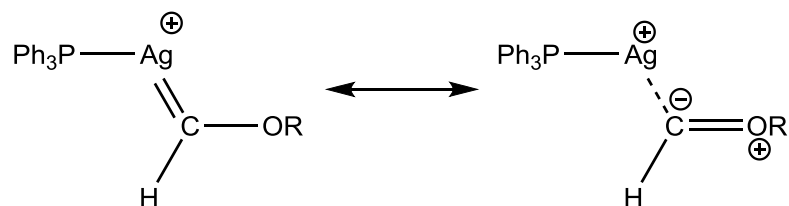


Figure 42. Isolation of 1,10 phenanthroline silver (I) ion with a 30 ms reaction time.

Moving forward, we changed the ligands of the silver complex in the attempt to alter the reactivity. To accomplish this we synthesized the 1,10 phenanthroline silver (I) complex and allowed it to react with the diazoacetates. A mass spectrum of this complex is given in Figure 43. We chose 1,10 phenanthroline for its rigid nature and its bidentate character. In related systems of copper, it has been shown to alter reactivity and prevent detrimental insertion reactions from occurring. Upon allowing the 1,10 phenanthroline silver complex to react with diazoacetates we observed an addition of the diazoacetates along with the loss of N₂ and CO. The spectrum is shown in Figure

43, where 1,10 phenanthroline silver (I) is allowed to react with tert-butyl diazoacetate. When isolating this alkoxy carbene species and allowing it to react olefins we observed no reaction. A mass spectrum of 1,10 phenanthroline silver (I) being allowed to react with a mixture of tert-butyl diazoacetate and ethyl vinyl ether is given in Figure 44. These results led us to pursue other avenues for the formation of silver-carbene complexes.

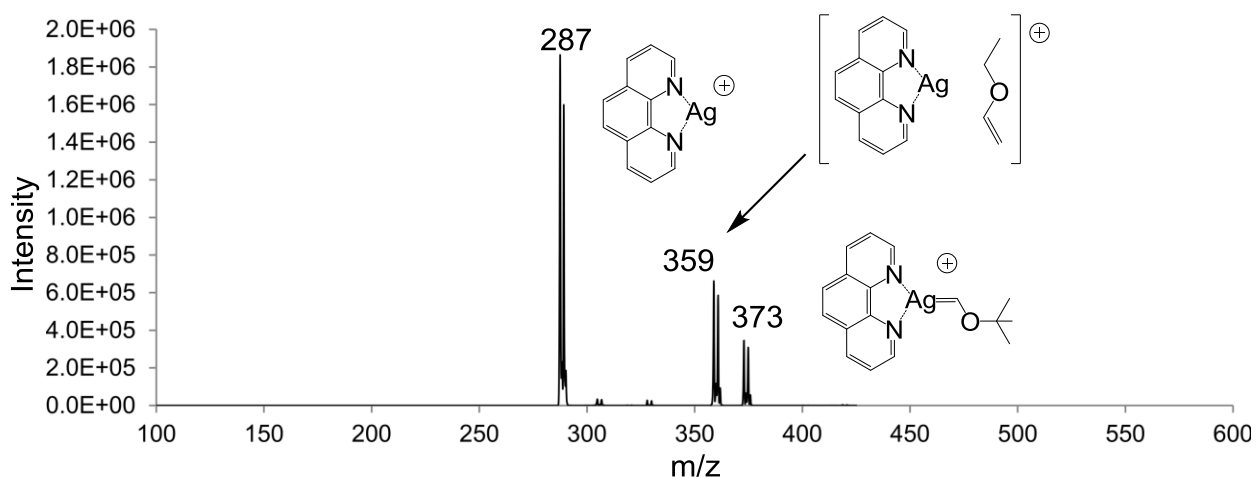


Figure 43. Reaction of 1,10 phenanthroline silver (I) ion with a 1:1 mix of tert-butyl diazoacetate and ethyl vinyl ether.

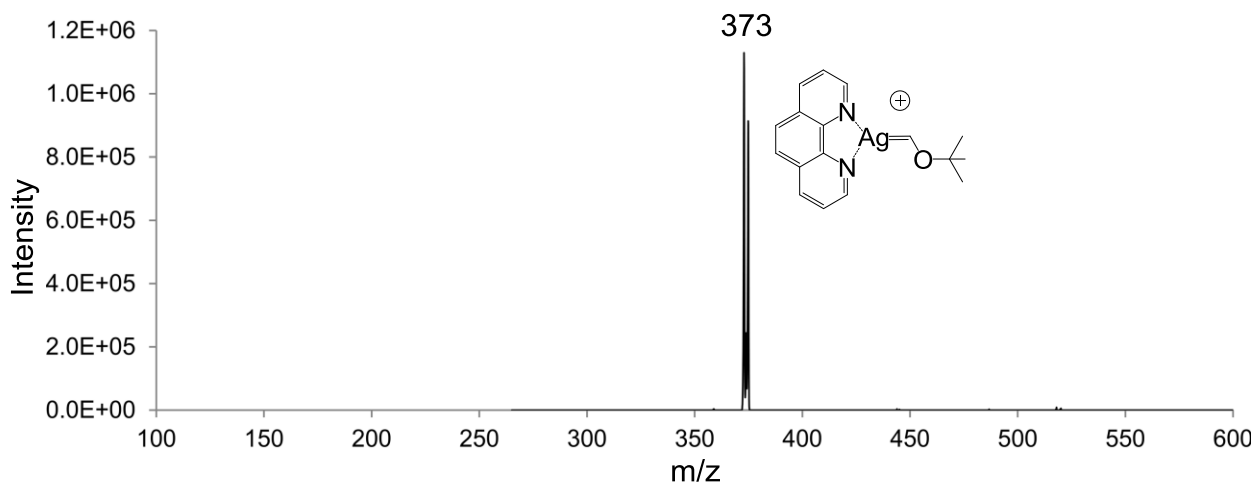
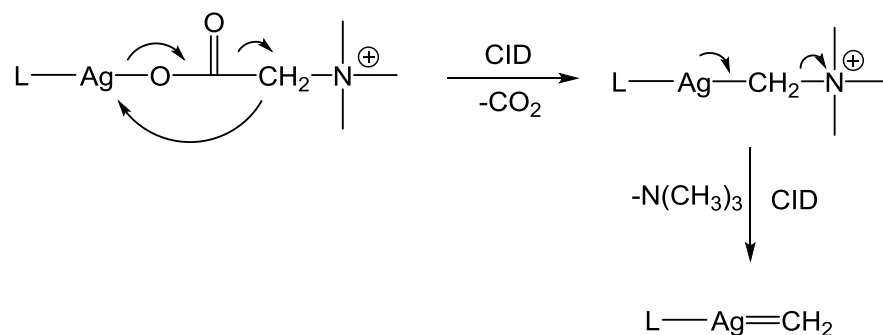


Figure 44. Reaction of 1,10 phenanthroline silver (I) ion with a 1:1 mix of tert-butyl diazoacetate and ethyl vinyl ether. Initially, Ag(phen) is isolated at m/z 287 and is allowed to react with a 1:1 mix of tert-butyl diazoacetate and ethyl vinyl ether. Then the alkoxy carbene is isolated at m/z 373 and allowed to react for 1000 ms.

For an alternative route to forming silver-carbene complexes in the gas phase, we turned to forming ylides in the condensed phase and breaking them down in the gas phase to reveal carbenes. With inspiration from Chen, and his work with the dissociation of gold (I) ylides, and our own work with gold ylides we synthesized silver betaine ylide complexes.^{103,107} For this process, CID is applied to the betaine complex inducing a rearrangement and loss of CO₂ as described in Scheme 26.

Scheme 26. Degradation of silver betaine complex.



We were able to successfully form a 1,10 phenanthroline silver (I) betaine complex in the condensed phase and transfer it to the gas phase via ESI. A mass spectrum is given in Figure 45, where the silver-betaine complex can be observed. Upon isolation and application of CID to this betaine complex, we observed a loss of CO₂. This indicated that the betaine was indeed bound to silver complex as described. Further CID however revealed a loss of the 1,10 phenanthroline rather than a loss of N(Me)₃, as hoped. We applied lower amounts of CID for longer intervals to help stimulate the desired fragmentation, as has worked in copper systems in our lab, however we had no success with this method either. This led us to move on from this silver endeavor. These data can be seen in the mass spectrum in Figure 46 and Figure 47, where the silver-betaine complex is isolated and CID is applied. In Figure 47 the m/z of 180 and 182 is a mixture of ionize phenanthroline and AgC₄H₁₁N.

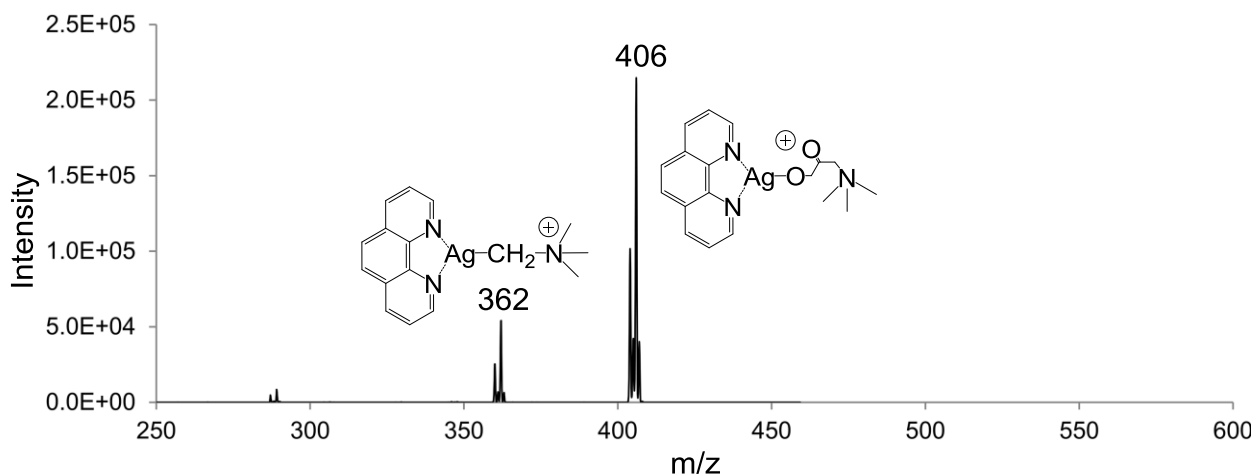


Figure 45. Formation of 1,10 phenanthroline silver (I) betaine complex. The 1,10 phenanthroline silver (I) betaine complex is selected at m/z 406. Some degradation of the complex is observed at m/z 362.

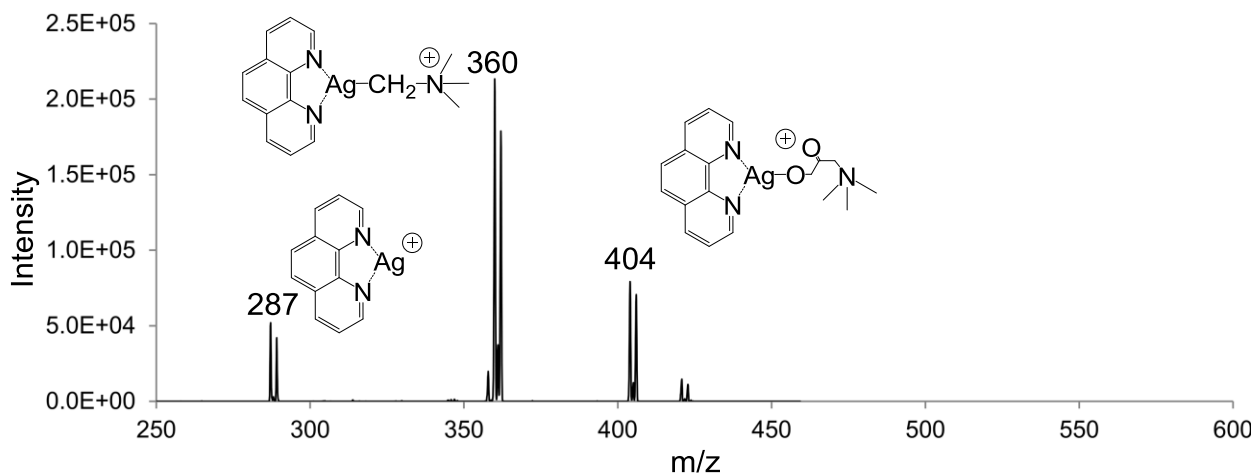


Figure 46. Degradation of 1,10 phenanthroline silver (I) betaine complex. The 1,10 phenanthroline silver (I) betaine complex was isolated at 404 and subjected to CID.

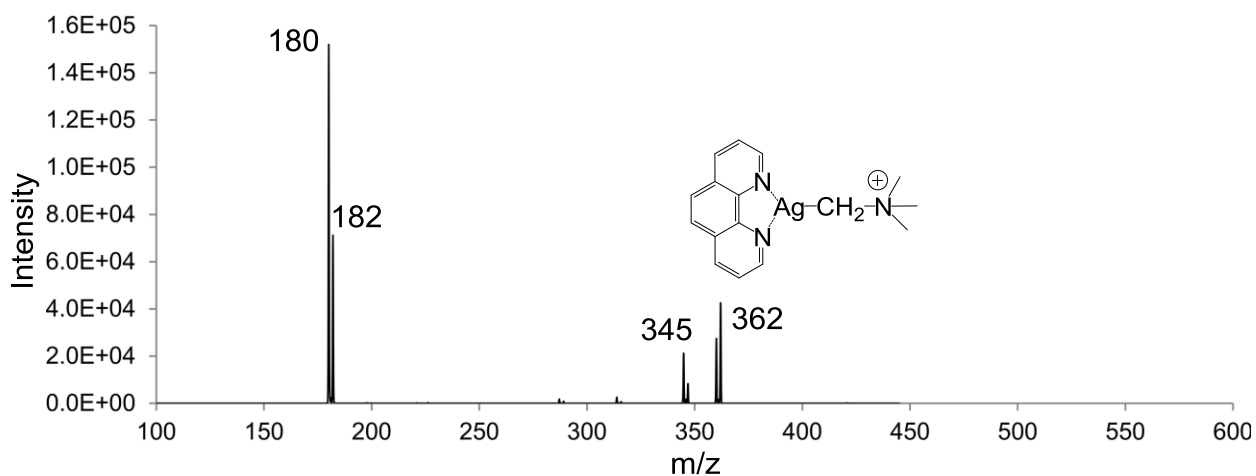


Figure 47. Degradation of 1,10 phenanthroline silver (I) betaine complex. The 1,10 phenanthroline silver (I) betaine complex was isolated at 404 and subjected to CID. Then m/z 362 was isolated and subjected to CID.

4.5– Conclusion

In conclusion, we were successful in synthesizing silver complexes in the condensed phase and transferring them to the gas phase. These complexes, when allowed to react with diazoacetates, degraded diazo compounds and underwent Wolff rearrangements with rapid CO losses. These results are similar to what has been observed in gold as well as copper, indicating that there is some similarity in reactivity going down the coinage metal row. However unique to silver, when using a monodentate ligand we observe multiple additions of diazo compounds and we presume this is due to silver's desire to maintain a larger coordination sphere. Upon allowing these alkoxy carbene complexes to react with olefins, no reactivity was observed. This is rationalized by the formation of the ylide resonance structure which

sufficiently stabilizes the carbene and prohibits carbene reactivity inside of the kinetic window in which we are able to study.

We also were successful in synthesizing silver-betaine ylide complexes in the condensed phase and transferring them to the gas phase. With the hopes that these ylides would degrade to give reactive carbenes as has been observed in similar systems in gold as well as copper, we applied CID only to have the CO₂ dissociate followed by catastrophic degradation.^{103,104} We didn't observe any evidence that a silver-carbene had been formed. Having seen this process work in both gold and copper, it was rather a disappointing result. We presume that silver does not possess this type of reactivity due to it not being small enough in size to mix with the carbon orbitals well, as copper does, and not being polarizable enough stabilize carbenes either, as gold does. Therefore, we propose that silver is a metal that is playing the "middle man" and is left out of this fascinating reactivity that is observed in both copper and gold.

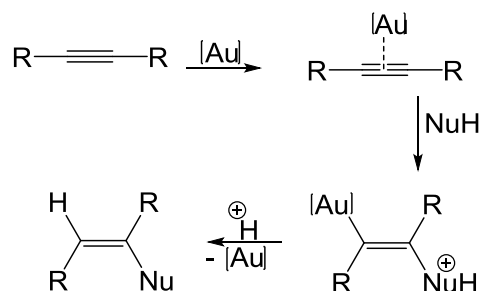
Chapter 5 – Mechanistic Details of Gold-Catalyzed Alkyne Rearrangements in the Gas Phase

5.1– Introduction

Gas-phase studies have become an important tool in understanding the underlying reactivity of compounds and mechanisms of reactions. They provide us with the ability to probe reactive intermediates in the inert gas of a mass spectrometer. Transition-metal stabilized carbenes have proven themselves to be useful intermediates in the synthesis of a wide variety of target molecules.¹³⁶ However, as useful as these compounds are they are difficult to study due to their transient nature. This characteristic of carbenes makes them an ideal analyte for gas-phase studies where we are able to work within carbene reaction times. Previously, we have reported the gas-phase synthesis iron, cobalt and gold carbenes that were synthesized by a reaction of the ligated metal with diazoacetate esters.^{93,94,103} In each case the carbenes were susceptible to rearrangements, metal-ligand insertions in iron and cobalt and a Wolff rearrangement with a CO loss in gold, which rendered them either unreactive as carbenes or too slow for us to measure in our system.^{93,103} We have also reported the gas-phase synthesis gold carbenes via the dissociation of ylides.¹⁰³ This method being is useful for carbene formation in the gas-phase only when the ylide is of a structure that can stabilize the carbene and not rearrange upon dissociation, thus resulting in a narrow scope.

Here we probe the gold-catalyzed rearrangements of propargyl acetates, propargyl ethers, propargyl acetals, and propargyl carbonates. Gold has attracted much attention in the recent years for its ability to activate unsaturated C-C bonds toward nucleophilic attack, enabled by gold's Lewis acidic character which depletes the electron density and lengthens the C-C bond making it susceptible to attack (Scheme 27).^{95,116,126,136-141} This has become the most common use for gold catalysts.¹³⁶ Toste and co-workers have studied propargyl acetates and shown that in the condensed phase they rearrange forming carbenes (Scheme 1).¹⁴² They have shown that this rearrangement is applicable to a wide variety of propargyl pivaloate esters.¹⁴² In this study, we have tested the generality of this approach to form gold (I) carbenes in the gas phase. Gagosz and co-workers have studied the rearrangement of propargyl ethers by gold (I) in the condensed phase and shown that they undergo a hydride transfer followed by a fragmentation.¹⁴³ In the present study we will probe the generality of this rearrangement by gold (I) in the gas phase. The results are supported by density functional theory (DFT) calculations and highlight the important intermediates on the reaction surface.

Scheme 27. Activation of alkynes by gold.

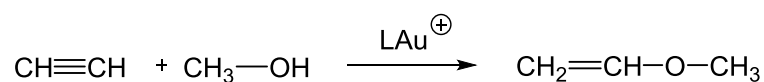


However, even though this is relatively common gold catalysis, little is understood about the process.¹³⁶ This is demonstrated by the use of silver in some gold-catalyzed reactions and not in others for unspecified reasons.¹⁴⁴ The use of silver in gold-catalyzed reactions has been termed the silver effect and is only qualitatively understood.¹⁴⁴ Xiaodong and co-workers revealed that gold-catalyzed alkyne-rearrangement reactions can be separated into three categories: (1) genuine gold catalyzed, reactions catalyzed by gold alone (2) gold-silver bi-metallic catalyzed, reactions catalyzed only by a gold and silver mixture (3) silver assisted, reactions catalyzed by either gold, silver, or a gold/silver mixture.¹⁴⁴ This apparent lack of understand of these gold catalyzed alkyne rearrangements has created a demand fundamental studies on these processes.

This increasing demand, led Schroder and co-workers to conduct a study in the gas phase of the nucleophilic addition of methanol to acetylene (Scheme 28).¹⁴⁵ In their study, they allowed gold to interact with a mixture of methanol and acetylene at the ESI interface of a double quadrupole MS. They observed adducts of gold with acetylene and

gold with methanol, but no combination of the two of them. From these results, they concluded that the kinetics of gold-catalyzed nucleophilic additions to alkynes would not allow them to be studied in the gas phase. These kinetic issues to a lack of interest in studying these reactions in the gas phase until now.

Scheme 28. Gold-catalyzed addition of methanol to acetylene.

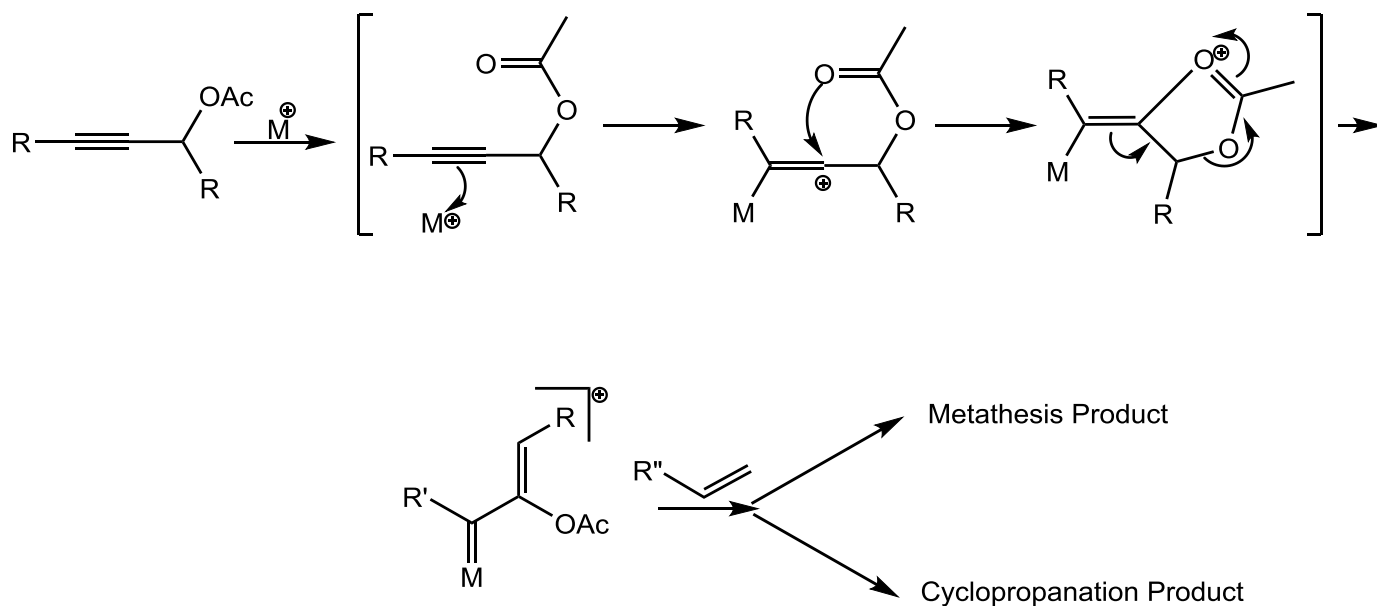


To circumvent the kinetic issues that plagued Schroder in his investigation of gold-catalyzed alkyne reactions the nucleophile for the reaction could be attached to the alkyne substrate. This methodology effectively eliminates the kinetic issues with these reactions in the gas phase. Therefore in our present study we set out to study intramolecular gold-catalyzed reactions in the gas phase. An inherent issue that must be addressed with intramolecular reactions in the gas phase is, that the reaction products can be difficult or impossible to characterize due to having the same m/z ratio as the starting reagents. This limits the types of intramolecular reactions that are able to be probed; however, there are ways to circumvent this issue. One way around this issue is to study intramolecular reactions that lead to fragmentations, which will produce a shift in the m/z ratio and provide identification of reactions completion. Another type of reaction that can be probed is one that upon reaction completion form a reactive complexes that can undergo a second characteristic reaction with another substrate

producing a m/z shift. In our present study, we utilize both of these techniques to probe gold-catalyzed intramolecular reactions in the gas phase.

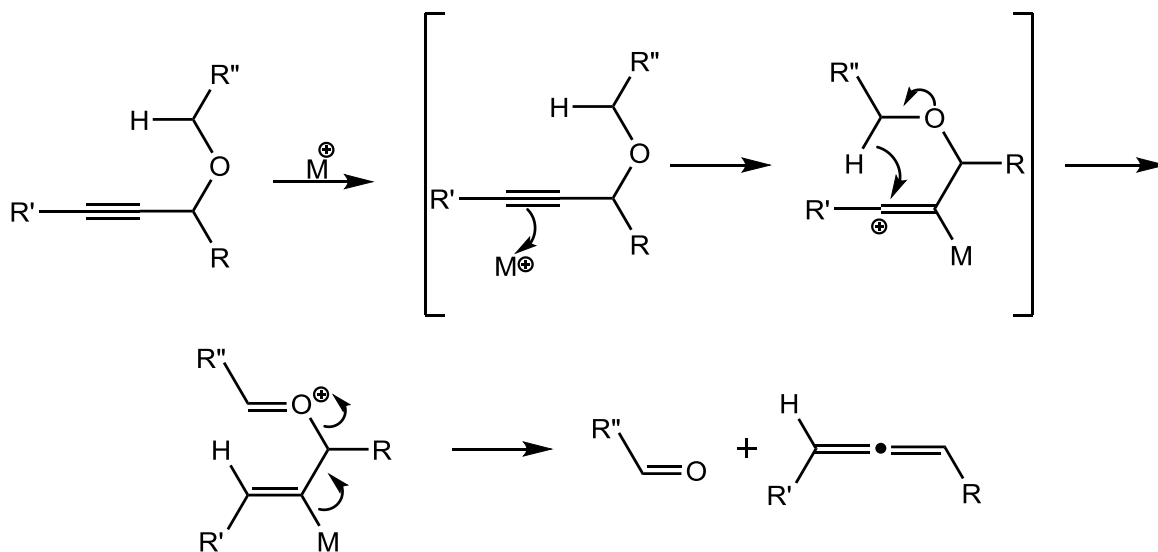
We probe gold-catalyzed rearrangements and degradations of propargyl acetates, propargyl ethers, propargyl acetals, and propargyl carbonates. These reactions are interesting for two reasons; they allow us to probe gold-catalyzed reactions in the gas phase and they us to study the reactions in an environment free from silver to determine if gold alone is able to catalyze the reactions. Toste and co-workers have studied propargyl acetates in the condensed phase and shown that they rearrange, forming carbenes.¹⁴² They have shown that this rearrangement is applicable to a variety of propargyl pivaloate esters (Scheme 29).¹⁴² This rearrangement is of interest because it has the ability to provide carbenes that are unique to others that have been studied in the gas phase, allowing us to probe the reactivity of this class of carbenes. For this study, we have tested the generality of this approach to form gold (I) carbenes in the gas phase.

Scheme 29. Rearrangement of propargyl acetates in the condensed phase.



Gagosz and co-workers have also studied a gold-catalyzed intramolecular reaction.¹⁴³ In this study, they demonstrated gold's ability to catalyze a hydride transfer and subsequent degradation of propargyl ethers in the condensed phase forming allenes and aldehydes (Scheme 30). This is an interesting reaction that provides us with the opportunity to probe a gold-catalyzed reaction in the gas phase. Recently, Fiksdahl reported results of a similar study, where they showed that propargyl acetals undergo a similar rearrangement but have lower reaction barriers.¹⁴⁶

Scheme 30. Gold-catalyzed rearrangement and degradation of propargyl ethers in the condensed phase.



In the present study we probe the generality of this rearrangement by gold (I) in the gas phase. The results are supported by density functional theory (DFT) calculations and highlight the important intermediates on the reaction surface.

5.2– Experimental Procedures

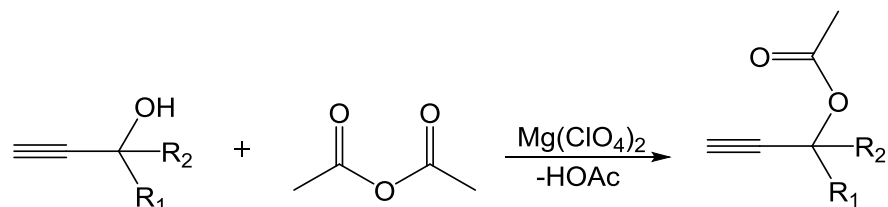
All experiments were conducted in a modified ThermoFinnigan LCQ Deca XP Plus quadrupole ion trap mass spectrometer equipped with ESI. Gold(I) salts were dissolved in methanol at 10^{-4} - 10^{-5} M. Typical ESI conditions involved flow rates of 3-5 μ L/min with needle potentials between 3.5 and 6 kV and heated capillary temperatures from 125 to 200 $^{\circ}$ C. A notched waveform is used for isolating the ionic species. Upon

obtaining a stable signal, neutral reagents can be spiked into the helium stream via a custom gas-handling system which has been described above.

Most neutral reagents were obtained from commercial sources in the highest purity available and used without further purification. Some neutral reagents were synthesized and are reported below. As needed, neutral reagents were diluted in cyclohexane.

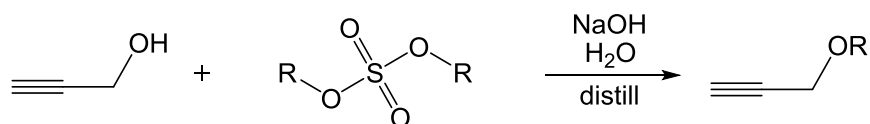
5.3– Synthetic Procedures

Scheme 31. Synthesis of propargyl acetates.¹⁴⁷



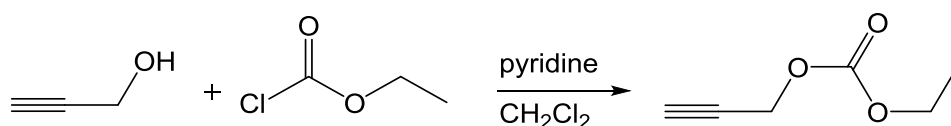
Adapting a previously reported synthesis, 0.01 equivalent of Mg(ClO₄)₂ is diluted in 1.1 equivalent of acetic anhydride at room temperature in a nitrogen environment. Then 1 equivalent of the desired propargyl alcohol is added dropwise under a nitrogen environment and stirred for one hour. Once completed, the reaction is quenched with sodium bicarbonate and extracted with diethyl ether.

Scheme 32. Synthesis of propargyl ethers.¹⁴⁸



Following a previously reported synthesis, 1 equivalent of propargyl alcohol was added to a 1.5 M solution of sodium hydroxide. 0.5 equivalent of diethyl ether was added dropwise and upon completion the product was distilled.

Scheme 33. Synthesis of ethyl prop-2-yn-1-yl carbonate.¹⁴⁹



Following a previously reported synthesis, propargyl alcohol was mixed with 5 mL of pyridine and 15 mL of dichloromethane under nitrogen, to which 1.2 equivalent of ethyl chloroformate was added dropwise at 0° and mixed for three hours at room temperature. After the mixing, the reaction was quenched with 5 mL of water and extracted with diethyl ether.

5.4– Results and Discussion

5.4.1– Propargyl Acetates

To investigate the generality of the gold-catalyzed rearrangements of propargyl acetates we examined three compounds: 1,1-dimethyl-2-propynyl acetate, 1-phenyl-2-propynyl acetate, and ethyl 2-acetoxybut-3-ynoate as substrates for the rearrangement. In these studies, we employed triphenylphosphine gold (I) as the catalyst. The reactions initially lead to the formation of an adduct of triphenylphosphine gold (I) cation with the alkyne. The adducts were then isolated in the ion trap and allowed to react with olefins. We utilized styrene and 4-vinylanisole to probe the presumed carbene intermediate.

With 1-phenyl-2-propynyl acetate as the substrate, the gold adduct was unreactive with olefins, suggesting that a rearrangement to form a carbene had not taken place. This is a compound that Toste reported was effective for carbene formation in the condensed phase.¹⁴² Upon allowing a gold (I) cation to react with this compound, we observed an initial adduct formation between the ligated gold (I) cation and 1-phenyl-2-propynyl acetate. These results are given in Figure 48, where triphenylphosphine gold (I) was allowed to react with 1-phenyl-2-propynyl acetate.

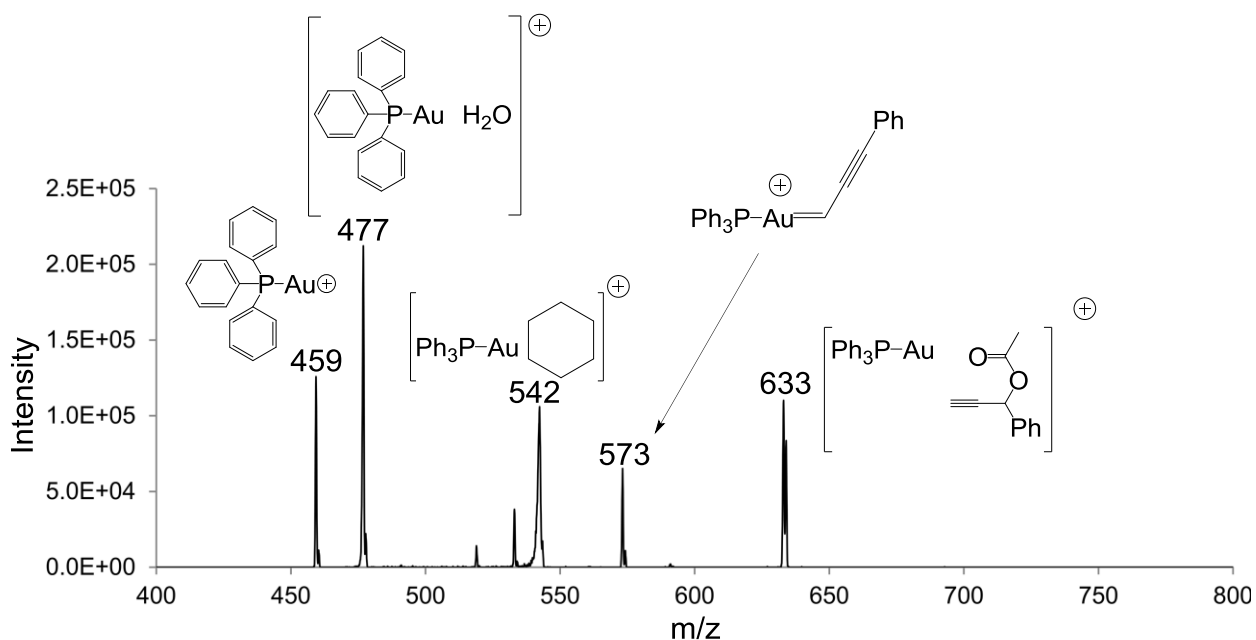
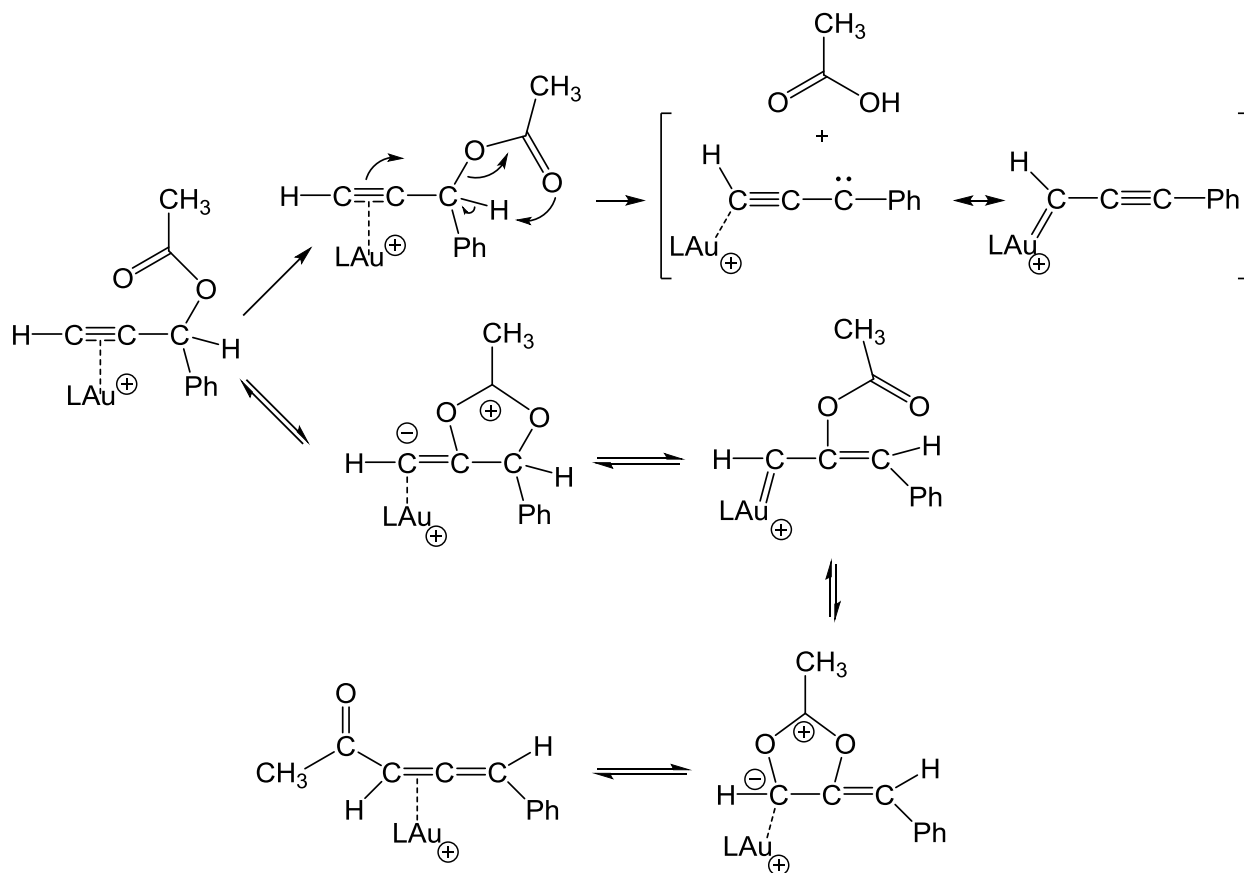


Figure 48. Reaction of AuPPh_3 with 1-phenylprop-2-yn-1-yl acetate. The adduct of AuPPh_3 with 1-phenylprop-2-yn-1-yl acetate was selected at m/z 633 and subjected to CID at 25%.

Upon isolation, this adduct was unreactive with olefins indicating that a rearrangement to form a carbene had not taken place. We then applied a small amount of CID to provide some internal energy to try to stimulate a rearrangement; however this proved to be unproductive. After application of a large amount of CID, a loss of a mass that corresponds to acetic acid was observed along with what appeared to be the formation of a novel carbene (Scheme 34). It reacts with olefins to give an addition product, which gives a very slow reaction with additional olefin in the ion trap. The second olefin molecule displaces the newly-formed cyclopropane in the gold complex (Scheme 35). When the addition product (i.e., putative cyclopropane complex) is

subjected to CID, we also see a metathesis pathway that leads to a new gold carbene product. Both of these pathways have been identified in earlier studies of gold carbenes and the metathesis provides strong evidence of a carbene intermediate. The remaining question is why the initial adduct was incapable of carbene chemistry. This suggests that either it does not rearrange to a carbene or that the carbene is unreactive with olefins. To gain more insight, the system was modeled with the M06 DFT functional. For optimizations, a mixed basis set was used (lanl2dz on Au and 6-311+G** on other atoms). The results indicate that the acetate is able to move along the propargyl backbone via bridging structures. Several bridged and unbridged structures have reasonably similar energies, but the lowest energy species is an allene (i.e., result of 1,3 shift of acetate). The least stable is the carbene species that results from a 1,2-shift of the acetate; therefore, the resting state for the species is not expected to have carbene character. There could be several routes to acetic acid loss from this suite of structures, but the best that we have located is an alpha elimination from the starting propargyl complex. Data from the novel carbene reacting with 4-vinylanisole with and without application of CID are given in Figures 49, 50 and 51.

Scheme 34. Triphenylphosphine gold (I) forming a novel carbene by reacting with 1-phenyl-2-propynyl acetate.



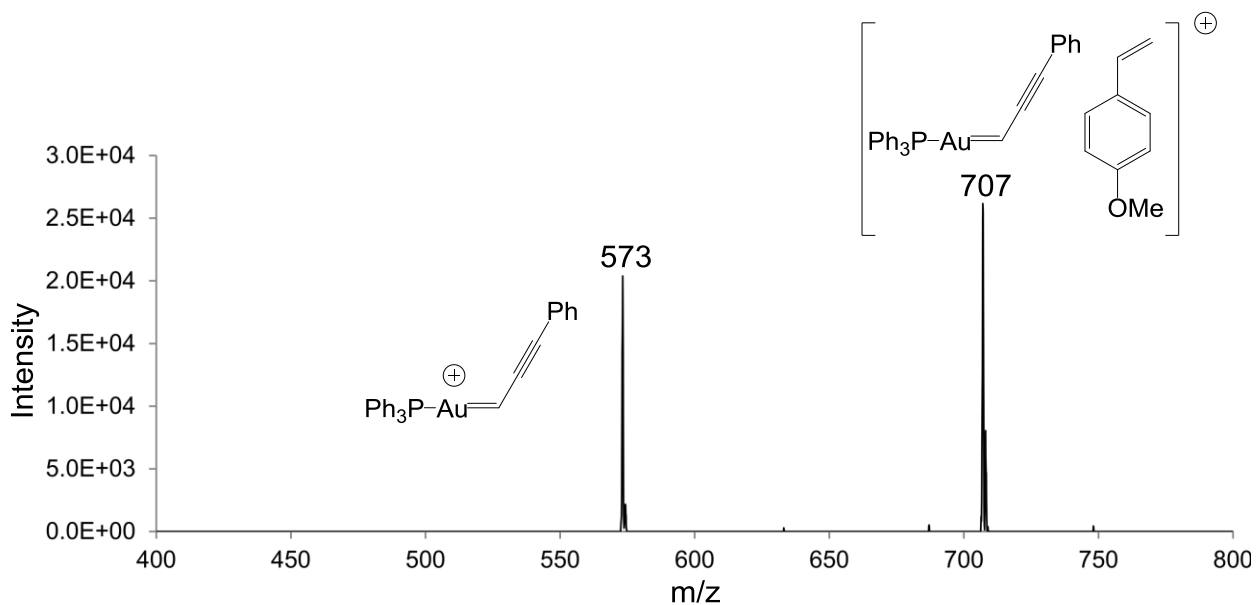


Figure 49. Reaction of AuPPh_3 with a 5:2 mixture of 1-phenylprop-2-yn-1-yl acetate and 4-vinylanisole. The adduct of AuPPh_3 with 1-phenylprop-2-yn-1-yl acetate was selected at m/z 633 and subjected to CID at 25%. Then, the carbene was selected at m/z 573 and allowed to react for 500 ms.

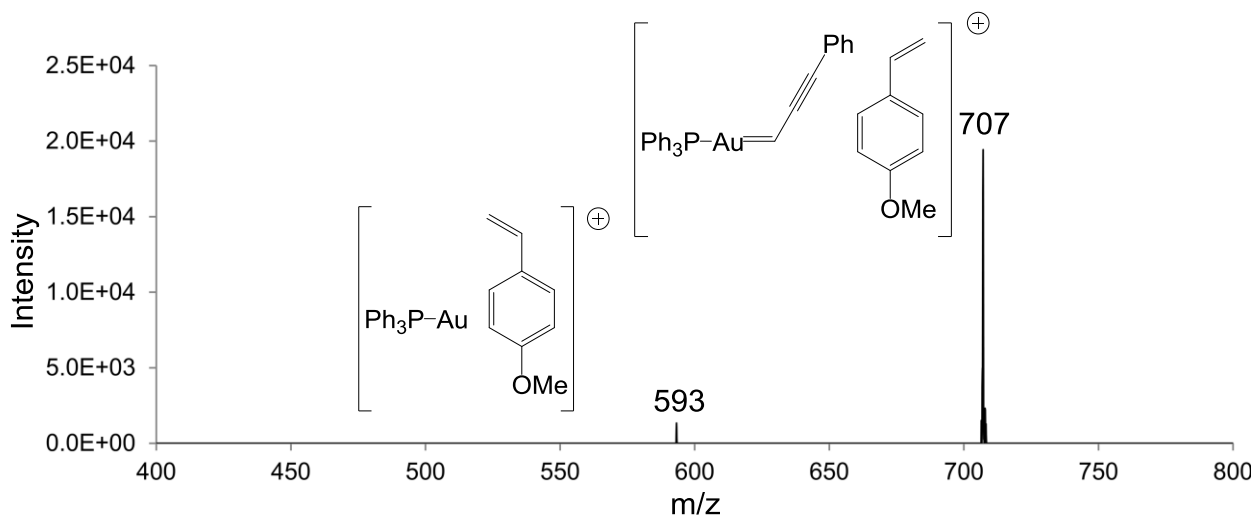


Figure 50. Reaction of AuPPh₃ with a 5:2 mixture of 1-phenylprop-2-yn-1-yl acetate and 4-vinylanisole. The adduct of AuPPh₃ with 1-phenylprop-2-yn-1-yl acetate was selected at m/z 633 and subjected to CID at 25%. Then, the carbene was selected at m/z 573 and allowed to react for 500 ms. The reaction product at m/z 707 was then selected and allowed to react for 10000 ms.

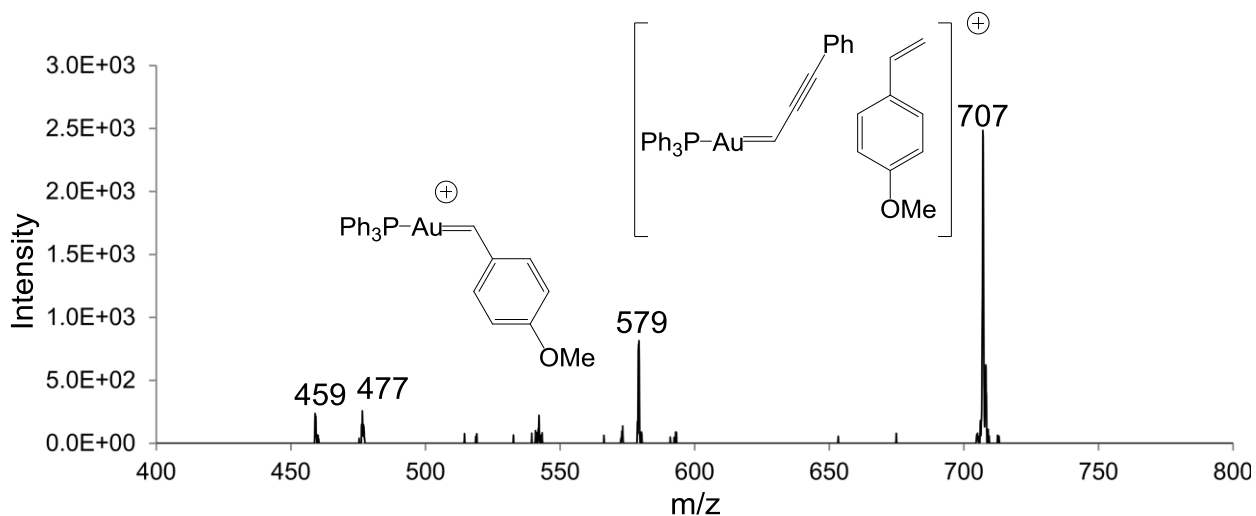
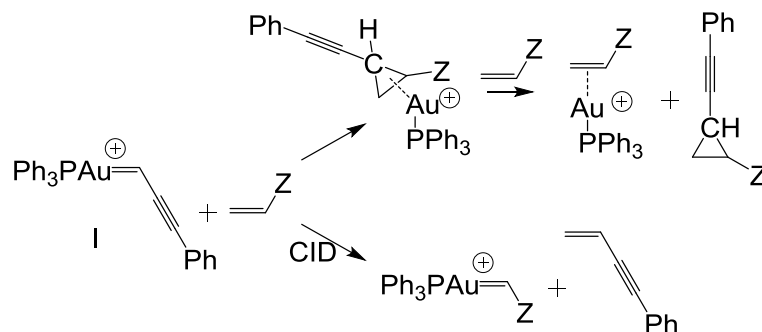


Figure 51. Reaction of AuPPh₃ with a 5:2 mixture of 1-phenylprop-2-yn-1-yl acetate and 4-vinylanisole. The adduct of AuPPh₃ with 1-phenylprop-2-yn-1-yl acetate was selected at m/z 633 and subjected to CID at 25%. Then, the carbene was selected at m/z 573 and allowed to react for 500 ms. The reaction product at m/z 707 was then selected and allowed to react for 10000 ms and subjected to CID at 27%. AuPPh₃ can be observed at m/z 459 and with its adduct with water at m/z 477.

Scheme 35. Cyclopropanation and metathesis processes of carbene **I** with olefins.



Toste and co-workers have employed 1,1-dimethyl-2-propynyl acetate in some of their condensed-phase studies of propargyl acetate rearrangements. This substrate lacks a proton at the propargyl carbon and cannot undergo the acetate-loss mechanism that can be seen in Scheme 34.

When allowed to react with the triphenylphosphine gold (I) cation, it forms an adduct. This adduct is also unreactive with olefins. When subjected to CID conditions, the adduct loses acetic acid, which we interpret as a typical ester elimination pathway and results in a gold complex of an enyne (Scheme 36). The resulting complex forms adducts and undergoes a ligand swapping reaction with the probe olefins (i.e., olefin replaces the substrate fragment) when subjected to mild CID conditions. It is likely that the gold complex of this precursor also can explore a variety of structures and that the carbene is not well represented in the distribution. Under the conditions of the ion trap, the carbene chemistry could be too slow. Unlike the previous system, the loss of acetic acid does not lock the system into a carbene structure; instead it produces an enyne species that does simple ligand swapping chemistry. An example of this is shown in Figure 52, where triphenylphosphine gold (I) was allowed to react with 1,1-dimethyl-2-propynyl acetate.

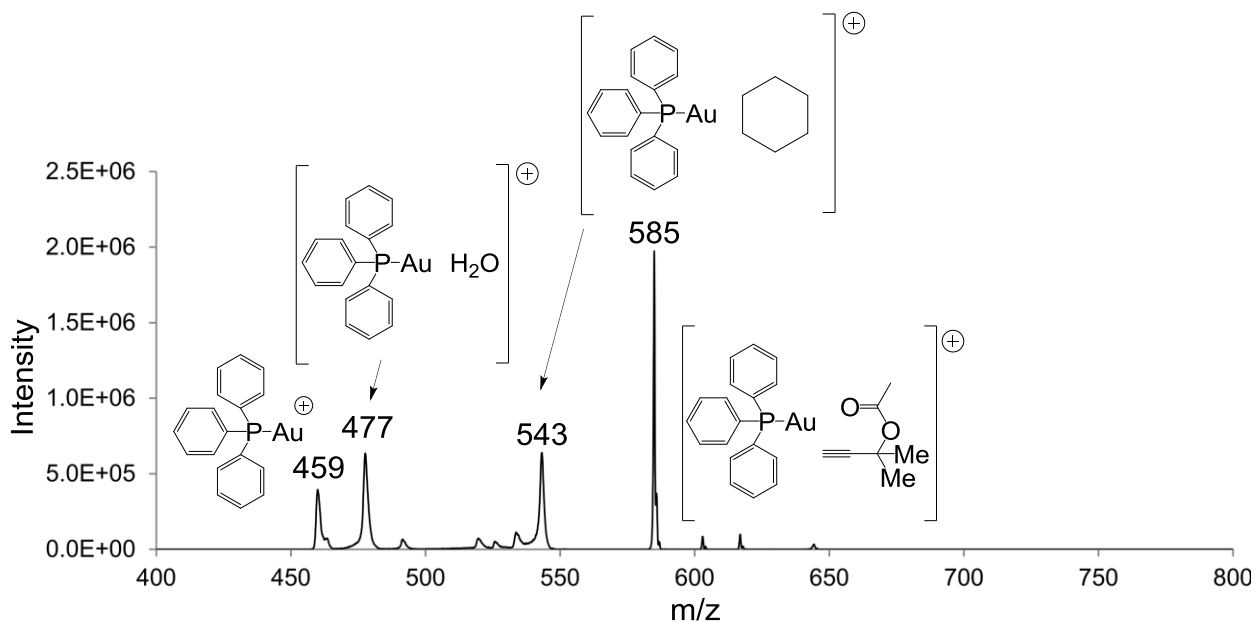


Figure 52. Reaction of AuPPh₃ with 1,1-dimethyl-2-propynyl acetate.

These adducts are then able to be isolated, allowed to react with olefins, and provided energy by the application collision induced dissociation (CID) yielding various results. For 1,1-dimethyl-2-propynyl acetate, which Toste and co-workers had previously shown efficient for this reaction in the condensed phase, the adduct with the gold (I) cation was isolated and allowed to react with styrene and 4-vinylanisole but was unreactive.¹⁴² An example of this is given in Figure 53, where the adduct of the gold and alkyne is allowed to react with styrene. CID of this complex is shown in Figure 54. Upon isolation of the adduct of the gold ion with 1,1-dimethyl-2-propynyl acetate and application of CID, a loss of a mass that corresponds to acetic acid was observed (Scheme 36). These results are given in Figure 55.

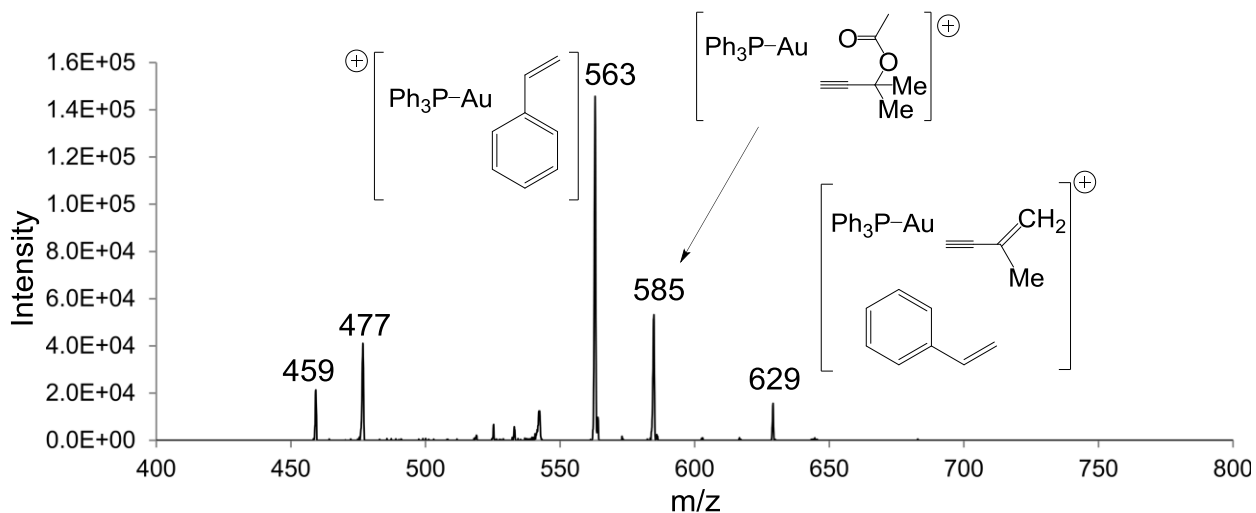


Figure 53. Reaction of AuPPh₃ with a 1:2 mixture of 2-methylbut-3-yn-2-yl acetate and styrene. The adduct of AuPPh₃ with 1,1-dimethyl-2-propynyl acetate was selected at m/z 585 and subjected to CID at 10%. Then the reaction product was selected at m/z 629 and subjected to CID at 30%. AuPPh₃ can be observed at m/z 459 and with its adduct with water at m/z 477.

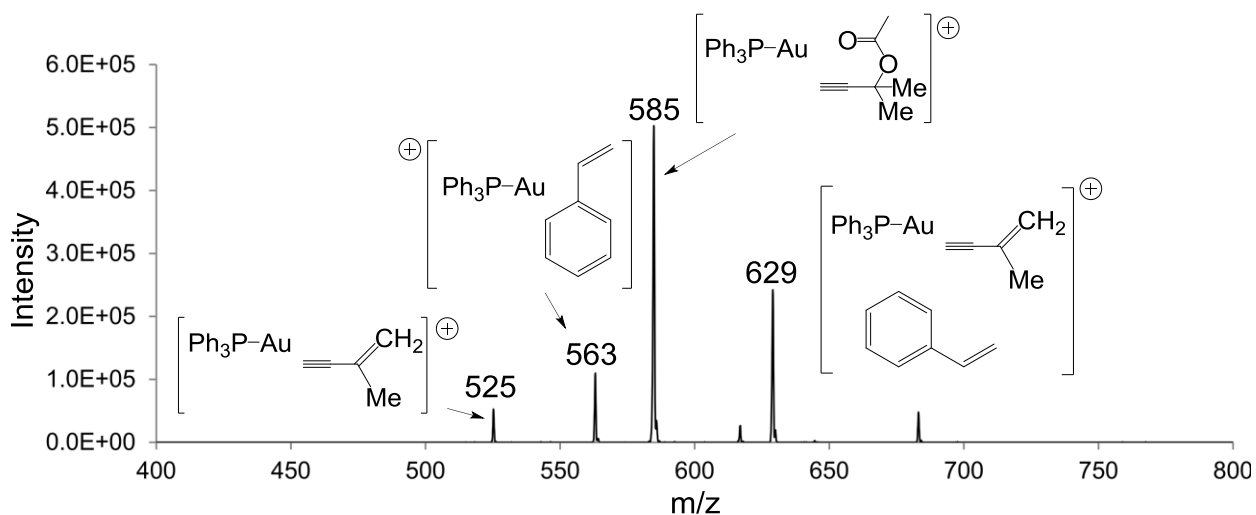


Figure 54. Reaction of AuPPh₃ with a 1:2 mixture of 1,1-dimethyl-2-propynyl acetate and styrene. The adduct of AuPPh₃ with 1,1-dimethyl-2-propynyl acetate was selected at m/z 585 and allowed to react for 5000 ms and subjected to CID at 10%.

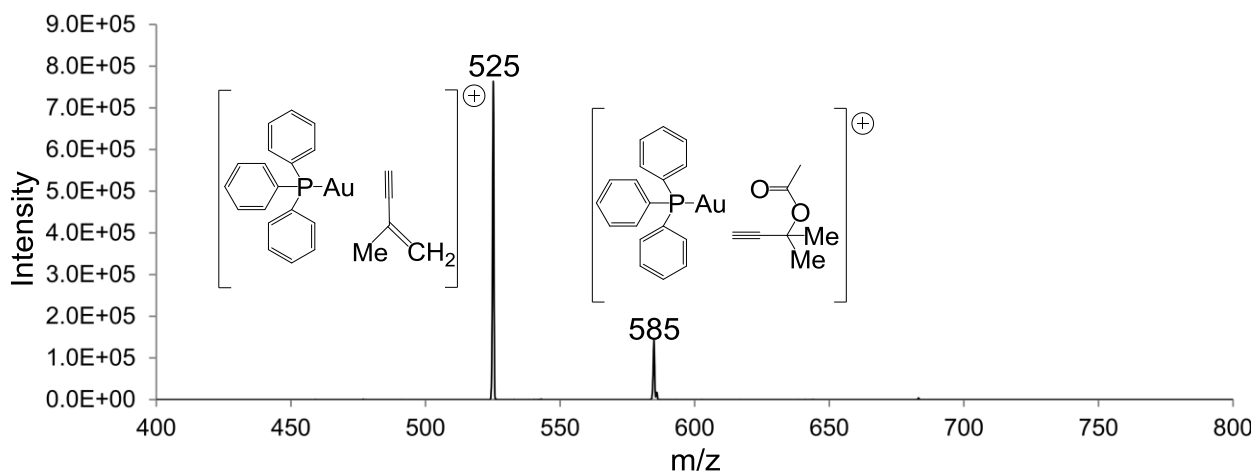
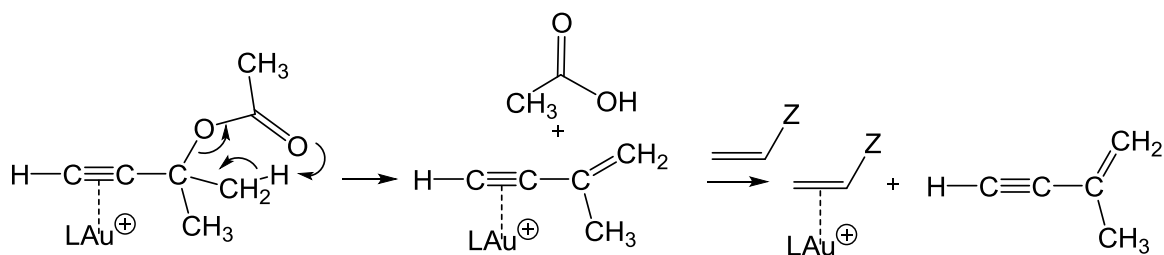


Figure 55. Reaction of AuPPh₃ and 1,1-dimethyl-2-propynyl acetate. The adduct of AuPPh₃ with 1,1-dimethyl-2-propynyl acetate was selected and subjected to CID.

Scheme 36. Triphenylphosphine gold (I) reacting with 1,1-dimethyl-2-propynyl acetate.



Important to note, we did observe a small adduct of the triphenylphosphine gold (I) cation with this fragment of 1,1-dimethyl-2-propynyl acetate and an olefin however this did not degrade to form carbene reaction products. Therefore, we concluded that this was not a carbene.

Seeing that the path to a reactive carbene involves the removal of a proton on the propargyl carbon (Scheme 34), we synthesized a compound bearing an electron withdrawing group at this position to make the proton more acidic. A mass spectrum of the formation of this compound complexing with triphenylphosphine gold (I) can be seen in Figure 56.

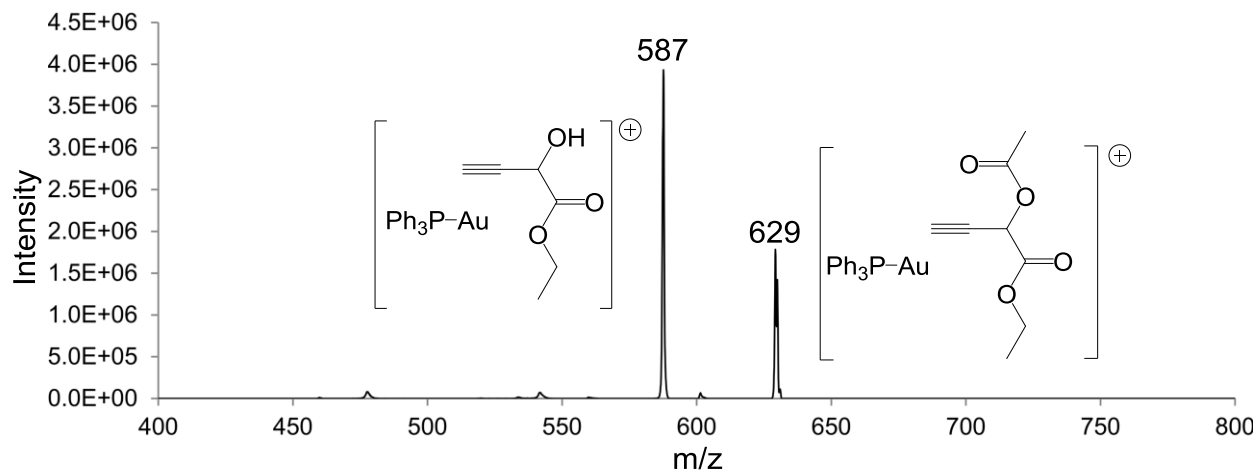


Figure 56. Reaction of AuPPh₃ with ethyl 2-acetoxybut-3-ynoate. The adduct of AuPPh₃ with ethyl 2-acetoxybut-3-ynoate was selected at m/z 629 m/z and subjected to CID at 25%.

When allowing ethyl 2-acetoxybut-3-ynoate to react with we first observed an adduct formation with the gold (I) cation. Collision induced dissociation was applied to this adduct upon isolation and an ion was observed that corresponds to a loss of ethenone (Scheme 37). A mass spectrum of these results are given in Figure 57.

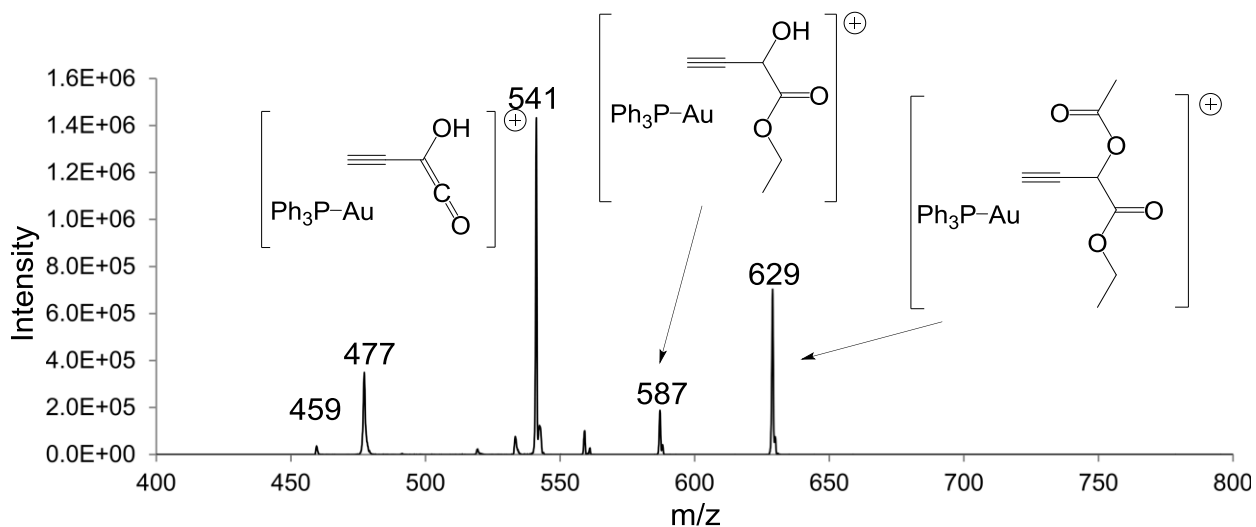


Figure 57. Reaction of AuPPh₃ with ethyl 2-acetoxybut-3-ynoate. The adduct of AuPPh₃ with ethyl 2-acetoxybut-3-ynoate was selected at m/z 629 m/z and subjected to CID at 25%. Then, the degradation product at 587 was selected at m/z 587 and subjected to CID at 25%. AuPPh₃ can be observed at m/z 459 and with its adduct with water at m/z 477.

The appearance of this product indicates that the acetate group is not stepping over the alkyne and rearranging in the manner that is seen in the condensed phase. The electron withdrawing group, rather than increasing the rate of the acetic acid, provided the steric hindrance necessary to force the loss of ethenone. Further CID on this compound revealed a compound that had lost a mass corresponding to ethanol (Scheme 37). Isolation and dissociation of this compound produces a compound that has lost CO. From this point additional CID leads to a bare gold (I) ion. When an olefin was allowed to react with these compounds they did not undergo any observable reactions, thus indicating that no carbene was formed in this process. These results are

given in Figure 58, where triphenylphosphine gold (I) is allowed to react with a mixture of ethyl 2-acetoxybut-3-ynoate and 4-vinylanisole.

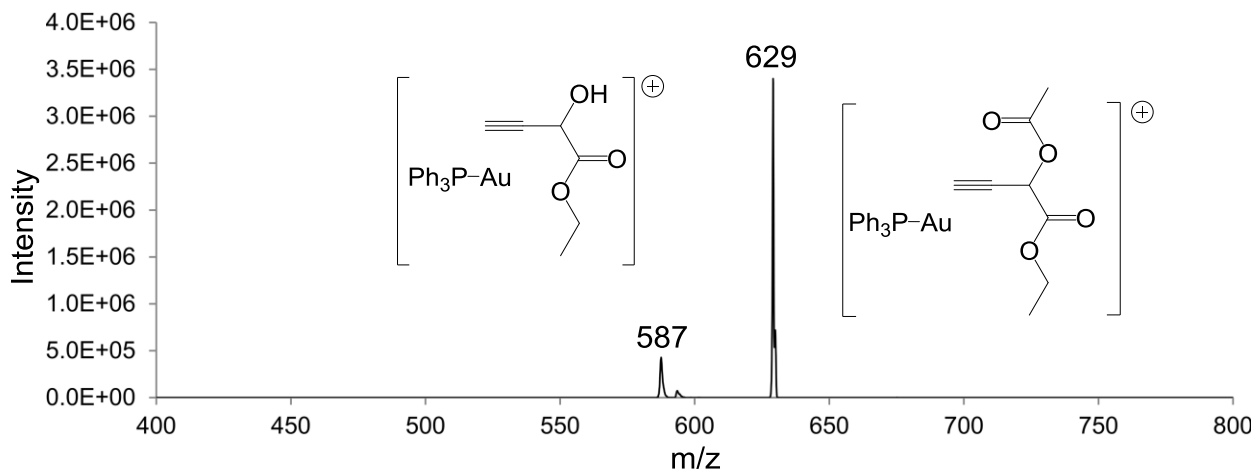
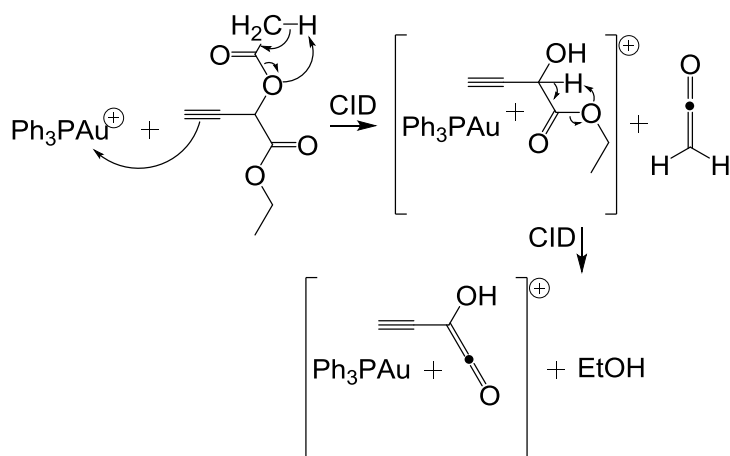


Figure 58. Reaction of AuPPh_3 with a 5:2 mixture of ethyl 2-acetoxybut-3-ynoate and 4-vinylanisole. The adduct of AuPPh_3 with ethyl 2-acetoxybut-3-ynoate was selected at m/z 629 m/z and subjected to CID at 17% and allowed to react for 5000 ms.

Scheme 37. Triphenylphosphine gold (I) reactivity with ethyl 2-acetoxybut-3-ynoate.



5.4.2– Propargyl Ethers

For our study into the viability of gold-catalyzed hydride transfer and degradation of propargyl ethers in the gas-phase, we looked at three propargyl ethers, benzyl propargyl ether, ethyl propargyl ether, and methyl propargyl ether. These compounds were chosen do to their similarity to propargyl ethers that have been used for this reaction in the condensed phase.¹⁴³ We employed triphenylphosphine gold(I), dimethylsulfide gold(I), and 1,3-diisopropylimidazolium gold(I) in order to explore the impacts of these three general classes of ligands and were due to their similarity to complexes that were active towards catalyzing these reactions in the condensed phase. We also explored triphenylphosphine silver (I) as a catalyst for this process. We chose to do so because the condensed-phase studies of these reactions use silver along with gold in this process. Therefore, we were interested in probing these reactions with gold and silver separately to see if we could learn anything about the “silver effect”, and if there was any such thing in this process. The products for these reactions indicate an initial adduct formation of the propargyl ether with the gold or silver (I) ion. A mass spectrum of this is given in Figure 59.

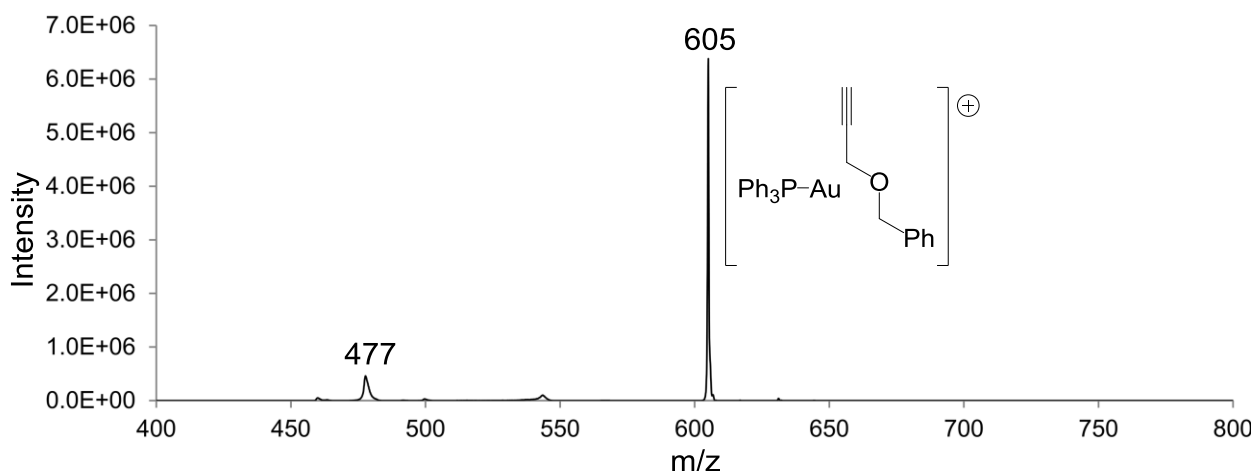


Figure 59. Reaction of AuPPh₃ with benzyl propargyl ether. AuPPh₃ with its adduct with water at m/z 477.

These adducts can be then isolated and energetically exited through the application of CID, producing, for the gold-catalyzed reaction, compounds that correspond to the mass of a allene bound to the gold (I) ion (Scheme 38). An example of this can be seen in Figure 60, where triphenylphosphine gold (I) was allowed to react with benzyl propargyl ether with CID applied to the addition complex. This reactivity is similar to the results that have been reported for the condensed phase.¹⁴³ Triphenylphosphine silver (I) did not catalyze this reaction, rather it formed an adduct with the propargyl ethers that dissociated under CID. All three ligand systems on the gold afforded the same reactivity with the propargyl ethers, indicating that the electronic characteristics of the ligand do not control the reactivity in these reactions.

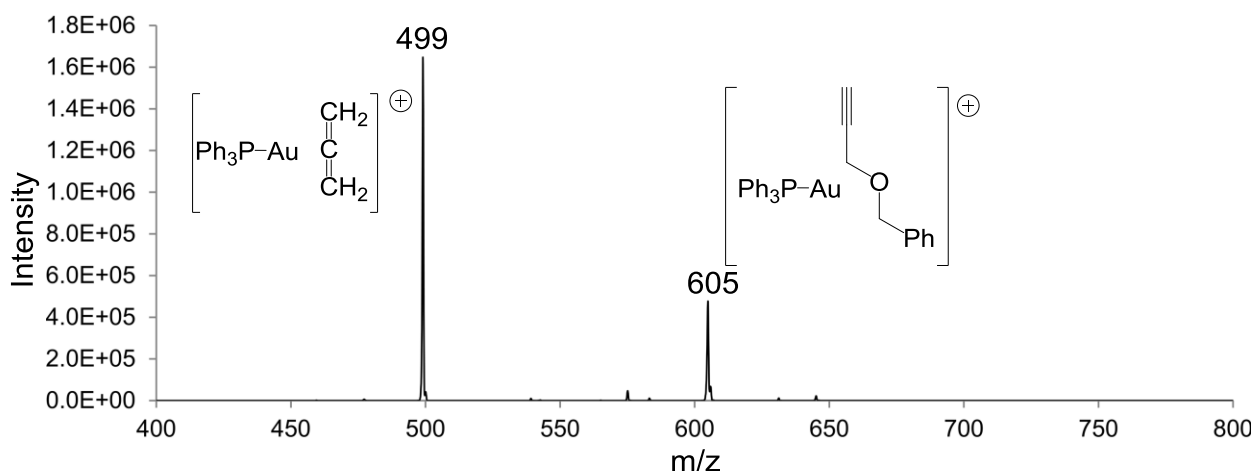
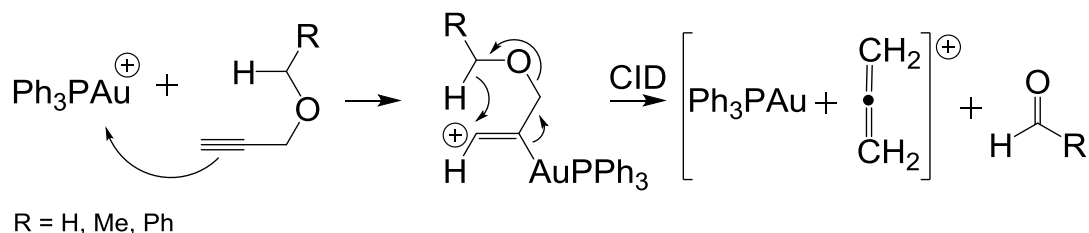


Figure 60. Reaction of AuPPh₃ with benzyl propargyl ether. The adduct of AuPPh₃ with benzyl propargyl ether was selected at m/z 605 m/z and subjected to CID at 20%.

Scheme 38. Triphenylphosphine gold (I) reactivity with propargyl ethers.



5.4.3– Propargyl Acetals

Given the reactivity of the propargyl ethers in the gas phase we probed more alkyne substrates to explore the generality of this reaction. Fiksdahl and co-workers have recently reported the effectiveness of the rearrangement of propargyl acetals by gold (I) complexes, indicating that they rearrange more readily than propargyl ethers.¹⁴⁶

When acetaldehyde ethyl propargyl acetal is allowed to react with triphenylphosphine gold (I) we observe an initial adduct formation followed by a rearrangement and degradation to form an allene (Scheme 39). Results from this reaction can be seen in Figure 61. This propargyl acetal underwent the rearrangement to form an allene more readily than the propargyl ethers. These results are similar to what was observed by Fiksdahl in the condensed phase and indicates that the reaction barriers are decreased in the gas phase for the rearrangement of propargyl acetals when compared to propargyl ethers. This process did not require CID.

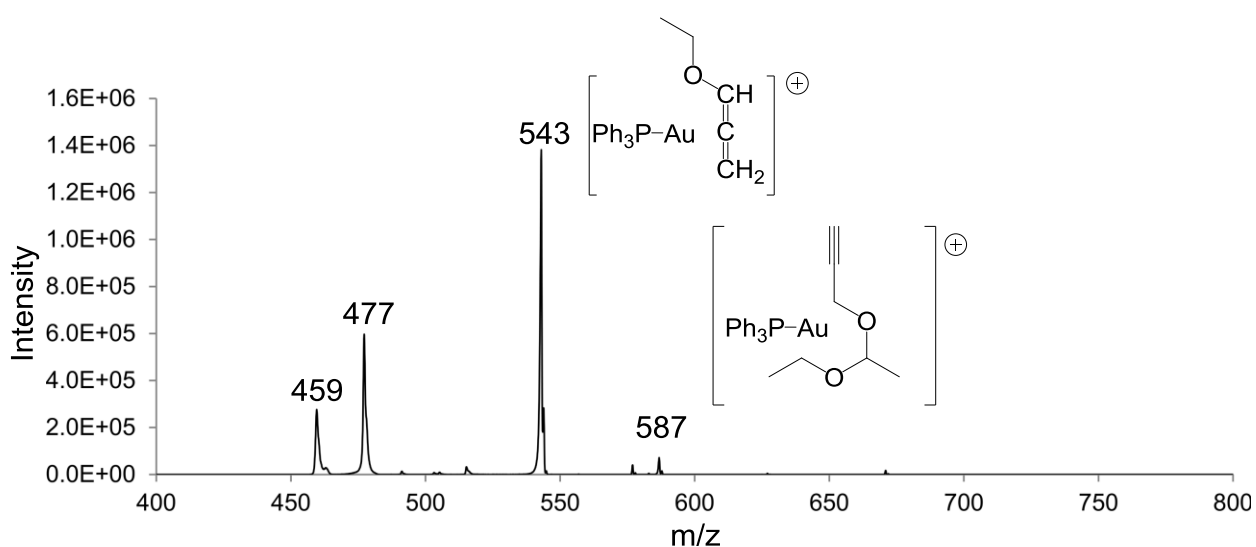
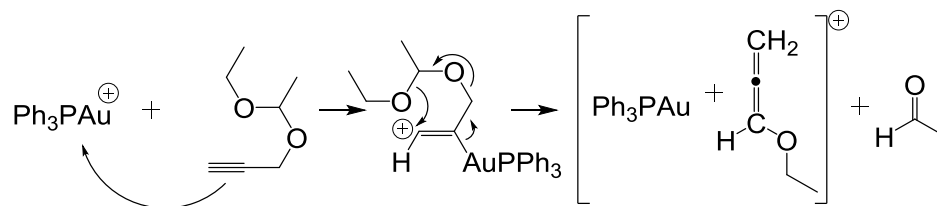


Figure 61. Reaction of AuPPh₃ with 3-(1-ethoxyethoxy)prop-1-yne. The adduct of AuPPh₃ with 3-(1-ethoxyethoxy)prop-1-yne was selected at m/z 587 and subjected to CID. AuPPh₃ can be observed at m/z 459 and with its adduct with water at m/z 477.

Scheme 39. Triphenylphosphine gold (I) reacting with acetaldehyde ethyl propargyl acetal.



5.4.4– Propargyl Carbonates

After observing the enhanced reactivity of propargyl acetals over propargyl ethers we next probed the reactivity of propargyl carbonates in the gas phase. We synthesized ethyl prop-2-yn-1-yl carbonate from a previously reported synthesis and allowed it to react with triphenylphosphine gold (I) in the gas phase.¹⁴⁹ For this reaction, we observe an initial adduct formation of the gold (I) complex and the propargyl carbonate. Upon isolation and application of CID, we observe the expected allene product along with the formation of propargyl alcohol (Scheme 40). These spectrum can be seen in Figure 62. We had predicted that propargyl carbonates would react more readily than propargyl acetals with gold (I) complexes due to the expulsion of CO_2 , but this was not the case. Instead, these compounds formed multiple degradation products as seen in Scheme 40. The predicted compound was indeed formed therefore indicating that this process can proceed in a path similar to the propargyl acetals, however the formation of other products does complicate this process.

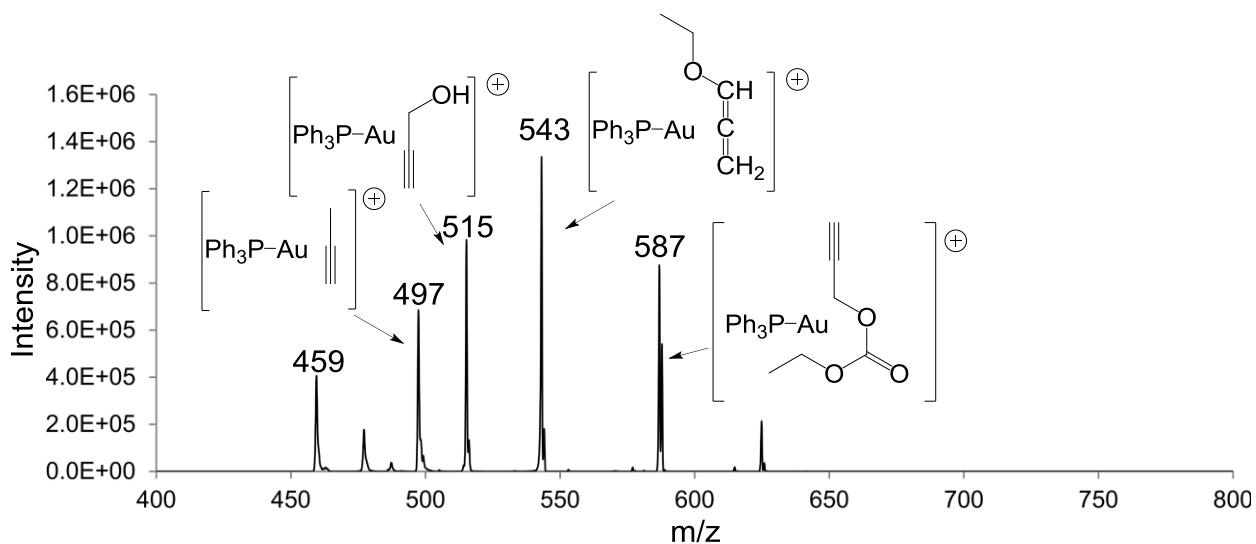
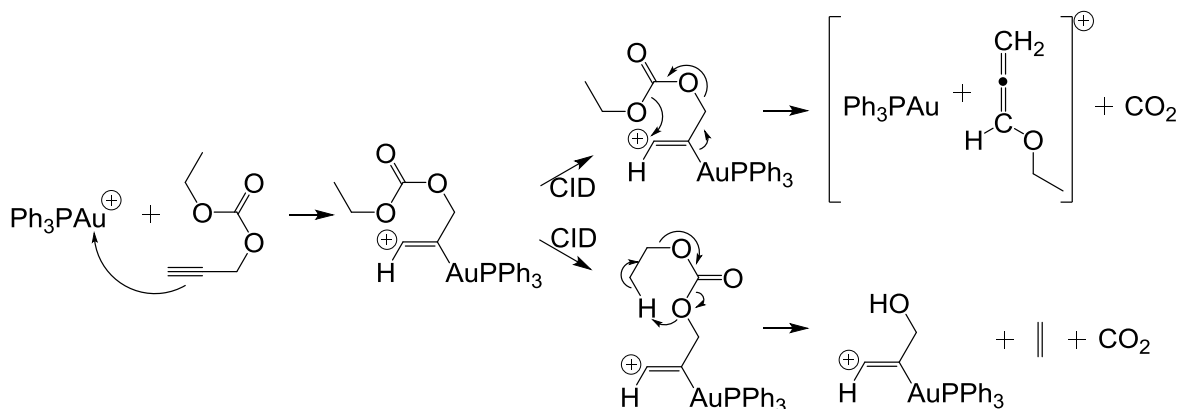


Figure 62. Reaction of AuPPh₃ with ethyl prop-2-yn-1-yl carbonate. The adduct of AuPPh₃ with ethyl prop-2-yn-1-yl carbonate was selected at m/z 587 and subjected to CID. AuPPh₃ can be observed at m/z 459 and with its adduct with water at m/z 477.

Scheme 40. Triphenylphosphine gold (I) reacting with ethyl prop-2-yn-1-yl carbonate.



5.4.5– Related Propargyl Compounds

In an effort to probe the generality of this gold catalyzed rearrangement we probed five related propargyl compounds, propargyl alcohol, 3-methylaminoprop-1-yne, 1-dimethylaminoprop-2-yne, 1-(trimethylsilyl)-2-propyne, and (2-propynyloxy)trimethylsilane. Upon allowing 1-dimethylaminoprop-2-yne to react with triphenylphosphine gold (I), we first observe an adduct formation which upon isolation and application of CID we observe the formation of an allene product (Scheme 41). This is similar to the reactivity that was observed in the propargyl ethers. Results of this reaction are given in the spectrum in Figure 63.

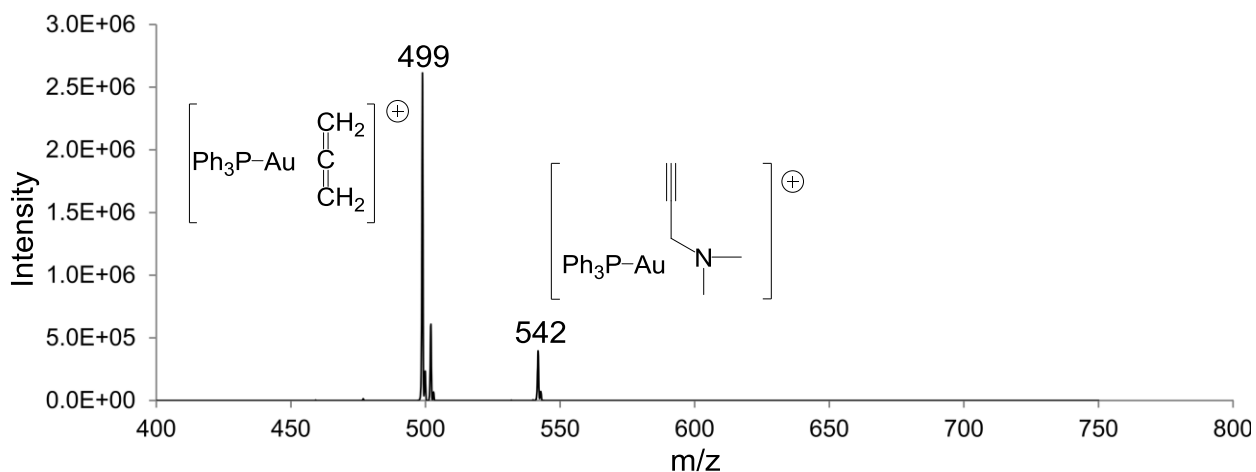
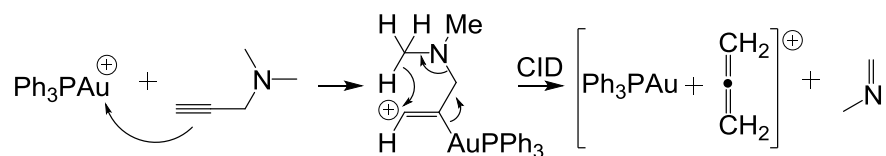


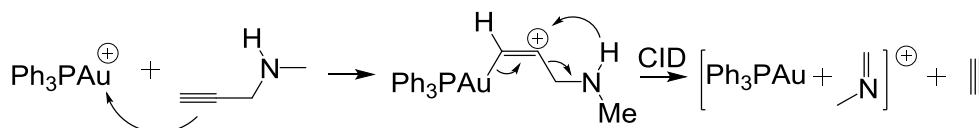
Figure 63. Reaction of AuPPh₃ with N,N-dimethylprop-2-yn-1-amine. The adduct of AuPPh₃ with N,N-dimethylprop-2-yn-1-amine was selected at m/z 542 and subjected to CID.

Scheme 41. Triphenylphosphine gold (I) reacting with 1-dimethylaminoprop-2-yne.



We then probed 3-methylaminoprop-1-yne for this reactivity however, rearrangement and allene formation was not observed. A possible rearrangement pathway is shown in Scheme 42.

Scheme 42. Triphenylphosphine gold (I) reacting with 3-methylaminoprop-1-yne.



To gain more insight into this presumed 1,3 rearrangement we probed propargyl alcohol for this reactivity. This only lead to an adduct formation with no observable reaction. Moving forward we then probed 1-(trimethylsilyl)-2-propyne and (2-propynyloxy)trimethylsilane. These both formed adducts with the gold complex with no observable secondary reactions.

5.5– Conclusions

In conclusion, transferring these gold-catalyzed reactions to the gas phase from the condensed phase provided insight into the mechanistic details and allowed for the survey of the reactivity of similar compounds. For the propargyl acetals, we presume that we observed a rearrangement occur to form a carbene species that was stabilized by an intramolecular interaction of the carbonyl with the carbene. This is bolstered by the loss of acetic acid observed upon CID and knowledge from our previous studies into the nature and reactivity of gold carbenes. The propargyl ether reaction occurred similarly to what was observed in the condensed phase. This reaction proceeded when catalyzed by gold alone and not with silver, indicating that silver does not play a significant role in catalyzing this reaction. We probed the generality of this process and discovered that propargyl acetals and propargyl carbonates undergo a similar reaction with the propargyl acetals having lower reaction barriers than the propargyl ethers. We also discovered that propargyl amines are able to undergo similar reactions when catalyzed by gold. This mechanistic study provides a foundation for the understanding of these reactions and allows for further expansion upon gold catalyzed alkyne reactions.

Chapter 6 – C-H bond Activation by Cationic Iridium (III) Complexes in the Gas Phase

6.1– Introduction

C-H activation has been described as the “holy grail of chemistry” and remains a very active research field.^{150–152} However, the ability to initiate reactivity at unactivated C-H bonds remains a challenge. In the past, cationic iridium (III) complexes have been shown to be effective catalysts for the activation of C-H bonds in the condensed phase and related chemistry has been demonstrated in the gas phase.^{153–159} Much of the previous work has utilized Cp* ligands on the iridium with only a few examples of other ligand systems.^{155,158,160,161} In the present study we report the first example of bimolecular C-H activation by a cationic iridium(III) dichloride phenanthroline complex in the gas phase (Figure 64). This is a 14-electron species with a tetracoordinate iridium. The work includes kinetic measurements and is supported by computational modeling using density functional theory.

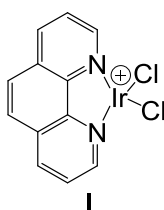


Figure 64. Cationic iridium(III) dichloride phenanthroline complex I.

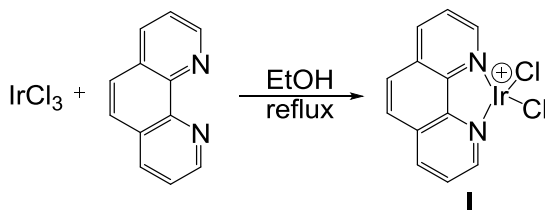
6.2– Experimental Procedures

All experiments were conducted in a modified ThermoFinnigan LCQ Deca XP Plus quadrupole ion trap mass spectrometer equipped with ESI. Iridium (III) salts were dissolved in methanol at 10^{-4} - 10^{-5} M. Typical ESI conditions involved flow rates of 3-5 μ L/min with needle potentials between 3.5 and 6 kV and heated capillary temperatures from 125 to 200 °C. A notched waveform is used for isolating the ionic species. Upon obtaining a stable signal, neutral reagents can be spiked into the helium stream via a custom gas-handling system which has been described above.

Most neutral reagents were obtained from commercial sources in the highest purity available and used without further purification. Some neutral reagents were synthesized and are reported below.

6.3– Synthetic Procedures

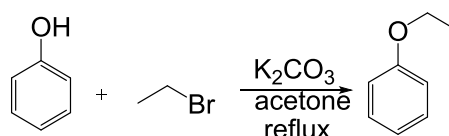
Scheme 43. Synthesis iridium (III) trichloride phenanthroline complex (**I**).



A crude solution of the iridium (III) phenanthroline complex was generated by treating IrCl_3 with one equivalent of 1,10 phenanthroline in refluxing ethanol for 2 h followed by

rotary evaporation. The resulting solid was re-suspended in methanol and used without further purification.

Scheme 44. Synthesis of ethoxybenzene compounds.



Phenol was treated with 3 equivalent of potassium carbonate followed by the dropwise addition of 1.1 equivalent of bromoethane in refluxing acetone. The resulting mixture was filtered and roto evaporated. After dry, the oil was dissolved in ethyl acetate and washed over 10% sodium hydroxide and then over a brine solution. The solution was then dried over sodium sulfate and roto evaporated to reveal a clear oil.

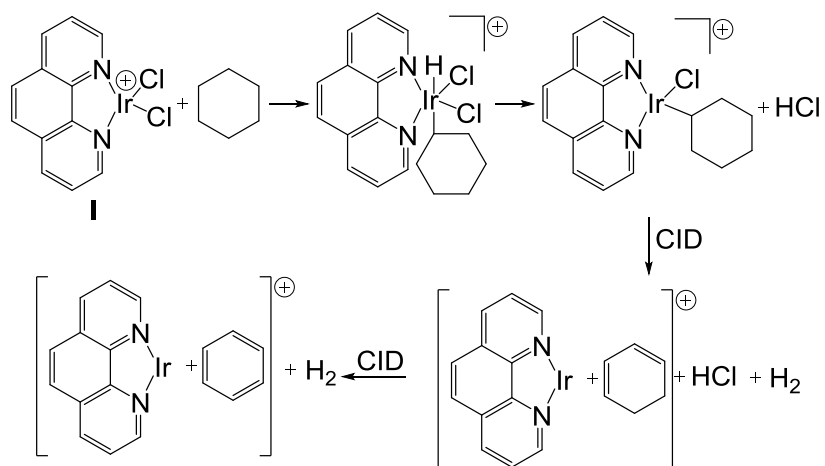
6.4– Results and Discussion

6.4.1– Cyclohexane

While surveying complex I's reactivity as a catalyst for diazoester decomposition, we were surprised by the observation of a relatively rapid reaction with the cyclohexane that was used to dilute the diazo ester. With cyclohexane, I mainly gives addition with the loss of HCl, which we interpret as a C-H activation process followed by reductive

elimination of HCl (Scheme 45).¹⁵⁶ A mass spectrum of these data are given in Figure 65, where complex I was allowed to react with cyclohexane.

Scheme 45. Reaction of compound I with cyclohexane



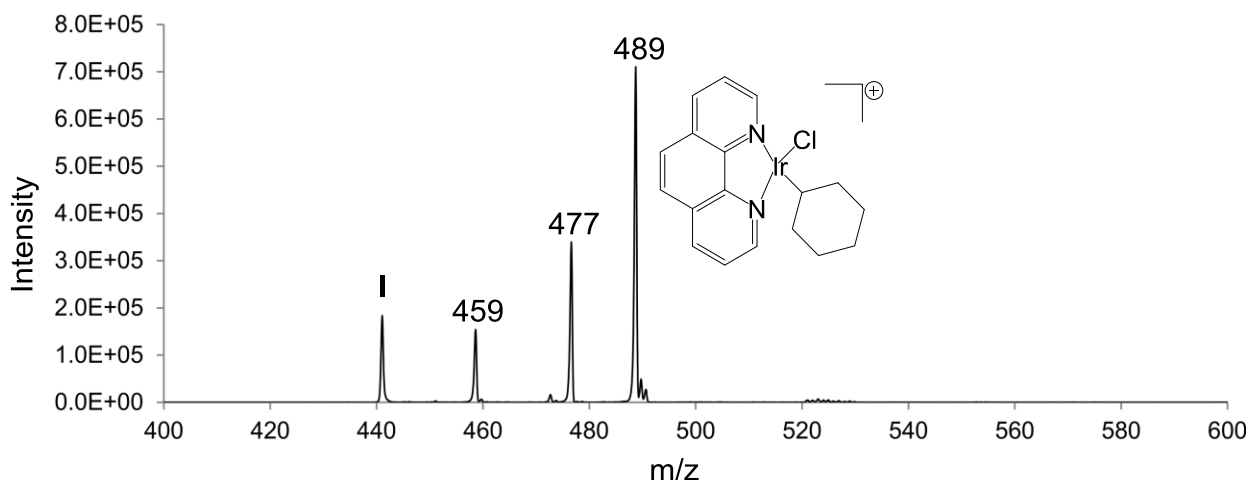


Figure 65. Mass spectrum of complex **I** reacting with cyclohexane. The reactant ion at m/z 441 is mainly the, $^{191}\text{Ir}^{12}\text{C}_{12}^{14}\text{N}_2^1\text{H}_8^{35}\text{Cl}_2$ isotopomer. C-H activation corresponds to the peak at m/z 489, while the peaks at m/z 459 and 477 are single and double adducts of **I** with adventitious water in the ion trap.

This reactivity pattern follows what has been observed by Bergman with other cationic iridium (III) systems.¹⁶² However, unactivated secondary C-H bonds are not cleaved in the condensed-phase by cationic Ir (III) complexes such as $\text{Cp}^*(\text{PMe}_3)\text{IrMeOTf}$.¹⁶² This difference highlights the unusual reactivity of the phenanthroline complex. The kinetics of the reaction were measured and the process has an efficiency ($k_{\text{observed}}/k_{\text{collision}}$) of nearly 10% (Table 6).

Table 6. Rate constants for complex I^a.

Neutral Reagent	<i>k</i>	Efficiency	Product Ratio
Cyclohexane	0.7	9%	100 : 0
Toluene	4.9	59%	95 : 5
Toluene-d ₈	4.3	52%	46 : 54
Ethylbenzene	6.4	82%	100 : 0
Isopropylbenzene	5.9	78%	16 : 84

^aRate constants in units of $10^{-10} \text{ cm}^3 \text{ molecule}^{-1} \text{ sec}^{-1}$. ^b k/k_{coll} where the collision rate is calculated by the method of Su and Bowers.⁸² Product ratio corresponds to C-H activation : adduct formation.

Upon application of collision-induced dissociation (CID), we observe an additional loss of HCl and H₂, which we interpret as a dehydrogenation producing a cyclohexadiene complex. When this complex is selected and CID is applied again, we then observe a loss of H₂, forming a benzene complex. Mass spectra of the application of CID are given in Figures 66 and 67. The dehydrogenation and loss of HCl is apparent in Figure 66. Additional application of CID reveals further dehydrogenation which is apparent in Figure 67. In both of the mass spectra the reactant ion is at *m/z* 441, and is mainly the ¹⁹¹Ir₁₂¹⁴N₂¹H₈³⁵Cl₂ isotopomer.

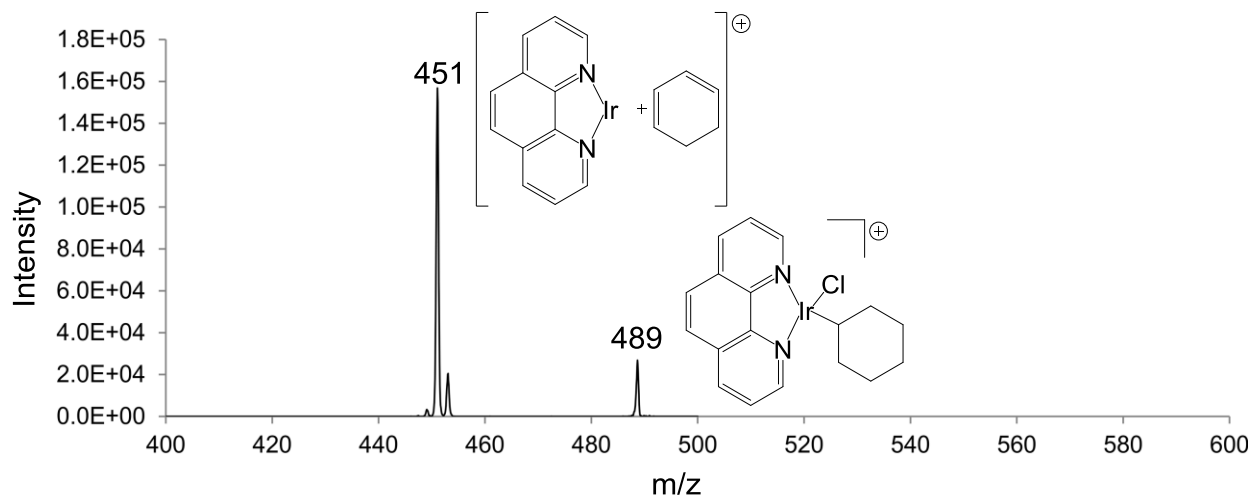


Figure 66. Mass spectrum of complex **I** reacting with cyclohexane with application of CID to the C-H activation product. C-H activation corresponds to the peak at m/z 489 which was isolated and then subjected to CID. The peak at m/z 451 corresponds to a loss of HCl.

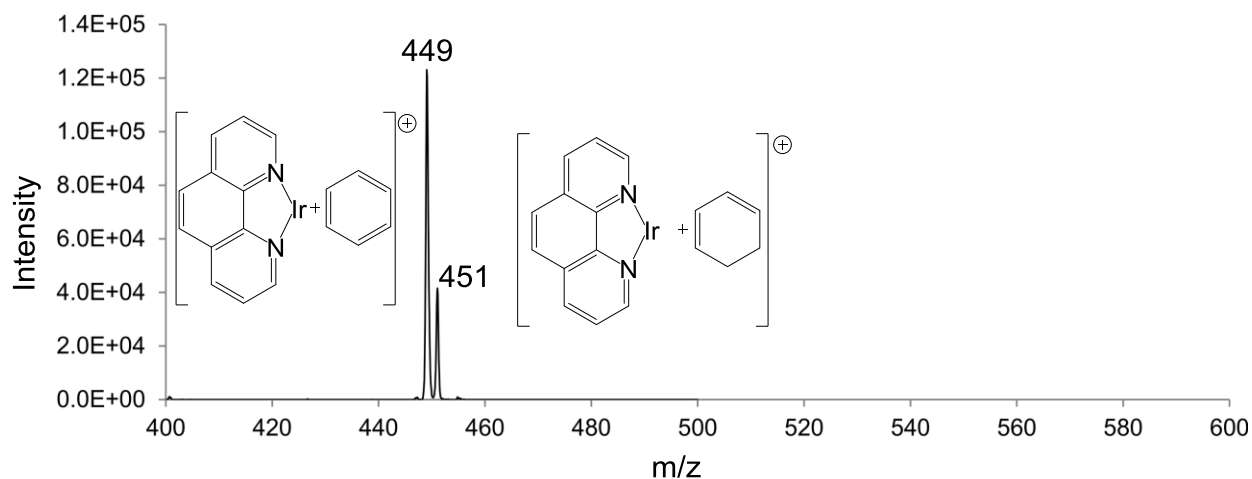


Figure 67. Mass spectrum of complex **I** reacting with cyclohexane with application of CID to 451 m/z. A mass loss of 2HCl corresponds to the peak at m/z 451, which was isolated and subjected to CID. The peak at m/z 449 corresponds to a loss of H₂.

6.4.2– Toluene Series

Inspired by the C-H activation and dehydrogenation reaction with cyclohexane, we turned to a wider set of species (Figure 68) to explore the generality of the C-H activation process and to establish reactivity patterns. Cyclohexene offers the ability to probe the dehydrogenation process that occurs with cyclohexane. Upon allowing complex I to react with cyclohexene, we observe a rapid loss of two HCl giving the cyclohexadiene complex without any application of CID. Further application of CID leads to a loss of H₂, producing the benzene complex. The dehydrogenation that occurs upon allowing cyclohexene to react with complex I can be seen in the mass spectrum shown in Figure 69. This process was quick and needed no additional energy from CID. Further dehydrogenation of cyclohexadiene, forming benzene, is shown in Figure 70. In both of these reactions the reactant ion at m/z 441 is mainly the ¹⁹¹Ir₁₂C₁₂¹⁴N₂¹H₈³⁵Cl₂ isotopomer.

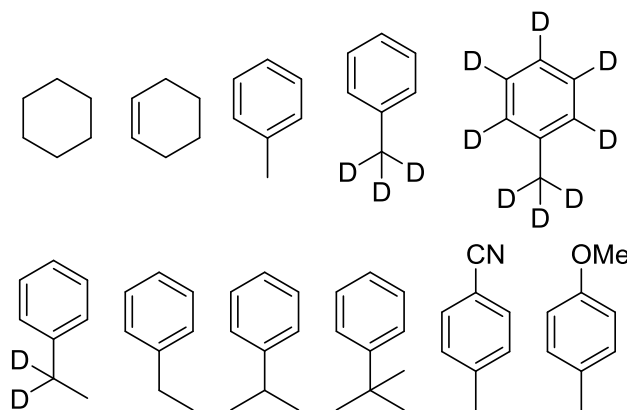


Figure 68. Compounds in this series that were allowed to react with complex I.

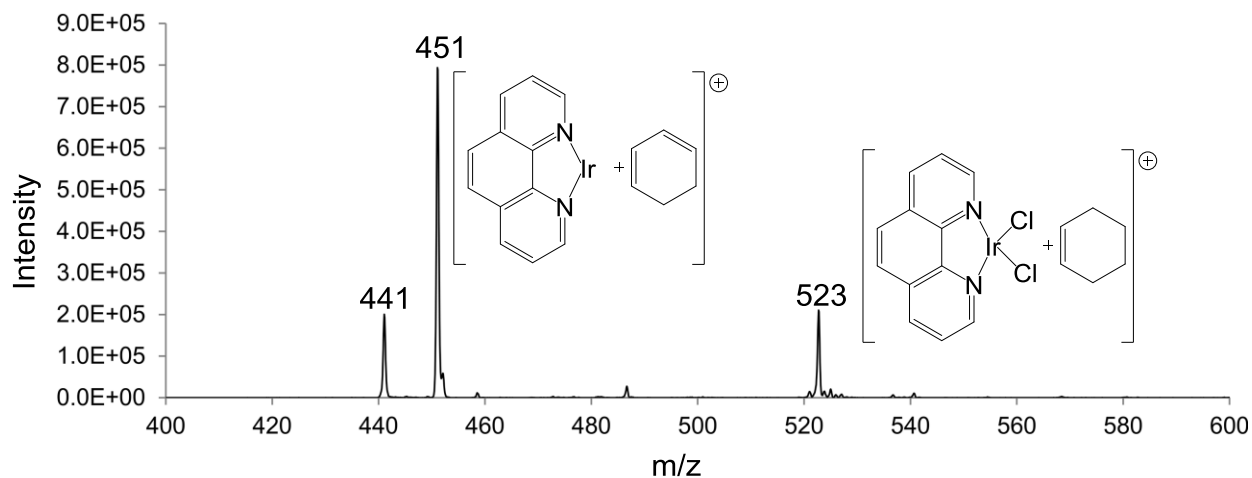


Figure 69. Mass spectrum of complex **I** reacting with cyclohexene. The adduct of complex **I** with cyclohexene was selected at allowed to react. An adduct of cyclohexadiene with complex **I** corresponds to the peak at m/z 451 and the peak at m/z 523 corresponds to an addition of cyclohexene to complex **I**.

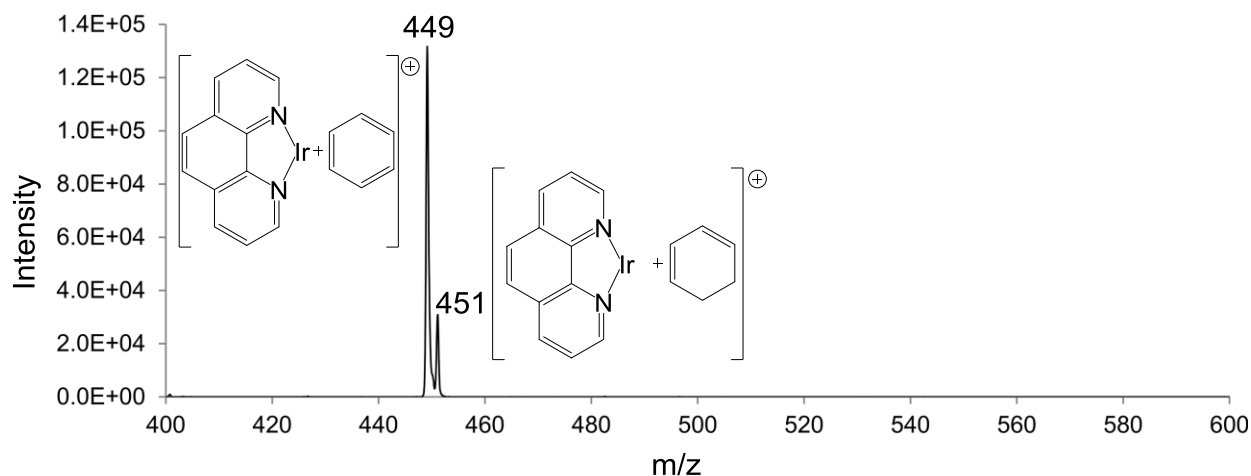


Figure 70. Mass spectrum of complex **I** reacting with cyclohexene. The adduct of complex **I** with cyclohexene was selected and allowed to react. Then, the adduct of cyclohexadiene with complex **I** was selected and subjected to CID. An adduct of cyclohexadiene with complex **I** corresponds to the peak at 451 m/z, which was isolated and subjected to CID. The peak at 449 m/z corresponds to a loss of H₂.

Toluene provides an activated sp³ C-H bond as well as sp² C-H bonds. When complex **I** is allowed to react with toluene, rapid C-H activation is observed, as indicated by addition followed by the loss of HCl. To confirm the site of C-H activation, we employed toluene-d₃. Although it is not possible to eliminate all the interference from the multiple isotopes of Ir and Cl, it appears that reactivity is exclusively at the methyl group. Mass spectra of these results are shown in Figures 71 and 72. In Figure 71 where complex **I** was allowed to react with toluene, the reactant ion at m/z 443 is mainly the most intense ¹⁹³Ir¹²C₁₂¹⁴N₂¹H₈³⁵Cl₂ isotopomer. Whereas, in Figure 72 where complex **I** was allowed to react with toluene-d₃, the reactant ion at m/z 441 is mainly the ¹⁹¹Ir¹²C₁₂¹⁴N₂¹H₈³⁵Cl₂ isotopomer.

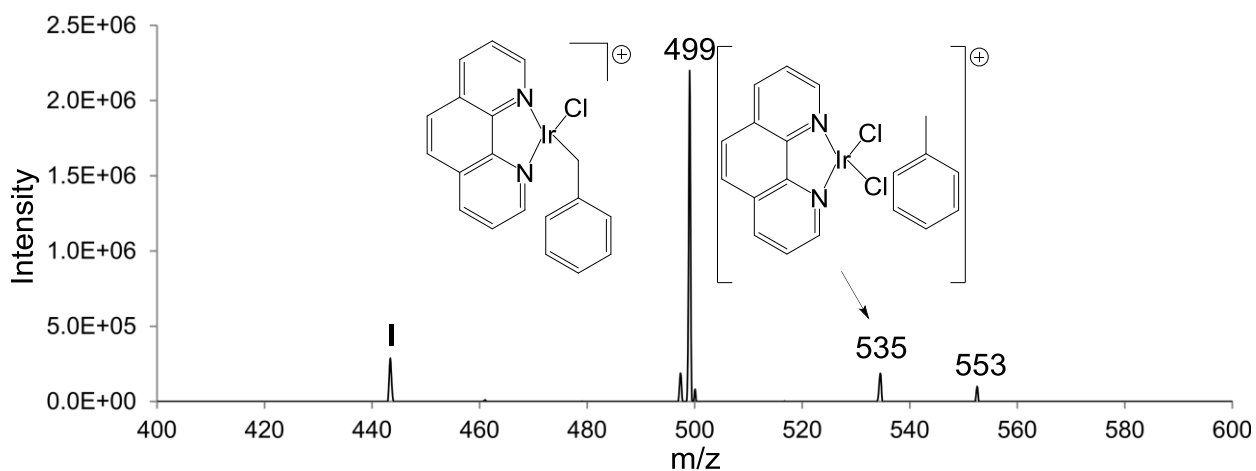


Figure 71. Mass spectrum of complex **I** reacting with toluene. The addition of toluene to complex **I** corresponds to m/z 535. While, the m/z at 553 is an addition of toluene and H_2O to complex **I**. The addition of toluene and loss of HCl can be seen at m/z 499.

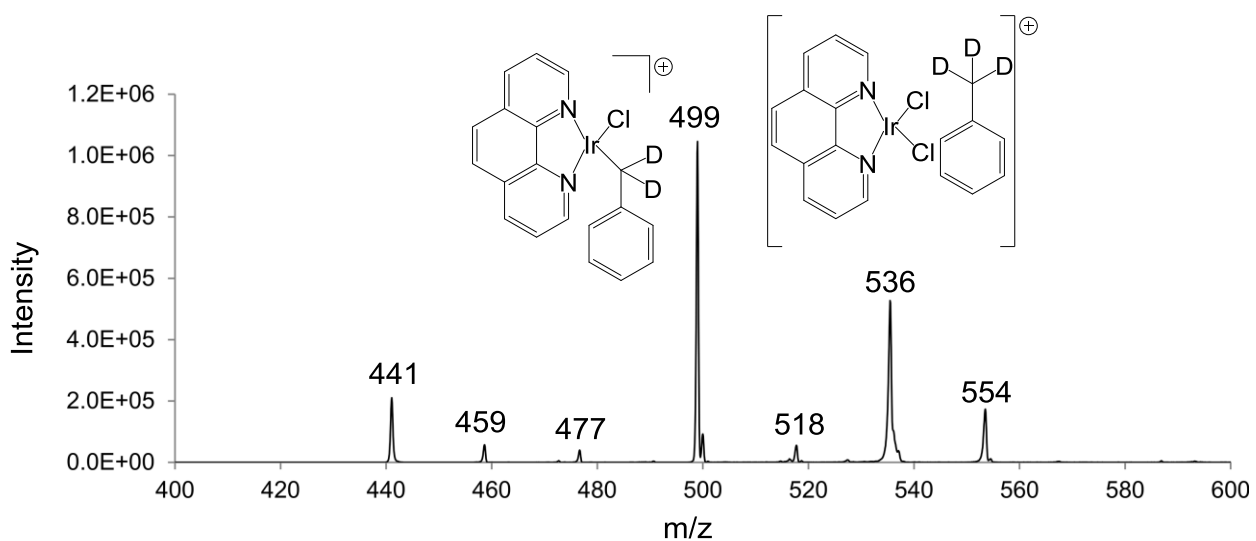


Figure 72. Mass spectrum of complex **I** reacting with toluene- d_3 . The addition of toluene- d_3 to complex **I** corresponds to m/z 536 while, m/z 554 is an additional addition of H_2O . The addition of toluene- d_3 and loss of DCI can be seen at m/z 499.

The preference for C-H activation at a benzylic group rather than on the benzene ring is in opposition to what has been reported in the condensed phase by Ito et al. with a similar cationic Ir (III) bis-oxazoline complex and by Bergman with Cp* ligated complexes.^{158,162} Ito saw C-H activation at the ortho and para positions of the benzene ring rather than at the benzylic carbon. To probe for isotope effects, the kinetics were also measured with toluene-d₈. The primary kinetic deuterium isotope, k_H/k_D , is approximately 2.5 when comparing the partial rate constants for the formation of C-H activation products and suggests that the product-determining step is linked to a hydrogen transfer process. It appears that deuteration prevents the initial addition product from progressing to C-H activation products (see below) and therefore favors adduct formation.

To examine the potential for secondary reactions of the C-H activation products, we introduced a mixture of toluene and toluene-d₈ into the ion trap and allowed **I** to react with it. The initial toluene C-H activation product (**II**) was isolated in the ion trap using its mass selectivity capabilities (*i.e.*, MSⁿ scanning) and then was allowed to react with the gas mixture. The reaction produces d₇-labeled **II**, indicating that **II** is also capable of C-H activation and can engage in a catalytic H/D exchange cycle (Scheme 46). The system reaches a pseudo-equilibrium and the ratio of m/z 499 to 506 reflects the isotope effect in the process. Cationic iridium (III) complexes that are C-H activators in the condensed phase have also been shown to be low temperature H/D exchange

catalysts as well.¹⁶³ The rate constant for the process is moderately low, 1.95×10^{-11} $\text{cm}^3 \text{ molecule}^{-1} \text{ sec}^{-1}$, which corresponds to an efficiency of 2.5 %. Mass spectra for this process are given in Figure 73, where complex I was allowed to react with a 1:1 mixture of toluene and toluene- d_8 . For this process the reactant ion at m/z 443 is mainly the most intense, $^{193}\text{Ir}^{12}\text{C}_{12}^{14}\text{N}_2^1\text{H}_8^{35}\text{Cl}_2$ isotopomer.

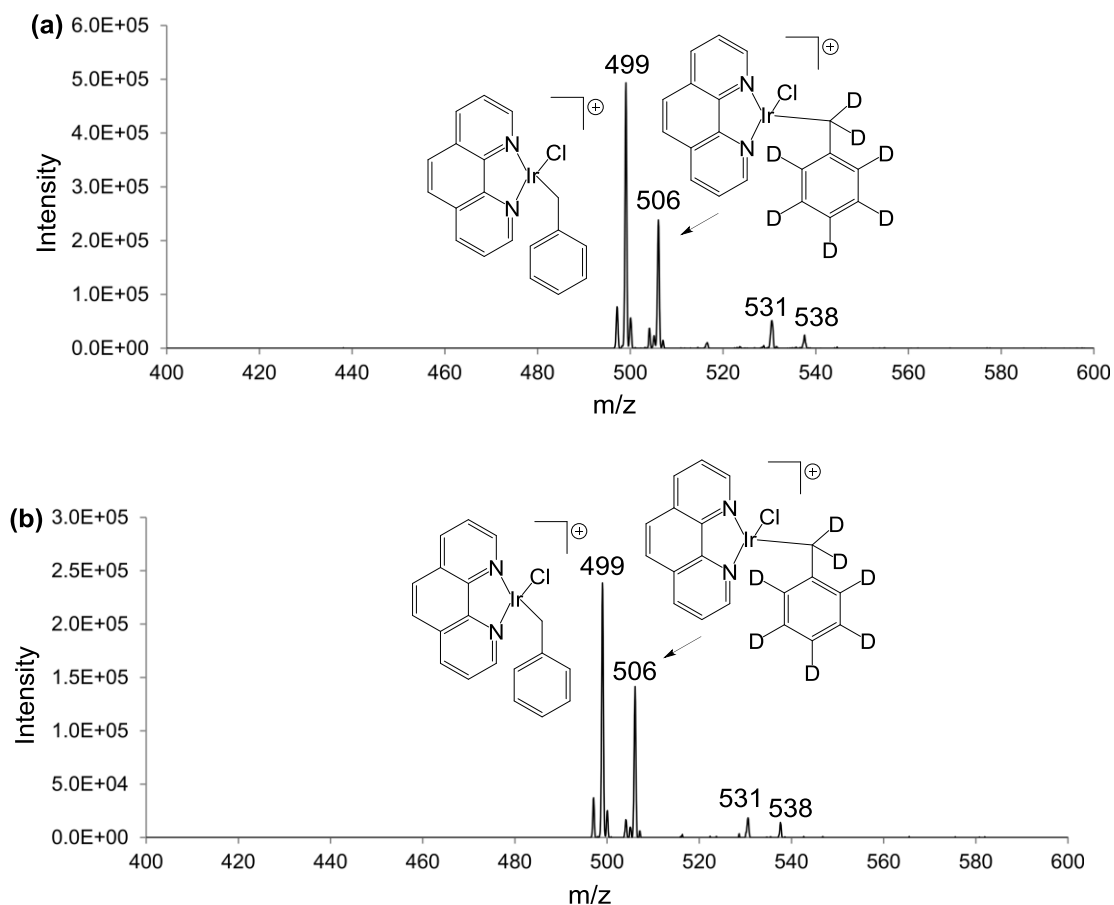
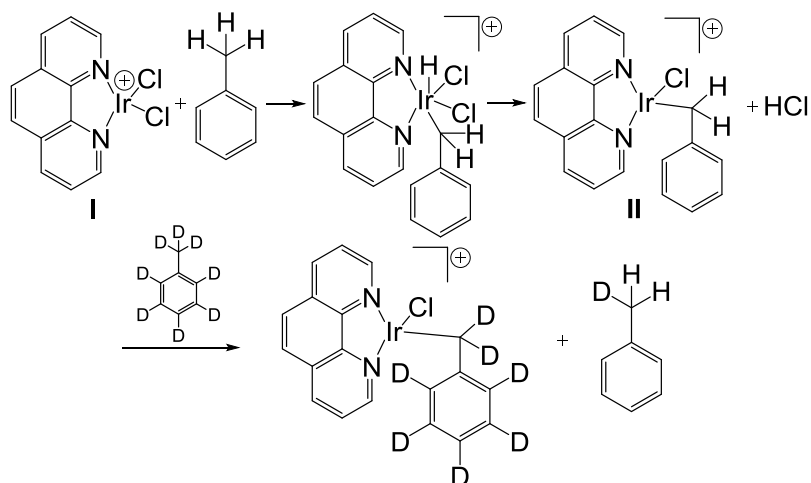


Figure 73. Mass spectra of complex I reacting with a 1:1 ratio of toluene:toluene- d_8 .

The ion at m/z 499 corresponds to **II**. The ion at m/z 506 corresponds **II-d₇**. The ions at m/z 531 and 538 are adducts of **II** and **II-d₇** with adventitious MeOH, respectively. In (a), m/z 499 is isolated and allowed to react with the gas mixture. In (b), m/z 506 is isolated and allowed to react with the gas mixture.

Scheme 46. H/D exchange process.



We next examined the impact of the substitution pattern on the C-H reactivity of benzylic systems. To do so, we allowed complex I to react with toluene, ethylbenzene, and isopropylbenzene. The rate constants are all near the collision-controlled limit, with ethylbenzene giving the highest rate constant. These rate constants can be seen in Table 1. In isopropylbenzene, the product mixture shifts to mainly adduct formation. It is likely that steric effects with the 3° center are inhibiting C-H activation. Mass spectra of complex I reacting with ethylbenzene and isopropylbenzene are given in Figures 74 and 75. In these reactions, the reactant ion at m/z 443 is mainly the most intense, $^{193}\text{Ir}^{12}\text{C}_{12}^{14}\text{N}_2^1\text{H}_8^{35}\text{Cl}_2$ isotopomer.

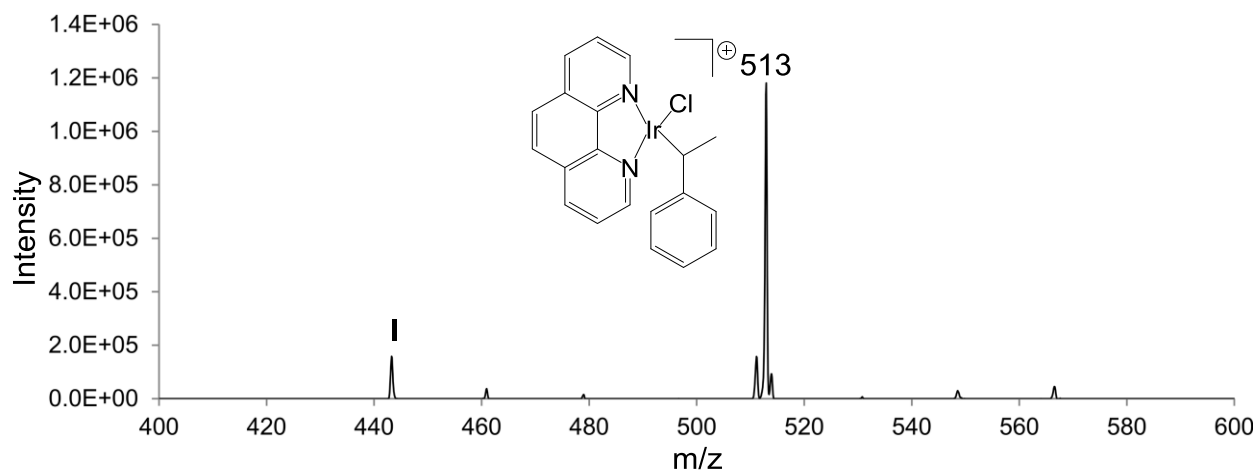


Figure 74. Mass spectrum of complex I reacting with ethylbenzene.

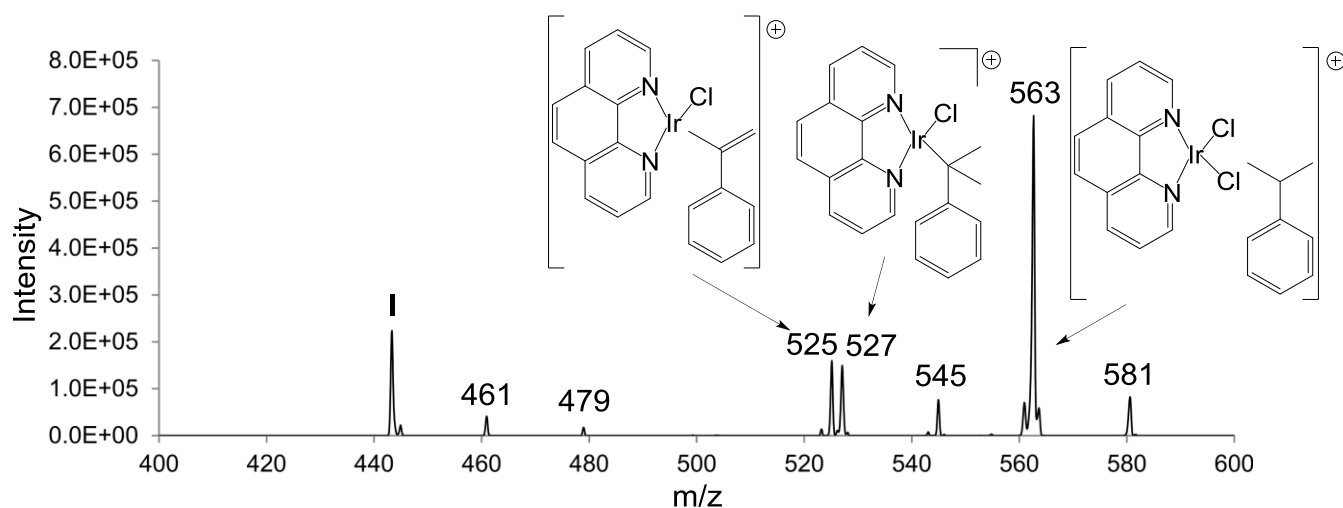


Figure 75. Mass spectrum of complex I reacting with cumene. An addition of H_2O and two H_2O to complex I, corresponds to m/z 461 and m/z 479 respectively. An addition of cumene to complex I with a loss of HCl corresponds to m/z 527 and m/z 545 corresponds to an addition of H_2O . While, m/z 525 is a loss of H_2 from this complex. The adduct of cumene to complex I can be seen at m/z 563 and m/z 581 is an addition of H_2O to this complex.

To insure that these species were only giving activation at the benzylic center, experiments were also completed with ethylbenzene-d₂. As expected, addition with exclusive loss of DCI is observed with this substrate. When *t*-butylbenzene is allowed to react with I, no C-H activation is observed (an adduct is formed), indicating that unactivated 1° centers are not suitable substrates. Mass spectra of the reactions of complex I with ethylbenzene-d₂ and *t*-butylbenzene can be seen in Figures 76 and 77. In these reactions, the reactant ion at m/z 443 is mainly the most intense ¹⁹³Ir¹²C₁₂¹⁴N₂¹H₈³⁵Cl₂ isotopomer.

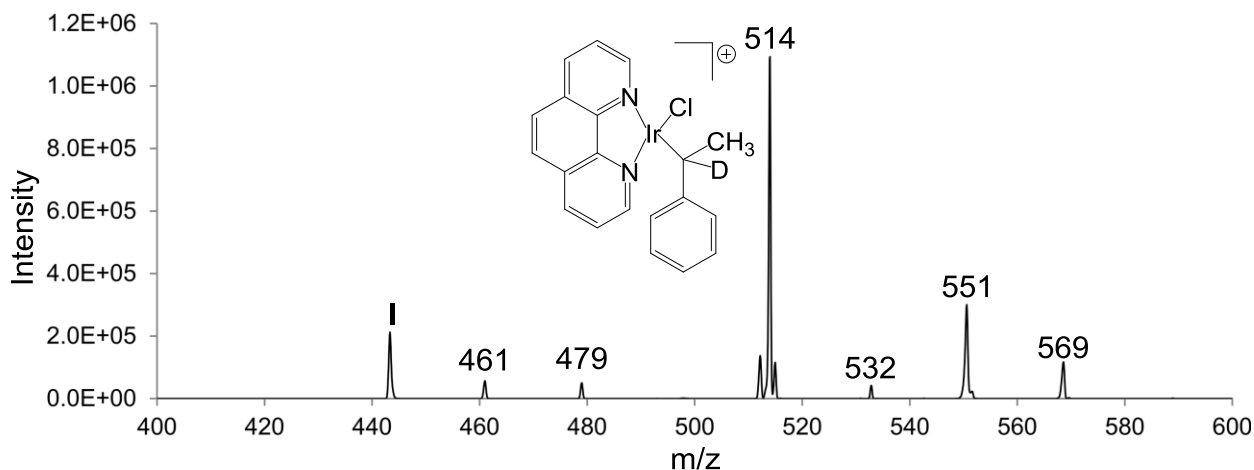


Figure 76. Mass spectrum of complex I reacting with ethylbenzene-d₂. An addition of H₂O and two H₂O to complex I, corresponds to m/z 461 and m/z 479 respectively. An addition of ethylbenzene-d₂ to complex I with a loss of HCl is seen at m/z 514, with m/z 532 being an addition of H₂O to this complex. While, m/z 551 corresponds to an addition of ethylbenzene-d₂ to complex I and m/z 569 an addition of H₂O to this complex.

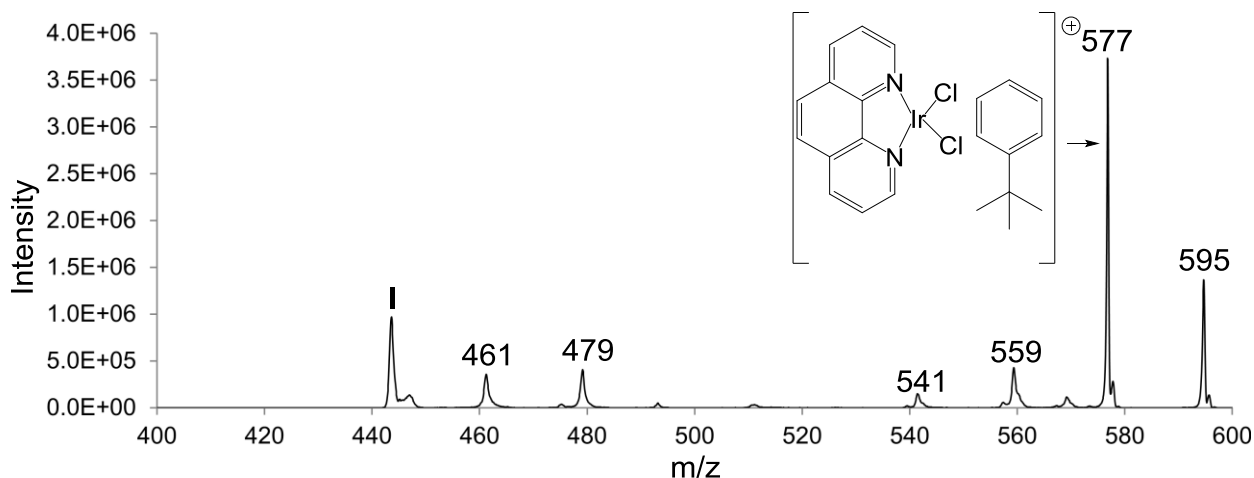


Figure 77. Mass spectrum of complex **I** reacting with t-butylbenzene. An addition of H₂O and two H₂O to complex **I**, corresponds to m/z 461 and m/z 479 respectively. An addition of t-butylbenzene to complex **I** with a loss of HCl corresponds to m/z 541, with m/z 559 being an addition of H₂O to this complex. An addition of t-butylbenzene to complex **I** is seen at m/z 577 and m/z 595 is an addition of H₂O to this complex.

To probe the effects of polar substituents on the C-H activation process, we allowed complex **I** to react with p-tolunitrile and 4-methylanisole. Ito et al. had reported that with bis-oxazoline ligated iridium (III) complexes, both electron-donating and electron-withdrawing groups increased the rate of C-H activation.¹⁵⁸ With **I**, these substituted toluenes lead to stable adducts and it appears that they preferentially use there substituents to act as ligands for the iridium.

To gain more insight into the C-H activation process, the reaction of **I** with a 2° hydrogen in propane was modeled in Gaussian09¹⁶⁴ using the M06 functional with an effective core potential (ECP) basis set on iridium (lanl2dz) and a 6-311+G** basis set

on the other atoms. This DFT work was completed by our group. The reported energies are from single-point calculations at the M06/QZVP level with thermal enthalpy corrections from the calculations with the mixed ECP/6-311+G** basis set. Complex I has a roughly square planar coordination geometry, but the chlorines are tilted in and out of the plane leading to a C₂-symmetric system with a C-N-Ir-Cl dihedral of 41° (Figure 78a). The initial reaction with propane leads to an unusually stable ion/molecule complex for a non-polar substrate (enthalpy of association = -14.8 kcal/mol). The complex (Figure 78b) is pseudo-octahedral at the iridium and is characterized by strong agostic interactions with a 2° (1.82 Å) and a 1° hydrogen (1.89 Å). The C-H bonds are stretched to 1.18 and 1.16 Å, respectively. We sought a pathway involving oxidative addition followed by reductive elimination of HCl. Although we were able to find a stable oxidative addition intermediate with the lan12dz basis set on all atoms, it was less stable than the transition state leading to it when zero-point energies were included. Using the larger, mixed basis set we identified what appears to be a concerted (or nearly so) pathway with a transition state that is located late in the HCl expulsion pathway (Figure 78c). Intrinsic reaction coordinate calculations link this transition state to the initial propane complex and an HCl complex of the reaction product. This transition state is 2.1 kcal/mol below the separated reactants. Given the level of theory employed it is not possible to rule out a 2-step mechanism with a distinct oxidative addition intermediate, but the calculations clearly suggest that surface is relatively flat in this region. The computed barrier suggests a moderately fast reaction with 2° centers and is consistent the experimental observations with cyclohexane. The HCl-expulsion product (Figure 78d) has an Ir-C bond (2.05 Å) as well as a strong agostic interaction with a methyl

hydrogen ($\text{Ir-H} = 1.82 \text{ \AA}$). This structure is on the threshold of being an iridium hydride complex with a propene ligand. The overall process is calculated to be favorable by 14.8 kcal/mol.

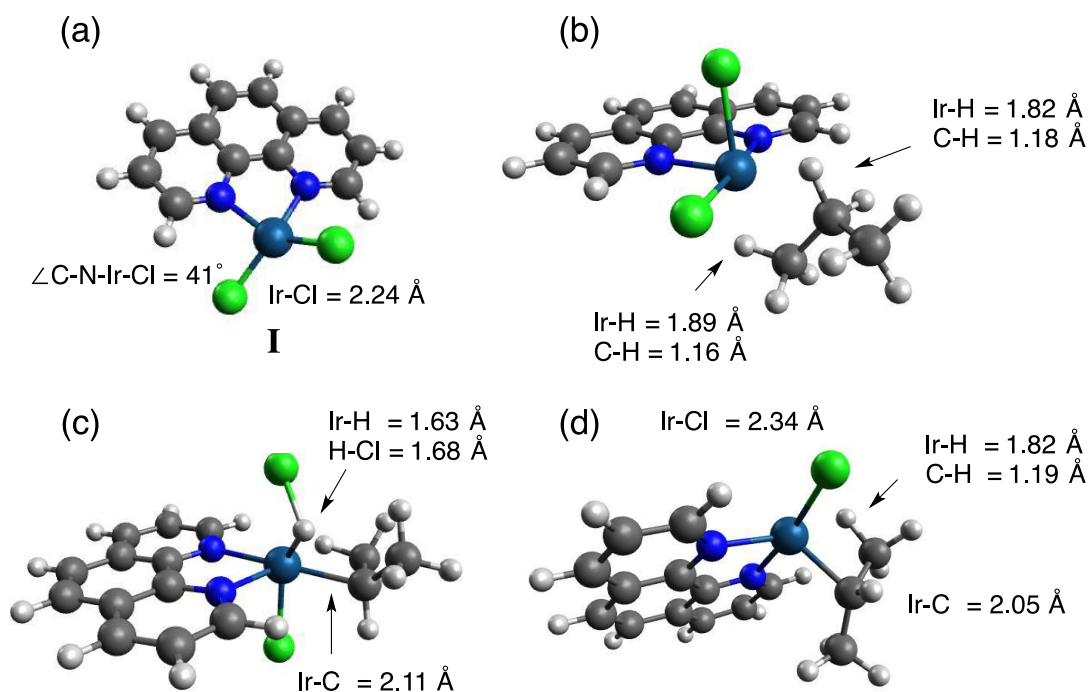


Figure 78. Geometries of key species in reaction of **I** with 2° hydrogen of propane. (a) **I**; (b) addition complex; (c) transition state; (d) product. Computations were completed in our group with M06 functional and a mixed lanl2dz/6-311+G** basis set.

A similar pathway was computed for the reaction with toluene. The C-H activation barrier is over 11 kcal/mol below the entrance channel (the TS was linked to reactants/products by an IRC calculation). Using differences in computed enthalpy corrections (including zero-point energies), the calculations suggest a kinetic deuterium isotope effect of 4.0 at room temperature. Given the level of theory and possible dynamic effects related to the low barrier, this is an acceptable level of consistency with experiment. The initial complex is very stable (binding enthalpy of 26.9 kcal/mol) and this may explain the shift to adduct formation upon deuteration despite the low transition state energy. Computations also indicate that isopropylbenzene has a higher barrier than toluene in its reaction with **I** and the transition state structure exhibits crowding between a chloride and methyl group.

6.4.3– Alcohol Series

After observing complex **I**'s high reactivity toward C-H activation in alkanes, we were interested in probing its effectiveness towards activating alcohols. Upon allowing this complex to react with various alcohols, we observed primarily adduct formation with the smaller alcohols and C-H activation on the larger alcohols. The alcohols that were probed for reactivity with complex **I** are shown in Figure 79.

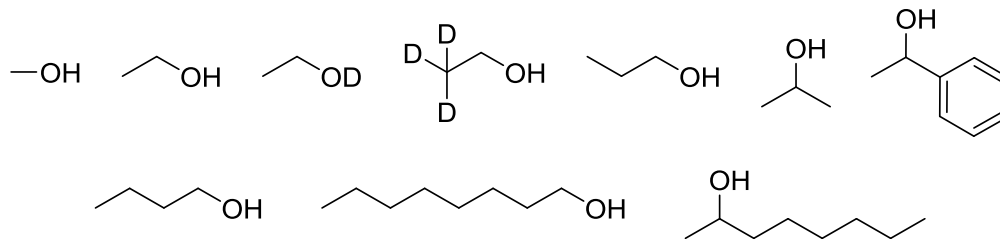


Figure 79. Alcohols that were allowed to react with complex I.

We began this series by studying the complex I's ability to activate methanol towards C-H activation, however rather than forming C-H activation products we only observed adduct formations. This is most likely due to the electron rich oxygen atom preferentially binding to the iridium and acting as a ligand. This then quenches any C-H activation by orienting the hydrogens on the α carbon so that iridium is unable to activate them. Similar results were observed with substituted toluene compounds, where the electron rich substituents coordinated with the iridium and oriented the hydrogens so that they are unable to be activated. An example of complex I reacting with methanol is given in Figure 80, where the reactant ion is at m/z 443 and is mainly the most intense $^{193}\text{Ir}^{12}\text{C}_{12}^{14}\text{N}_2^1\text{H}_8^{35}\text{Cl}_2$ isotopomer.

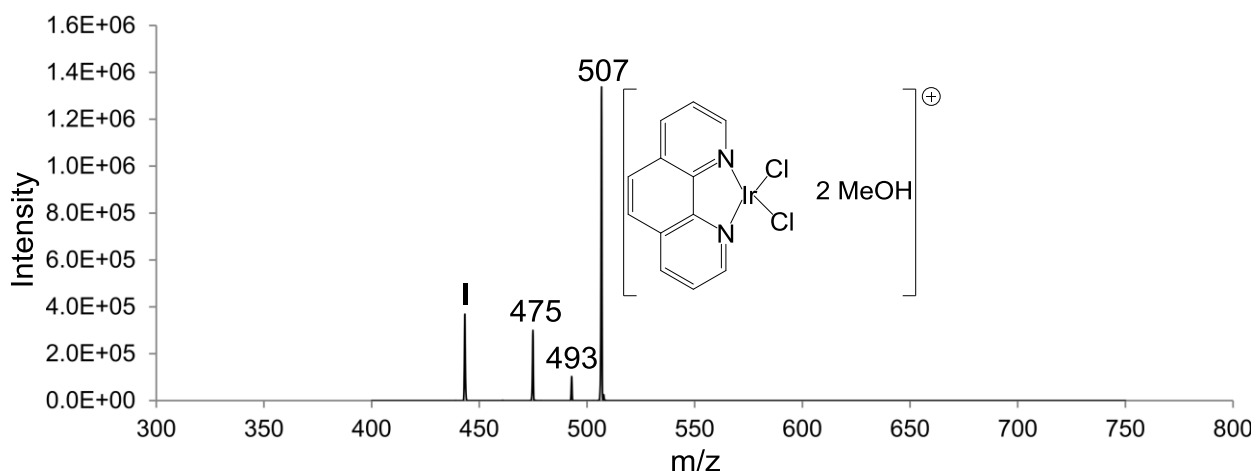


Figure 80. Mass spectrum of complex I reacting with methanol. An addition of methanol to complex I is seen at m/z 475, with m/z 493 being an addition of H₂O to this complex. An addition of two methanol compounds to complex I can be seen at m/z 507.

Moving forward we began probing alcohols with increasingly longer alkyl chains. When allowing ethanol to react with complex I, we observed adduct formation and small amounts of C-H activation. We also observed a mass loss of two, that indicates dehydrogenation of the alcohol. To determine where this dehydrogenation was occurring, we probed deuterated ethanol compounds, ethanol-d and ethanol-d₃. This study revealed that the hydrogens that were being removed were located on the oxygen and at the α carbon. This dehydrogenation of ethanol therefore provides aldehyde products. For this process to proceed, the oxygen is most likely coordinating with the iridium allowing an oxidative addition to occur. This forms an iridium hydride that is then able to pull off a hydrogen on the α carbon, oxidizing the molecule and producing an aldehyde (Scheme 47). Spectra related to this C-H activation and dehydrogenation of

ethanol by complex **I** are given in Figure 81, 82 and 83, where the reactant ion is at m/z 443 and is mainly the most intense $^{193}\text{Ir}^{12}\text{C}_{12}^{14}\text{N}_2^1\text{H}_8^{35}\text{Cl}_2$ isotopomer.

Scheme 47. Proposed dehydrogenation mechanism for complex **I** reacting with alcohols.

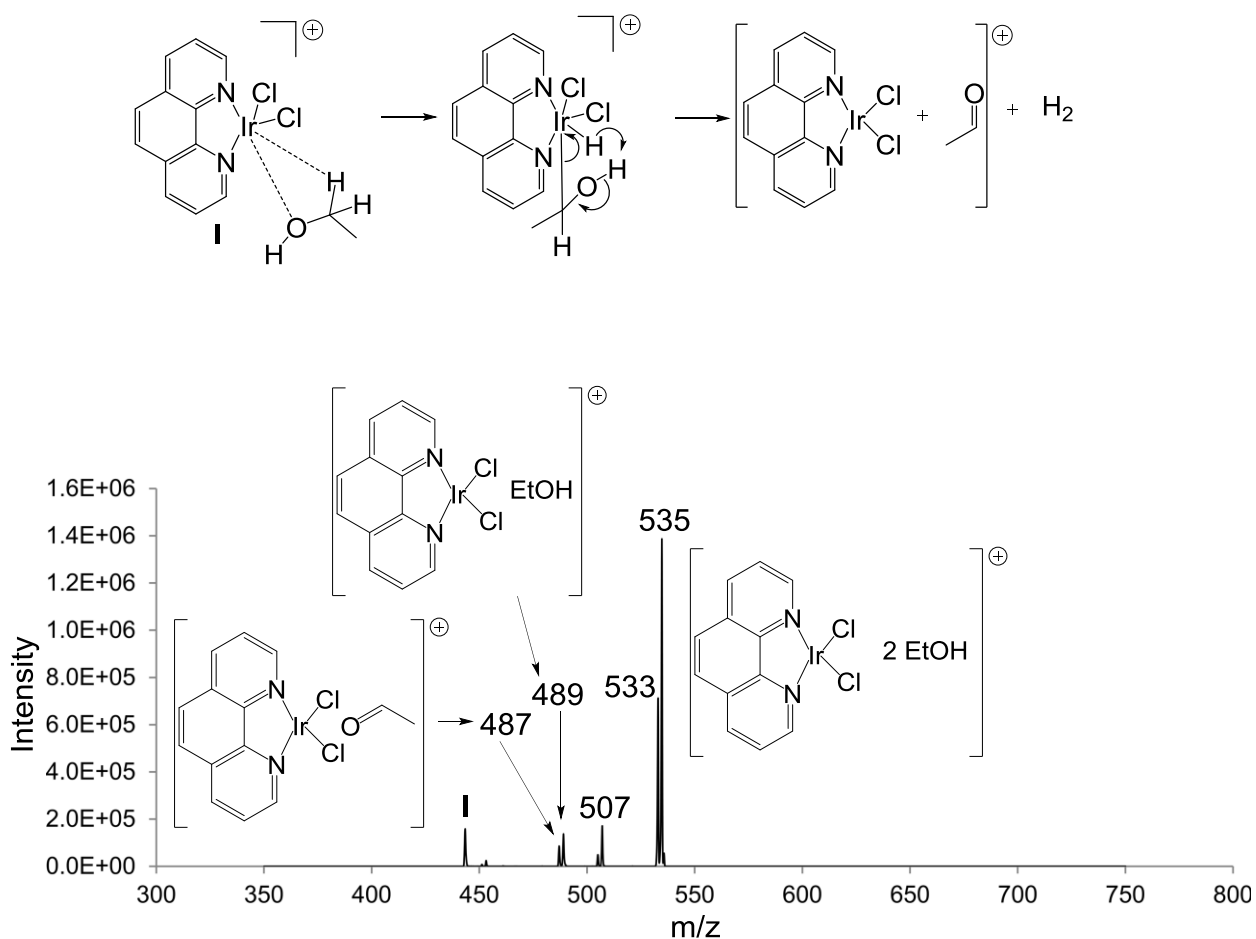


Figure 81. Mass spectrum of complex **I** reacting with ethanol. An addition of ethanol to complex **I** m/z 489, with m/z 507 being an addition of H_2O to this complex and m/z 535 corresponding to an addition of two ethanol molecules to complex **I**. Dehydrogenation products can be seen at m/z 487 and m/z 533.

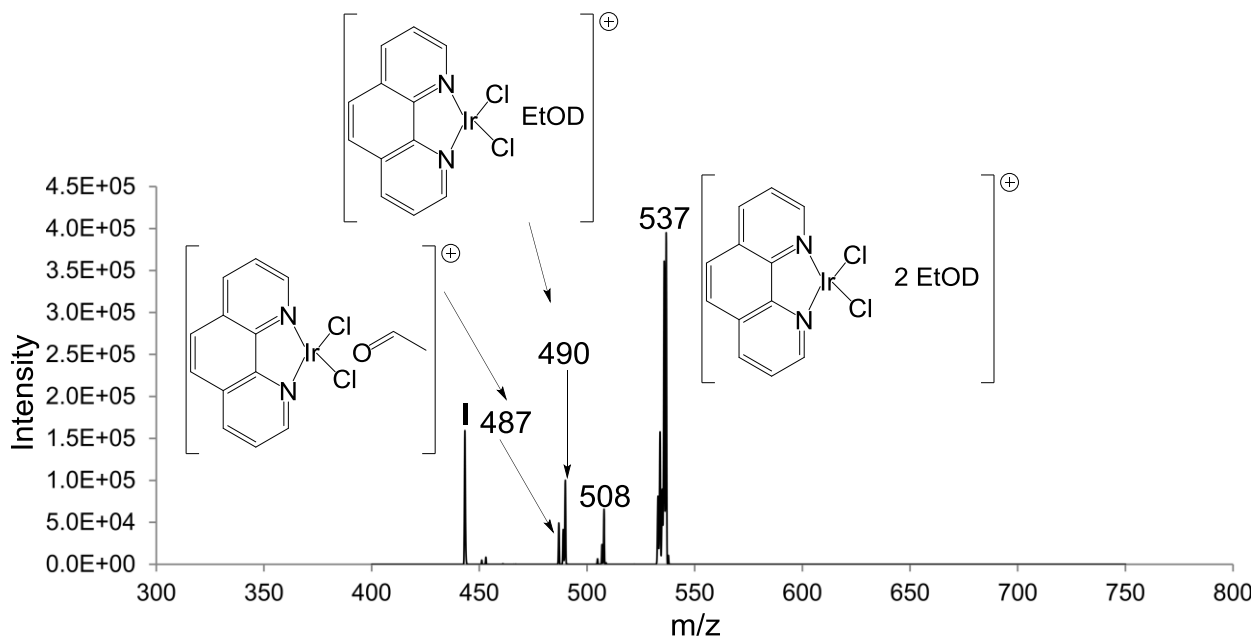


Figure 82. Mass spectrum of complex **I** reacting with ethanol-d. An addition of ethanol-d to complex **I** is seen at m/z 490, with m/z 508 being an addition of H₂O to this complex. While, m/z 537 corresponds to an addition of two ethanol-d molecules to complex **I**. A dehydrogenation product can be seen at m/z 487.

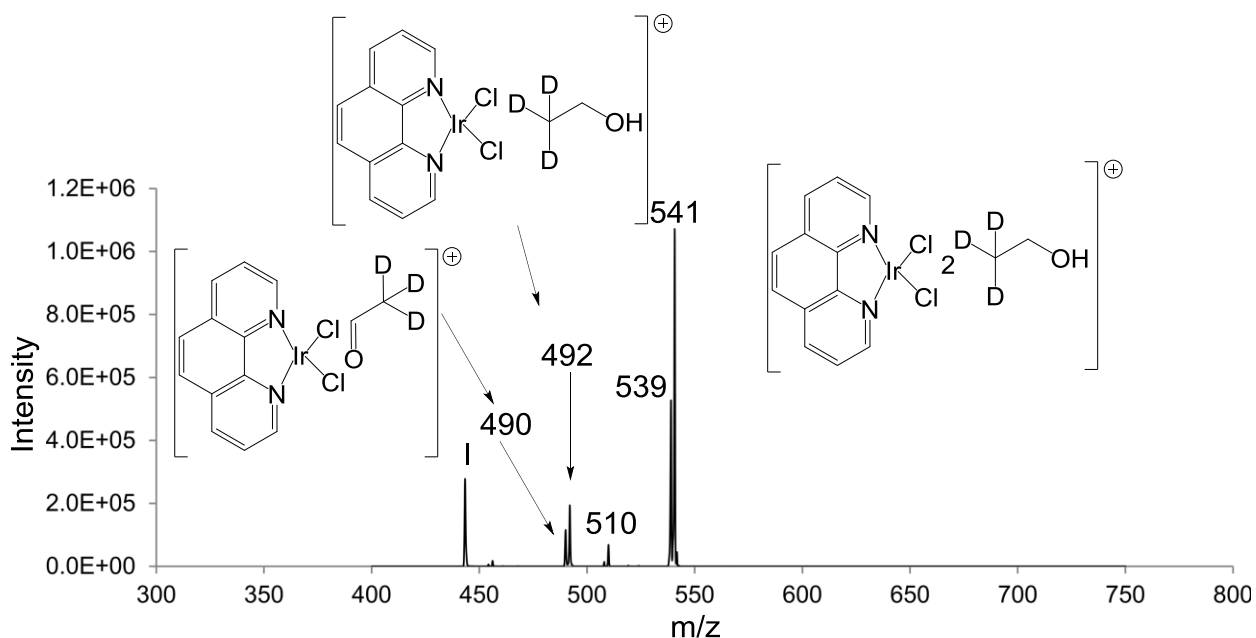


Figure 83. Mass spectrum of complex **I** reacting with ethanol- d_3 . An addition of ethanol- d_3 to complex **I** is seen at m/z 492, with m/z 510 being an addition of H_2O to this complex. An addition of two ethanol- d_3 molecules to complex **I** can be seen at m/z 541. Dehydrogenation product can be seen at m/z 490 and m/z 539.

We then probed isopropanol as a substrate. When isopropanol was allowed to react with complex **I**, we saw even greater amounts of dehydrogenation occurring, in this instance producing a ketone (Scheme 48). The increased rate of the dehydrogenation process indicates that the when isopropanol is coordinating with the iridium its additional methyl group orients the molecule more favorably for dehydrogenation. Spectra for complex **I** reacting with isopropanol are given in Figure 84. In this example the reactant ion is at m/z 443 and is mainly the most intense $^{193}\text{Ir}^{12}\text{C}_{12}^{14}\text{N}_2^1\text{H}_8^{35}\text{Cl}_2$ isotopomer.

Scheme 48. Dehydrogenation of isopropanol.

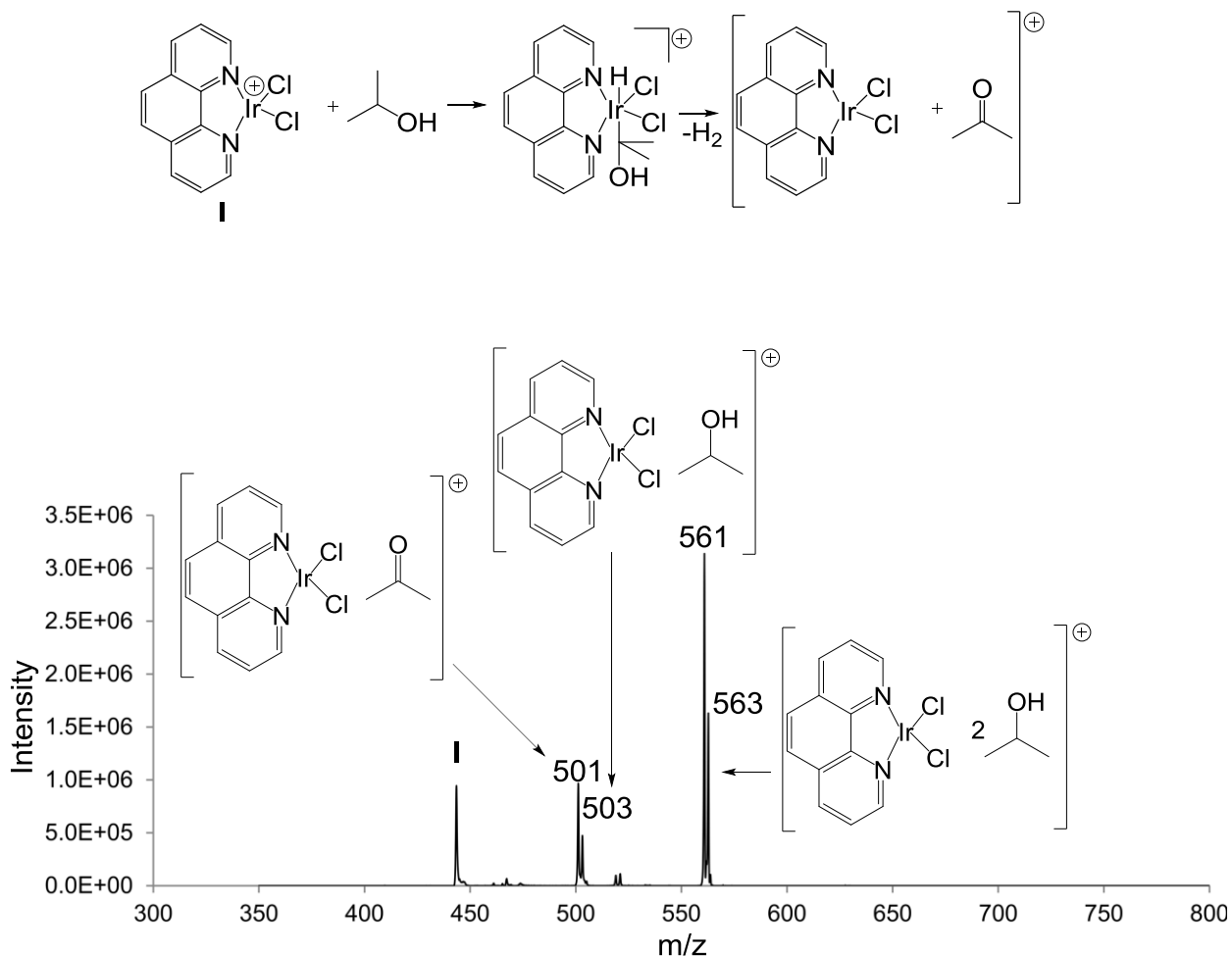


Figure 84. Mass spectrum of complex I reacting with isopropanol. An addition of isopropanol to complex I is seen at m/z 503. While, an addition of two isopropanol compounds to complex I can be seen at m/z 563. Dehydrogenation products can be seen at m/z 501 and m/z 561.

To try to understand this dehydrogenation further, we next probed 1-phenylethanol.

We anticipated that this would undergo a similar dehydrogenation as isopropanol due to

its similarity in structure. However, upon allowing it to react with complex **I** we observed large amounts of HCl loss with little to no dehydrogenation. This indicates that either the bulk of the phenyl group or coordination with the oxygen directs the C-H activation and allows it to proceed more rapidly than the dehydrogenation process. Most likely, the phenyl ring is involved in lowering the reaction barrier enough for C-H activation.

Spectra of this reaction are shown in Figure 85, where complex **I** was allowed to react 1-phenylethanol. The reactant ion for this reaction is at m/z 443 and is mainly the most intense $^{193}\text{Ir}^{12}\text{C}_{12}^{14}\text{N}_2^1\text{H}_8^{35}\text{Cl}_2$ isotopomer.

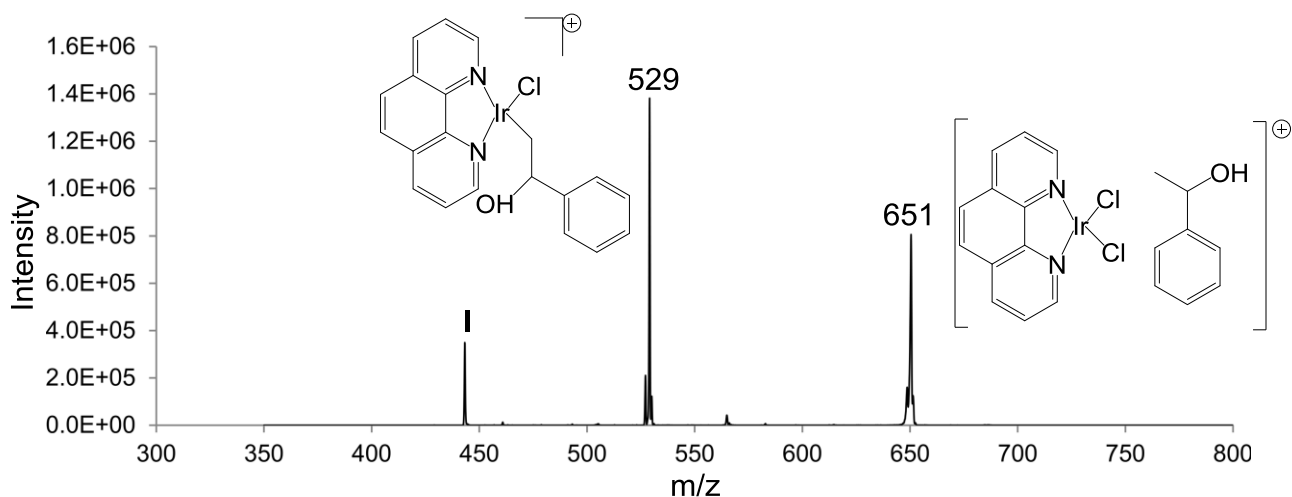


Figure 85. Mass spectrum of complex **I** reacting with 1-phenylethanol. An addition of 1-phenylethanol to complex **I** with a loss of HCl can be seen at m/z 529. While, m/z 651 is an addition of two 1-phenylethanol compounds to complex **I**.

To address the problems of the steric hindrance directing C-H activation rather than dehydrogenation, we probed 1-propanol for dehydrogenation. Upon allowing it to react

with complex **I**, we observed little to no dehydrogenation, but rather HCl loss and adduct formation. This indicates that extension to a γ carbon must be affecting the C-H activation process. Spectra for complex **I** reacting with 1-propanol are given in Figure 86. For this reaction, the reactant ion is at m/z 443 and is mainly the most intense $^{193}\text{Ir}^{12}\text{C}_{12}^{14}\text{N}_2^1\text{H}_8^{35}\text{Cl}_2$ isotopomer.

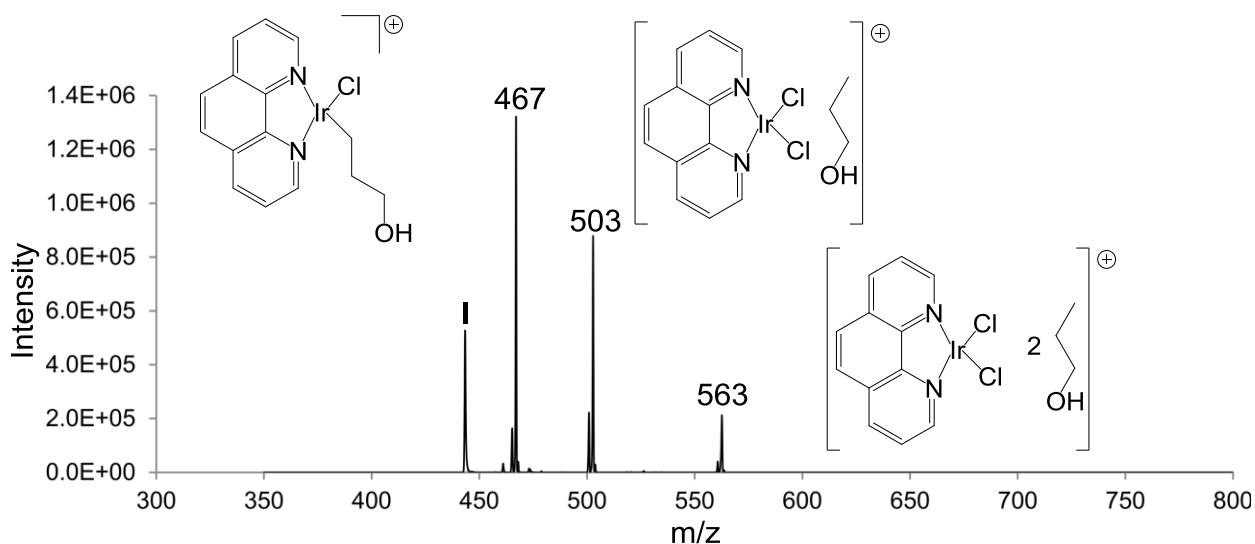


Figure 86. Mass spectrum of complex **I** reacting with 1-propanol. An addition of 1-propanol to complex **I** with a loss of HCl can be seen at m/z 467. While adduct formations with complex **I** and 1-propanol are seen at m/z 503 and m/z 563. Shown with modification at the γ carbon, but could also be at the β carbon.

Moving forward, we probed 1-butanol, 1-octanol and 2-octanol for C-H activation by complex **I**. For these alcohols, we observed primarily C-H activation and adduct formation. Little to no dehydrogenation was observed due to the presence of a γ carbon creating steric hindrance, similar to what was seen in 1-propanol. It appears that this

complex prefers a 6-membered transition state involving an agostic interaction with the hydrogen where the C-H activation will occur. Once the iridium inserts itself into the C-H bond, it slides to a 5-membered transition state. Therefore complex **I** is only effective at dehydrogenating small alcohols that do not have a γ carbon present to direct C-H activation. These compounds followed the general trend of the alcohols, reacting at a high rate with complex **I**. The rates of these reactions were outside of our kinetic window due to the inability to dilute the reagents with an inert solvent. This prevented us from recording kinetics for the C-H activation process. Spectra for these reactions are given in Figures 87, 88 and 89. The reactant ion for these reactions is at m/z 443 and is mainly the most intense $^{193}\text{Ir}^{12}\text{C}_{12}^{14}\text{N}_2^1\text{H}_8^{35}\text{Cl}_2$ isotopomer.

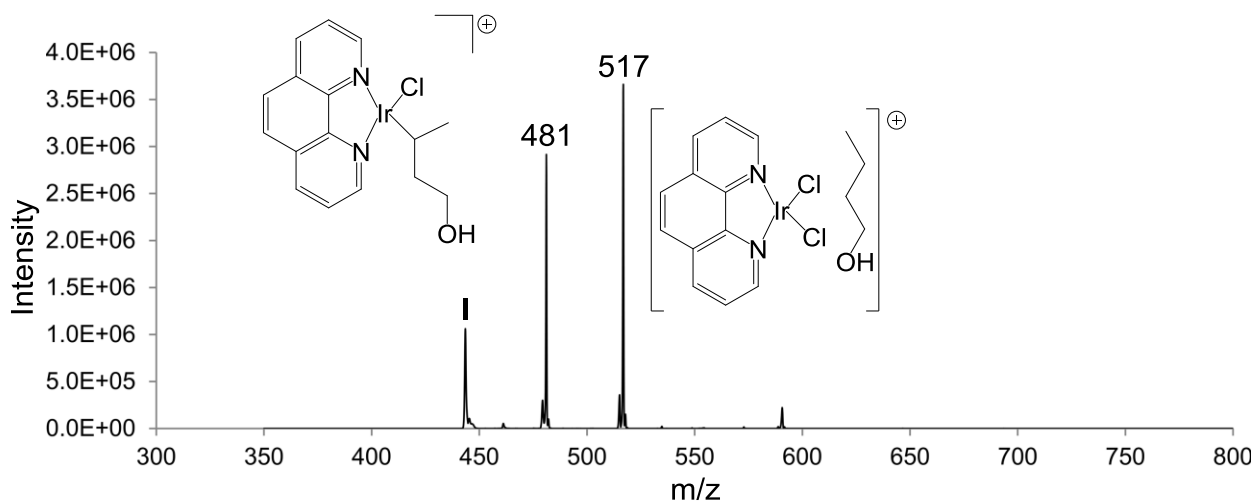


Figure 87. Mass spectrum of complex **I** reacting with 1-butanol. The addition of 1-butanol with a loss of HCl is observed at m/z 481. While, an adduct of complex **I** with 1-butanol is seen at m/z 517. Shown with modification at the γ carbon, but could also be at the β carbon.

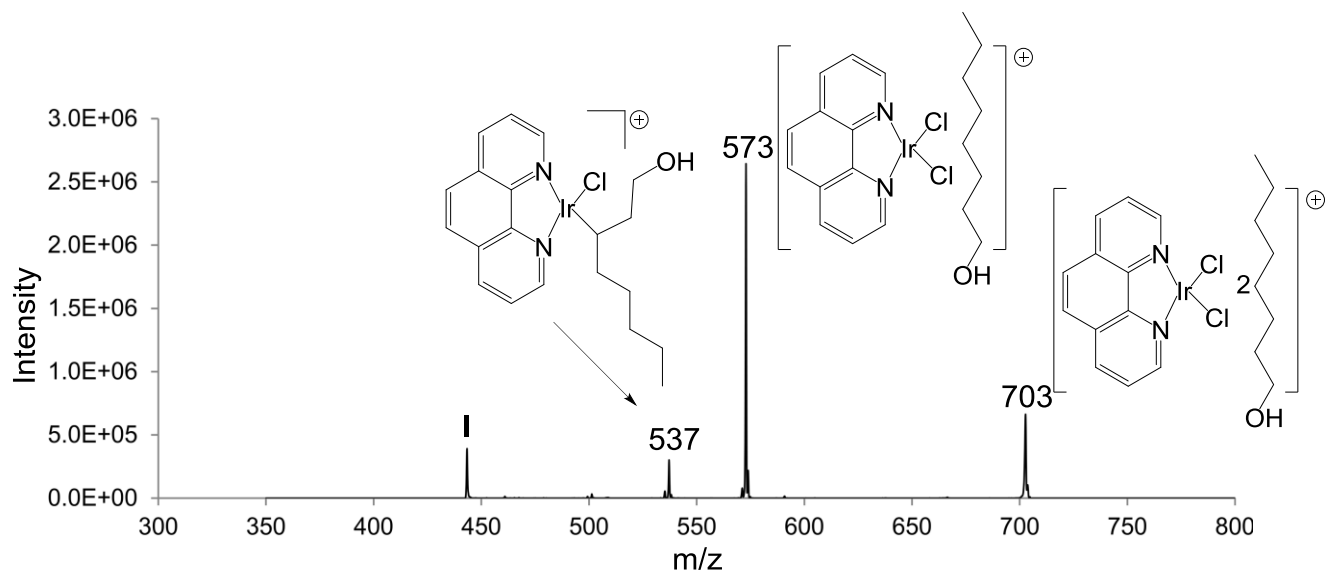


Figure 88. Mass spectrum of complex **I** reacting with 1-octanol. An addition of 1-octanol to complex **I** with a loss of HCl can be observed at m/z 537. While, adduct formations of complex **I** with 1-octanol can be seen at m/z 573 and m/z 703. Shown with modification at the γ carbon, but could also be at the β carbon.

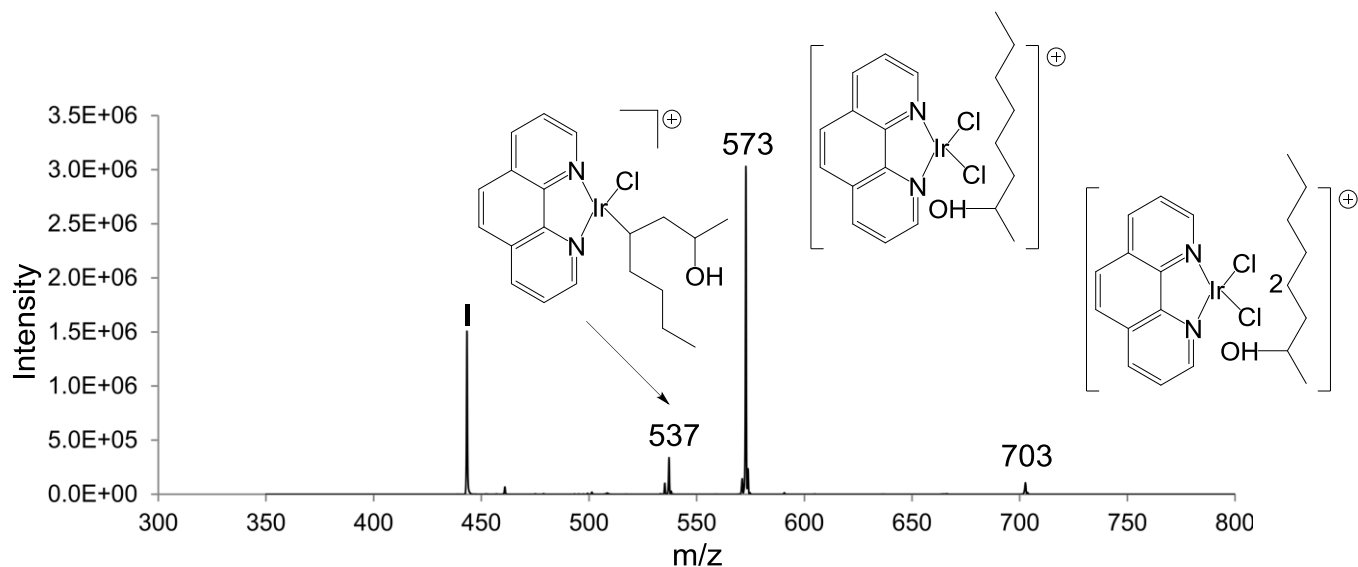


Figure 89. Mass spectrum of complex **I** reacting with 2-octanol. An addition of 2-octanol to complex **I** with a loss of HCl can be observed at m/z 537. While, adduct formations of complex **I** with 2-octanol can be seen at m/z 573 and m/z 703. Shown with modification at the γ carbon, but could also be at the β carbon.

6.4.4– Amine Series

To further explore the reactivity of complex **I**, we next probed a series of amines. The interest in amines was sparked by the unique reactivity of alcohols and how some can easily be dehydrogenated when allowed to react with complex **I**. To compare the reactivity of amines versus alcohols we chose a series of amines that were

representative of the different structures of alcohols that were studied. These amines are shown in Figure 90.

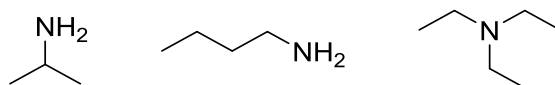


Figure 90. Amines that were allowed to react with complex I.

We began this series by probing complex I's reactivity with 1-butylamine. When allowed to react we observed primarily C-H activation of the compound. This reactivity is similar to what was observed in 1-butanol. We had thought that the reactivity of amines may be different than alcohols with more dehydrogenation occurring due to the additional hydrogen available on the nitrogen when compared to alcohols. However, this similarity between the alcohols and the amines indicates that the additional hydrogen seems to have little effect and that the controlling factor in dehydrogenation is the steric hindrance of the γ carbon. Therefore, 1-butylamine reacted similarly to 1-butanol, forming an initial complexation with the nitrogen followed by C-H activation at the γ -carbon (Scheme 49). This is most likely due to coordination of the nitrogen with iridium, directing C-H activation at this site. Results from this experiment are presented in Figure 91, where complex I was allowed to react with 1-butylamine. The reactant ion for this reaction is at m/z 443 and is mainly the most intense $^{193}\text{Ir}^{12}\text{C}_{12}^{14}\text{N}_2^1\text{H}_8^{35}\text{Cl}_2$ isotopomer.

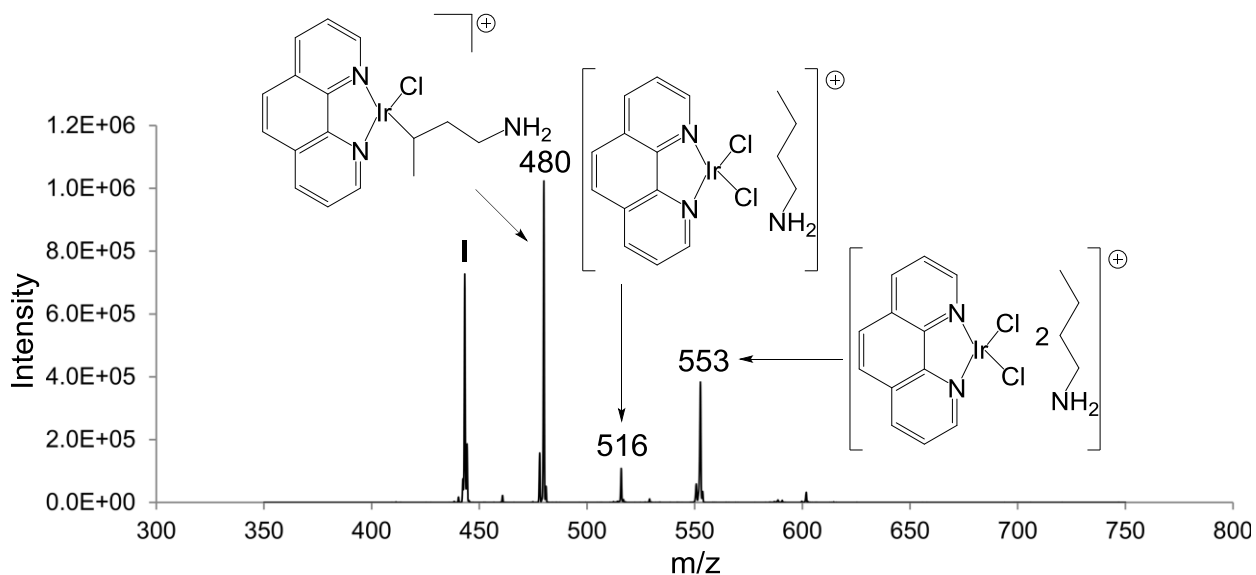
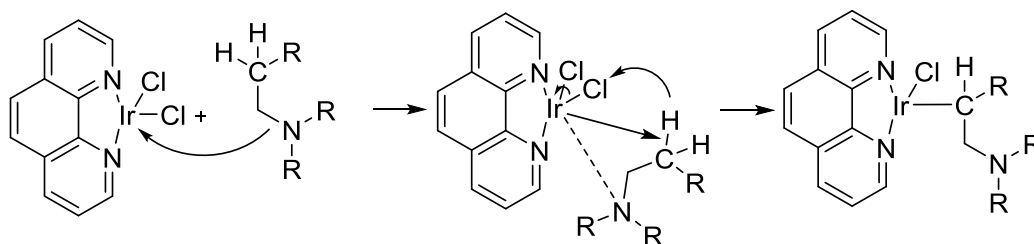


Figure 91. Mass spectrum of complex **I** reacting with 1-butylamine. An addition of 1-butylamine to complex **I** with a loss of HCl is observed at m/z 480. While, an adduct of complex **I** with 1-butylamine is seen at m/z 516 and an addition of a second 1-butylamine with a loss of HCl at m/z 553. Shown with modification at the γ carbon, but could also be at the β carbon.

Scheme 49. Proposed reaction mechanism of amines with complex **I**.



Moving forward, we next probed complex **I**'s reactivity with isopropylamine. For this reaction we were interested in discovering if isopropylamine reacted similarly to

isopropyl alcohol. Upon allowing complex **I** to react with this amine we observed primarily adduct formation. This is different than what is observed in isopropanol, suggesting that there is a change in the transition state when switching from an alcohol to an amine. The most probable explanation is that the nitrogen is coordinating to the iridium strong enough to prevent both dehydrogenation and C-H activation. This is not observed for the reaction of complex **I** with isopropanol due to weaker coordination of the oxygen with the iridium when compared to the complexation of nitrogen with iridium. The data from this reaction can be seen in Figure 92. The reactant ion for this reaction is at m/z 443 and is mainly the most intense $^{193}\text{Ir}^{12}\text{C}_{12}^{14}\text{N}_2^1\text{H}_8^{35}\text{Cl}_2$ isotopomer.

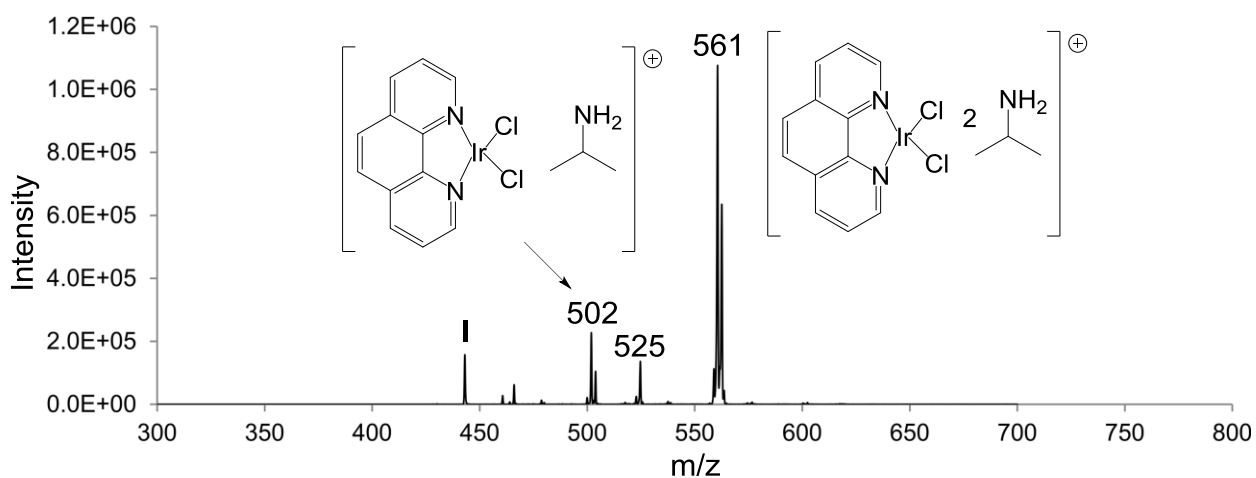


Figure 92. Mass spectrum of complex **I** reacting with isopropylamine. An addition of isopropylamine to complex **I** is seen at m/z 502. While, m/z 561 is an addition of two isopropylamine compounds to complex **I**, with m/z 525 corresponding to a loss of HCl.

We then probed triethylamine, a compound with no hydrogens on the nitrogen which, therefore cannot undergo dehydrogenation. We would expect to see primarily C-

H activation. Upon allowing complex I to react with this compound we did observe primarily C-H activation as predicted. This is similar to the reactivity that was seen in the alcohols, where there is an initial complexation with the nitrogen followed by C-H activation at the β -carbon (Scheme 49). The data from this reaction are shown in Figure 93. The reactant ion for this reaction is at m/z 443 and is mainly the most intense $^{193}\text{Ir}^{12}\text{C}_{12}^{14}\text{N}_2^1\text{H}_8^{35}\text{Cl}_2$ isotopomer. Since the most intense peak was selected and not the isotopically pure peak, there is a 50% chance that there will be a ^{37}Cl in the selected complex.

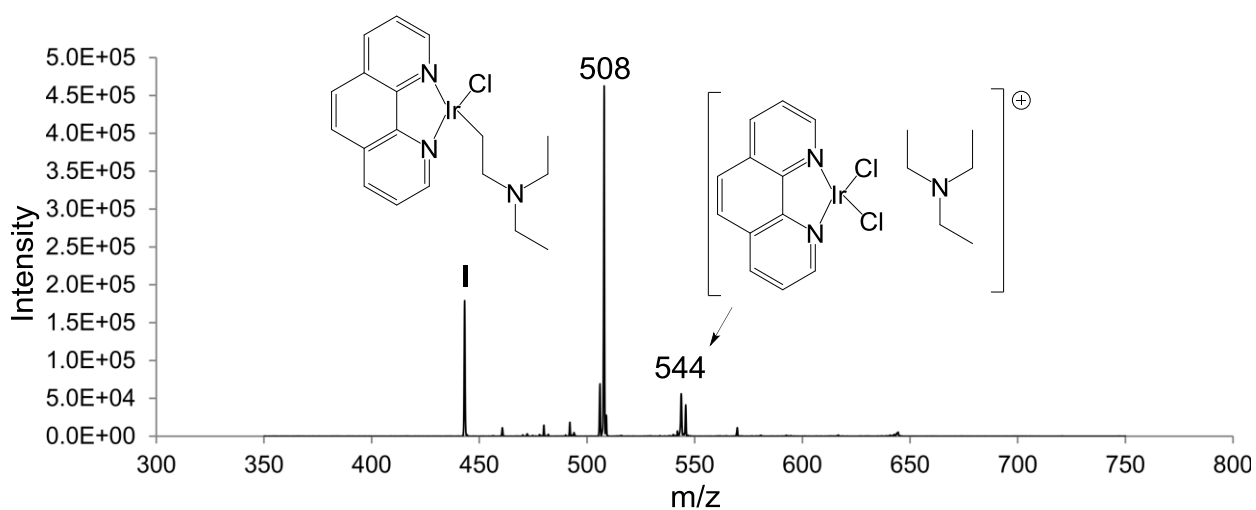


Figure 93. Mass spectrum of complex I reacting with triethylamine. An addition of triethylamine to complex I can be observed at m/z 544, with loss of HCl seen at m/z 508.

6.4.5– Ether Series

To further explore the C-H activation ability of complex I, we probed a set of ethers. The ethers that were probed are shown in Figure 94.

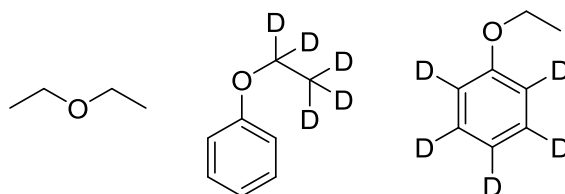


Figure 94. Ethers that were allowed to react with complex I.

To begin this series, we began with diethyl ether, a simple and symmetric ether. Upon allowing diethyl ether to react with complex I, we observed C-H activation along with adduct formation. This process has a high rate and is similar to the alcohols that were probed previously. When selecting the C-H activation product and applying CID, we observed an additional C-H activation reaction. This reactivity is most likely caused by the oxygen coordinating with the iridium and orienting the molecule so that iridium is in close enough proximity to a hydrogen so that another C-H activation can occur (Scheme 50). Spectra for these reactions are given in Figures 95 and 96, where the reactant ion is at m/z 443 and is mainly the most intense $^{193}\text{Ir}^{12}\text{C}_{12}^{14}\text{N}_2^1\text{H}_8^{35}\text{Cl}_2$ isotopomer.

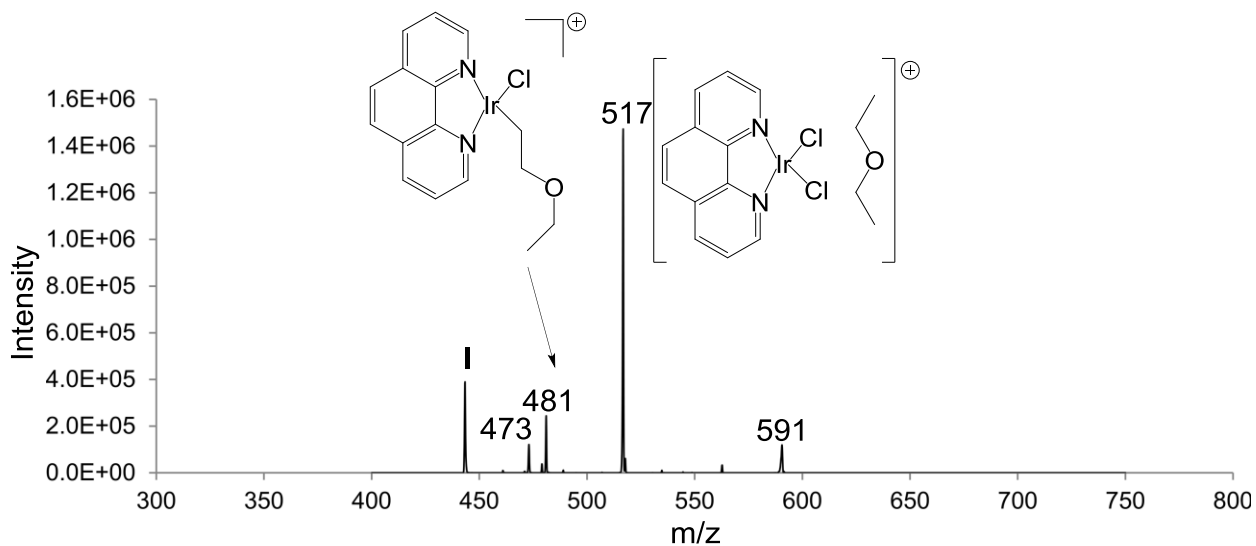


Figure 95. Mass spectrum of complex **I** reacting with diethyl ether. An addition of diethyl ether to complex **I** can be observed at m/z 517, with a loss of HCl present at m/z 481. While an addition of two diethyl ethers to complex **I** can be seen at m/z 591.

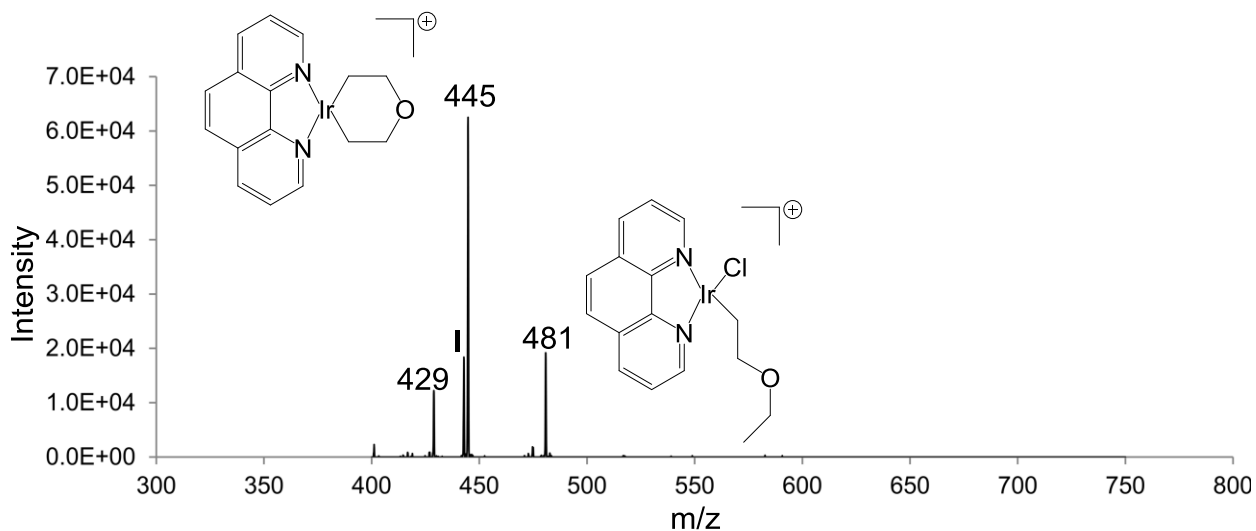
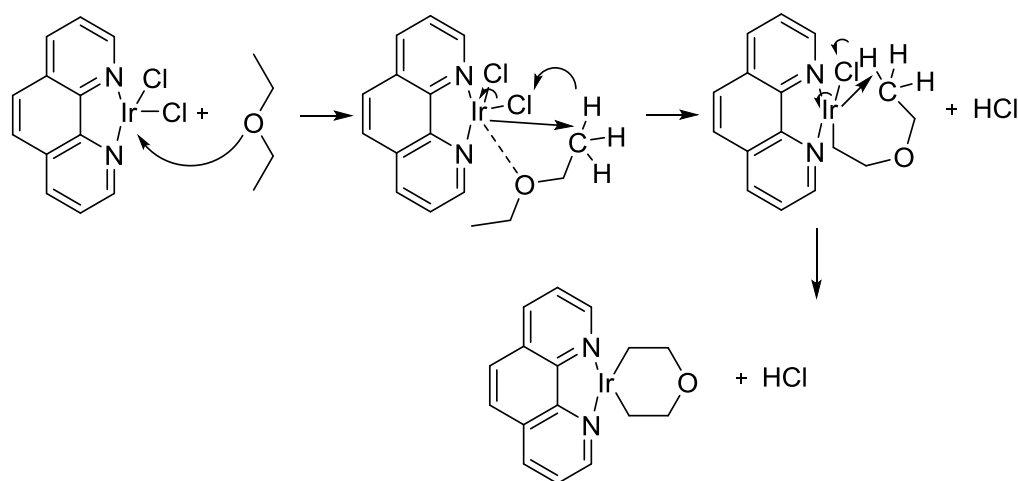


Figure 96. Mass spectrum of complex **I** reacting with diethyl ether. The adduct of complex **I** with diethyl ether and a loss of HCl is selected at m/z 481 and subjected to CID at 22%.

Scheme 50. Proposed mechanism for complex **I** reacting with ethers.



This reactivity was intriguing and unique to ethers. In previously studied compounds we saw no sequential C-H activation occur. Therefore, in an attempt to determine the location of the two C-H activations, we probed deuterated ethoxybenzene compounds. These are compounds that are not symmetric, meaning that they have different groups on either side of the oxygen which are deuterated on one side of the oxygen or the other. When allowed to react with complex I, we observed a C-H activation on the phenyl ring first with the second activation occurring on the ethoxy group, presumably forming a six-membered metallocycle that can be seen in Scheme 51. The activation of the phenyl ring is rather surprising due to the lack of activity that was observed on the sp_2 -hybridized carbons in toluene and related compounds. This activation of the phenyl ring is most likely due to the electron-donating effects of the ethoxy group. This therefore indicates that the selectivity of complex I for the activation of sp_2 carbons over sp_3 carbons can be altered through the electronic characteristics of the substituent groups on the carbons being activated. This effectively lowers the activation energy for the C-H activation process on the phenyl ring enough to allow it to occur. Results from this study are given in Figures 97, 98, 99, and 100, where the reactant ion is at m/z 443 and is mainly the most intense $^{193}\text{Ir}^{12}\text{C}_{12}^{14}\text{N}_2^1\text{H}_8^{35}\text{Cl}_2$ isotopomer.

Scheme 51. C-H activation of ethoxybenzene-d₅ by complex I.

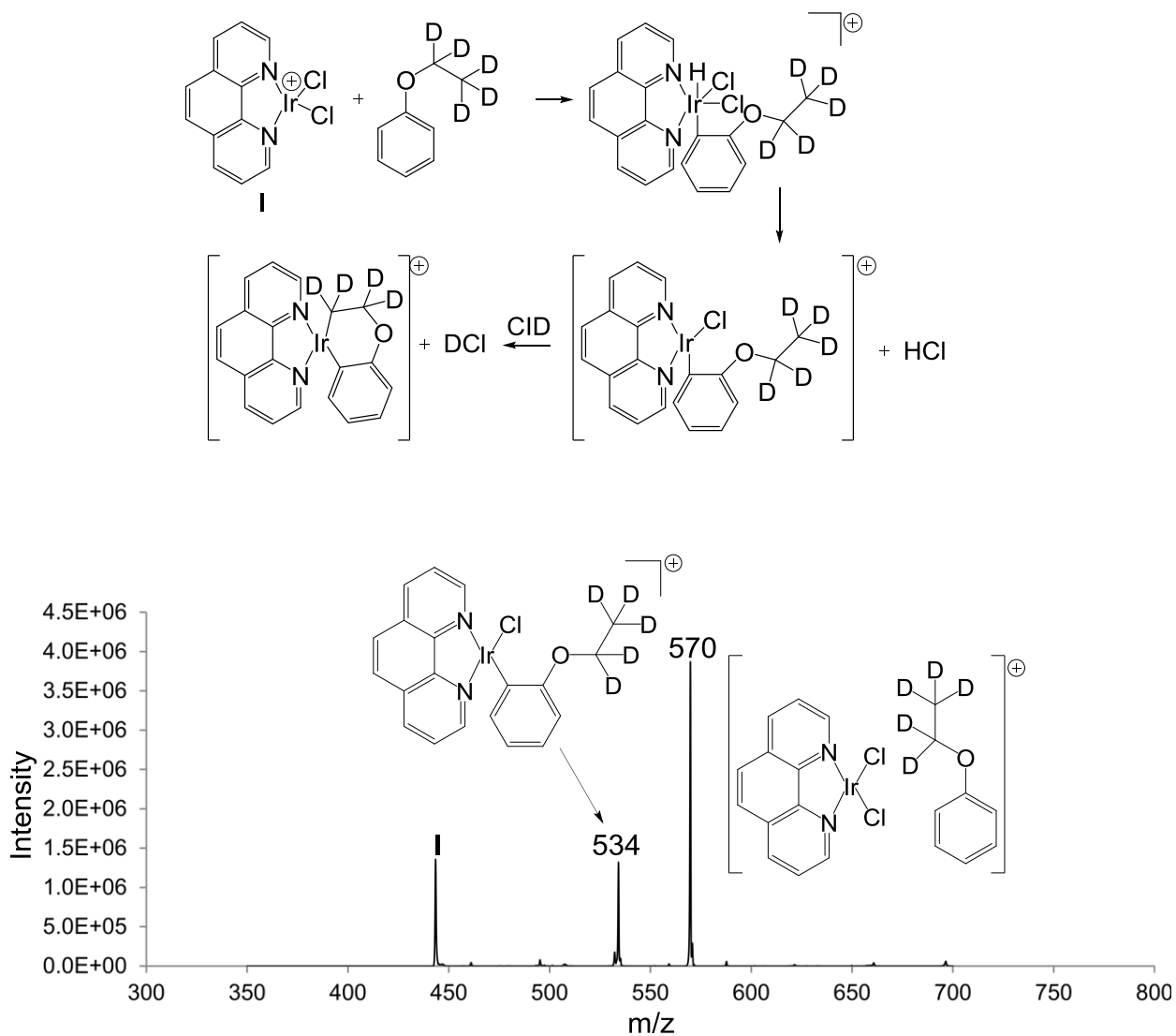


Figure 97. Mass spectrum of complex I reacting with ethoxybenzene-d₅ (deuterated on the ethoxy).

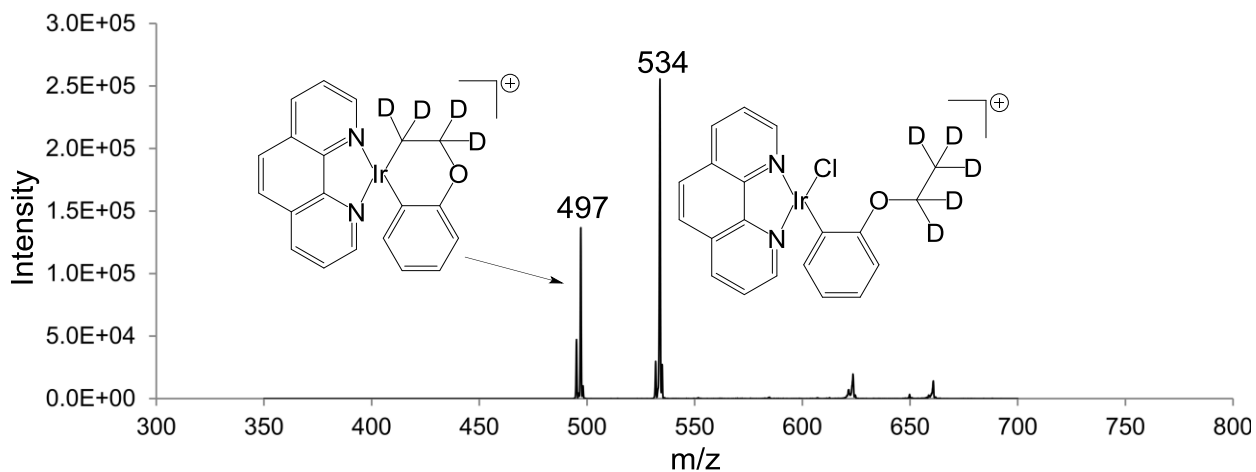


Figure 98. Mass spectrum of complex I reacting with ethoxybenzene-d5 (deuterated on the ethoxy). The adduct of complex I with ethoxybenzene-d5 (deuterated on the ethoxy) and a loss of HCl is selected at m/z 534 and subjected to CID at 15%.

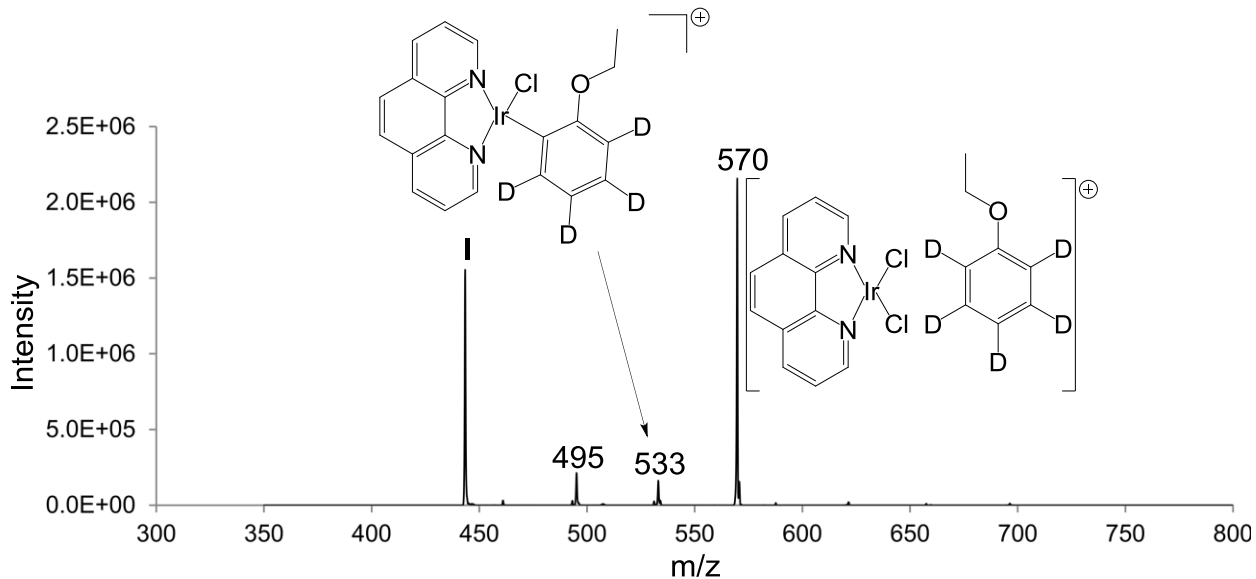


Figure 99. Mass spectrum of complex I reacting with ethoxybenzene-d5 with the phenol ring deuterated.

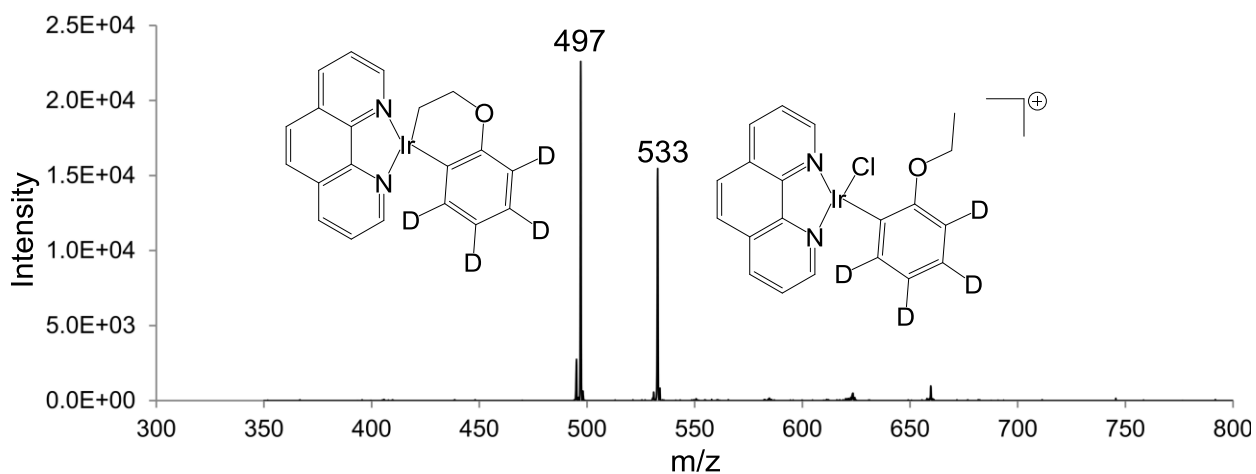


Figure 100. Mass spectrum of complex **I** reacting with ethoxybenzene- d_5 , with the phenol ring deuterated. The adduct of complex **I** with ethoxybenzene- d_5 (deuterated on the phenol ring) and a loss of DCI is selected at m/z 533 and subjected to CID at 15%.

6.4.6– Other Compounds

In an effort to survey a wider variety of compounds for C-H activation by complex **I**, we probed bromoalkanes, ketones, acetates and disulfide compounds. The compounds that were probed for this series are given in Figure 101.

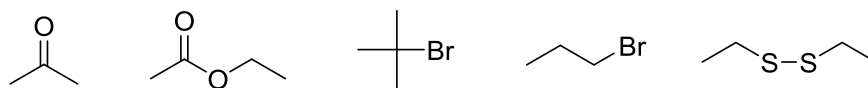


Figure 101. Compounds in this series that were allowed to react with complex **I**.

Acetone allows us to survey complex I's ability to activate ketones. In this instance we observed acetone's preference to act as a ligand and coordinate to the iridium complex. There was some C-H activation, however adduct formation was the primary product. This behavior is similar to what was observed with small alcohols, such as methanol, where the coordination with the iridium places the hydrogens in locations where they are unable to be activated. The spectrum of this reaction can be seen in Figure 102, where complex I was allowed to react with acetone. The reactant ion for this reaction is at m/z 443 and is mainly the most intense $^{193}\text{Ir}^{12}\text{C}_{12}^{14}\text{N}_2^1\text{H}_8^{35}\text{Cl}_2$ isotopomer.

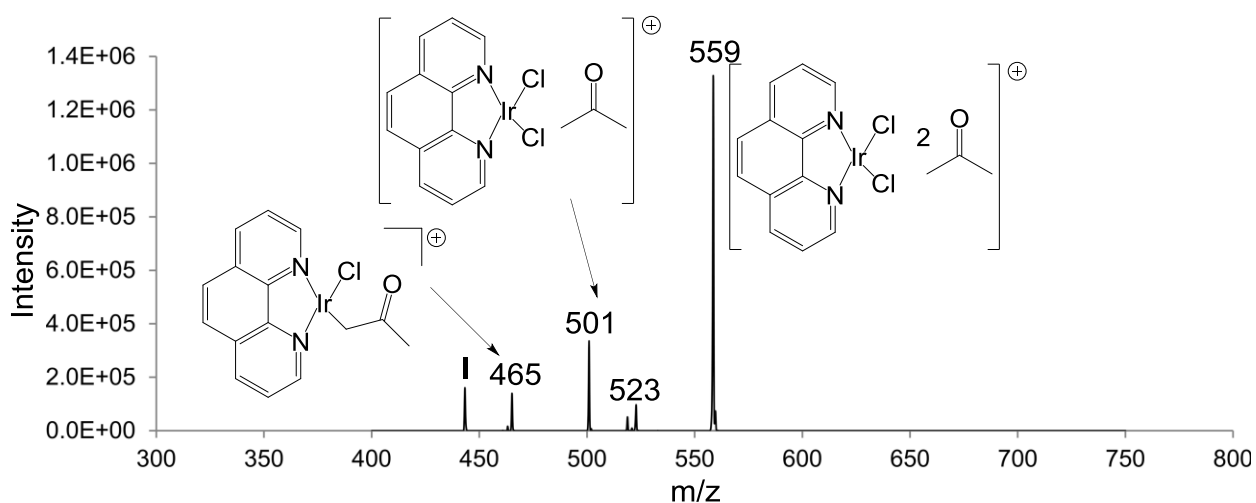


Figure 102. Mass spectrum of complex I reacting with acetone. An addition of acetone to complex I can be seen at m/z 501, with a loss of HCl at m/z 465. An adduct of two acetones with complex I is seen at m/z 559 and loss of HCl from this complex at m/z 523.

We next probed ethyl acetate thinking that it may react similar to ethers and give two C-H activations. In this case complex **I** was able to activate the ethyl acetate toward one C-H activation but not two. For ethyl acetate the ethyl group is attached to an electron donating group whereas the methyl group attached to the carbonyl is on the electron withdrawing side of the ester, this most likely slows the second C-H activation process down enough to where we do not observe it occurring. Another explanation could be, that once the first activation has occurred the on the ethoxy side, the carbonyl then coordinates with the iridium. This would place the hydrogens on the methyl group attached to the carbonyl in a location where the iridium would be unable to activate them. Data from this reaction can be seen in Figure 103, where complex **I** was allowed to react with ethyl acetate. In this reaction, the reactant ion is at m/z 443 and is mainly the most intense $^{193}\text{Ir}^{12}\text{C}_{12}^{14}\text{N}_2^1\text{H}_8^{35}\text{Cl}_2$ isotopomer.

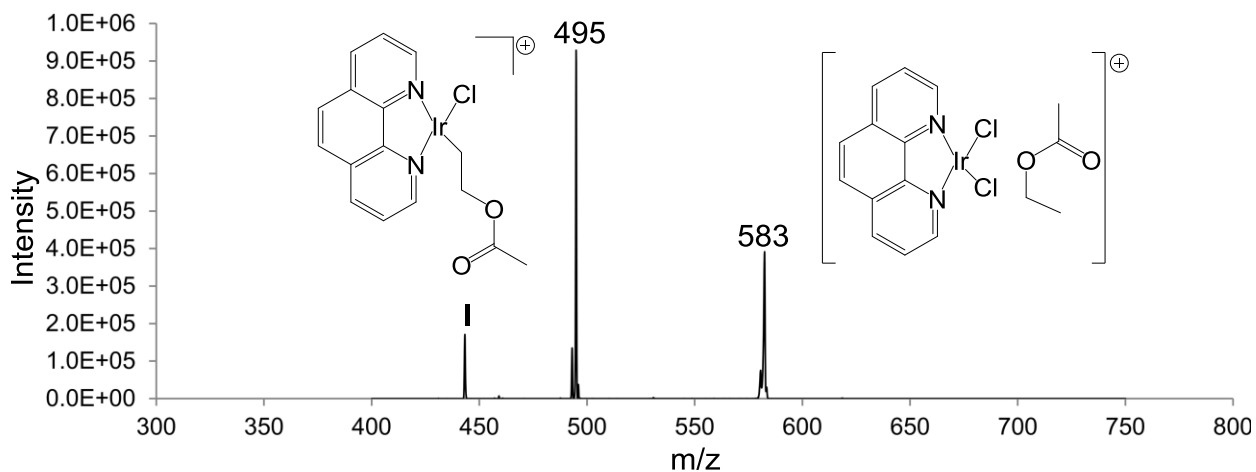


Figure 103. Mass spectrum of complex **I** reacting with ethyl acetate.

We next directed our attention toward bromoalkanes to survey their reactivity with complex **I**. These bromoalkanes readily produced C-H activation products. This process was faster than what was observed with non-activated sp_3 hybridized alkanes, indicating that the bromine substituent is able to increase the rate of C-H activation. This is most likely due to initial coordination of the bromine with iridium which then directs the C-H activation toward the γ carbon. When probing tert-butyl bromide we observed an initial C-H activation along with a loss of HBr as described in Scheme 52. This is similar to a dehydrogenation process, where the hydrogen on the α carbon is able to be activated along with the coordination to the bromine. For this process, the iridium first coordinates to the iridium through agostic interactions with the hydrogen. After this occurs, an oxidative addition takes place forming an iridium hydride followed by a rapid loss of HBr. While this newly formed molecule is still in proximity to the iridium, another oxidative addition occurs followed by a loss of HCl. This proposed mechanism can be seen in Scheme 52. Examples of this reactivity can be seen in Figures 104 and 105. For these reactions, the reactant ion is at m/z 443 and is mainly the most intense $^{193}\text{Ir}^{12}\text{C}_{12}^{14}\text{N}_2^1\text{H}_8^{35}\text{Cl}_2$ isotopomer. We also surveyed the reactivity of diethyl disulfide with complex **I**, which provided primarily C-H activation products. An example of this is given in Figure 106 with the reactant ion at m/z 443, mainly the most intense $^{193}\text{Ir}^{12}\text{C}_{12}^{14}\text{N}_2^1\text{H}_8^{35}\text{Cl}_2$ isotopomer.

Scheme 52. Proposed reaction mechanism of complex **I** reacting with tert-butyl bromide.

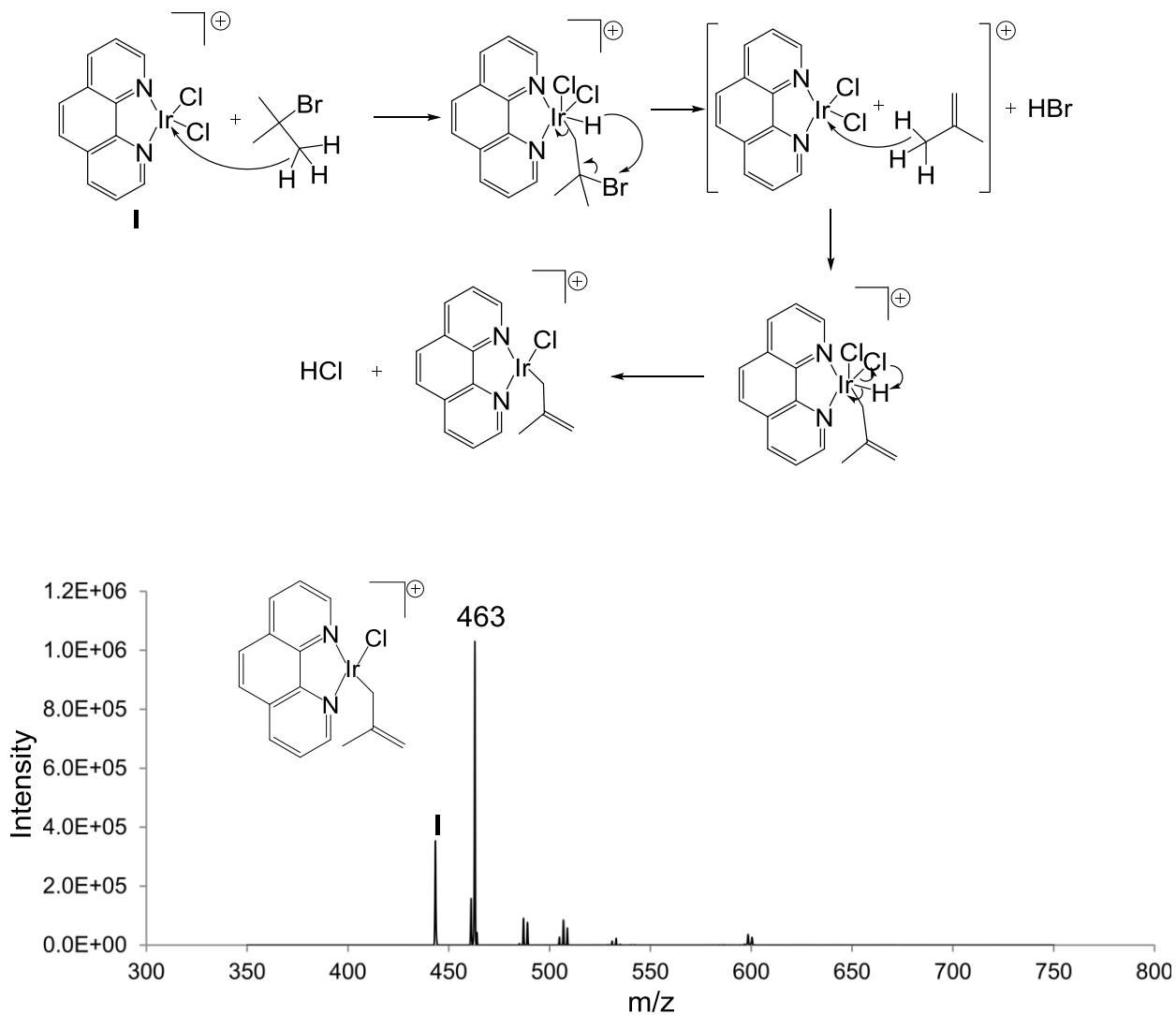


Figure 104. Mass spectrum of complex **I** reacting with tert-butyl bromide.

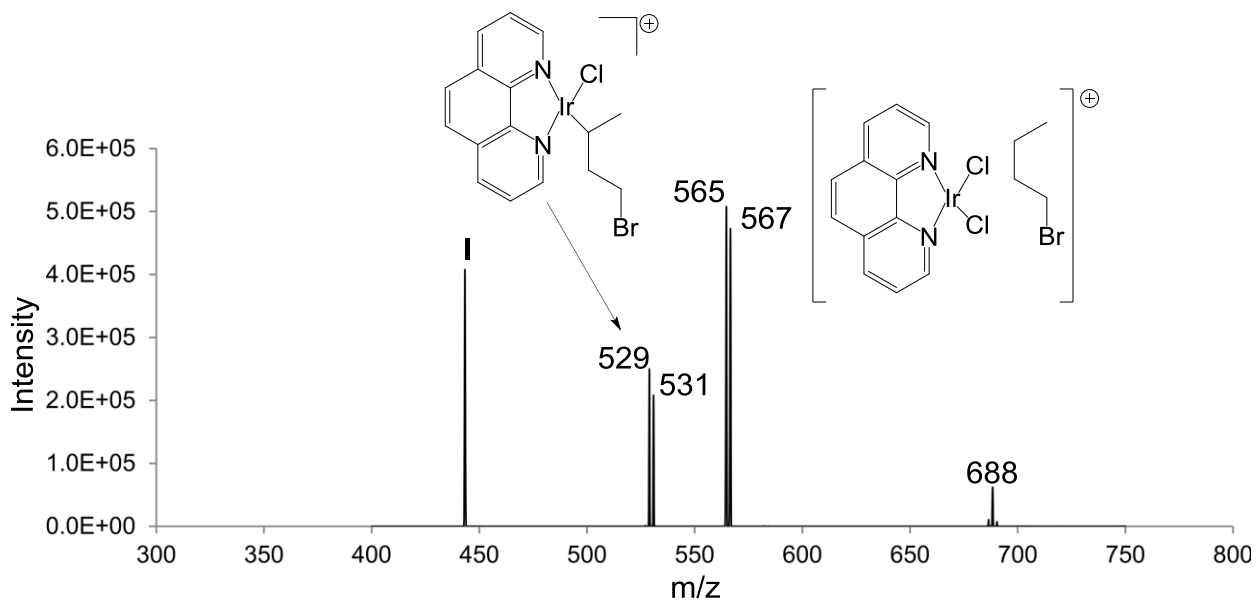


Figure 105. Mass spectrum of complex **I** reacting with 1-bromopropane. An addition of 1-bromopropane to complex **I** can be seen at m/z 565 and 567, with a loss of HCl at m/z 529 and 531. While, m/z 688 is an addition of two 1-bromopropane compounds to complex **I**. Shown with modification at the γ carbon, but could also be at the β carbon.

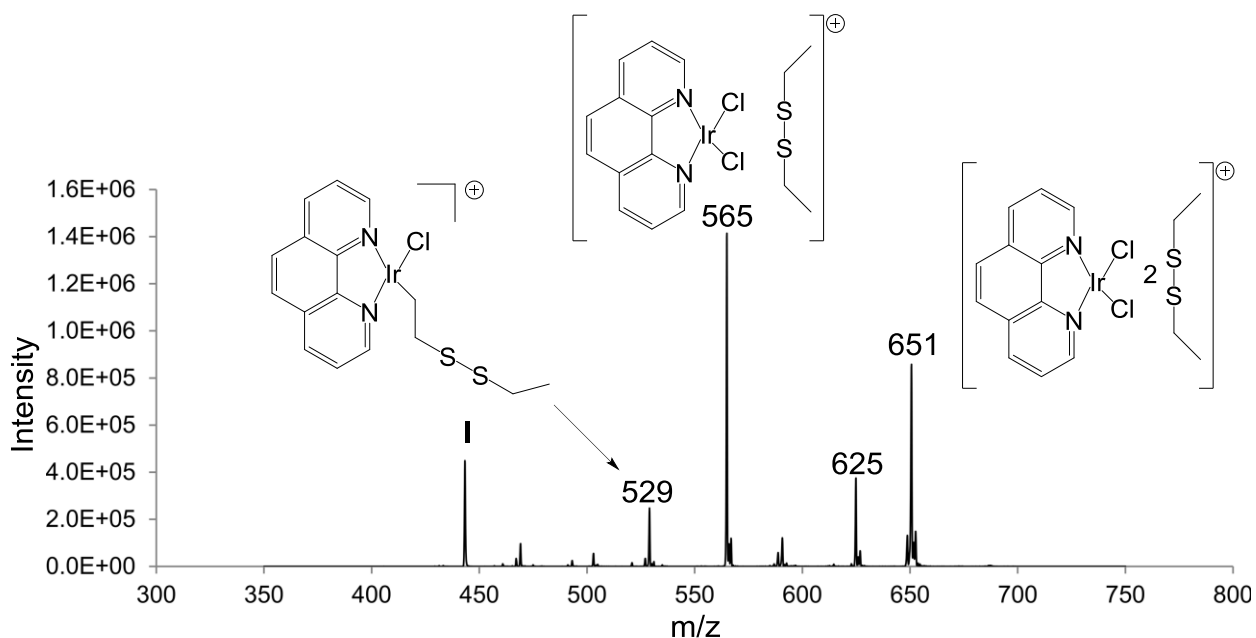


Figure 106. Mass spectrum of complex **I** reacting with diethyl disulfide. An addition of diethyl disulfide to complex **I** can be seen at m/z 565, with a loss of HCl seen at m/z 529. While, m/z 651 is addition of two diethyl disulfide compounds to complex **I** and 625 m/z is a loss of HCl.

6.5– Conclusions

In summary, we have developed a novel C-H activation system that can cleave unactivated 2° C-H bonds as well as benzylic C-H bonds. This cationic dichloride iridium (III) phenanthroline complex is active not only towards C-H activation but also dehydrogenation of alcohols. This complex is also an active H/D exchange catalyst which is similar to other cationic iridium (III) complexes described by Bergman.¹⁶³ Computational modeling that was completed on the toluene series of compounds

reacting with complex I, suggests a concerted pathway with low barriers for the C-H activation process.

List of References

- (1) Griffiths, J. *Anal. Chem.* **2009**, *80*, 5678–5683.
- (2) Thompson, J. J. *Proc. R. Soc. Lond. A* **1913**, *89*, 1–20.
- (3) Yamashitat, M.; Fenn, J. B. *J. Phys. Chem.* **1984**, *434*, 4451–4459.
- (4) Fenn, J. B. *Electrospray Ionization Mass Spectrometry: Fundamentals, Instrumentations & Applications*; Cole, R., Ed.; Wiley: New York, 1997.
- (5) Yamashitat, M. *J. Phys. Chem.* **1984**, *750*, 4611–4615.
- (6) Fenn, J. B. *Fenn Nobel Prize 2002*; The Nobel Prize Foundation: Stockholm, 2002.
- (7) Loo, J. a. *Int. J. Mass Spectrom.* **2000**, *200*, 175–186.
- (8) Gaskell, S. J. *J. Mass Spectrom.* **1997**, *32*, 677–688.
- (9) Fenn, J. B.; Mann, M.; Meng, C. K.; Wong, S. F.; Whitehouse, C. M. *Mass Spectrom. Rev.* **1990**, *9*, 37–70.
- (10) Kebarle, P.; Tang, L. *Anal. Chem.* **1993**, *65*, 972–986.
- (11) Fenn, J. B. *J. Am. Soc. Mass Spectrom.* **1993**, *4*, 524–535.
- (12) Dole, M. *J. Chem. Phys.* **1968**, *49*, 2240–2249.
- (13) Rayleigh, L. *Philos. Mag.* **1882**, *14*, 184–186.
- (14) Fernandez de la Mora, J. *Anal. Chim. Acta* **2000**, *406*, 93–104.
- (15) Hogan, C. J.; Carroll, J. a; Rohrs, H. W.; Biswas, P.; Gross, M. L. *Anal. Chem.* **2009**, *81*, 369–377.
- (16) Iribarne, J.; Thompson, B. *J. Chem. Phys.* **1976**, *64*, 2287–2294.
- (17) Thompson, B.; Iribarne, J. *J. Chem. Phys.* **1979**, *71*, 4451–4463.
- (18) Wong, P. S. H.; Cooks, G. R. *Curr. Sep.* **1997**, *16*.
- (19) Finnigan, R. E. *Anal. Chem.* **1994**, *66*, 969–975.
- (20) March, R. E. *J. Mass Spectrom.* **1997**, *32*, 351–369.

- (21) Paul, W.; Steinwedel, H. *Ger. Pat.* **1956**, 944 900.
- (22) Paul, W. *Angew. Chem.* **1990**, *102*, 780–789.
- (23) Knight, R. *Int. J. Mass Spectrom. Ion Phys.* **1983**, *51*, 127–131.
- (24) March, R. E. *J. Mass Spec.* **1997**, *32*, 351–369.
- (25) Mathieu, E. *J. Math. Pure Appl.* **1868**, *13*, 137.
- (26) Todd, J. F. J.; Penman, a. D.; Smith, R. D. *Int. J. Mass Spectrom. Ion Process.* **1991**, *106*, 117–135.
- (27) Cooks, R. G.; Glish, G. L.; McLuckey, S. A.; Kaiser, R. E. *Chem. Eng. News* **1991**, *69*, 26.
- (28) Stafford, G. *Am. Soc. Mass Spectrom.* **2002**, *13*, 589–596.
- (29) Jonscher, K. R.; Yates, J. R. *Anal. Biochem.* **1997**, *244*, 1–15.
- (30) Stafford, G.; Kelley, P.; Syka, J. E. P.; Reynolds, W. E.; Todd, J. F. J. *Int. J. Mass Spectrom. Ion Process.* **1984**, *60*, 85–98.
- (31) Kaiser, R. E.; Graham Cooks, R.; Stafford, G. C.; Syka, J. E. P.; Hemberger, P. H. *Int. J. Mass Spectrom. Ion Process.* **1991**, *106*, 79–115.
- (32) Sleno, L.; Volmer, D. a. *J. mass Spectrom.* **2004**, *39*, 1091–1112.
- (33) Jennings, K. R. *Int. J. Mass Spectrom.* **2000**, *200*, 479–493.
- (34) Shukla, A. K.; Futrell, J. H. *J. mass Spectrom.* **2000**, *1090*, 1069–1090.
- (35) Cooks, G. *J. Mass Spectrom.* **1995**, *30*, 1215–1221.
- (36) Mcluckey, S. A. *J. Soc. Mass Spectrom.* **1992**, *3*, 599–614.
- (37) Ottens, A. K.; Arkin, C. R.; Griffin, T. P.; Palmer, P. T.; Harrison, W. W. *Int. J. Mass Spectrom.* **2005**, *243*, 31–39.
- (38) Yamashita, M.; Fenn, J. B. *J Phys.Chem.* **1984**, *88*, 4451–4459.
- (39) Traeger, J. *Int. J. Mass Spectrom.* **2000**, *200*, 387–401.
- (40) Dyson, P. J.; McIndoe, J. S. *Inorganica Chim. Acta* **2003**, *354*, 68–74.

- (41) Kane-Maguire, L. a. P.; Kanitz, R.; Sheil, M. M. *J. Organomet. Chem.* **1995**, *486*, 243–248.
- (42) Katta, V.; Chowdhury, S.; Chait, B. T. *J. Am. Chem. Soc.* **1990**, 5348–5349.
- (43) Dempster, A. J. *Philos. Mag.* **1916**, *31*, 438.
- (44) Brodbelt, J. S. *Mass Spectrom. Rev.* **1997**, *16*, 91–110.
- (45) Munson, M.; Field, F. *J. Am. Chem. Soc.* **1966**, *88*, 2621–2630.
- (46) Yost, R. A.; Enke, C. G. *Anal. Chem.* **1979**, *51*, 1251–1262.
- (47) Beynon, J. H.; Cooks, R. G.; A, J. W.; Baitinger, W. E.; Ridley, T. Y. *Anal. Chem.* **1973**, *45*, 1023A – 1031A.
- (48) Hail, M. E.; Berberich, D. W.; Yost, R. A. *Anal. Chem.* **1989**, 1874–1879.
- (49) Fetterolf, D.; Yost, R.; Eyler, J. **1984**, *19*, 104–105.
- (50) Jalonen, J. *J. Chem. Soc. Chem. Commun.* **1985**, 872–874.
- (51) Fedorov, A.; Batiste, L.; Bach, A.; Birney, D. M.; Chen, P. *J. Am. Chem. Soc.* **2011**, *133*, 12162–12171.
- (52) Teloy, E.; Gerlich, D. *Chem. Physics* **1974**, *4*, 417–427.
- (53) Armentrout, P. In *Guided Ion Beam Studies of Thermochemistry*, 1992; pp. 83–119.
- (54) McMahon, T. B.; Kebarle, P. *J. Am. Chem. Soc.* **1977**, *99*, 2222–2230.
- (55) Caldwell, G.; Magnera, T. F.; Kebarle, P. *J. Am. Chem. Soc.* **1984**, *106*, 959–966.
- (56) Hiraoka, K.; Mizuse, S.; Yamabe, S. *J. Phys. Chem.* **1988**, 3943–3952.
- (57) Ikuta, S.; Kebarle, P. *J. Am. Chem. Soc.* **1982**, 1462–1469.
- (58) Muntean, F.; Armentrout, P. B. *J. Chem. Phys.* **2001**, *115*, 1213–1228.
- (59) Bierbaum, V. M. *Int. J. Mass Spectrom.* **2014**, In Press.
- (60) Nibbering, N. *Acc. Chem. Res.* **1997**, *23*, 279–285.
- (61) Comisarow, M.; Marshall, A. G. *Can. J. Chem.* **1974**, *52*, 1997–1999.

- (62) Comisarow Melvin B.; Marshall Alan G. *Chem. Phys. Lett.* **1974**, *25*, 282–283.
- (63) Louris, J.; Amy, J.; Ridley, T.; Cooks, R. G. *Int. J. Mass Spectrom. Ion Process.* **1989**, *88*, 97–111.
- (64) Rettinghaus, V. G. *Angew. Phys.* **1967**, *22*, 321.
- (65) Gronert, S. *Mass Spectrom. Rev.* **2005**, *24*, 100–120.
- (66) Nettey, S.; Swift, C. A.; Joviliano, R.; Noin, D. O.; Gronert, S. *J. Am. Chem. Soc.* **2012**.
- (67) O'Hair, R. a J. *Chem. Commun.* **2006**, 1469–1481.
- (68) Reid, G. E.; McLuckey, S. a. *J. Mass Spectrom.* **2002**, *37*, 663–675.
- (69) Wang, H.; Agnes, G. R. *Anal. Chem.* **1999**, *71*, 3785–3792.
- (70) Carlin, T. J.; Freiser, B. S. *Anal. Chem.* **1983**, *55*, 571–574.
- (71) Cody, R. B.; Freiser, B. S. *Anal. Chem.* **1982**, *54*, 1431–1433.
- (72) Emary, W. B.; Kaiser, R. E.; Kenttiimaa, H. I.; Cooks, R. G. *J. Am. Soc. Mass Spectrom.* **1990**, *1*, 308–311.
- (73) Liere, P.; March, R. E.; Blasco, T.; Tabet, J.-C. *Int. J. Mass Spectrom. Ion Process.* **1996**, *153*, 101–117.
- (74) Ottens, A. K.; Harrison, W. W.; Griffin, T. P.; Helms, W. R. *J. Am. Soc. Mass Spectrom.* **2002**, *13*, 1120–1128.
- (75) McLuckey, S. a; Wells, J. M. *Chem. Rev.* **2001**, *101*, 571–606.
- (76) Gronert, S. *Chem. Rev.* **2001**, *101*, 329–360.
- (77) Gronert, S. *J. Am. Soc. Mass Spectrom.* **1998**, *9*, 845–848.
- (78) Gronert, S. *Chem. Rev.* **2001**, *101*, 329–360.
- (79) Turulski, J.; Niedzielski, J. *Int. J. Mass Spectrom. Ion Process.* **1994**, *139*, 155–162.
- (80) Eichelberger, B. R.; Snow, T. P.; Bierbaum, V. M. *J. Am. Soc. Mass Spectrom.* **2003**, *14*, 501–505.
- (81) Su, T.; Bowers, M. T. *J. Chem. Phys.* **1973**, *58*, 3027–3037.

- (82) Su, T.; Bowers, M. T. In *Gas Phase Ion Chemistry*; Bowers, M. T., Ed.; Academic Press: New York, 1979; p. 83.
- (83) Donald, W. A.; Khairallah, G. N.; O'Hair, R. A. J. *Am. Soc. Mass Spectrom.* **2013**, *24*, 811–815.
- (84) Asano, K. G.; Goeringer, D. E.; Butcher, D. J.; McLuckey, S. a. *Int. J. Mass Spectrom.* **1999**, *190-191*, 281–293.
- (85) Robinson, P. S. D.; Khairallah, G. N.; Silva, G.; Lioe, H.; O'Hair, R. A. J. *Angew. Chem. Int Ed.* **2012**, *51*, 3812–3817.
- (86) Rijs, N. J.; O'Hair, R. A. J. *Organometallics* **2009**, *28*, 2684–2692.
- (87) Henderson, M. A.; Kwok, S.; Mcindoe, J. S. *J. Am. Soc. Mass Spectrom.* **2009**, *20*, 658–666.
- (88) Vikse, K.; Khairallah, G. N.; Mcindoe, J. S.; O'Hair, R. A. J. *Dalt. Trans.* **2013**, *42*, 6440–6449.
- (89) Bourissou, D.; Guerret, O.; Gabbai, F. P.; Bertrand, G. *Chem. Rev.* **2000**, *100*, 39–91.
- (90) Davies, H. M. L.; Beckwith, R. E. J. *Chem. Rev.* **2003**, *103*, 2861–2904.
- (91) Díez-González, S.; Marion, N.; Nolan, S. P. *Chem. Rev.* **2009**, *109*, 3612–3676.
- (92) Lin, J. C. Y.; Huang, R. T. W.; Lee, C. S.; Bhattacharyya, A.; Hwang, W. S.; Lin, I. J. B. *Chem. Rev.* **2009**, *109*, 3561–3598.
- (93) Aldajaei, J. T.; Gronert, S. *Int. J. Mass Spectrom.* **2012**, *316-318*, 68–75.
- (94) Koehn, S. K.; Gronert, S.; Aldajaei, J. T. *Org. Lett.* **2010**, *12*, 676–679.
- (95) Hashmi, A. S. K. *Chem. Rev.* **2007**, *107*, 3180–3211.
- (96) Geuther, A.; Hermann, M. *Liebigs Ann. Chem.* **1855**, *95*, 211.
- (97) Pryor, W. A. *Organic Free Radicals*; American Chemical Society: Washington, DC, 1977.
- (98) Kimse, W. *Carbene Chemistry*; Academic Press: New York, 1964.
- (99) Doering, W. E.; Hoffman, A. K. *J. Am. Chem. Soc.* **1954**, *5607*, 6162–6165.
- (100) De Frémont, P.; Marion, N.; Nolan, S. P. *Coord. Chem. Rev.* **2009**, *253*, 862–892.

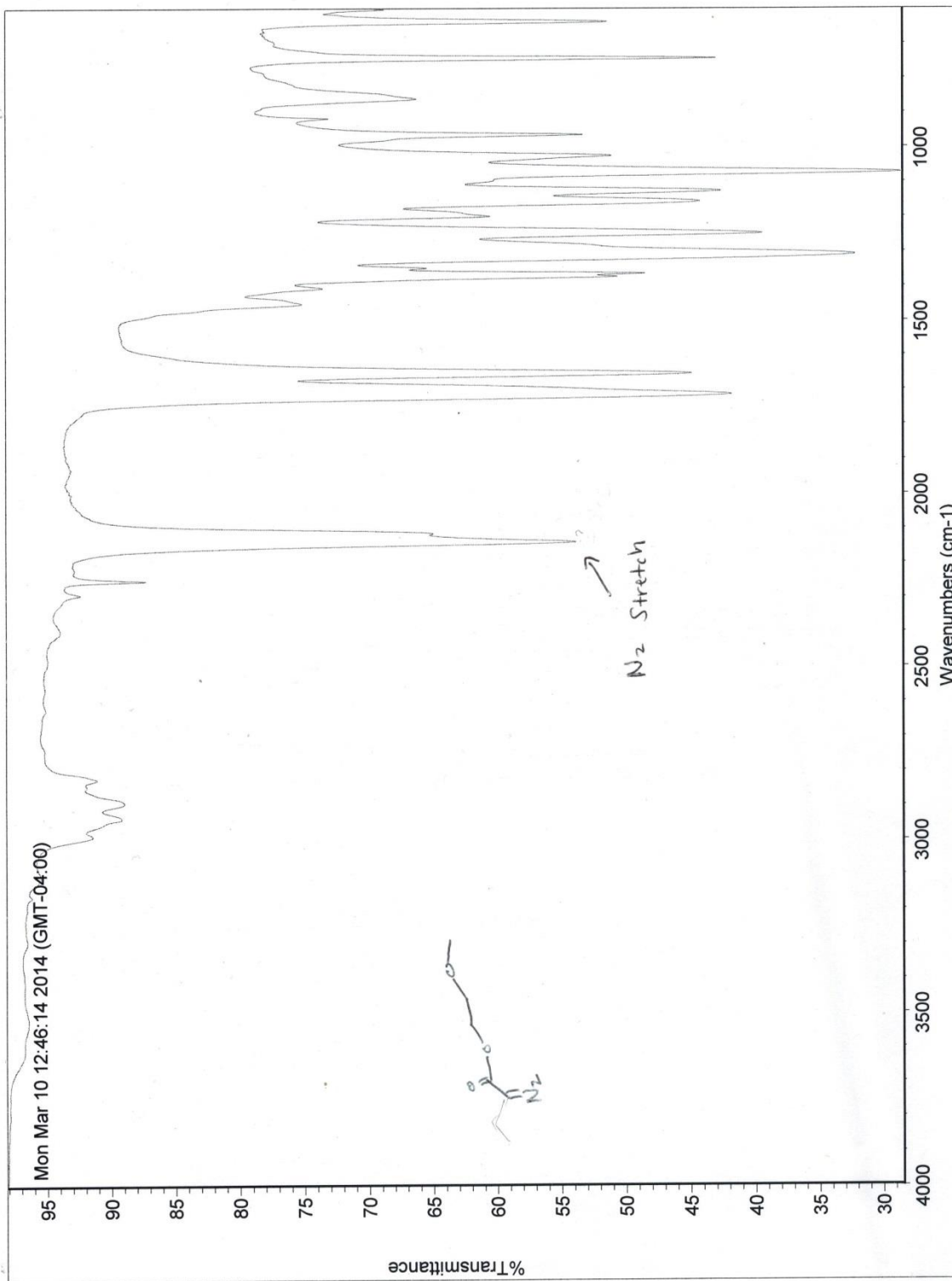
- (101) Fischer, E. O.; Massbo, A. *Angew. Chem. Int Ed.* **1964**, 3, 580–581.
- (102) Schrock, R. *J. Am. Chem. Soc.* **1974**, 6796–6797.
- (103) Swift, C. A.; Gronert, S. *Organometallics* **2014**, 33, 7135–7140.
- (104) Ringger, D. H.; Chen, P. *Angew. Chem. Int Ed.* **2013**, 52, 4686–4689.
- (105) Fedorov, A.; Batiste, L.; Bach, A.; Birney, D. M.; Chen, P. *J. Am. Chem. Soc.* **2011**, 133, 12162–12171.
- (106) Fedorov, A.; Chen, P. *Organometallics* **2009**, 28, 1278–1281.
- (107) Fedorov, A.; Moret, M.-E.; Chen, P. *J. Am. Chem. Soc.* **2008**, 130, 8880–8881.
- (108) Doyle, M. P.; Oeveren, A. Van; Westrum, L. J.; Protopopova, M. N.; Clayton, T. W. *J. Am. Chem. Soc.* **1991**, 113, 8982–8984.
- (109) Potts, K. T.; Bordeaux, K. G.; Kuehnling, W. R.; Salisbury, R. L. *J. Org. Chem.* **1985**, 22, 1666–1676.
- (110) Taber, D. F.; Ruckle, R. E.; Hennessy, M. J. *J. Org. Chem.* **1986**, 51, 4077–4078.
- (111) Fèvre, M.; Pinaud, J.; Leteneur, A.; Gnanou, Y.; Vignolle, J.; Taton, D.; Miqueu, K.; Sotiropoulos, J.-M. *J. Am. Chem. Soc.* **2012**, 134, 6776–67784.
- (112) Preliminary, lower-level calculations using the M06 functional with a general basis set (6-311+G** on C, H, P and SDD on Au) indicate a binding energy of 35 kcal/mol for Ph₃PAu⁺ to trans 1, 2-diphenylcyclopropane and 28 kcal/mol to styrene. An advantage is, ligand exchange is expected to occur despite being endothermic. .
- (113) Díaz-Requejo, M. M.; Pérez, P. J. *J. Organomet. Chem.* **2005**, 690, 5441–5450.
- (114) Nakata, K.; Fujio, M.; Nishimoto, K.; Tsuno, Y. *Chempluschem* **2013**, 78, 1099–1108.
- (115) The binding to styrene is computed to be 40.3 kcal/mol and to trans-1, 2-diphenylcyclopropane is computed to be 30.1 kcal/mol at the M06/QZVP level with enthalpy corrections at the Lanl2dz level – the largest system exceeded our computational limits for Q.
- (116) Jasíková, L.; Roithova, J. *Organometallics* **2012**, 31, 1935–1942.
- (117) Fructos, M. R.; Fre, P. De; Nolan, S. P.; Díaz-Requejo, M. M.; Perez, P. J. *Organometallics* **2006**, 25, 2237–2241.

- (118) Ungvári, N.; Fördös, E.; Kégl, T.; Ungváry, F. *Inorg. Chim. Acta* **2010**, 363, 2016–2028.
- (119) Chattopadhyay, P.; Matsuo, T.; Tsuji, T.; Ohbayashi, J.; Hayashi, T. *Organometallics* **2011**, 1869–1873.
- (120) Delgado-Rebollo, M.; Beltrán, Á.; Prieto, A.; Mar Díaz-Requejo, M.; Echavarren, A. M.; Pérez, P. J. *Eur. J. Inorg. Chem.* **2012**, 2012, 1380–1386.
- (121) Qian, Y.; Zavalij, P. J.; Hu, W.; Doyle, M. P. *Org. Lett.* **2013**, 15, 1564–1567.
- (122) Johnson, A.; Laguna, A.; Concepción Gimeno, M. *J. Am. Chem. Soc.* **2014**, 3–6.
- (123) Julian, R. R.; May, J. A.; Stoltz, B. M.; Beauchamp, J. L. *J. Am. Chem. Soc.* **2003**, 125, 4478–4486.
- (124) Schulz, J.; Jašíková, L.; Skříba, A.; Roithová, J. *J. Am. Chem. Soc.* **2014**, 11513–11523.
- (125) Gronert, S.; Keeffe, J. R. *J. Phys. Org. Chem.* **2013**, 26, 1023–1031.
- (126) Roithová, J.; Schröder, D. *Coord. Chem. Rev.* **2009**, 253, 666–677.
- (127) Zhao, X.; Zhang, Y.; Wang, J. *Chem. Commun.* **2012**, 48, 10162–10173.
- (128) Díaz-Requejo, M. M.; Pérez, P. J. *J. Organomet. Chem.* **2005**, 690, 5441–5450.
- (129) Fructos, M. R.; Fre, P. De; Nolan, S. P.; Di, M. M.; Pe, P. J. *Organometallics* **2006**, 25, 2237–2241.
- (130) Gaillard, S.; Cazin, C.; Nolan, S. P. *Acc. Chem. Res.* **2012**, 45, 778–787.
- (131) Straub, B. F.; Hofmann, P. *Angew. Chemie - Int. Ed.* **2001**, 40, 1288–1290.
- (132) Arnold, P. L. *Heteroat. Chem.* **2002**, 13, 534–539.
- (133) Davies, H. M. L.; Manning, J. R. *Nature* **2008**, 451, 417–424.
- (134) Garrison, J. C.; Youngs, W. J. *Chem. Rev.* **2005**, 105, 3978–4008.
- (135) Díaz-Requejo, M. M.; Pérez, P. J. *J. Organomet. Chem.* **2005**, 690, 5441–5450.
- (136) Hashmi, a S. K.; Hutchings, G. J. *Angew. Chem. Int. Ed. Engl.* **2006**, 45, 7896–7936.

- (137) Antoniotti, S.; Genin, E.; Michelet, V.; Genêt, J.-P. *J. Am. Chem. Soc.* **2005**, *127*, 9976–9977.
- (138) Ferrer, C.; Echavarren, A. M. *Angew. Chem. Int. Ed. Engl.* **2006**, *45*, 1105–1109.
- (139) Kennedy-smith, J. J.; Staben, S. T.; Toste, F. D. **2004**, 4526–4527.
- (140) Reetz, M. T.; Sommer, K. *European J. Org. Chem.* **2003**, *2003*, 3485–3496.
- (141) Staben, S. T.; Kennedy-Smith, J. J.; Toste, F. D. *Angew. Chem. Int. Ed. Engl.* **2004**, *43*, 5350–5352.
- (142) Johansson, M. J.; Gorin, D. J.; Staben, S. T.; Toste, F. D. *J. Am. Chem. Soc.* **2005**, *127*, 18002–18003.
- (143) Bolte, B.; Odabachian, Y.; Gagosz, F. *J. Am. Chem. Soc.* **2010**, *132*, 7294–7296.
- (144) Wang, D.; Cai, R.; Sharma, S.; Jirak, J.; Thummanapelli, S. K.; Akhmedov, N. G.; Zhang, H.; Liu, X.; Petersen, J. L.; Shi, X. *J. Am. Chem. Soc.* **2012**, *134*, 9012–9019.
- (145) Roithová, J.; Hrušák, J.; Schröder, D.; Schwarz, H. *Inorganica Chim. Acta* **2005**, *358*, 4287–4292.
- (146) Iqbal, N.; Sperger, C. A.; Fiksdahl, A. *European J. Org. Chem.* **2013**, *2013*, 907–914.
- (147) Bartoli, G.; Bosco, M.; Dalpozzo, R.; Marcantoni, E.; Massaccesi, M.; Rinaldi, S.; Smabri, L. *Synlett* **2003**, *1*, 39–42.
- (148) Srividhya, D.; Manjunathan, S.; Thirumaran, S.; Saravanan, C.; Senthil, S. *J. Mol. Struct.* **2009**, *927*, 7–13.
- (149) Nagase, Y.; Shirai, H.; Kaneko, M.; Shirakawa, E.; Tsuchimoto, T. *Org. Biomol. Chem.* **2013**, *11*, 1456–1459.
- (150) Arndtsen, B. A.; Bergman, R. G.; Mobley, T. A.; Peterson, T. H. *Acc. Chem. Res.* **1995**, *28*, 154–162.
- (151) Bergman, R. G. *Nature* **2007**, *446*, 391–393.
- (152) Lyons, T. W.; Sanford, M. S.; Formation, I. C. N. B. *Chem. Rev.* **2010**, *110*, 1147–1169.

- (153) Klei, S. R.; Tan, K. L.; Golden, J. T.; Yung, C. M.; Thalji, R. K.; Ahrendt, K. A.; Ellman, J. A.; Tilley, D. T.; Bergman, R. G. In *Activation and Functionalization of C-H bonds*; American Chemical Society: Washington, DC, 2004; pp. 46–55.
- (154) Lohrenz, J.; Jacobsen, H. *Angew. Chem. Int Ed.* **1996**, *35*, 1305–1307.
- (155) Suematsu, H.; Katsuki, T. *J. Am. Chem. Soc.* **2009**, *131*, 14218–14219.
- (156) Niu, S.; Hall, M. B. *J. Am. Chem. Soc.* **1998**, *7863*, 6169–6170.
- (157) Hinderling, C.; Feichtinger, D.; Plattner, D. A.; Chen, P. *J. Am. Chem. Soc.* **1997**, *119*, 10793–10804.
- (158) Ito, J.; Kaneda, T.; Nishiyama, H. *Organometallics* **2012**, *31*, 4442–4449.
- (159) Meredith, J. M.; Robinson, R.; Goldberg, K. I.; Kaminsky, W.; Heinekey, D. M. *Organometallics* **2012**, *31*, 1879–1887.
- (160) Cheng, C.; Hartwig, J. F. *J. Am. Chem. Soc.* **2015**, *137*, 592–595.
- (161) Seechurn, C. C. C. J.; Sivakumar, V.; Satoskar, D.; Colacot, T. J. *Organometallics* **2014**, *33*, 3514–3522.
- (162) Klei, S. R.; Golden, J. T.; Burger, P.; Bergman, R. G. *J. Mol. Catal. A Chem.* **2002**, *189*, 79–94.
- (163) Golden, J. T.; Andersen, R. A.; Bergman, R. G. *J. Am. Chem. Soc.* **2001**, 5837–5838.
- (164) Frisch, M. J. *Gaussian 09*; Gaussian Inc.: Pittsburgh, PA, 2009.

Appendix



Ethylindanone standard test sample
Recorded on 400-MR with OneNMR probe and F2T tuning

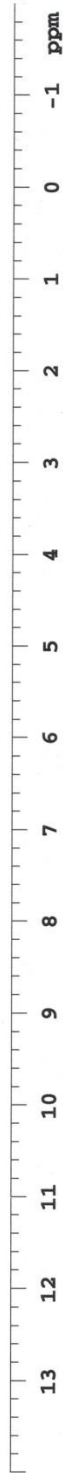
Sample Name:
Ethylindanone
Data Collected on:
Agilent-NMR-mercury300
Archive directory:
/home/vnmr1/vnmrSYS/data/fidlib
Sample directory:
Ethylindanone
Fidfile: PROTON

Pulse Sequence: PROTON (s2pul)
Solvent: cdcl3
Data collected on: Mar 11 2014

Temp. 25.0 C / 298.1 K
Operator: Gronert

Relax. delay 1.000 sec
Pulse 45.0 degrees
Acq. time 2.556 sec
Width 4798.5 Hz
16 repetitions
OBSERVE H1, 299.9142799 MHz
DATA PROCESSING
FT size 131072
Total time 0 min 59 sec

Agilent Technologies



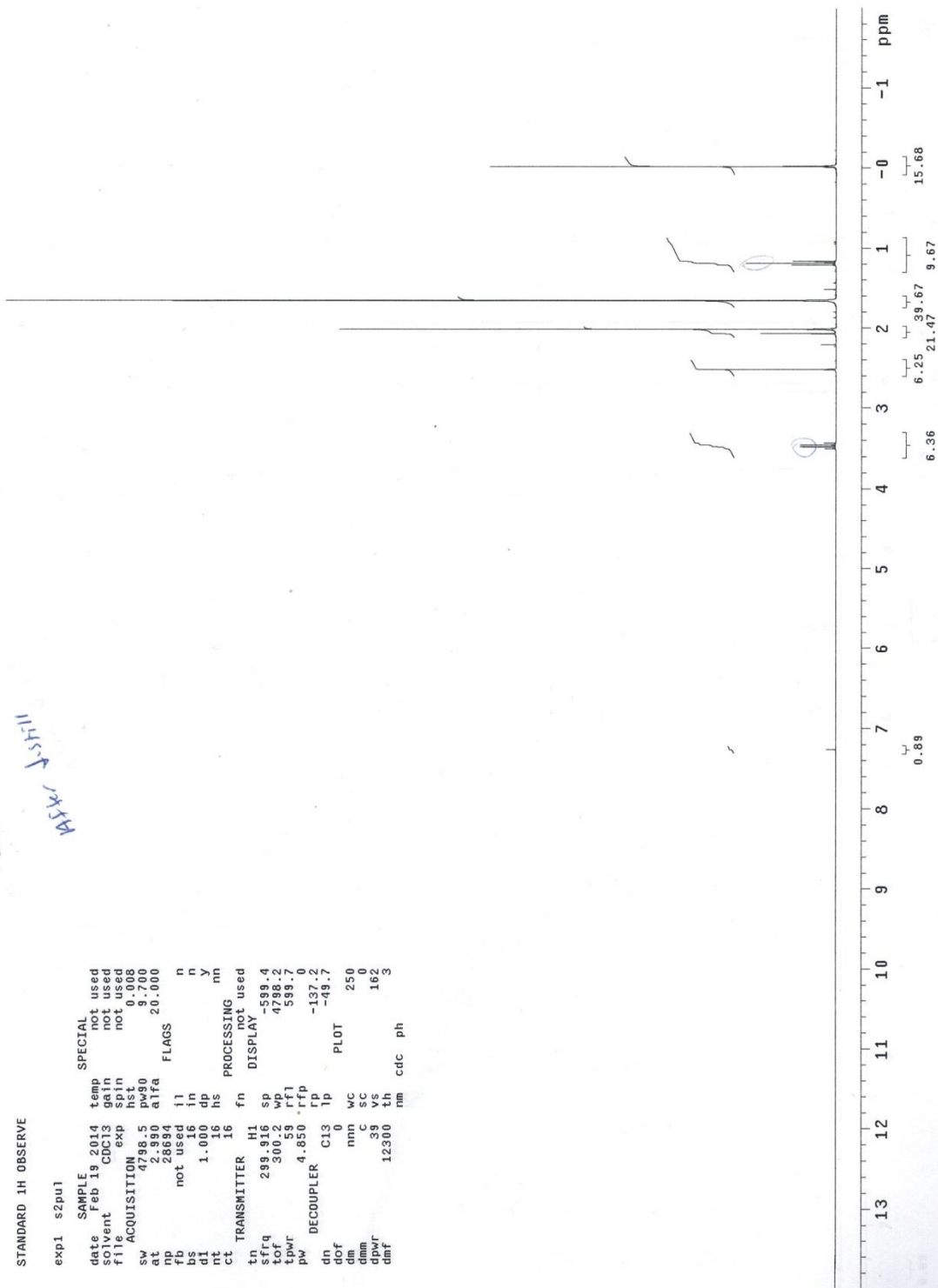


1H NMR

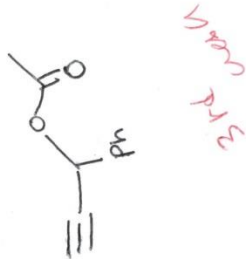
STANDARD 1H OBSERVE

```

exp1 s2pu1
SAMPLE
date Feb 19 2014
solvent CDC13
file CDC13
ACQUISITION
at 4788.5
pp 2390
ps not used
ds 1.000
d1 16
nt 16
ct 16
TRANSMITTER
tn HI
srfq 239.016
rf 30052
tpwr 4.850
pw DECOUPLER C13 lp
dn dof 0
dm nnn wc
dmm C SC
dmar 98
dmf 12300
nm cdc ph
SPECIAL
temp not used
gain not used
spin not used
hst 0.008
pw90 9.700
aifa 20.000
FLAGS
n
n
Y
nn
fn not used
DISPLAY
588.4
4788.2
588.7
588.7
-137.2
-49.7
PLOT
250
162
73
  
```

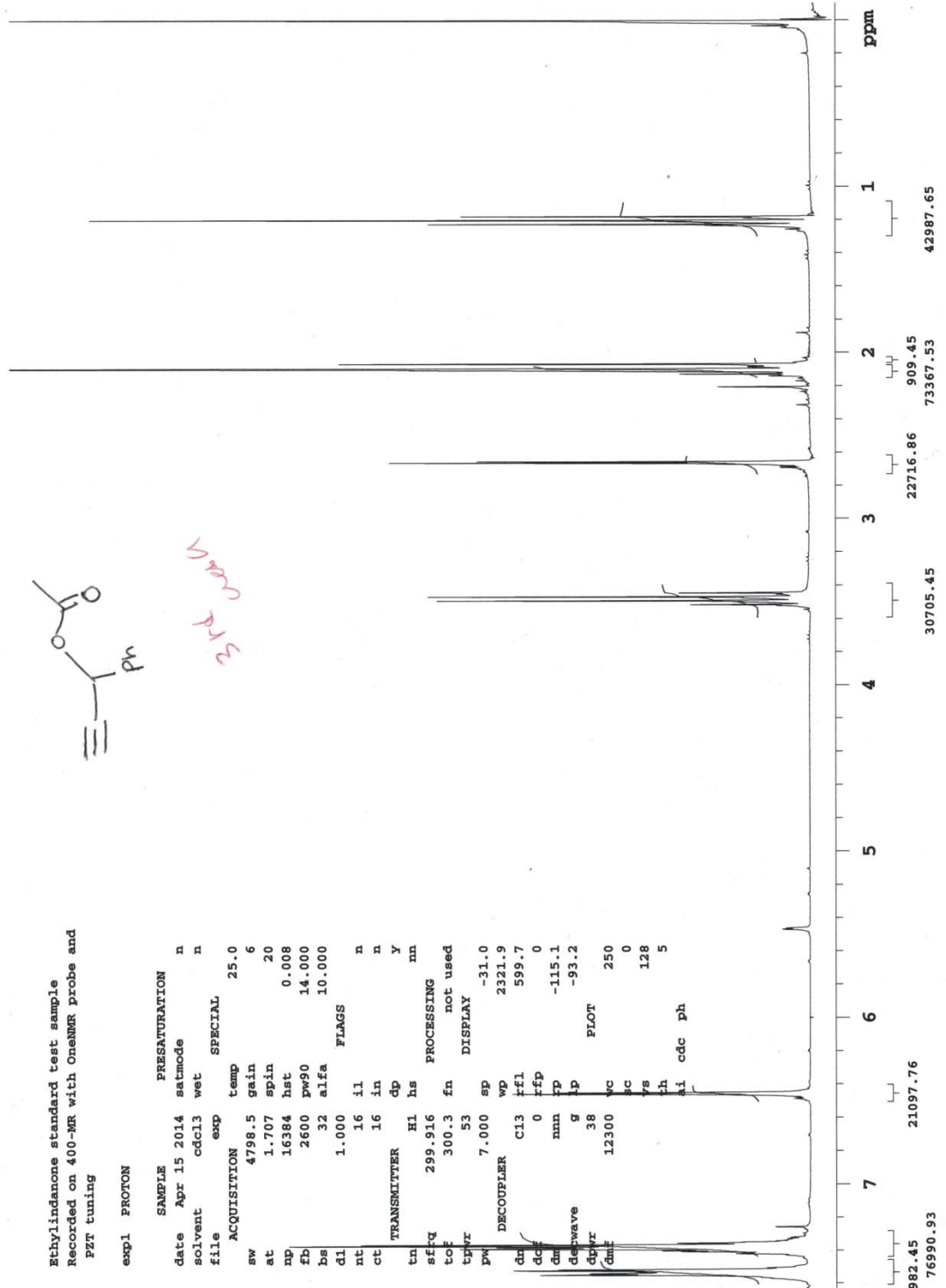


Ethylindane standard test sample
 Recorded on 400-MR with OneNMN probe and
 PZT tuning



exp1 PROTON

date	Apr 15 2014	satmode	n
solvent	cdcl3	wet	n
file	exp	SPECIAL	
ACQUISITION			
sw	4798.5	gain	6
at	1.707	spin	20
np	16384	hst	0.008
fb	2600	pw90	14.000
bs	32	alfa	10.000
d1	1.000	FLAGS	
nt	16	il	n
ct	16	in	n
tn	H1	hs	nn
sfreq	299.916	dp	y
tof	300.3	fn	not used
tpwr	53	DISPLAY	
pw	7.000	sp	-31.0
DECOUPLER			
ch	C13	wp	2321.9
dch	0	rfl	599.7
dm	nnn	fp	0
dephase	g	lp	-115.1
cbpr	38		-93.2
gme	12300	vc	250
		pc	0
		ys	128
		th	5
		ai	cdc ph

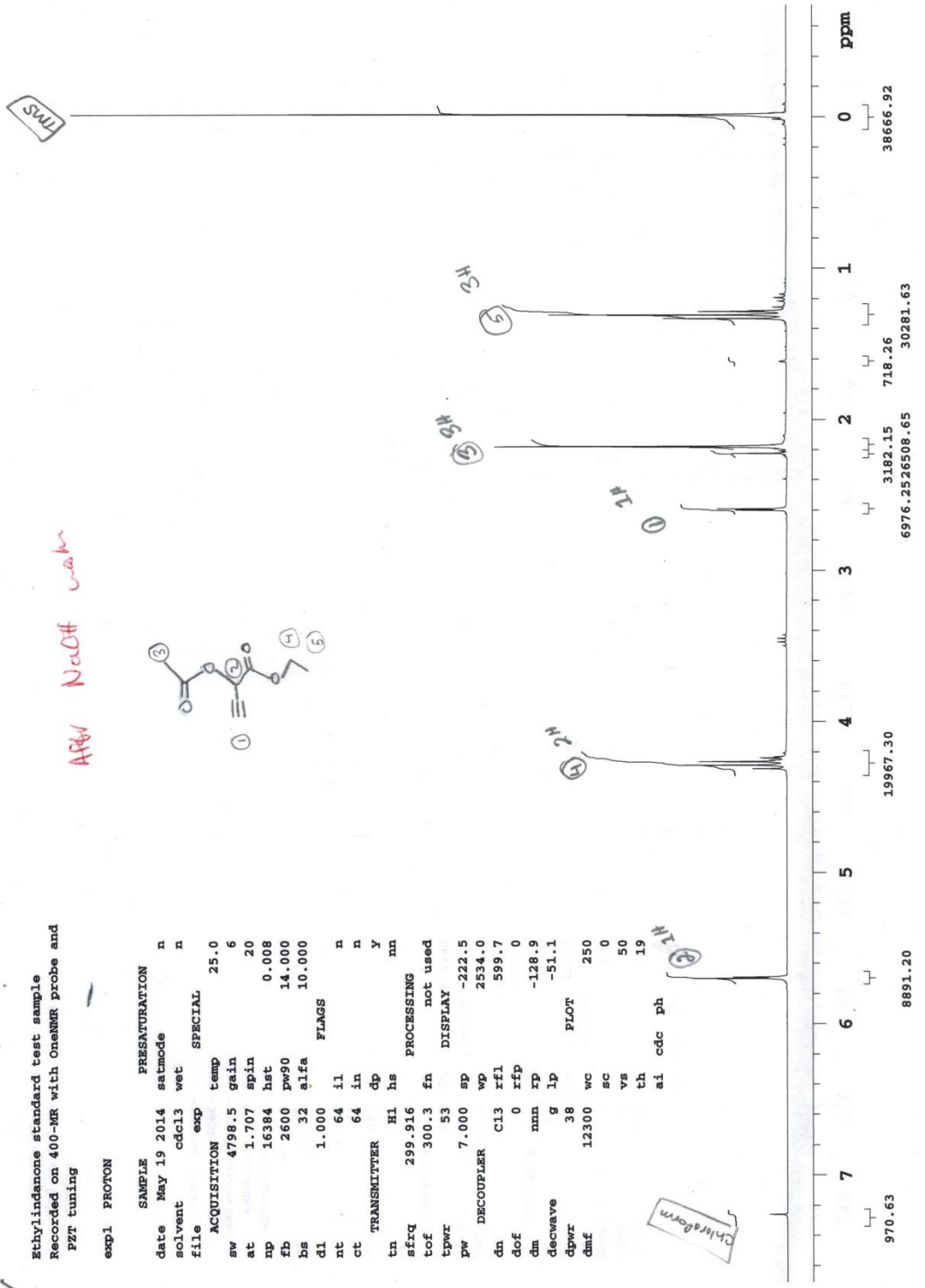
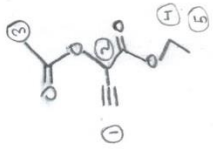


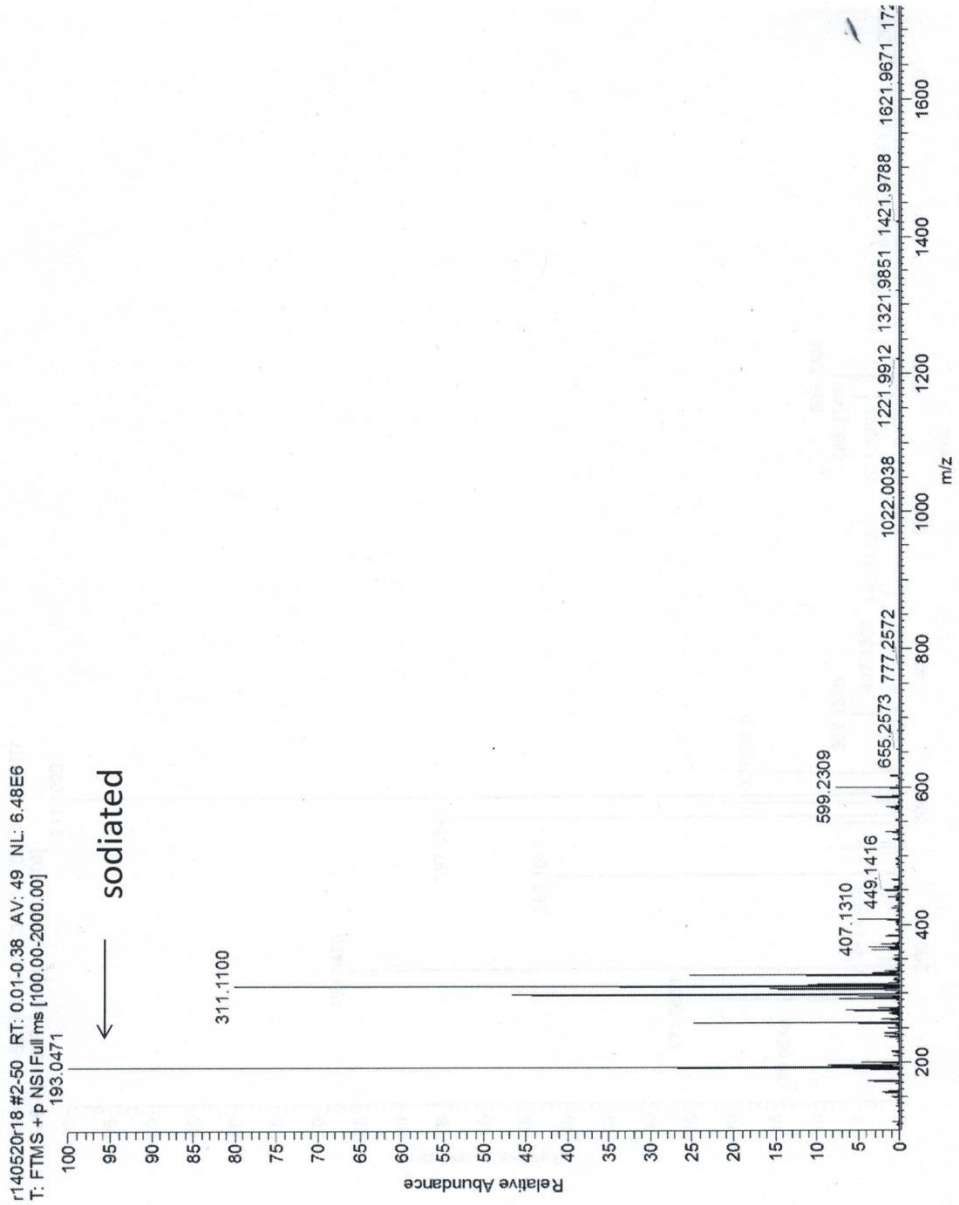
Ethylindane standard test sample
 Recorded on 400-MR with OneMR probe and
 PZT tuning

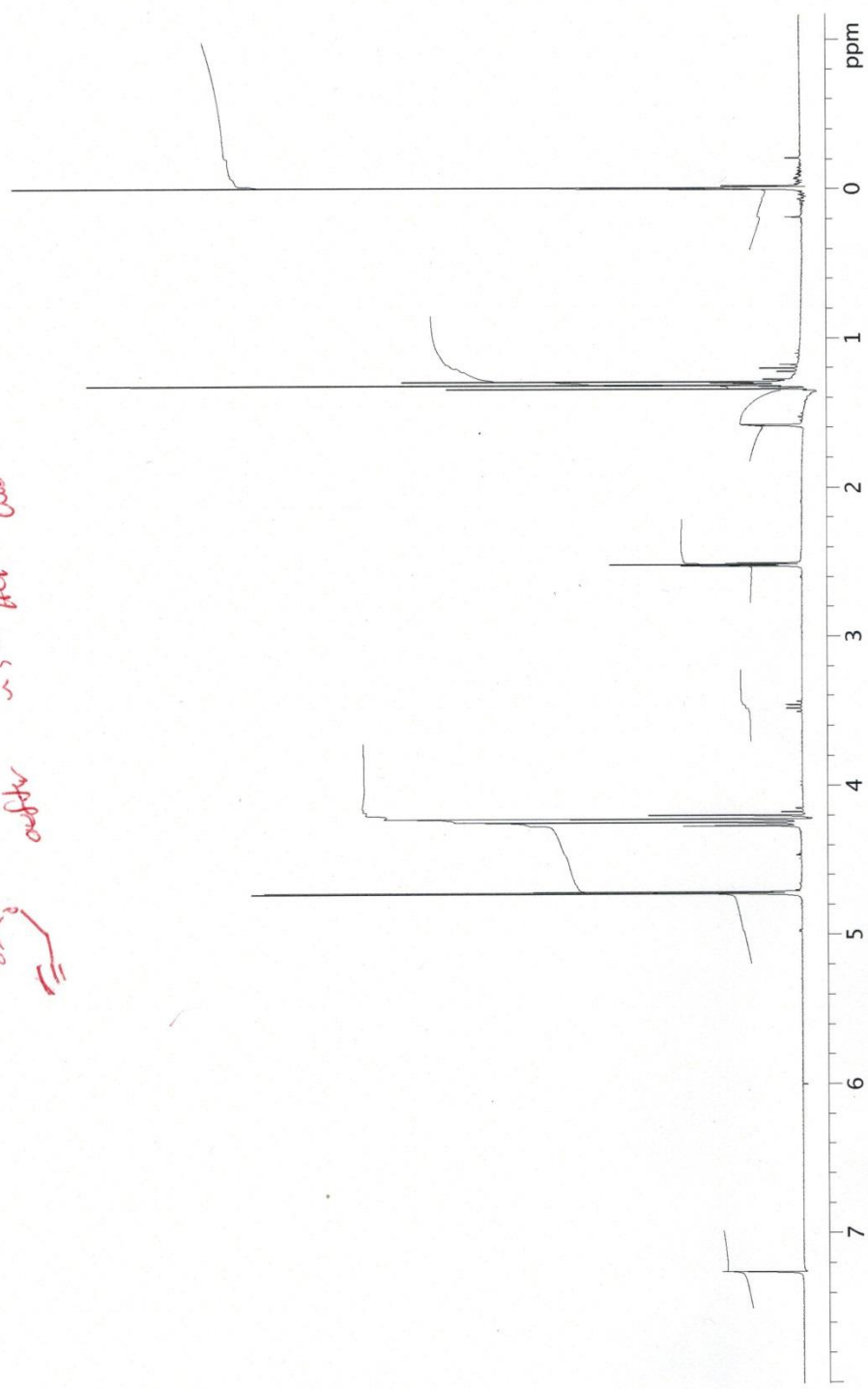
ARW NaOH wa.k

exp1 PROTON

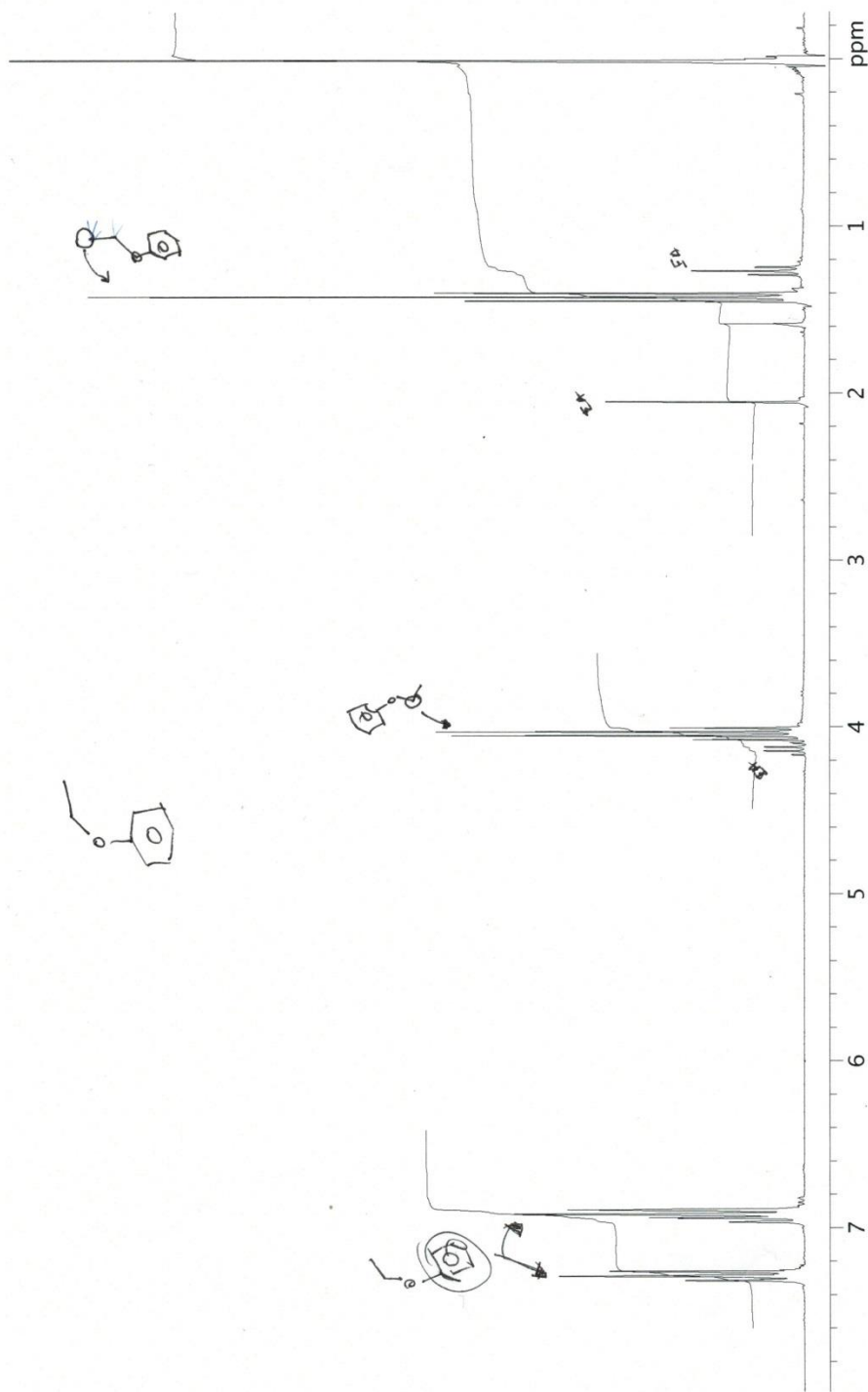
SAMPLE		PRESATURATION	
date	May 19 2014	satmode	n
solvent	cdcl3	wet	n
file	exp	SPECIAL	
ACQUISITION		temp	25.0
sv	4798.5	gain	6
at	1.707	spin	20
np	16384	hst	0.008
fb	2600	pw90	14.000
bs	32	alfa	10.000
d1	1.000	FLAGS	
nt	64	il	n
ct	64	in	n
TRANSMITTER		dp	y
tn	H1	hs	nn
sfrq	299.916	PROCESSING	
tof	300.3	fn	not used
tpwr	53	DISPLAY	
pw	7.000	sp	-222.5
DECOUPLER		wp	2534.0
dn	C13	rfl	599.7
dof	0	rfp	0
dm	mnn	rp	-128.9
decwave	g	lp	-51.1
dprw	38	PLOT	
dmf	12300	wc	250
		sc	0
		vs	50
		th	19
		ai	cdc
		ph	







io 10.0
 cr 5.71
 is 1582.4
 delta



io 10.0
 cr 5.92
 is 771.5
 delta

